Synthesis and Application of a Highly Fluorinated Ether Molecule as an Electrolyte Co-solvent for Enhanced Performance Rechargeable Lithium Batteries

by

Ruo Wang

(███████████████

A thesis submitted to the University of Birmingham for the degree of
DOCTOR OF PHILOSOPHY

School of Geography, Earth and Environmental Sciences
College of Life and Environmental Sciences
University of Birmingham
September 2023

Abstract

The demand for high-performance energy storage systems has driven significant research efforts in the field of secondary lithium batteries. As one of the key components of these batteries, electrolytes play a crucial role in determining their electrochemical performance and stability. In this thesis, a novel electrolyte has been explored to address the challenges and limitations associated with conventional electrolyte systems, which are described in Chapter 1. These challenges and limitations include compatibility issues with high-voltage cathodes, lithium metal anode, and graphite anode, as well as the electrolyte's high-voltage tolerance and stability under high temperature. These issues are critical factors that need to be addressed in battery technology development, as they are essential for improving battery performance and safety. Given the critical role of the solid electrolyte interphase (SEI) and cathode electrolyte interface (CEI) on electrode surfaces in influencing battery cycling, this thesis endeavours to develop and design an electrolyte that fosters the creation of highly stable SEI and CEI layers. The primary goal is to render this electrolyte compatible with high-energy-density, high-voltage lithium metal batteries initially, and subsequently expand its applicability to a broader range of electrode materials and operating temperatures.

The methods and approaches utilized in the thesis are presented in Chapter 2. Localized high-concentration electrolytes (LHCE) exhibit excellent compatibility

with both the lithium metal anode and the high-voltage cathodes. In Chapter 3, the development of LHCE is delved into, utilizing the meticulously designed and synthesized molecule, TTME (1,1,1-trifluoro-2-[(2,2,2-trifluoroethoxy) methoxy] ethane). The symmetrical structure of TTME reduces the overall molecule's polarity, thereby endowing it with diluent-like properties akin to traditional localized high-concentration electrolytes. Additionally, the competitive interaction between the strong electronegativity of oxygen and the -CF$_3$ group allows TTME to partially participate in the solvation structure of Li+ ions. The unique solvation structure of TTME facilitated the coordination of Li$^+$ ions, providing insights into electrolyte design.

In Chapter 4, the performance of TTME-d electrolyte, consisting of 1.4 M LiFSI and DME-TTME (1:4 by volume of 1,2-Dimethoxyethane and TTME) was investigated and found to have excellent electrochemical performance. Lithium metal cells made using this electrolyte demonstrated excellent stability, forming a double-layer SEI structure on the lithium metal surface, which can inhibit dendrite growth and ensure good cycling performance of lithium metal batteries. Additionally, this electrolyte can also generate a more stable CEI film on the cathode side, which helps prevent cathode pulverization and inhibits the dissolution of transition metal ions, thereby extending the cycling capacity.

Chapter 5 explored the co-intercalation of DME with graphite in Li||graphite cells using the TTME-d electrolyte, leading to stabilized performance and capacity retention. The fluorinated ether electrolyte system exhibited superior stability

compared to the conventional carbonate electrolyte, showing promise for high-voltage applications such as electric vehicles. Large-capacity NCM811||graphite pouch cells, utilizing the fluorinated ether electrolyte outperformed cells with a carbonate electrolyte under different temperature conditions were tested, and found to retain 91.7% capacity after 300 cycles.

Overall, the insights gained from this research provide valuable contributions to the field of secondary lithium batteries, particularly in the area of advanced electrolyte systems. The exceptional solvation structure of TTME, along with the formation of robust SEI on both anode and cathode, has opened new avenues for the design and optimization of electrolytes to meet the growing demand for high-performance energy storage technologies in various applications. These findings contribute to the development of more efficient and reliable secondary lithium batteries, bringing us closer to a sustainable and greener future.

Acknowledgments

instrumental in guiding my research direction. I would like to thank Prof. Jun Wang for his meticulous supervision as my co-supervisor. He patiently assisted me in refining each presentation, cheering me on before each report. He also dedicated time to revise my posters and papers, providing care and support during my times of illness. The members of the "Huiyuan Team" laboratory have also been immensely supportive and helpful. Together, we have shared a wonderful time of camaraderie and hard work. I am truly grateful for their encouragement and assistance.

My parents, despite never having traveled abroad, have always stood firmly behind me, supporting every decision I made. Their unwavering love has been my source of strength, and providing them with a better life remains my ultimate goal. I miss them dearly.

I have many long-time friends who may not have been involved in my academic pursuits, but their company always brings me a sense of freedom and relaxation. They have helped me understand the kind of life I aspire to, and I am thankful for their presence in my life.

Lastly, I want to express my appreciation to myself. Despite facing pandemic lockdowns in both the UK and China, enduring the torment of illness, and experiencing the loss of loved one and friend, I have persevered until now. Every experience has been meaningful, and I will continue to stay true to my initial aspirations and forge ahead with determination.

Contents

Abbreviations

ADN Adiponitrile

BTFE Bis(2,2,2-trifluoroethyl) ether

C Charge/Discharge Current

CC-CV Constant Current-Constant Voltage

CE Coulombic efficiency

Cryo-TEM Cryogenic transmission electron microscopy

CV Cyclic Voltammetry

DCIR Direct Current Internal Resistance

DEC Diethyl Carbonate

DEMS Differential Electrochemical Mass Spectrometry

DFT Density Functional Theory

DMC Dimethyl Carbonate

DME 1,2-Dimethoxyethane

DME-d 1,2-Dimethoxyethane-based electrolyte

DMS Dimethyl Sulfoxide

DOL 1,3-Dioxolane

EC Ethylene Carbonate

EIS Electrochemical Impedance Spectroscopy

EMC Ethyl Methyl Carbonate

ESW Electrochemical Stability Window

EV Electric Vehicles

FTIR Fourier Transform Infrared Spectroscopy

HCE High Concentration Electrolyte

HFE Hydrofluoroethers

HOMO Highest Occupied Molecular Orbital

ICP-MS Inductively Coupled Plasma–Mass Spectrometry

IL Ionic liquids

LCO LiCoO$_2$

LHCE Localized High Concentration Electrolyte

Li Lithium

LIB Lithium Ion Batteries

LiDFBOP Lithium Difluoro(oxalate)phosphate

LiDFP Lithium Difluorophosphate

LiFSI Lithium Bis(fluorosulfonyl)imide

LiTFSI Lithium Bis(trifluoromethanesulfonyl)imide

LiTFPFB Lithium Trifluoro(perfluorotert-butoxy)borate

LMB Li Metal Batteries

LSV Linear Sweep Voltammetry

LUMO Lowest Unoccupied Molecular Orbital

M mol/L

MD Molecular Dynamics

NCA LiNi$_{1-x-y}$Co$_x$Al$_y$O$_2$ cathode material

NCM LiNi$_{1-x-y}$Co$_x$Mn$_y$O$_2$ cathode material

NCM811 LiNi$_{0.8}$Co$_{0.1}$Mn$_{0.1}$O$_2$

NMP N-methyl-2-pyrrolidone

NMR Nuclear Magnetic Resonance

PC Propylene Carbonate

PFG-NMR Pulsed-field gradient nuclear magnetic resonance

PS 1,3-Propanesultone

Q Capacity Density

ROLi Lithium Alkoxides

SEI Solid Electrolyte Interface

SEM Scanning Electron Microscopy

SL Sulfolane

SN Succinonitrile

SOC State of Charge

TEM Transmission Electron Microscope

TFEO Tris(2,2,2-trifluoroethyl) orthoformate

TTE 1,1,2,2-Tetrafluoroethyl-2,2,3-tetrafluoropropyl

TTME 1,1,1-Trifluoro-2-[(2,2,2-trifluoroethoxy) methoxy] ethane

TTME-d 1,1,1-Trifluoro-2-[(2,2,2-trifluoroethoxy) methoxy] ethane-based electrolyte

V Operating Voltage

VC Vinylene Carbonate

W Energy Density

XRD X-ray Diffraction

XPS X-ray Photoelectron Spectroscopy

List of Figures

List of Tables

Chapter 1: Introduction

1.1 Rechargeable lithium batteries

1.1.1 Background

The energy crisis and environmental pollution have emerged as two major challenges limiting the sustainable development of human society. The rapid growth of the economy has led to the relentless consumption and excessive exploitation of non-renewable fossil fuels like coal, oil, and natural gas, intensifying the global energy crisis[1]. Concurrently, the utilization of fossil fuels has triggered global climate change and ecological pollution, significantly impacting human existence and sustainable progress[2,3].

Since the beginning of the 21st century, the development and utilization of renewable and clean energy sources such as solar energy, wind energy, hydroelectric power, and geothermal energy have become the essential path to address the global energy and environmental crises and promote sustainable social development[4–6]. However, these renewable energy sources face limitations imposed by factors such as time, location, climate, and cost, making it challenging to achieve a direct and stable energy supply. To overcome these challenges, it is typically necessary to convert the energy generated by these renewable sources into electricity and store, transport, and utilize it for secondary purposes. Moreover, clean energy sources like solar, wind, and

hydroelectric power exhibit periodic and intermittent characteristics, leading to irregular fluctuations in the generated electricity over time. Directly integrating this irregularly fluctuating electricity into the power grid for transmission and utilization can cause disturbances. Therefore, the development of efficient and stable systems for electrical energy storage and conversion is fundamental to achieving stable transmission and utilization of renewable energy. Table 1.1 provides a summary of common methods for energy storage and conversion, along with a brief introduction and a list of their respective disadvantages [7-19].

Table 1.1 Summary of current energy storage and conversion methods.

Methods		Introduction	Disadvantages
Physical energy storage	Pumped energy storage[7]	Water from the lower reservoir is pumped to the upper reservoir for storage, while at peak electricity load electricity is generated from the stored water.	Requires special geographic conditions such as ramped elevation and water.
	Compressed air energy storage[8]	Utilizes surplus power to compress air and store it, releasing it at times of peak grid load to drive a gas turbine to generate electricity.	High investment costs; not suitable for small power systems.

	Flywheel energy storage[9]	Uses the high-speed rotating flywheel core as the medium for energy storage.	High demands on raw materials and technology.
Chemical energy storage	Lead-acid battery[10,11]	The oldest chemical energy storage method, widely used for electric bicycle or motorcycle power, backup power and lighting power, etc.	Small charge current, difficult to apply to large-scale storage.
	Sodium-Sulfur battery[12]	At a certain operating temperature, a reversible reaction occurs between sodium ions and sulfur, resulting in the release and storage of energy.	Heating equipment is required to maintain temperature, low safety.
	All-Vanadium flow battery[13]	The electrolyte flows to the electrode surface and reacts, the double electrode plate collects and conducts the current to convert it to energy.	Low specific energy, large electrolyte reservoirs, difficult to manage.
	Nickel Cadmium battery[14]	A direct-current powered battery in which Cadmium and hydroxide ions combine to form cadmium hydroxide and release electrons.	Cadmium is an environmental pollutant; short life cycle.

	Nickel metal hydride battery[15]	Hydrogen storage via aluminum alloy is used instead of cadmium to reduce environmental pollution.	High cost, lower safety than the traditional (i.e., Nickel Cadmium) battery .
	Rechargeable lithium (Li) batteries[16]	Best overall performance, adjustable battery size for specific needs. (How this battery works is described in section 1.1.2 below).	Safety under extreme conditions still needs to be improved.
Electromagnetic energy storage[17]		Converts electrical energy into magnetic energy and stores it in the magnetic field of a superconducting coil.	Superconducting states require extremely low temperatures.
Phase change energy storage[18,19]		Certain substances absorb or release energy through a phase change at specific temperatures.	High requirement for ambient temperature and high costs.

Among the various energy storage and conversion methods, electrochemical technology has emerged as one of the most viable and efficient means of energy conversion and storage. Within this domain, rechargeable (or secondary) lithium batteries play an exceptionally critical role[20].

In 1991, Sony Corporation of Japan achieved the commercialization of the graphite||LiCoO$_2$ battery. This type of battery enables charging and discharging

through the migration of lithium ions, without the presence of elemental lithium within the battery. Hence, it is named the "**Lithium ion Battery (LIB)** "[21] . Over the subsequent three decades, lithium ion batteries with superior energy density and extended lifespans steadily ascended to a position of prominence in the secondary battery market [22]. As depicted in Figure 1.1, the demand for lithium ion batteries has exhibited continuous annual growth, with its pace accelerating progressively. Projections indicate that by the year 2030, the demand is anticipated to soar to an impressive 2000 GWh[23].
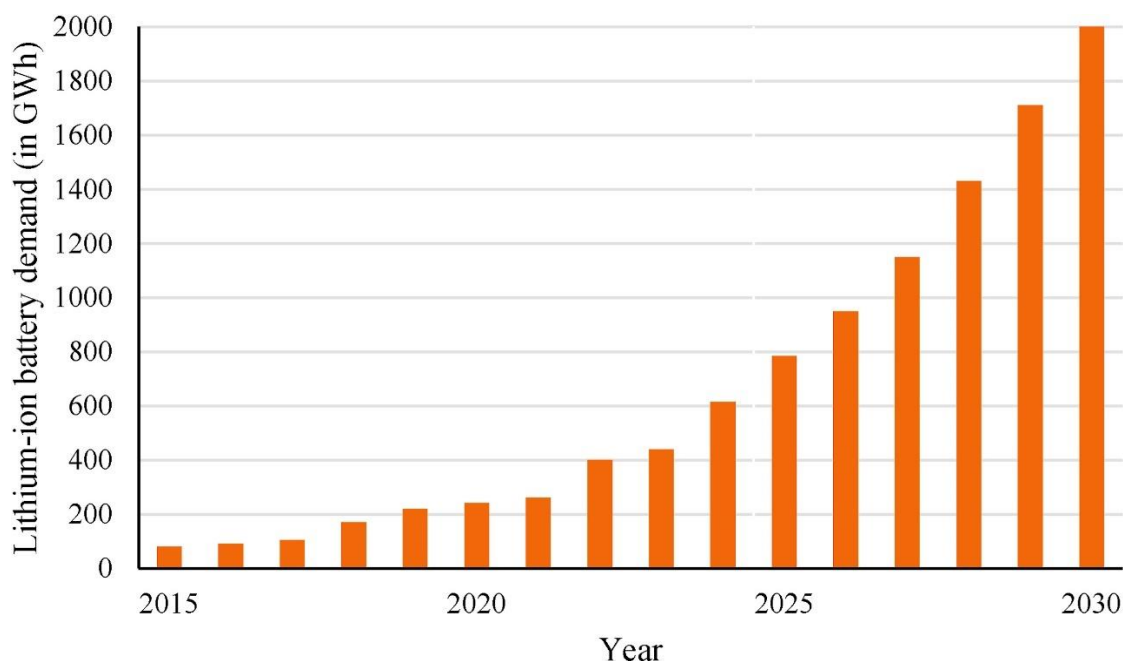
Fig. 1.1. Current battery demand and forecast future growth [23].

A major driver for the increased battery demand is the growth in availability of electric vehicles (EVs), which have become widely integrated into the automobile industry as the most promising alternative for addressing global

warming issues related to transport. The global sales of EVs have witnessed

steady growth over time, and projections indicate that by 2040, approximately

54 million EVs will have been sold, as depicted in Figure 1.2. By the year 2040,

the estimated global EV production is anticipated to reach a significant

milestone of around 60 million units.
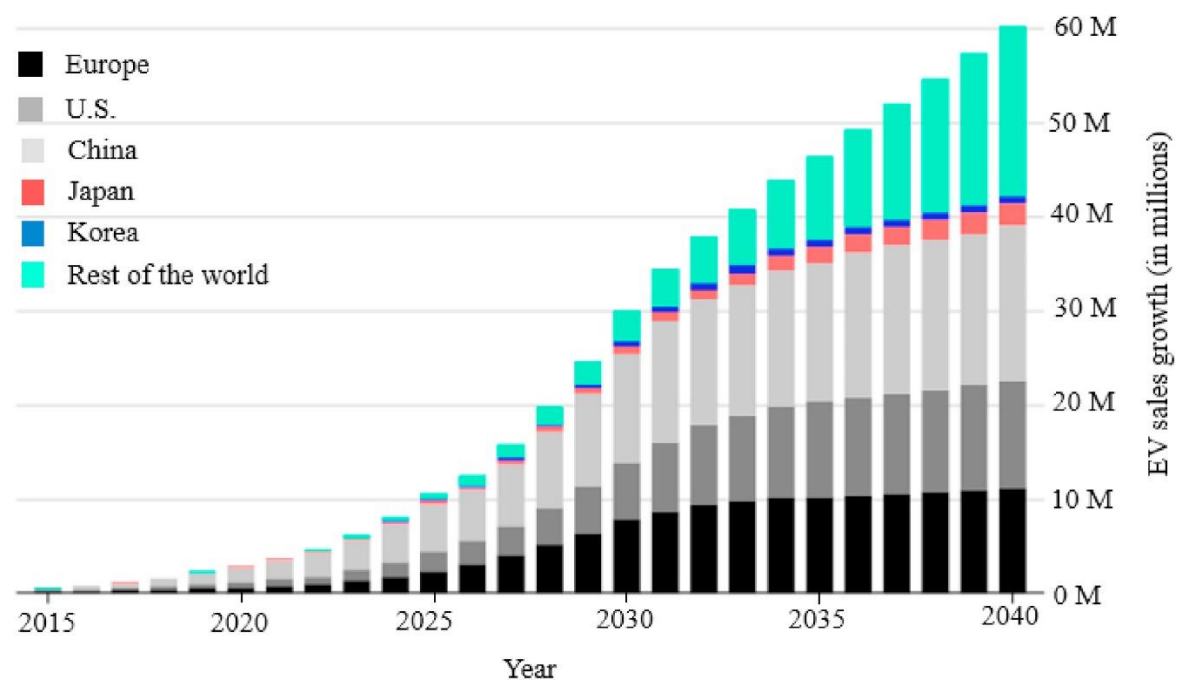
Fig. 1.2. Electric vehicles sales and forecast sales [23].

As the demand for EVs continues to surge, the usage of lithium ion batteries,

which are crucial components for these vehicles, is set to reach unprecedented

levels. The rise in EV adoption will be accompanied by a proportional increase

in lithium ion battery deployment, underscoring the essential role that lithium

ion batteries play in the ongoing transformation of the automotive industry [24,25].

1.1.2 Components of rechargeable lithium batteries and their functions

Rechargeable lithium batteries can be broadly classified into two categories based on their anodes: lithium ion batteries (LIB) and lithium metal batteries (LMB). Both types of batteries operate on a fundamentally similar principle. In the case of LIB, the anode consists of intercalation (like graphite), alloy (like silicon), or conversion materials (like molybdenum oxides). Conversion involves significant chemical changes and the creation of new compounds, while alloying maintains the crystal structure of the material with added lithium atoms[25]. In contrast, LMB are distinctively characterized by their use of metallic lithium as the anode[26].

Figure 1.3 presents the fundamental structure of an LIB with graphite anode and its operational mechanism during the charge and discharge processes. The cathodes and anodes play a central role in the chemical reactions involving lithium ions. To prevent direct electrical contact between the electrodes, separators are placed between them. Current collectors are utilized to gather the generated current from the electrodes and establish a connection with the external circuit. Serving as the vital "lifeblood" of the battery, the electrolyte acts as an indispensable medium for the transfer of lithium ions between the cathodes and anodes [27,28].
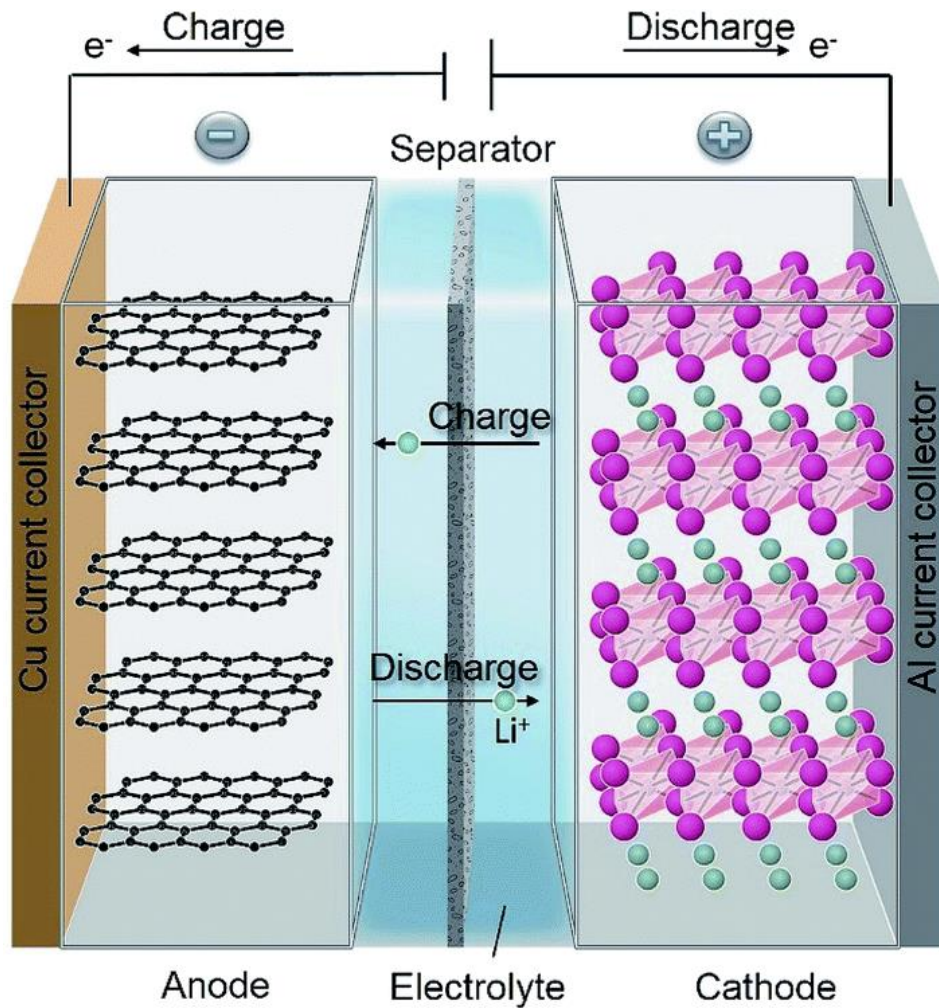
Fig. 1.3. Working mechanism of a typical intercalation anode (graphite) LIB[27].

The cathode materials are generally composed of lithium iron phosphate, lithium cobalt, lithium nickel manganate, lithium manganate, or other lithium-rich materials, and ternary materials, which are typically blended with conductive agents and binders before being coated onto aluminum foil, as shown in Fig. 1.3 Anode materials include graphite, lithium titanate, intermediate-phase carbon microspheres, silicon-carbon materials, and other substances that are mixed with conductive agents and binders and then coated

on copper foil, as shown in Fig. 1.3. The separator primarily consists of polyethylene, polypropylene, and other polymeric materials[29,30].

In a lithium cobalt oxide - graphite (LiCoO$_2$||graphite) LIB, during charging, lithium ions from the electrolyte interact with the graphite host on the anode side, forming the corresponding lithiated products (LiC$_x$). At the same time, lithium ions are released from the LiCoO$_2$ on the cathode side and replenished into the electrolyte. During discharging, lithium ions from the electrolyte are embedded into the delithiated LiCoO$_2$, and at the same time, lithium ions are released from the anode to replenish the electrolyte. The reaction equations for these processes are as follows: Equations 1-1, 1-2, and 1-3 represent the cathode reaction, anode reaction, and the overall electrochemical reaction of the battery during the entire charging and discharging process, respectively[31].

Cathode reaction：$LiCoO_2 \leftrightarrow Li_{1-x}CoO_2 + xLi^+ + xe^-$ (1-1)

Anode reaction：$6C + xLi^+ + xe^- \leftrightarrow Li_xC_6$ (1-2)

Battery reaction：$LiCoO_2 + 6C \leftrightarrow Li_xC_6 + Li_{1-x}CoO_2$ (1-3)
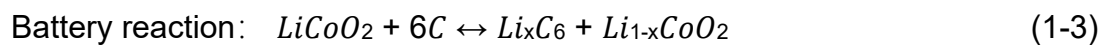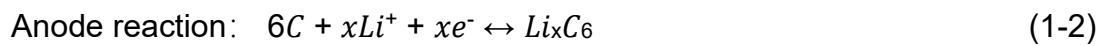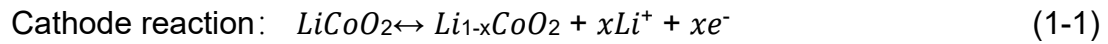
In LMB, the reaction mechanism of the lithium metal anode is of a deposition/stripping type. Taking the example of a LiCoO$_2$||lithium battery: during charging, lithium ions in the electrolyte gain electrons at the surface of the anode current collector (or lithium foil) and are deposited in the form of metallic lithium. At the same time, lithium ions are released from the LiCoO$_2$ on the cathode side and replenished the electrolyte. During discharging, lithium

ions from the electrolyte are embedded into the delithiated $LiCoO_2$, and at the same time, the metallic lithium on the anode side loses electrons and is stripped, transforming back into lithium ions that replenish the electrolyte. The reaction equations for the cathode reaction (Equation 1-4), anode reaction (Equation 1-5), and the overall electrochemical reaction (Equation 1-6) are as follows[32,33]:

Cathode reaction：$LiCoO_2 \leftrightarrow Li_{1-x}CoO_2 + xLi^+ + xe^-$ (1-4)

Anode reaction：$xLi^+ + xe^- \leftrightarrow xLi^0$ (1-5)

Battery reaction：$LiCoO_2 \leftrightarrow xLi^0 + Li_{1-x}CoO_2$ (1-6)
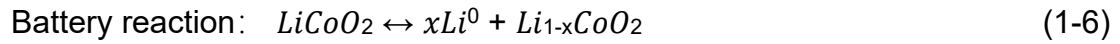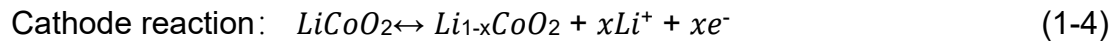
1.2 Overview of electrode materials in secondary lithium batteries

Secondary lithium batteries' energy density, which measures how much energy a battery can store relative to its weight, can be approximately calculated using Equation 1-7. In this equation, "W" represents the energy density (unit: Wh/kg), "Q" stands for the battery's charge capacity (unit: Ah/kg), and "V" denotes the battery's operating voltage (unit: V)[34].

$W = Q \times V$ (1-7)

To boost the energy density of the battery, the most direct and effective approach is to increase the capacity density (i.e., the (energy) generating capacity per unit mass) of the cathodes and anodes, as well as the voltage

difference between them[35].

1.2.1 Cathode materials

Currently, widely used cathode materials in both industrial applications and academic research include $LiFePO_4$, $LiMn_xFe_{1-x}PO_4$, $LiCoO_2$, $LiMn_2O_4$, ternary cathodes ($LiNi_{1-x-y}Co_xMn_yO_2$ (NCM), and $LiNi_{1-x-y}Co_xAl_yO_2$ (NCA)), and lithium-rich layered cathode materials such as $LiNi_{0.5}Mn_{1.5}O_4$, among others[36]. The performance characteristics of these typical materials are detailed in Table 1.2. In addition, Figure 1.4 shows the crystal structure of typical cathode materials. Among them, $LiFePO_4$ and $LiMn_xFe_{1-x}PO_4$ have slightly lower capacities that the other materials, but their existing technologies are relatively mature, with practical capacity reaching close to their theoretical capacity[37,38]. The development of the next-generation cathode materials will focus on achieving high voltage and high capacity [39,40]. Currently, various cathode materials have shown promising potential for development and for industrial applications, including $LiNi_{0.5}Mn_{1.5}O_4$, high-voltage $LiCoO_2$, high-nickel ternary materials, lithium-rich layered materials, and sulfur-based cathodes[41–47].

Table 1.2 Summary of the properties of typical cathode materials [41-47].

	$LiCoO_2$	$LiFePO_4$	$LiNi_8Co_1Mn_1O_2$	$LiNi_{0.5}Mn_{1.5}O_4$
Crystal structure	layered	olivine	layered	spinel
Average nominal voltage vs lithium metal (V)	3.7-3.8 (High-voltage: 4.4-4.5)	3.3-3.4	4.15-4.4	4.7-4.8
Theoretical specific capacity (mAh/g)	274	170	280	147
Actual specific capacity (mAh/g)	140-160 (High-voltage: 185)	140-160	170-200	120-130
Tap density (g/cm^3)	2.9-3.2	2.9-3.3	2.8-3.2	2.8-3.2
Mass energy density (Wh/kg)	440-540 (High-voltage: 580-650)	120-140	550-650	530-600
Volumetric energy density (Wh/L)	1100-1350 (High-voltage: 1400-1600)	350-400	1300-1500	1600-1800
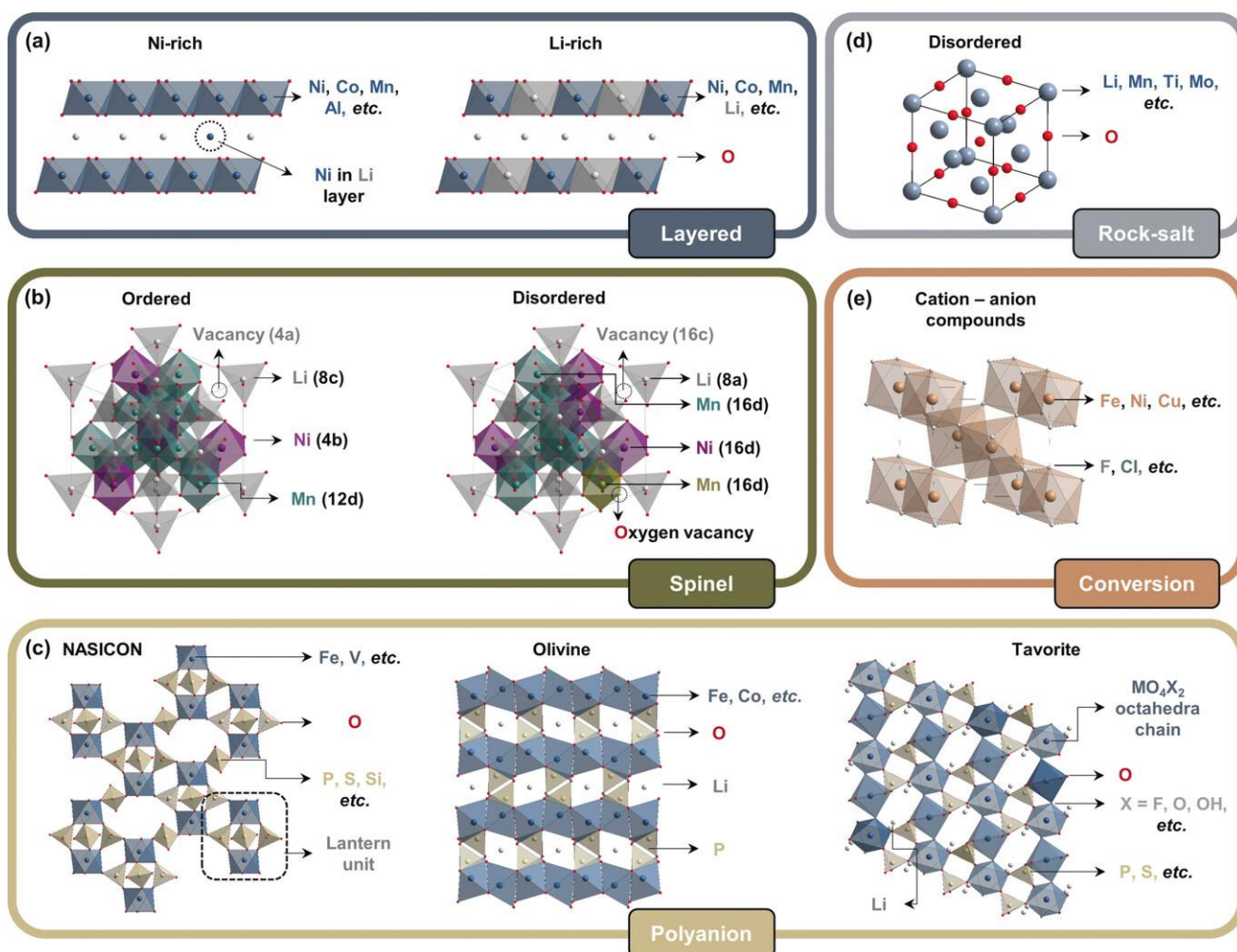
Fig. 1.4. Diagrammatic sketch of the crystal structure of typical cathode materials. Reproduced from[53].

Compared to other cathode materials, $LiCoO_2$ has many advantages, including high lithium content and high electronic conductivity, high mass energy density, and a long cycle life[48,49]. Therefore, even 30 years since its initial discovery, $LiCoO_2$ remains the primary cathode material in consumer electronic batteries. In the early applications of $LiCoO_2$, the cutoff voltage was generally limited to 4.2 V to avoid rapid degradation of the cycle life caused by material phase transitions. At this voltage, only 0.5 moles of Li^+ are deintercalated per mole of

$LiCoO_2$, resulting in a specific capacity of approximately 140 mAh/g. To meet the increasing demand for high energy density LIBs for so called 3C (Communication, Computer, Consumer-Electronic) products, both the academic and industrial communities are exploring methods to improve the high-voltage stability of $LiCoO_2$. Nowadays, the highest cutoff voltage for commercial $LiCoO_2$ has been increased to 4.5 V, achieving a reversible capacity of about 185 mAh/g with a considerable cycle life. Although the charging voltage of $LiCoO_2$ has been raised to 4.6 V at the laboratory level, it still faces challenges in terms of long-term cycle stability and safety when used in full cells [a, 50]. Considering that the compaction density of $LiCoO_2$ is much higher than that of other common cathodes, LIBs based on $LiCoO_2$ can have a higher volumetric energy density, further promoting the application of $LiCoO_2$ cathodes in portable devices.

The high cost of the Co element in $LiCoO_2$ materials has prompted researchers to seek low-cost and high-capacity alternative materials to reduce the cost of energy storage. Ternary materials such as NCM or NCA, which replace Co with Mn, Ni, or Al in the layered structure, have been proven to offer better battery performance at lower cost, making them the most promising cathode materials for the next generation of LIBs for automotive applications[51,52]. As shown in

---

[a] A full cell is where the two electrodes are connected by a salt bridge, whereas a half-cell configuration, often used to test battery performance, is where one of the electrodes is placed into an electrolyte solution with a lithium metal electrode acting as both the counter and reference electrode.

Figure 1.5, the typical ternary powder particles consist of micrometer-scale secondary particles composed of multiple nanoscale primary particles[53]. This structural feature significantly increases the tap density, which is one effective strategy to improve the energy density of ternary cathode materials[51,54].
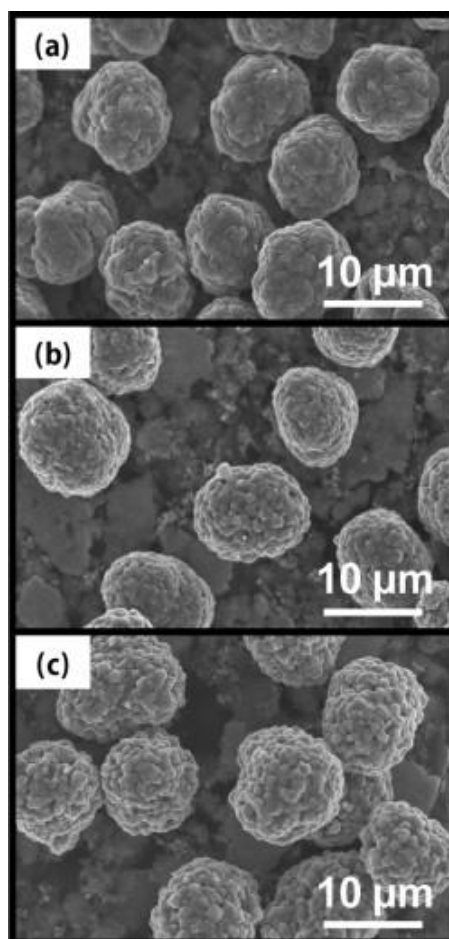
Fig. 1.5. Scanning Electron Microscopy (SEM) images of as-prepared Li[Ni$_x$Co$_y$Mn$_z$]O$_2$ powders: (a) x = 1/3, (b) x = 0.5, (c) x = 0.6. Image reproduced from[53].

Other effective methods to increase the energy density of ternary cathode materials include increasing the nickel content and modifying the materials to elevate the cutoff voltage[55]. Materials with higher nickel content exhibit high specific capacity, high working voltage, and relatively lower cost [56].

1.2.2 Anode materials

In the early stages of development of rechargeable lithium batteries, lithium metal was used as the anode. However, safety issues arose due to the growth of lithium dendrites. It was not until 1991 when Sony Corporation developed graphite anodes capable of reversible lithium-ion insertion and extraction, that LIBs truly became commercialized [57,58]. Currently, graphite remains the most widely used anode material in commercial LIBs, with complete lithium insertion forming LiC_6 and theoretically offering a specific capacity of 372 mAh/g. After nearly 30 years of development, the practical specific capacity of graphite anodes has reached approximately 365 mAh/g, approaching its theoretical capacity. However, it is still significantly lower than the increasing demand for energy density in electric vehicles (EVs). Moreover, during repeated charge and discharge cycles, graphite anodes and some components of the ether-based electrolyte and carbonate-based components undergo co-intercalation, leading to material degradation and performance deterioration [58–61].

There is now a growing demand for the development of higher-capacity anode materials. Among the emerging high-capacity anode materials, silicon-based anodes have shown the most promising potential for industrial applications [62]. Lithium metal anodes, on the other hand, are highly sought after due to their lowest potential and exceptionally high capacity, making them the "holy grail" of

lithium batteries[63].

Silicon is the most widely studied alloy-type anode and has already achieved some commercial applications. Elemental silicon possesses a theoretical specific capacity ranging from 3,579 mAh/g to 4,200 mAh/g ($Li_{3.75}Si$ to $Li_{4.4}Si$), whilst also having the advantages of abundant resources, low cost, and environmental friendliness. However, the direct application of elemental silicon as an anode material also faces some serious challenges[64,65]. The reaction between silicon and lithium results in a two-phase reaction, with part of the silicon lithiated into amorphous Li_xSi and the un-lithiated part remaining as crystalline Si. As silicon anodes experience a volume change of up to 300-400% upon complete lithiation, pressure gradients and anisotropic stress exist at the interface between Li_xSi and Si, ultimately leading to material cracking [66]. Additionally, the intense volume change causes continuous cracking and repair of the surface solid electrolyte interphase (SEI), leading to numerous side reactions and decreased Coulombic efficiency. Methods such as silicon particle nano-sizing, silicon-carbon composites, the use of silicon oxides, pre-lithiation, and the development of new binders have been effective in enhancing the stability of silicon anodes [67].

As the demand for higher battery energy densities increases, the academic and industrial communities are once again focusing on the development of lithium metal anodes. Lithium metal boasts a lower density (0.534 g/cm^3) and a theoretical specific capacity ten times greater than that of graphite anodes

(3,860 mAh/g vs. 372 mAh/g) [68,69]. Moreover, the lithium metal anode features

a low electrode potential (-3.04 V, vs the standard hydrogen electrode potential).

This attribute maximizes the utilization of the cathode material's reaction

potential, leading to a higher operating voltage and increased energy output of

the battery[70]. However, the lithium metal anode faces serious challenges such

as dendrite growth, interface instability, and significant volume expansion, as

shown in Figure 1.6, which are interconnected issues [71]. For instance, dendrite

growth can lead to the destruction of the solid electrolyte interphase (SEI),

exposing fresh lithium metal surface that reacts with the electrolyte, resulting in

further electrolyte consumption. Conversely, incomplete SEI or uneven lithium

plating can also trigger dendritic lithium formation[72].

Fig. 1.6. Correlations among the challenges in utilizing Li metal anodes: high
reactivity and infinite relative volume change and the resulting changes to the
electrode structure and surface, including disruption of the SEI[71].

To address these challenging issues, researchers have proposed various strategies to suppress dendrite growth, improve interface stability, and mitigate the volume expansion behavior, aiming to enhance the electrochemical stability of the lithium metal anode. These strategies include [73]:

(1) Electrolyte optimization: By refining the formulation and composition of the electrolyte, adverse interactions with lithium metal can be reduced, thereby improving battery performance.

(2) Three-dimensional frameworks: Using electrode materials with three-dimensional structures can provide a larger surface area, aiding in the dispersion of lithium ions, mitigating volume expansion, and promoting more stable electrochemical reactions.

(3) Interface layer modifications: Introducing a layer of higher stability material on the surface of lithium metal can reduce adverse reactions with the electrolyte, enhancing interface stability.

(4) Membrane modifications: Adding thin films or layers with specific properties can form protective layers on the lithium metal surface, reducing internal chemical reactions and improving battery lifespan.

These strategies aim to address the challenges associated with the lithium metal anode, with the goal of enhancing battery performance and stability. Each strategy has its advantages and applications, allowing for the selection of appropriate methods based on specific requirements.

1.3 Basic composition and functions of high-voltage LIB electrolytes

The requirements for liquid electrolytes in LIBs are as follows [74]:

(1) Low melting point and high boiling point: The state of the electrolyte is a crucial factor in determining the temperature range of battery operation. Having a low melting point and high boiling point ensures that the electrolyte remains in a liquid state over a wide temperature range, allowing the battery to operate in a broad temperature range.

(2) Low electronic conductivity and high ionic conductivity: Low electronic conductivity reduces self-discharge rates [b] due to reduced internal electrochemical reactions and enhances charge retention[c] by the electrolyte. High ionic conductivity improves the battery's rate capability [d] and reduces

---

[b] Self-discharge rate refers to the rate at which a battery system loses charge when not in use. It is caused by imperfect isolation within the battery or inevitable internal reactions. A low self-discharge rate is desirable because it indicates that the battery can maintain its charge state during storage without rapidly losing energy.

[c] Charge retention refers to the ability of a battery to maintain the stored charge level after being charged. Good charge retention means that the battery can hold its charge for a period of time without rapidly losing it. This is crucial for long-term storage and use of batteries, especially for applications where interrupted power storage and electrically dependent devices are involved.

[d] Rate capability refers to the ability of a battery to perform efficiently under different charge and discharge rates. It determines how much current a battery can provide or absorb in a short period, which is especially important for high-power applications such as electric vehicles, mobile devices, and energy storage systems. High ionic conductivity contributes to improved charge rate capability because it allows ions to move quickly within the battery, supporting faster charge and discharge rates.

ohmic polarization [e].

(3) Large lithium-ion migration number: Lithium ions in the electrolyte play a key role in the electrochemical reactions during battery operation. During charging and discharging, the electric field between the cathodes and anodes drives the migration of ions (lithium ions with a positive charge migrate towards the anode under the influence of the electric field, while anions such as PF_6^- with a negative charge migrate towards the cathode). Therefore, the electrical conductivity of the electrolyte is determined by the migration of both positive and negative ions (so a high electrical conductivity does not necessarily mean a high lithium-ion migration efficiency). However, in reality, only the migration of lithium ions is meaningful to us. Therefore, we define the migration number of lithium ions as the proportion of Li^{+} ion migration to the total ion migration in the electrolyte, as shown in equation 1-8. In this equation, "t_{Li+}" represents the lithium-ion migration number, "Q_+" represents the charge carried by positive ions, and "Q_-" represents the charge carried by negative ions.

$$t_{Li+} = \frac{Q_+}{Q_+ + Q_-} \tag{1-8}$$

From the above equation, we can see that the theoretical maximum value

---

[e] Ohmic polarization is the voltage loss caused by internal resistance within a battery. This voltage loss occurs due to the resistance between the battery's internal electrolyte and electrodes, resulting in extra heat generation and voltage drop during high-power applications. High ionic conductivity can reduce ohmic polarization by decreasing internal resistance, thereby improving the battery's efficiency and performance.

for the Li^+ ion migration number is 1, indicating that all lithium ions can fully migrate under the influence of an electric field. However, in practical LIBs, due to the characteristics of the electrolyte and interactions between Li^+ ions and other ions, the Li^+ ion migration number is typically less than 1. For example, current commercially available LIB electrolytes typically use $LiPF_6$ as the electrolyte salt. Although they have high electrical conductivity, their Li^+ transport numbers are generally below 0.5. This means that a significant portion of the electrical conductivity is provided by the anion PF_6^-. The main reason for this phenomenon is that when Li^+ dissolves in the electrolyte, it undergoes solvation, forming a solvation shell that limits the migration speed of Li^+ ions. Meanwhile, a concentration gradient of Li^+ ions occurs, leading to a larger concentration polarization, which affects the migration speed of ions. A large Li^+ ion migration number is crucial for the rapid charging and discharging processes of batteries.

(4) Large chemical and electrochemical windows: A large chemical window [f] ensures good compatibility between the electrolyte and other internal components of the battery (including the battery shell, current collector, electrode active material, conductive additive, binder, separator, etc. – see also Figure 1.3), preventing unintended (side) chemical reactions. A large electrochemical window [g] raises the upper limit of the battery's working

---

[f] A chemical window refers to the range or conditions under which electrochemical reactions can take place without being affected by other chemical reactions.
[g] An electrochemical window refers to the permissible potential range in an electrolyte solution

voltage, increasing the energy density of the battery, and reducing the number of series-connected cells required in the battery pack, thus reducing individual cell inconsistency and enhancing overall battery safety.

(5) Temperature adaptability: Lithium batteries must operate within varying temperature ranges. At low temperatures, electrolyte fluidity and ion conductivity decrease, affecting battery performance. Conversely, elevated temperatures can lead to increased evaporation and decomposition rates, impacting battery safety. Consequently, developing electrolytes with wide temperature adaptability is crucial.

(6) Environmental friendliness: Given the growing emphasis on environmental sustainability, it is vital to consider the environmental impact of the electrolyte. Opting for environmentally friendly and renewable solvents and additives, while minimizing the use of toxic substances, contributes to the overall sustainability of lithium batteries.

---

beyond which redox reactions become irreversible or undesirable reactions occur. The electrochemical window typically involves the redox potential in the electrolyte solution and the stability of the battery or electrode materials.
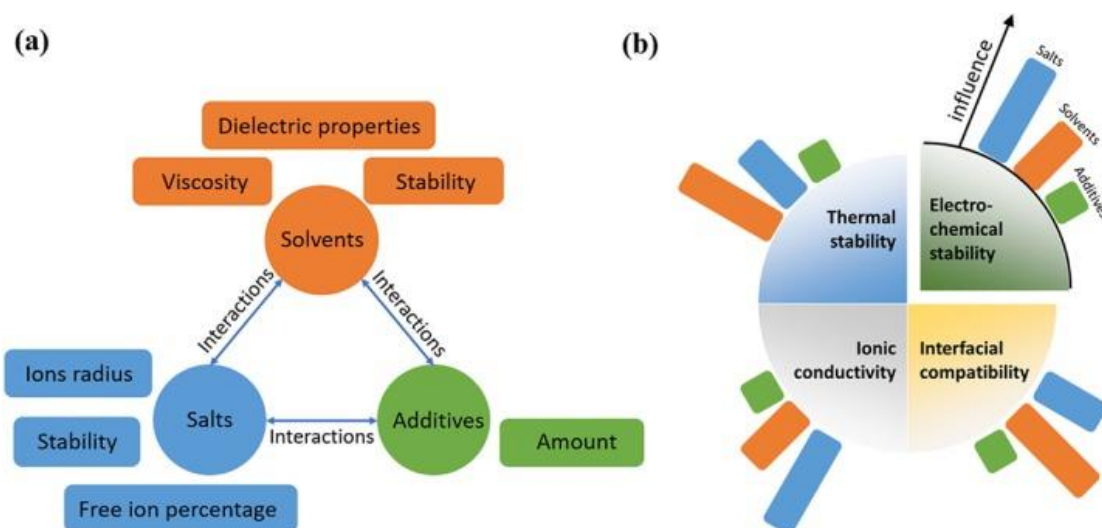
Fig. 1.7. (a) Design principles for the salts, solvents, and additives in liquid electrolyte and (b) Influence of each composition on the characteristics of electrolyte. Reproduced from[75].

LIB electrolytes are primarily composed of a mixture of various solvents with different properties, in which different lithium salts are dissolved to prepare the resulting electrolyte solution. Based on this, researchers consider adding different additives to enhance specific properties of the electrolyte to meet the required specifications, as shown schematically in Fig. 1.7[76]. Each of the specific components that need to be added to the electrolyte are discussed in Sections 1.3.1 – 1.3.3 below.

1.3.1 Solvents

The solvent for LIB electrolytes needs to possess a range of essential properties to meet its requirements. Firstly, the solvent should have a high dielectric constant and significant polarity. A higher dielectric constant and stronger polarity enable better dissolution of lithium salts, facilitating the "dissociation" of lithium ions and corresponding anions under the influence of an electric field, thereby enhancing the electrolyte conductivity. Secondly, the solvent's viscosity should be minimized to ensure high ionic conductivity. High viscosity can impede fluid flow, affecting the electrolyte's transport properties and, subsequently, reducing battery performance. Moreover, the liquid temperature range of the electrolyte is largely determined by the nature of the solvent. Hence, it is crucial to select a solvent with a broad liquid temperature range, especially where batteries are required to perform under extreme temperature conditions, in order to maintain the electrolyte's stability and performance. This implies that considerations of the solvent's melting point, boiling point, and flash point are essential when designing the electrolyte. Additionally, the solvent should be compatible with all components of the LIB to ensure battery stability and longevity. Considering the overall energy density of the battery, the relative molecular mass and density of the solvent molecules should also be kept in check. Lastly, cost-effectiveness is an important factor to consider.

The chosen solvent should be economically viable to ensure controlled battery

manufacturing costs. Figure 1.8 shows the structure of the most commercially used carbonate electrolyte solvents: ethylene carbonate (EC), propylene carbonate (PC), diethyl carbonate (DEC), dimethyl carbonate (DMC), and ethyl methyl carbonate (EMC)[77]. Table 1.3 presents the physical properties of these solvents.
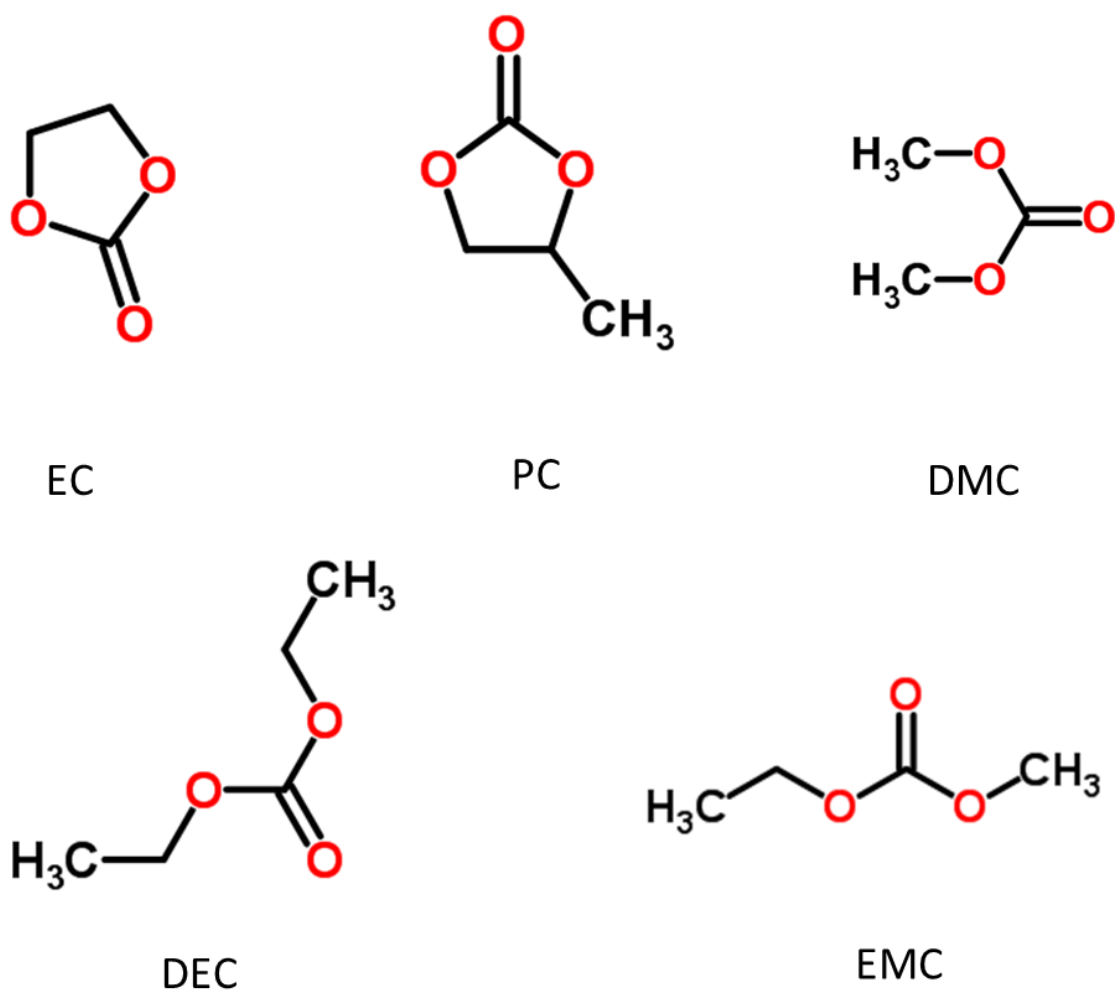
Fig. 1.8. Chemical structures of the commercially used carbonate electrolyte solvents.

Table 1.3. Physical properties of conventional carbonate solvents[75,77].

	EC	PC	DEC	DMC	EMC
Molar mass (g/mol)	88	102	118	90	104
Dielectric constant	89.8	66.1	2.8	3.1	2.4
Melting point (ºC)	36.4	-53	-43	4.6	-55
Boiling point (ºC)	248	242	126	90	108
Flash point (ºC)	160	132	31	18	23.9
Viscosity (mPa*s)	1.90 (40 ºC)	2.53	0.75	0.58	0.65
Density (g/cm³)	1.32	1.2	0.97	1.06	1.01

The development of LIB electrolyte solvents involves several key aspects [78,79]:

(1) Solvent selection and mixing: The selection and mixing of solvents are carried out based on careful consideration of their physical and chemical parameters. For example, a combination of solvents with high dielectric constants (having relatively high melting and boiling points) and solvents with lower dielectric constants (with generally lower melting points) is used to extend the temperature range of usability.

(2) Consideration of synergistic effects: Achieving optimal compatibility between the mixed solvent and electrode active materials is crucial. The mixed solvent should also be compatible with other components within the lithium-ion battery, such as the cathode aluminum foil.

(3) Avoidance of chemical/electrochemical reactions: Special attention is given to preventing any potential chemical or electrochemical reactions between different solvents that could negatively impact the electrolyte's performance.

(4) Balancing performance, price, and cost: Striking a balance between performance, price, and cost is essential to ensure that the selected mixed solvent meets both technical and economic requirements.

As a result, the formulation of mixed solvents and salts relies on empirical factors, considering the complex interplay of various parameters to achieve optimal performance and compatibility in LIB electrolytes.

1.3.2 Salts

The general formula for lithium salts is LiX, and the dissociation reaction is expressed as per equation 1-8 below:

$$LiX \rightarrow Li^+ + X^- \qquad\qquad (1\text{-}8)$$
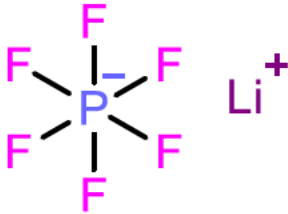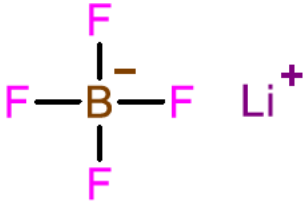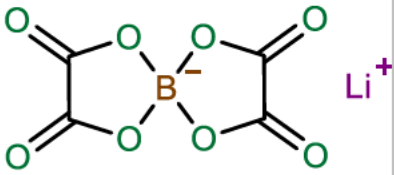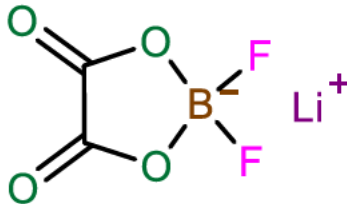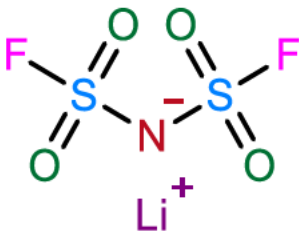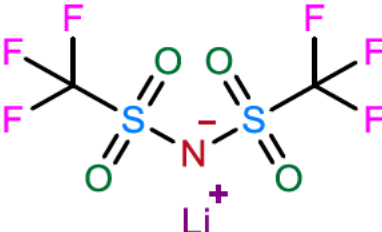
The dissociation reaction is governed by the solvation of lithium ions and anions in the solvent. Ideally, the anion (X^-) should exhibit strong interaction with the

solvent, while the solvation of the Li$^+$ ion should be relatively weaker[80]. However, in practice, the solvation ability of the anion X$^-$ is often lower due to its larger size, while the smaller Li$^+$ ion exhibits higher solvation, resulting in high solubility of the lithium salts but relatively low lithium ion mobility. The lithium ion migration numbers typically range from 0.2 to 0.45, with the majority concentrated around 0.25. In specific solvents like EC, DMC, and DEC, the lithium ion migration numbers fall within the range of 0.35 to 0.50[77,81].

The most commonly used lithium salt in LIBs is Lithium hexafluorophosphate, LiPF$_6$, while other extensively studied lithium salts include lithium tetrafluoroborate (LiBF$_4$), lithium bis(oxalato)borate (LiBOB), lithium bis(oxalato)trifluoroborate (LiDFOB), lithium bis(trifluoromethanesulfonyl)imide (LiTFSI), and lithium bis(fluorosulfonyl)imide (LiFSI) [82–87]. These newer lithium salts can compensate for some of the drawbacks of LiPF$_6$ such as its poor solubility in ether-based solvents and poor thermal stability (see Tabel 1.4). However, they each of the salts brings its own challenges, as each have some disadvantages in other aspects, such as ion conductivity and price, as shown in Table 1.4[88].

Table 1.4. The advantages and disadvantages of commonly used lithium salts[89].

Lithium salts	Structure	Advantages	Disadvantages
LiPF$_6$		(1) High ion conductivity; (2) Ability to form a stable protective film on the electrode surfaces.	(1) Poor solubility in ether-based solvents; (2) Poor thermal stability.
LiBF$_4$		(1) Wide operating temperature range; (2) Ability to form a stable protective film on the electrode surfaces.	Low ion conductivity.
LiBOB		(1) High ion conductivity; (2) Wide electrochemical window; (3) Good thermal stability; (4) Passivation protection for aluminum foils.	Poor solubility.
LiDFOB		(1) Good film-forming properties; (2) Good performance at low temperatures; (3) Ability to form a passivation layer on aluminum foils.	Relatively high cost.

LiFSI		(1) High ion conductivity; (2) Low sensitivity to water; (3) Good thermal stability.	Corrosion of aluminum foils at voltages above 4.2 V.
LiTFSI		(1) High solubility and ion conductivity; (2) Good thermal stability.	Corrosion of aluminum foils at voltages above 3.7 V.

The proper understanding and selection of lithium salts are pivotal in optimizing the performance and efficiency of LIBs.

1.3.3 Electrolyte additives

Additives play a crucial role as the third essential component in functional electrolytes for lithium batteries. They are primarily employed to address certain limitations that cannot be fully resolved by optimizing the choice of lithium salts and solvents alone. Although additives are typically used in small quantities (<10 % of the total electrolyte mass), they can significantly enhance the performance of the electrolyte. The selection of additives depends on the specific performance requirements of the battery[89].

Film-forming additives take precedence in the electrolyte composition, as they participate in oxidation/reduction reactions, forming protective interfacial layers

on the cathode and anode surfaces (called CEI and SEI, respectively)[90,91]. Cathode protectors are designed to reduce the impact of impurities like HF, which could potentially damage the cathode structure, and they mitigate the reactivity between the cathode and electrolyte at high charge states[92]. Improving wetting additives work to reduce the contact angle between the electrolyte and the separator and electrode, thereby facilitating faster and more uniform penetration of the electrolyte into the gaps of the separator and electrode. Additionally, flame retardant additives act to disrupt the chain reaction of thermal runaway by releasing phosphorus or fluorine radicals, effectively preventing further combustion and decomposition of the electrolyte[93]. On the other hand, overcharge additives undergo oxidation at the cathode side when the voltage surpasses a specific threshold. This process leads to the formation of polymer barriers that hinder charge transfer or generate redox shuttles to consume excess charge[94,95].

It is essential to carefully determine the appropriate amount and type of additives to add, as using too little or too much may fail to meet the specific functional requirements or even compromise the overall battery performance. A well-thought-out selection and incorporation of additives can significantly contribute to the overall stability, safety, and efficiency of lithium batteries[96,97].

1.4 Challenges and requirements of high-voltage LMB electrolytes

As a high-energy-density battery, lithium metal batteries (LMBs) face serious challenges in their electrolyte during the deposition and stripping processes of lithium, such as dendrite growth, interface instability, and volume expansion. These challenges significantly impact battery performance, safety, and overall efficiency. In order to advance the technology and realize the full potential of LMBs, addressing these challenges and meeting specific performance demands are of the utmost importance.

Figure 1.9 illustrates the relationship between the electronic energy levels of the electrolyte and the electrode material Fermi levels under ideal and actual conditions. Under ideal conditions, the Highest Occupied Molecular Orbital (HOMO) of the electrolyte is lower than the Fermi level of the cathode material throughout the charge and discharge processes, while the Lowest Unoccupied Molecular Orbital (LUMO) is higher than the Fermi level of the anode material[98]. In this situation, the Electrochemical Stability Window (ESW) of the electrolyte fully encompasses the working voltage range of both the cathode and anode, and no oxidation or reduction reactions occur at the electrolyte-electrode interfaces. However, in reality, the electronic energy levels of the cathode may partially or even completely exceed the HOMO level of the electrolyte, and the same applies to the anode. In this case, electrons may transfer from the higher energy level component to the lower energy level component of the electrolyte,

resulting in the oxidative/reductive decomposition of the electrolyte[94].
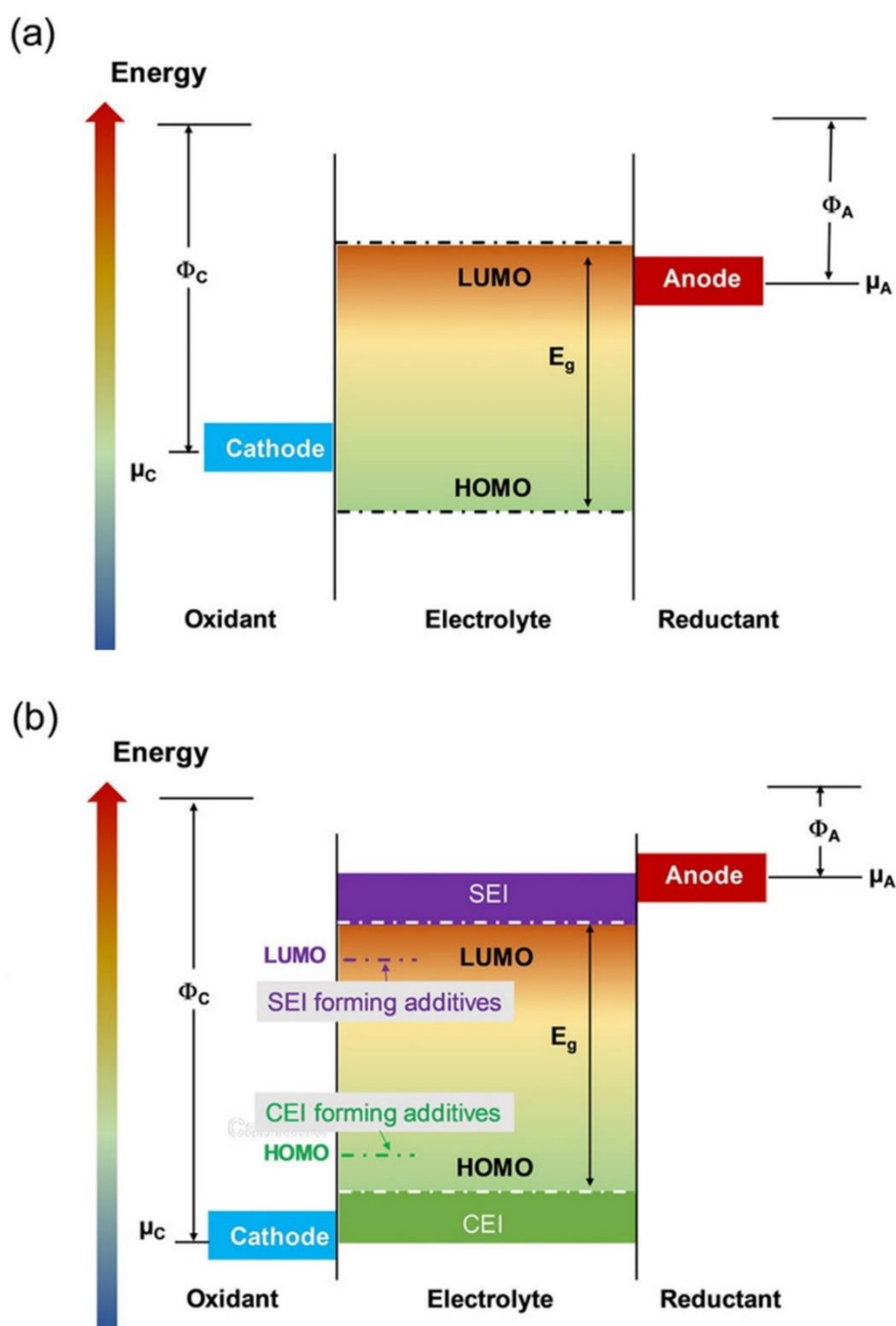
Fig. 1.9. Schematic energy diagram (a) without and (b) with film-forming additives[99].

Using additives with preferential reduction/oxidation characteristics to construct

a stable electrode-electrolyte interface layer is an effective approach to bridging

the energy level gap between the electrode and electrolyte, thereby reducing electrolyte side reactions, and improving electrode stability. Properties such as HOMO/LUMO energy levels, ionization potential/electron affinity, and chemical hardness are helpful for the rapid screening of potential film-forming additives. Cathode film-forming additives need to have a higher HOMO energy than the other components in the electrolyte to exhibit preferential oxidation. Lower ionization potential and chemical hardness are advantageous for the preferential oxidation of the additive. On the other hand, anode film-forming additives require a lower LUMO energy than the other components. Higher electron affinity and lower chemical hardness usually mean that the additive is more prone to reduction. However, meeting these energy level conditions does not guarantee the formation of a stable interface layer on the electrode surface. The decomposition products of the film-forming additives also need to be able to adhere stably to the electrode surface and provide high ionic conductivity and elastic modulus for the formed interface layer. In addition to constructing the interface layer, using solvents with higher oxidation/reduction stability can also contribute to improving the electrochemical window of the electrolyte and enhancing the interface stability between the electrolyte and high-voltage cathodes/lithium metal anodes [100].

1.4.1 Lithium metal - electrolyte interface challenges

The interface between lithium metal and the electrolyte is a critical aspect. The components and properties of the electrolyte may react with the lithium metal, leading to the formation of an unstable solid electrolyte interface (SEI). A stable and flexible SEI layer is essential to enable efficient lithium ion transport and ensure long-term battery performance [101].

The SEI layer on the lithium metal surface can be regulated *in situ* by the electrolyte. The structure of the SEI layer can be influenced by various components in the electrolyte, including the lithium salt, solvents, and additives.

Aurbach et al. studied the decomposition behavior of some lithium salts on the lithium metal surface. $LiPF_6$, $LiBF_4$, $LiSO_3CF_3$, and LiTFSI (highly reactive lithium salts) showed higher reactivity with metallic lithium compared to $LiClO_4$ and $LiAsF6$ (weakly reactive lithium salts) [102]. The SEI (Solid Electrolyte Interphase) layer formed by weakly reactive lithium salts is thinner and more stable on the lithium metal surface, while highly reactive lithium salts lead to the formation of a thicker SEI layer[103,104]. The SEI layer formed by some highly reactive lithium salts may increase in thickness during storage, thereby increasing the internal resistance of the battery. It was also found that solvents can undergo reduction decomposition on the lithium metal surface, and that the types of decomposition products are related to the type of solvent utilised. Among the cyclic carbonates, the main decomposition product of EC is $(CH_2OCO_2Li)_2$, and for PC, it is $CH_3CH–(OCO_2Li)CH_2OCO_2Li$. Among the linear chain carbonate solvents, the main decomposition products of DMC are

CH₃OLi and CH₃OCO₂Li, while for DEC, they are CH₃CH₂OCO₂Li and CH₃CH₂OLi[105,106]. With carboxylate esters, the main decomposition product of methyl formate is HCOOLi. For ethers, the decomposition product of tetrahydrofuran is ROLi($CH_3(CH_2)_3OLi$), while 1,3-dioxolane (DOL) mainly decomposes into $CH_3CH_2OCH_2OLi$ and HCO_2Li. The organic components in the SEI mainly come from solvent decomposition, while the inorganic components mainly come from lithium salt decomposition. The presence of water in the electrolyte suppresses the decomposition of both lithium salts and solvents and forms an SEI layer rich in Li_2CO_3, LiOH, and Li_2O on the lithium metal surface, as shown schematically in Fig. 1.10 [107].
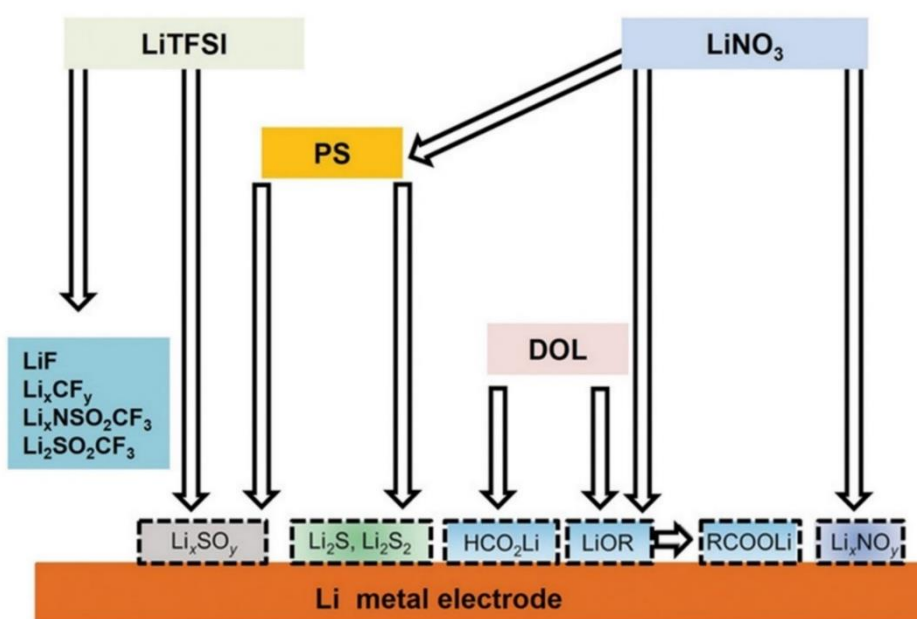
Fig. 1.10. Illustration of the decomposition products of a typical Li salt, solvent, and additives on a lithium metal anode[102].

Using suitable additives to enhance the stability of the SEI layer is an effective

approach to improve the SEI stability and durability. Additives targeting the high reactivity of lithium metal mainly function by preferential reduction to form a stable SEI layer or by adjusting the solvation structure of the electrolyte[108–110]. Typically, the reduction potential of film-forming additives should be higher than that of other components in the electrolyte, and the decomposition products should possess good chemical and electrochemical stability, allowing them to adhere to the lithium metal surface and thus to hinder electron transfer and facilitate Li^+ migration. The resulting SEI layer should have a high elastic modulus to inhibit the growth of lithium dendrites[111].

Besides directly constructing the SEI layer, the cations of $CsPF_6$ and KNO_3 can form an electrostatic shielding layer on the lithium metal surface, inhibiting further growth of lithium dendrites and promoting uniform Li^+ deposition[112,113]. AgTFSI can undergo a displacement reaction with lithium metal. The deposited Ag can act as nucleation sites for lithium deposition, promoting rapid and uniform lithium deposition. Additives containing Sn, Al, In, Ga, and other metals are introduced into lithium metal anode-based batteries to form a layer of lithium alloy on the lithium metal surface[114]. This alloy layer acts as a barrier between the lithium metal and the electrolyte, with its low impedance and high hardness, suppressing lithium dendrite growth. Similarly, MCl_x (M = In, Zn, Bi, As) additives can also react with lithium metal to form an alloy layer, which not only facilitates rapid lithium ion transport but also prevents the formation of lithium dendrites on the anode surface [115]. Crown ethers and hexafluoroacetylacetone

can directly regulate the solvation structure of Li$^+$, increase the number of nucleation sites for lithium deposition, and facilitate the formation of a smooth deposition morphology[116].

Traditional lithium borate salts such as LiBOB and LiDFOB have been proven to passivate the lithium metal anode surface as well[85,86]. New types of lithium salts, such as lithium difluorophosphate (LiDFP), lithium difluoro(oxalate)phosphate (LiDFBOP), LiCO$_2$CF$_3$, and lithium trifluoro(perfluorotert-butoxy)borate (LiTFPFB), can form SEI layers rich in LiF on the lithium metal surface with higher ionic conductivity and elastic modulus[100,117–119]. LiNO$_3$ can increase the content of Li$_3$N in the SEI, significantly enhancing the conductivity of the SEI and the exchange current density of the lithium metal anode[120].

1.4.2 Battery stability at high voltages

Under high voltage conditions, electrolyte stability becomes crucial. Intensified redox reactions within the electrolyte can accelerate its decomposition and oxidation, compromising battery efficiency and longevity. Hence, designing electrolytes capable of withstanding high voltages is imperative.

Figure 1.11 illustrates the common ways to improve the stability between the electrolyte and the high-voltage cathode[98]. The most direct and effective method to improve electrolyte compatibility with high-voltage cathodes is the

use of cathode film-forming additives[121]. Two silicon-containing film-forming additives, Tris(trimethylsilyl) phosphate (TMSP) and Tris(trimethylsilyl) borate (TMSB), can form stable CEI (solid electrolyte interphase) layers on the surface of high-voltage cathodes, enhancing the cyclic stability of the electrolyte over a wide temperature range[95,122].
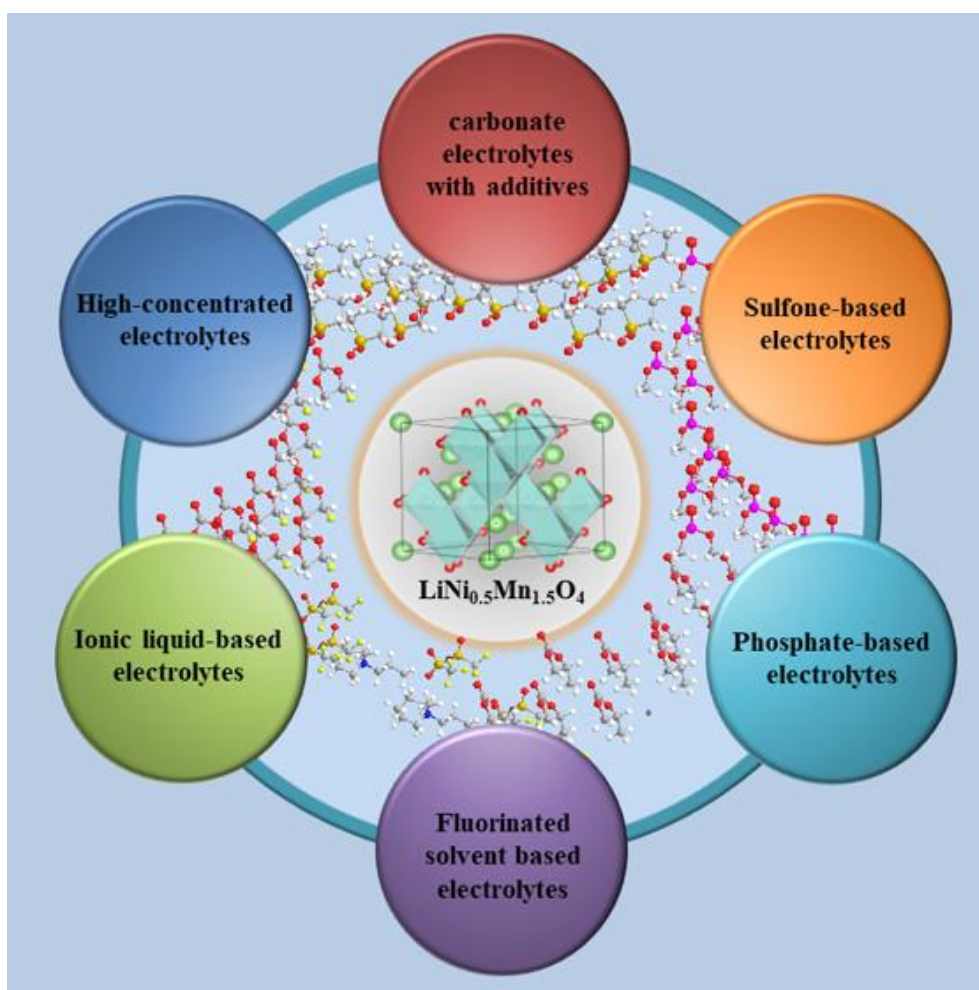
Fig. 1.11. Approaches to improve the high-voltage stability of the electrolyte. [98].

Carboxylate ester has also been proven to possess cathode film-forming capabilities. Dinitrile compounds, such as Succinonitrile (SN) and adiponitrile

(ADN), contribute to the formation of thin and dense CEI layers on the high-voltage cathode, inhibiting the dissolution of transition metal ions and improving the performance of the battery[123,124]. Some lithium salts, such as LiDFOB, and LiBOB, also exhibit cathode film-forming properties[94].

Radical scavengers can also enhance the performance of high-voltage electrolytes by slowing down or preventing decomposition chain reactions[125]. The development of novel additives with strong coordination to transition metal ions is also a vital research area to suppress side reactions related to transition metal ions[126].

Using solvents with higher antioxidant properties or high-concentration electrolytes can directly improve the oxidative stability of the electrolyte and enhance its compatibility with high-voltage cathodes[127,128]. Compared to commonly used ester and ether solvents, sulfone solvents have high dielectric constants (> 40) and high oxidation potentials (>5 V), making them highly compatible with high-voltage cathodes. Sulfone solvents with symmetrical structures, such as sulfolane (SL) and dimethyl sulfoxide (DMS), have relatively high melting points, which makes them difficult to be used as single solvents[129]. Lowering the melting point of sulfone solvents can be achieved by introducing asymmetric substituents. However, sulfone solvents have some drawbacks, such as high viscosity and complex synthesis, leading to low ionic conductivity and high costs of sulfone-based electrolytes [130].

Nitrile solvents are typically used not as single solvents but as co-solvents or additives. Common nitrile solvents can be classified into mononitrile and dinitrile solvents based on the number of nitrile groups in their molecular structure[130]. Among them, dinitrile solvents effectively improve the electrolyte's fluidity, thermal stability, and oxidation potential. However, nitrile solvents exhibit poor stability at low potentials, necessitating the addition of some anode film-forming additives to compensate for this deficiency[131,132].

The presence of some asymmetric substituents in the structure of ionic liquids hinders the crystallization of ions and reduces the melting points of the ionic liquids. The cations in ionic liquids include quaternary ammonium, imidazolium, pyridinium, pyrrolidinium, piperidinium, and morpholinium, all of which contain N, P, or S elements[133]. Common anions include TFSI-, FSI-, BF$_4$-, PF$_6$-, and so on. Ionic liquids (ILs) have a wide electrochemical window, high thermal stability, low volatility, and non-flammability, making them suitable solvents for high-voltage systems [134]. However, their high cost, high viscosity at room temperature, poor wetting of electrodes and separators, and poor compatibility with low-potential anodes hinder the practical application of ionic liquids[130,135].

Using high-concentration electrolytes with lithium salt concentrations exceeding 1 mol/L (M) can also enhance the oxidative stability of the electrolyte [136,137]. Compared to traditional electrolytes, high-concentration electrolytes have reduced free solvent molecules, and the ions form a multidimensional network structure, with ions primarily migrating along the network chains[138]. This unique

solvation structure enhances the chemical and electrochemical stability and safety of the electrolyte, including high oxidation stability, high reduction stability, inhibition of aluminum foil corrosion, fast electrode reaction rates, high thermal stability, and low volatility[136].

1.5 Application of ether-based electrolytes in lithium metal batteries

Commercial electrolytes mainly use carbonate solvents, but low-viscosity and highly wetting ether solvents have advantages in LMBs. In ether-based electrolytes, the lithium metal anode exhibits higher cycling stability than in other solvents. On the one hand, this is due to the higher LUMO energy and better reduction stability of ether solvents. On the other hand, the main decomposition products of ether solvents are ROLi (lithium alkoxides) and elastic oligomers. The SEI layer rich in these products can better accommodate the volume changes of the lithium-metal anode during cycling than the decomposition products of non-ether solvents[139]. Due to their good compatibility with the lithium-metal anode, ether solvents are widely used in Li-S and $Li-O_2$ batteries[140].

Ether-based electrolytes possess significant advantages when used in LMBs. They exhibit excellent reduction stability, resulting in better Coulombic efficiency and cycling performance of lithium metal deposition and stripping compared to

carbonate-based electrolytes[141]. For example, even with a 1 M concentration of LiTFSI dissolved in ethylene glycol dimethyl ether as a dilute ether electrolyte, the Coulombic efficiency of lithium metal anode deposition and stripping can exceed 95%[142].

Although ether-based electrolytes exhibit good compatibility with lithium metal, there are still some challenges to be addressed before applying these electrolytes to high-voltage lithium metal batteries, especially concerning the insufficient oxidative stability of the electrolyte[143]. In recent years, researchers have improved this situation by increasing the concentration of lithium salts in ether-based electrolytes to alter the solvation structure[142] (this was also mentioned in Section 1.4.2). The unique solvation structure enhances the chemical, and electrochemical stability, and safety of the electrolyte, including higher oxidative and reduction stability, inhibition of aluminum foil corrosion, rapid electrode reaction rate, high thermal stability, and low volatility.

However, despite the excellent performance of ether-based electrolytes, high-concentration electrolytes still face some issues[144]. Firstly, high-concentration electrolytes have high viscosity, making it challenging to effectively wet porous cathode materials. Porous cathode materials typically require good electrolyte wetting to ensure sufficient electrode kinetics, making these highly concentrated electrolytes impractical for use in LMBs. Secondly, these electrolytes demand a large quantity of expensive lithium salts, significantly increasing the cost of the electrolyte and battery[145].

To address these problems, researchers have added low-viscosity liquid substances with low dielectric constants into high-concentration electrolytes, such as ethers containing numerous fluorine atoms, especially 1,1,2,2-tetrafluoroethy1-2,2,3,3-tetrafluoroproxy ether and bis(2,2,2-trifluoroethy) ether[146,147]. These substances have a low dielectric constant, which prevents them from dissolving lithium salts or directly interacting with lithium ions [148]. Therefore, when these substances are added to the electrolyte, they can better preserve the solvation structure of the high-concentration electrolyte. As these low dielectric constant substances have almost no direct interaction with lithium ions, they effectively reduce the electrolyte's viscosity. Researchers have named these substances "diluents" [149]. It is generally believed that in such electrolytes, lithium ions and anions form numerous contact ion pairs and aggregates, which can move quickly back and forth between the electrodes in a medium filled with diluents[150] (see Figure 1.12). The structure of the high-concentration electrolyte becomes a collection of small clusters present in the diluent medium, leading researchers to term this electrolyte "localized high-concentration electrolyte"[151].
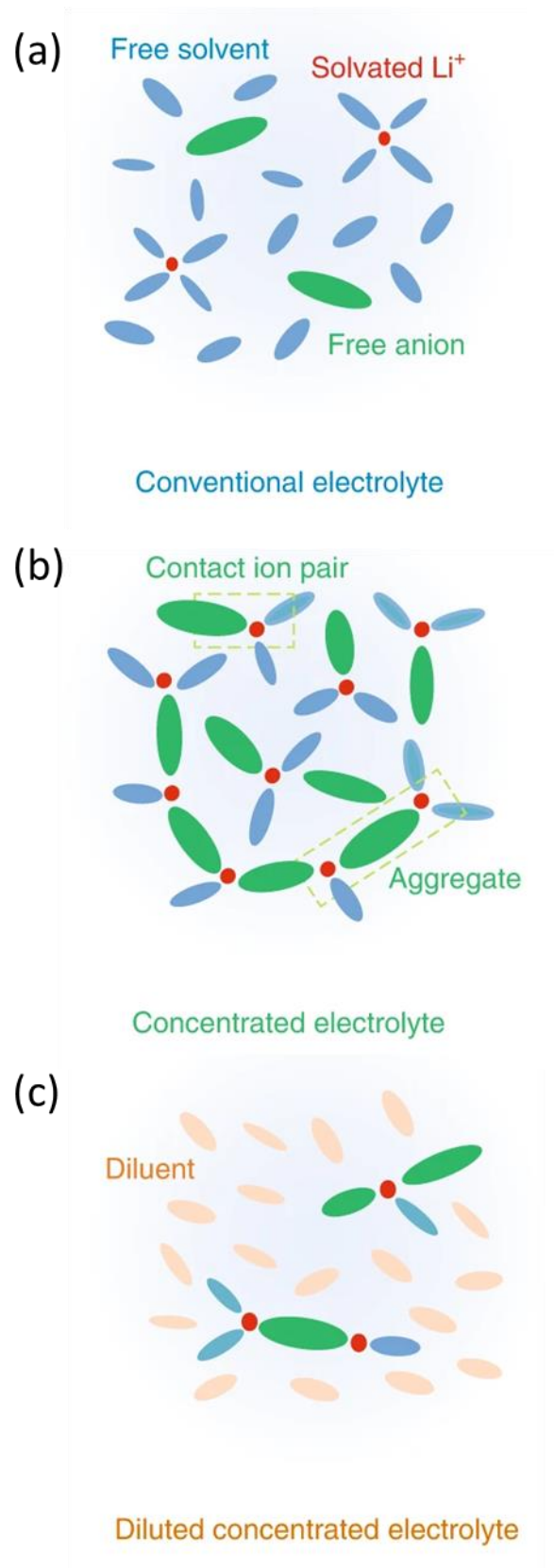
Fig. 1.12. Solution structures of (a) conventional (dilute) electrolyte, (b) concentrated electrolyte, and (c) diluted concentrated electrolyte where a low dielectric contract co-solvent is added as diluent. Reproduced from [150].

Based on the strategy of localized high-concentration electrolytes, researchers have developed a series of systems with performance superior to high-concentration electrolytes. Zhang et al. developed a localized high-concentration electrolyte composed of LiTFSI, ethylene glycol dimethyl ether, and 1,1,2,2-tetrafluoroethy 1-2,2,3,3-tetrafluoroproxy ether[152]. In this electrolyte, the lithium metal anode achieved an average Coulombic efficiency of 99.3% at a current density of 0.5 mA/cm^2, with stable cycling for 300 cycles. In comparison, the high-concentration electrolyte containing LiTFSI and ethylene glycol dimethyl ether showed a slightly reduced average Coulombic efficiency of 99.1% and a cycle life of 220 cycles[153]. Moreover, the low viscosity of the localized high-concentration electrolyte allows it to better wet the porous and loosely packed lithium metal surface formed during deposition and to suppress uneven lithium metal deposition caused by uneven lithium ion distribution, resulting in denser lithium metal deposition[154,155]. At a deposition capacity of 4 mAh/cm^2, the lithium metal thickness increased by 32 µm in the localized high-concentration electrolyte, whereas it increased by 40 µm in the high-concentration electrolyte[153]. The thinner lithium metal thickness in the localized high-concentration electrolyte indicates a denser deposition of lithium ions in this system.

Compared to other traditional strategies, the application of fluorinated ether-based LHCE represents an effective and straightforward method to achieve high battery efficiency. However, there are several unresolved issues that need

to be addressed [141-148,154], including:

1. How to reduce the high cost of lithium salts and co-solvents to facilitate the development of fluorinated ether-based LHCE and enhance lithium utilization efficiency.

2. How to optimize and screen the electrolyte formulation to ensure compatibility with a wider range of cathode and anode electrode materials, thereby reducing development costs.

3. How to understand and optimize the role and interactions of various components in the electrolyte, especially fluorinated ether molecules, during battery cycling to address the challenges encountered in fluorinated ether-based electrolytes.

4. How to adjust the solvation structure of the electrolyte to induce the formation of targeted SEI/CEI layers that are more suitable, thus protecting the positive and negative electrodes, improving battery CE, and enhancing overall efficiency and longevity.

These unresolved issues are critical for achieving a more stable and efficient battery technology, further advancing its commercial applications.

1.6 Application of theoretical calculations in electrolyte design

Designing new high-energy density energy storage systems typically requires a fundamental understanding of the atomic-level structure and processes of the materials. Theoretical computational models can characterize the structural changes, charge transfer, interactions, and other phenomena of materials at a microscopic level during electrochemical reactions in batteries. By exploring the relationship between material composition, structure, and properties, these models provide a theoretical basis for the development of new materials[156].

1.6.1 Density Functional Theory

Density functional theory (DFT) has played a significant role in the research into optimization of electrolytes for LIBs. DFT is a quantum mechanical approach that accurately describes the electronic structure and energetics of materials at the atomic level. In the context of electrolyte research, DFT enables the investigation of the interactions between lithium ions and solvent molecules, providing insights into the solvation structures and stability of various electrolyte components[157].

By employing DFT, researchers can study the redox potentials and stability of electrolyte species, which are crucial in understanding the electrochemical behavior of LIBs. DFT calculations also aid in exploring the thermodynamics and kinetics of lithium-ion diffusion within the electrolyte, providing valuable information on ion transport and conductivity. Furthermore, DFT can predict the

reaction mechanisms and activation barriers of electrolyte decomposition processes, offering valuable insights into the safety and stability of lithium-ion batteries [158]. The computational efficiency of DFT allows for the screening of various electrolyte materials, aiding in the design and optimization of novel electrolyte formulations with enhanced performance.

1.6.2 Molecular dynamics

Molecular Dynamics (MD) simulations have also been instrumental in the research on optimization of electrolytes for LIBs. By employing MD simulations, researchers can study the intricate dynamics and interactions of lithium ions and solvent molecules within the electrolyte at the atomic level. This enables a comprehensive understanding of the electrolyte's properties, such as ion diffusion, solvation structure, and conductivity. Additionally, MD simulations facilitate the investigation of electrolyte-electrode interfaces and the influence of different electrode materials on electrolyte performance[159].

MD simulations allow for exploration of the impact of various factors, such as temperature, pressure, and concentration, on the behavior of the electrolyte, providing insights into its behavior under different conditions. The ability to simulate complex molecular systems at the atomic level has contributed to advancing our knowledge of LIB electrolytes, aiding in the development of safer, more efficient, and high-performing battery technologies[160].

1.7   Key challenges addressed in this thesis

The quest for advanced energy storage solutions has spurred extensive research in the realm of secondary lithium batteries, which are designed for multiple recharge cycles. Among the vital constituents of these batteries, electrolytes assume a pivotal role in shaping their electrochemical capabilities and overall durability.

While carbonate-based electrolytes are currently the preferred choice for commercial LIB, they tend to undergo significant side reactions with lithium metal when applied in the development of next-generation high-voltage LMB. These reactions can lead to the growth of lithium dendrites and the formation of dead lithium, resulting in a range of safety concerns and irreversible capacity loss in the batteries. The controlled modification of electrolytes is considered a viable approach to addressing the aforementioned issues.

1.7.1 Design Strategy for the new molecule

Firstly, considering the compatibility between the electrolyte and lithium metal, ether-based electrolytes were chosen as the focal point of our research. Localized high-concentration electrolytes (LHCE) in ether-based electrolytes have been widely applied in high-voltage lithium metal batteries due to their enhancement of overall oxidation stability. Given the high cost of current LHCE

diluents, we conceived the idea of synthesizing new diluent molecules using inexpensive raw materials through a high-yield method.

A chain ether molecule with a terminal highly fluorinated (-CF$_3$) group was initially designed to meet the requirement for oxidation stability. Simultaneously, considering the characteristics of the diluent, a symmetrical structure of oxygen atoms and fluorine groups was designed to reduce the molecule's polarity. Ultimately, we selected 2,2,2-trifluoroethanol and dichloromethane, two cost-effective materials, to synthesize the new molecule: 1,1,1-trifluoro-2-[(2,2,2-trifluoroethoxy) methoxy] ethane (TTME). It is interesting to note that the synthesized molecule TTME, due to the competitive interaction between the strong electronegativity of oxygen and the -CF$_3$ group, possesses a relatively high electron cloud density compared to other diluents (shown in section 3.5), allowing it to partially interact with lithium ions based on the diluent function.

By employing this design strategy, the objective is to acquire a diluent molecule characterized by both high oxidation stability and cost-effectiveness, thereby offering a practical and economical solution for the exploration and utilization of high-voltage lithium metal batteries.

.

1.7.2 Thesis aims, objectives and hypotheses

The fundamental purpose of this thesis is to obtain the new molecule TTME through chemical synthesis and to assess its potential application as a co-

solvent in rechargeable lithium battery systems. By controlling the ratios of solvents and lithium salts, the objectives set out in Chapter 3 are to identify a suitable electrolyte formulation. Additionally, the unique properties of TTME are analyzed to investigate its role in the solvation structure of the electrolyte. This exploration seeks to determine whether TTME, besides acting as a conventional diluent, plays other roles in the electrolyte system, such as involvement in the inner solvation shell structure.

Given the generally better compatibility of ethers (compared to carbonates) with lithium metal, the TTME electrolyte formulation obtained will be applied to LMB systems in Chapter 4. The aim is to explore whether this formulation result in formation of a more stable SEI on the lithium metal surface compared to traditional ether solvents. Furthermore, its potential superiority in high-voltage cathodes will be examined.

To investigate the compatibility of this electrolyte formulation with various electrode materials, Chapter 5 will focus on its application in LIB with graphite electrodes. This is particularly important because graphite electrodes are often considered incompatible with ether-based electrolytes. The research will also assess whether this electrolyte can be employed in large-capacity commercial batteries.

Chapter 2 Experimental Details

This chapter focuses on battery cell preparation, equipment for material characterization, and performance of the various measurement methods used in this paper. Subsequent chapters will refer to the relevant content discussed in this chapter without repeating it.

2.1 General Cell Preparation

2.1.1 Coin cell assembly

The internal structure of a coin cell is shown in Figure 2.1. The cell assembly is conducted in the following sequence: cathode stainless steel can, cathode plate, separator, anode plate, spacer, spring, and anode stainless steel cap. During the assembly process, 25 µL of electrolyte is added on each side of the separator. For the assembly of a lithium-ion half cell, lithium foil is used instead of a conventional electrode for the negative electrode. It is essential to vacuum-dry all materials, except for the lithium foil, before usage to eliminate any potential moisture. Proper alignment of the cathode, separator, and anode during assembly is crucial to ensure the correct operation of the battery. The separator material employed is Celgard 2400 polypropylene film (diameter: 19 mm, thickness: 25 µm). Further chapters will provide detailed information on the preparation of the bespoke electrolyte as designed in this thesis and the

selection of the electrode materials.
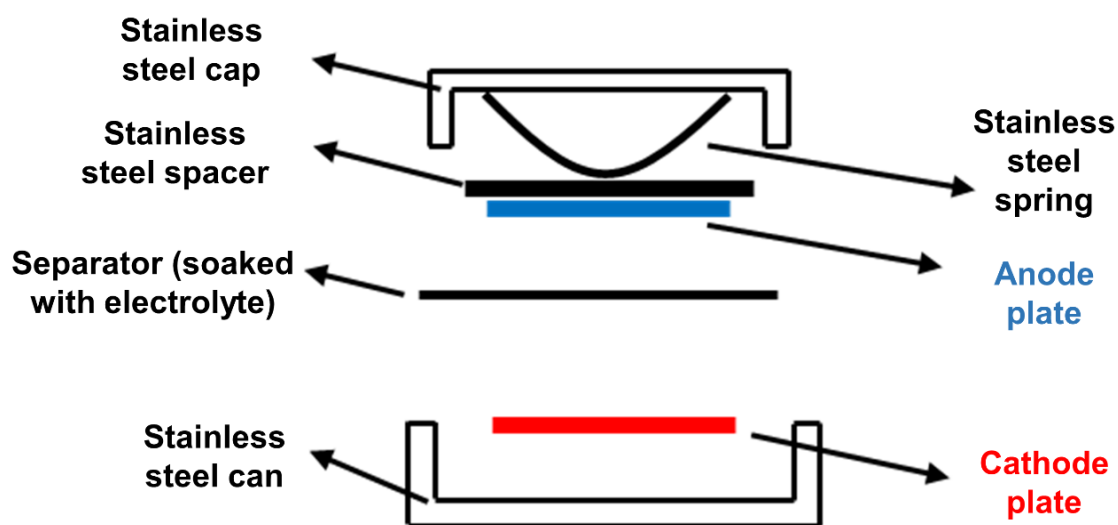
Fig. 2.1. Schematic representation of the structure of a coin cell battery.

2.1.2 Pouch cell preparation

The internal structure of a pouch cell is shown in Figure 2.2. The cell is comprised of an anode-separator-cathode-separator-anode loop. Typically, commercial pouch cells contain eight or more cathodes within a single cell[161]. The pouch batteries utilized in this thesis were provided by Capchem Technology Co. Ltd, China. To prepare the cells, the dry pouch cells were first cut and then subjected to a vacuum drying process at 85 ºC for 24 hours. Subsequently, 5.8 g of electrolyte was injected into the pouch cells, which were then sealed under a vacuum within an Ar-filled glove box. Following this, the cells underwent a 48-hour aging process in an oven set at 45 ºC, commonly known as the formation process.
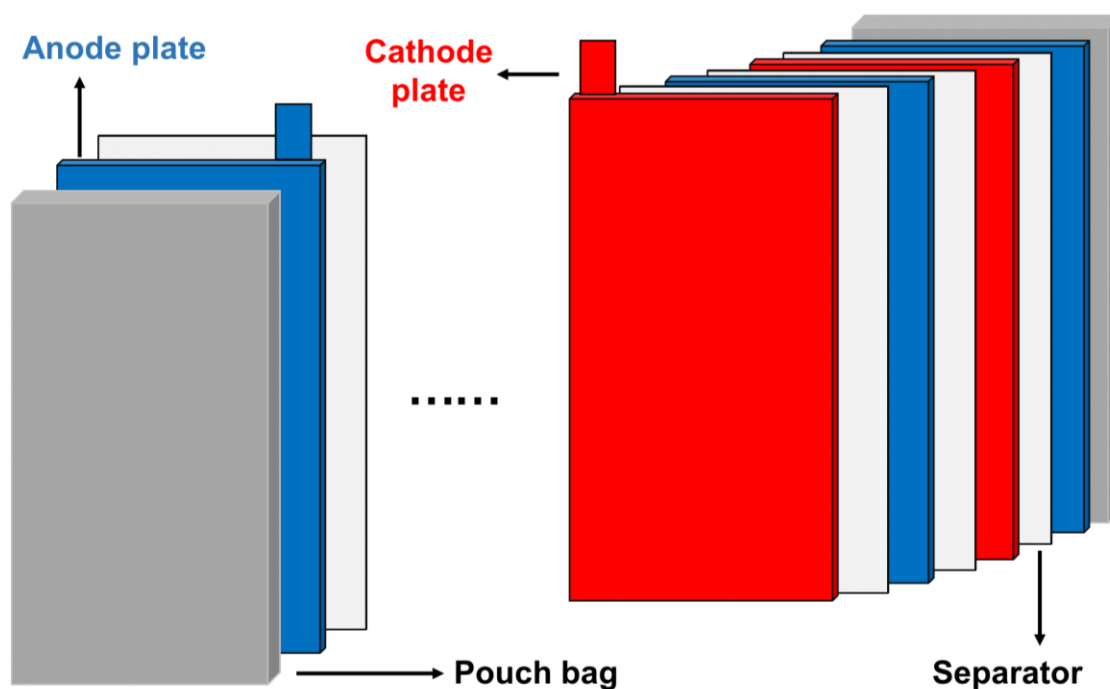
Fig. 2.2. Illustration of the structure of a pouch cell battery, showing the anode-separator-cathode-separator-anode loop.

Before the formal cycling process, pouch cells undergo a low-current pre-charge to accurately assess their capacity and select cells based on their performance. A group of three batteries with similar discharge capacities is carefully chosen for testing, reducing experimental errors. Subsequently, the pouches are carefully opened within a glove box to release any accumulated gases and promptly resealed. This step is crucial to maintaining a secure testing environment for subsequent experiments.

2.2 Electrochemical measurements

Unless otherwise specified, the temperature during testing is 25°C. All battery assembly processes are conducted inside a glovebox with water content below 1 ppm and oxygen content below 20 ppm.

2.2.1 Linear sweep voltammetry

The linear sweep voltammetry (LSV) test is a fundamental technique to evaluate the electrochemical stability window (ESW) of the electrolyte. A potential range is applied during the LSV test, starting from the lower limit and linearly scanning to the upper limit. It is generally believed that electrolytes start to fail and decompose when the current exceeds 0.01 mA, which corresponds to the maximum voltage they can withstand at that current.

Coin cells with lithium metal as the anode and aluminum foil as the cathode (Li||Al cells) were assembled for scanning tests within the voltage range from the open-circuit voltage [h] to 7 V. The cathode consisted of a 16 mm diameter aluminum foil, while the anode consisted of a 14 mm diameter, 400 µm thick lithium metal. The scanning rate was set at 0.5 mV/s. The experiments were performed using the Solartron electrochemical workstation (model 1470E, UK), as shown in Fig. 2.3.

---

[h] Open-circuit voltage is the voltage across the terminals of an electrical device when it is not connected to any load or current.

2.2.2 Cyclic voltammetry

Cyclic voltammetry (CV) is a highly useful electrochemical method employed to investigate the properties and mechanisms of chemical reactions. By repeatedly scanning the potential between two set voltages, different reduction and oxidation reactions occur alternately, and the current-potential curve is recorded. The shape of the curve provides information about the electrode reaction and its reversibility.

Several different battery configurations can be used for CV testing. For instance, in Chapter 4, a battery with lithium metal as the anode and copper foil as the cathode (Li||Cu cell) was used, operating within a voltage range of 0.01 V to 2 V. In Chapter 5, a battery with lithium metal as the anode and graphite as the cathode (Li||graphite cell) was utilized, with a voltage range of 0.01 V to 2 V.

2.2.3 Electrochemical impedance spectrometry

Electrochemical impedance spectroscopy (EIS) testing is employed to analyze the electrochemical impedance behaviour, providing insights into the battery/electrode's structure, solid electrolyte interface (SEI), thermodynamic characteristics, and other relevant information. To ensure consistent testing, the battery state of charge (SOC) was preconditioned to 50% by the program in the Neware battery tester. The testing conditions involved applying an AC voltage of 5 mV within a frequency range of 10^{-2} to 10^{6} Hz. The Solartron 1470E

electrochemical workstation (see Fig. 2.3), widely used for impedance spectroscopy, was utilized for conducting the impedance measurements.

Fig. 2.3. The Solartron 1470E electrochemical workstation.

2.2.4 Direct current internal resistance

When measuring Direct Current Internal Resistance (DCIR), it involves considering various types of resistances within the battery, including:

(1) Ohmic Resistance: Ohmic resistance is caused by the resistive properties of components within the battery, such as the electrolyte, electrodes, and connectors. It represents the total resistance encountered by the current as it flows through these components and is often temperature-dependent.

(2) Interface Impedance: Interface impedance refers to the impedance between the battery electrodes and the electrolyte. It may arise from chemical reactions at the electrode surface, structural characteristics, or material selection. High interface impedance can negatively impact battery performance.

(3) Charge Transfer Impedance: Charge transfer impedance involves the process of charge transfer from the electrode surface to the electrolyte within the battery. It is influenced by factors such as electrode material, electrolyte properties, and electrode reaction rates. High charge transfer impedance can reduce the efficiency of battery charge and discharge processes.

(4) Diffusion Impedance: Diffusion impedance relates to the diffusion of ions or molecules within the battery electrolyte. It is often associated with concentration gradients and diffusion rates within the electrolyte. High diffusion impedance may result in slower charge and discharge rates for the battery.

(5) Polarization Resistance: Polarization resistance encompasses Ohmic polarization, electrochemical polarization, and concentration polarization. Ohmic polarization is caused by voltage drops resulting from current flow through the battery components. Electrochemical polarization relates to the rates of electrochemical reactions within the battery.

These different types of resistances collectively influence the performance and efficiency of the battery. When measuring DCIR, analyzing these resistances provides a deeper understanding of the internal behavior of the battery, aiding in the optimization of battery design and performance. The DCIR was measured at 50% SOC during each cycle of pouch cells. The tests were conducted on the Neware battery tester (CT-4008T, China) , as shown in Fig. 2.4.
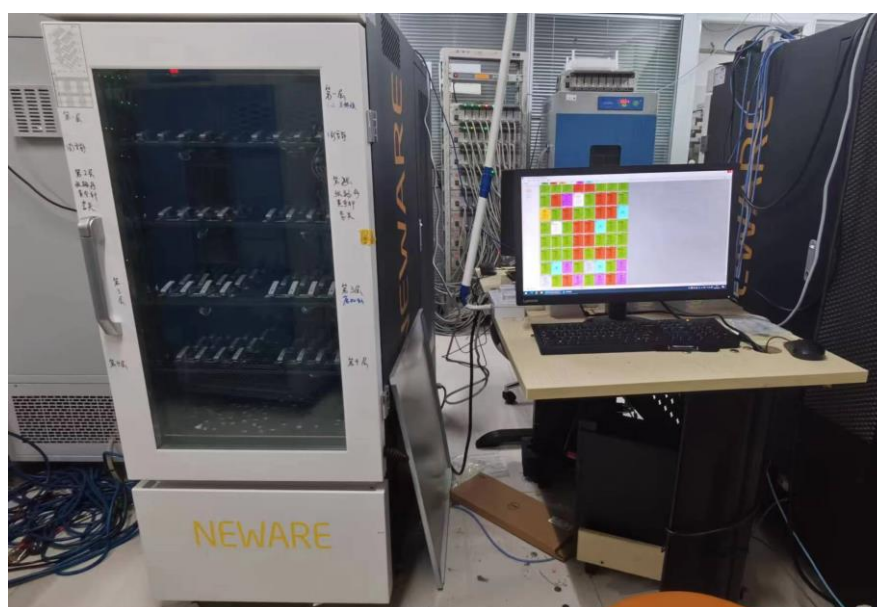
Fig. 2.4. The Neware battery tester.

2.2.5 Cycling test of Li||Cu cell

For the coin cell, a copper foil with a 16 mm diameter was chosen as the working electrode for the cathode, while a lithium foil with a thickness of 400 µm and a 14 mm diameter was selected for the anode. The experimental procedure begins with a discharge phase (lithium deposition) with current densities and areal capacities set at 0.5 mA/cm² @ 1 mAh/cm² and 1 mA/cm²

@ 1 mAh/cm², respectively. Following the discharge, a charging phase (dissolution) was conducted with a charging cutoff voltage of 1 V to assess the changes in Coulombic efficiency. The tests were conducted on the Neware battery tester (CT-4008T, China).

2.2.6 Cycling test of Li||Li symmetrical cell

The battery utilizes lithium foils with a diameter of 14 mm and a thickness of 400 μm for both the cathode and anode. The protection measures are implemented with voltage limits set at +5 V and -5 V, as well as current limits of +10 mA and -10 mA. These limitations are in place to safeguard the LI||LI battery from voltage and current overload, ensuring the battery operates within a safe range. The electrolyte stability was assessed by subjecting the battery to cycling tests under three different conditions: 0.5 mA/cm² @ 1 mAh/cm², 1 mA/cm² @ 1 mAh/cm², and 1 mA/cm² @ 4 mAh/cm². These tests aimed to evaluate the influence of the electrolyte on the stability of the lithium material. The tests were conducted on the Neware battery tester (CT-4008T, China) and continue until such point as the battery fails.

2.2.7 Cycling test of full cell

The cathode materials used in this thesis for the full-cell battery are $LiNi_{0.8}Co_{0.1}Mn_{0.1}O_2$ (NCM811) and $LiCoO_2$ (LCO). The anode materials include

lithium metal and artificial graphite. After the battery was assembled, it was left to stand for 12 hours to allow the electrolyte to fully soak in. Specific charge/discharge measurements in coin cells and pouch cells, including current magnitude and cutoff voltage, are described separately in the relevant chapters. The inside view of a battery tester is shown in Fig. 2.5.

The formula (2-1) for calculation of charge/discharge current is as follows:

Current = Rate × Specific capacity × Mass of active material   (2-1)

Through charge/discharge testing, the variations in specific capacity and Coulombic efficiency of the cathodes and anodes can be analyzed and deduced. This evaluation enabled an assessment of the capacity utilization and cycling stability of the battery.
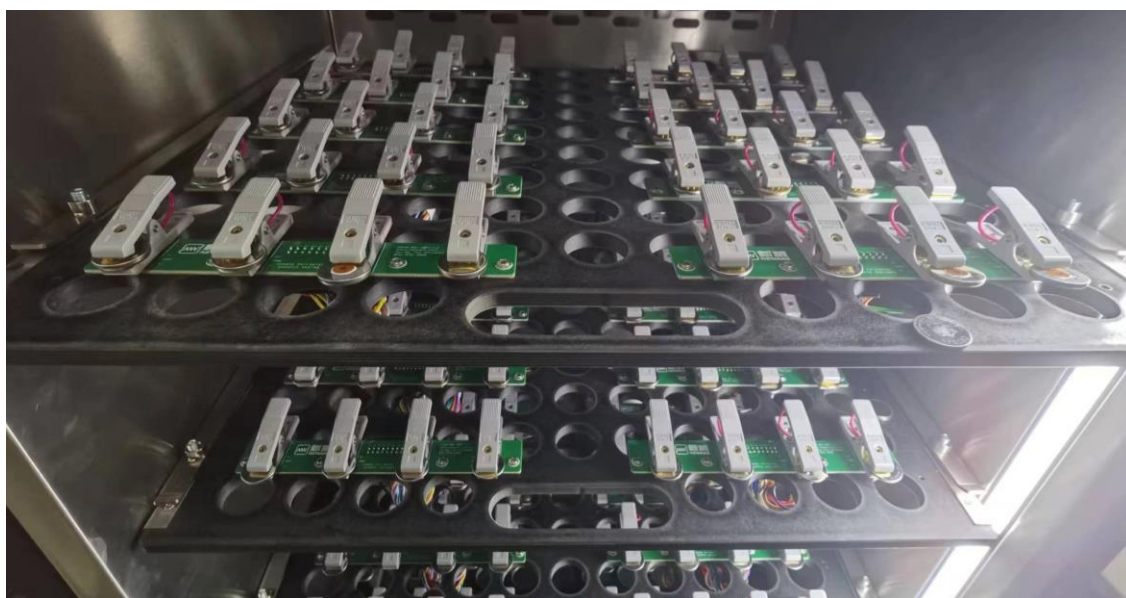
Fig. 2.5. Inside view of a battery tester.

2.2.8 Ionic conductivity

Ionic conductivity refers to the ability of a medium to conduct electric current through ions, typically used to assess the ion conduction performance of electrolytes. In this work, an ion conductivity meter was used to measure different electrolytes. Prior to testing, the ion conductivity meter needs to be calibrated using a standard KCl solution to adjust the conductivity coefficient. The probe is then immersed in the electrolyte, and the conductivity reading is directly obtained. The INESA DDS-11A conductivity meter was used for the tests. Each sample was tested three times, and the average value was recorded as the conductivity value.

2.3 Analytical characterization methods

2.3.1 Density functional theory

Density functional theory (DFT) calculation is an approach utilized to study the electronic structure of multi-electron systems. In this thesis, DFT calculations were performed to analyze the electrostatic potentials as well as the Highest Occupied Molecular Orbital (HOMO) and Lowest Unoccupied Molecular Orbital (LUMO) of different molecules being investigated for their potential to function as electrolytes for high performance batteries.

All molecules were drawn and calculated with Gaussian software. The DFT calculation was carried out in Opt + Freq job type (Optimization and Frequency

Calculation). Ground State method with default Spin was set, and the 6-31G [i]

basis set was used. In this context, the "6" denotes that the basis set which

comprises six Gaussian functions for each atomic nucleus, utilized for

characterizing the wavefunctions of individual electrons. The "31" signifies that

the basis set encompasses 31 basis functions, encompassing not only the

primary atomic orbitals but also polarization functions. These polarization

functions are incorporated to provide a more accurate description of the charge

distribution and electron interactions. These Gaussian functions have different

scales and shapes to better approximate the electron distribution. In this step,

the molecular geometry was first optimized, followed by the calculation of its

surrounding vibrational frequencies. These computations are valuable for

understanding the molecular structure and battery properties at the theoretical

level.

2.3.2 Nuclear magnetic resonance spectroscopy

Nuclear magnetic resonance (NMR) spectroscopy is a method utilized to

examine the absorption spectrum resulting from the resonant absorption of

radiofrequency radiation by atomic nuclei with non-zero magnetic moments

within a molecule. This absorption leads to the splitting of spin energy levels

---

[i] In DFT calculations, the 6-31G basis set refers to a set of mathematical basis functions used to describe the electronic structure of molecules. It is a standard basis set commonly used for calculations involving light elements such as hydrogen, carbon, nitrogen, oxygen, and others, especially in the context of organic molecules.

under the influence of an external magnetic field. NMR spectra provide valuable insights into the microstructural composition, conformation, and relaxation phenomena of molecules.

The detected nuclei range in this thesis includes ^{1}H, ^{7}Li, ^{13}C, and ^{19}F. For sample preparation, 0.5 mL of the liquid sample to be analyzed is placed in a thin-walled glass tube with an outer diameter of 6 mm. During testing, the field was pre−locked and shimmed using $CDCl_3$, and then the sample molecules or electrolytes were introduced directly. After tuning, the measurement was proceeded. The ASCEND 400 MHz equipment was used for the NMR measurements (Bruker, Germany), as shown in Fig. 2.6.

Fig. 2.6. Nuclear Magnetic Resonance Spectrometer 400 MHz.

2.3.3 Pulsed-field gradient nuclear magnetic resonance

Pulsed-field gradient nuclear magnetic resonance (PFG-NMR) is a technique that utilizes pulsed magnetic field gradients to control the spins in a sample. In diffusion−ordered spectroscopy analysis, the diffusion of molecules within the sample was induced using gradient pulses under the influence of a gradient magnetic field. By generating the diffusion spectrum, the diffusion coefficient of lithium ions in the electrolyte could be obtained.

During the experiments, ultrafine NMR tubes with a diameter of 3 mm were employed to minimize the interference caused by lithium salts in the NMR detection. During testing, the field was pre−locked and shimmed using $CDCl_3$, and then the sample molecules or electrolytes were introduced directly. After tuning, the measurement proceeded. The ASCEND 500 MHz NMR equipment was used for measurement (Bruker, Germany), as shown in Fig. 2.7.

Fig. 2.7. Nuclear Magnetic Resonance Spectrometer 500 MHz.

2.3.4 Raman spectrometry

Raman spectroscopy is employed to analyze the process of light scattering, providing insights into molecular vibrations, rotations, and intermolecular interactions, thus enabling the characterization of molecular structures. In electrolyte research, Raman spectroscopy is frequently utilized to characterize the solvent's solvation structure. By studying the solvation structure of a solvent, it is possible to predict the properties of the solvent under specific conditions.

Sample preparation method: Approximately 0.5 mL of the electrolyte is placed in a small vial and positioned on a glass slide for measurement. The wavelength is set at 532 nm, while the wavenumber range is configured from 1000 cm^{-1} to 2000 cm^{-1}. The equipment utilized for this study is the LabRAM HR Evolution (HORIBA, France).

2.3.5 Fourier transform infrared spectrometry

Fourier transform infrared spectroscopy (FTIR) is employed to analyze the functional composition of polymers by measuring the differential absorption and transmission of infrared light by different functional groups.

As the electrolyte contains lithium salts, the entire experiment is conducted within a glove box. The electrolytes and other liquid samples are firstly transferred into the test glove box and are then pipetted into the sample dish for analyzing. The equipment used in this thesis is VERTEX33 FTIR

spectrometer (Thermo, USA), as shown in Figure 2.8.
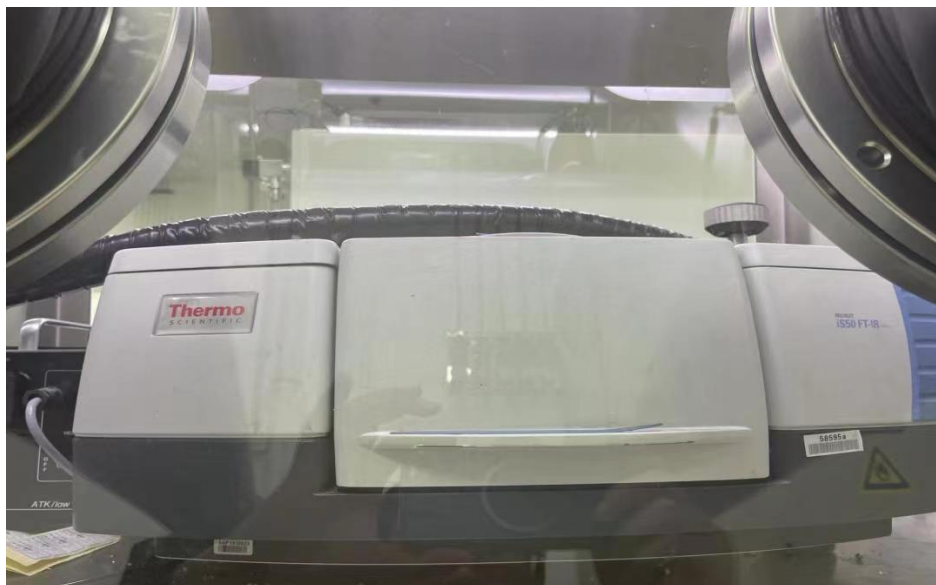
Fig. 2.8. The FTIR set-up in the glove box.

2.3.6 Scanning electron microscopy

Scanning electron microscopy (SEM) is a commonly employed analytical technique for characterizing the morphology of materials. It involves bombarding the sample surface with high-energy electron beams, which in turn excite secondary electrons, Auger electrons, backscattered electrons, and other signals. These signals are collected, processed by a computer, and transformed into images that reveal the material's morphological characteristics. In the study of electrolytes for LIB and LMB, SEM is frequently utilized to examine the morphology of the electrode surface.

The sample preparation procedure is as follows: The battery is disassembled in a glove box after cycling, and the electrodes are soaked in an appropriate

solvent to remove any residual lithium salts and impurities from their surfaces. As shown in Fig. 2.9, the electrodes were then cut into approximately 5 mm × 5 mm pieces and securely affixed to the SEM sample stage using conductive adhesive. The accelerating voltage for the SEM testing was set to 5 kV. The specific SEM instrument used in this thesis was the MIRA3 Field Emission SEM (TESCAN, Czech).

Fig. 2.9. A SEM sample stage with Cu foil samples.

2.3.7 X-ray photoelectron spectroscopy

X-ray photoelectron spectroscopy (XPS) is a widely used technique for analyzing the elemental composition of materials' surfaces. The positions, intensities, and areas of peaks in XPS spectra can provide valuable information about the types of elements present, the bonding between them, and their respective quantities. In battery characterization, XPS is commonly employed to analyze the formation of electrode surface layers, such as the solid

electrolyte interphase (SEI) and cathode electrolyte interface (CEI).

The sample preparation process for XPS is similar to that for SEM. Following the required number of cycling steps, the electrodes were disassembled and carefully cut into square pieces with dimensions of approximately 3 mm × 3 mm. These electrode samples were securely affixed to the XPS sample stage using conductive adhesive. Special precautions were taken to transfer the samples under vacuum conditions to prevent any reactions with atmospheric components. An Escalab Xi+ equipment was used (Thermo Avantage, USA) for testing, as shown in Fig. 2.10. An X-ray source with a diameter of 200 µm was utilized, and the carbon signal at 284.8 eV was employed as an internal standard to perform energy calibration and correct all binding energies in the XPS analysis. For lithium metal, an etching for 6 s was performed on its surface using an argon ion beam. The reference rate for depth profiling was calibrated to 1.6 nm/s on a Ta_2O_5 surface.

Fig. 2.10. An Escalab Xi+ XPS equipment.

2.3.8 Transmission Electron Microscopy

Transmission electron microscopy (TEM) is an advanced microscopy technique primarily used for observing and studying the microstructure and properties of materials. Compared to other microscopy techniques, TEM offers higher spatial resolution, allowing for the exploration of details and structural characteristics at the nanoscale.

The sample preparation procedure was as follows: The battery was disassembled in a glove box after 100 cycles, and the electrodes were soaked in an appropriate solvent (specifically, DME for ether system samples and DMC for carbonate system samples in this thesis) to remove any residual lithium salts and impurities from their surfaces. A small quantity of powder was collected from the electrode surface using a surgical knife. The powder was subsequently crushed on a glass slide and then adsorbed onto a copper grid for characterization. The aberration-corrected high-angle annular dark field-scanning transmission electron microscopy (HAADF-STEM) images were taken on a Titan Cubed Themis G2 300 (Thermo Scientific, USA).

2.3.9 Cryogenic transmission electron microscopy

Cryogenic transmission electron microscopy (Cryo-TEM) is an advanced electron microscopy technique used for observing the structure of frozen biological samples at low temperatures. Unlike conventional electron

microscopy, Cryo-TEM employs rapid freezing of the samples using liquid nitrogen to preserve their native morphology. Due to the sensitivity of lithium metal to electron beams, it can be damaged when exposed to high-dose electron beams, making it unsuitable for observation using conventional TEM. Therefore, Cryo-TEM is employed for the characterization of lithium metal.

The sample preparation procedure was as follows: A copper−TEM grid was deliberately positioned onto the copper surface of the working electrode. A certain amount of lithium metal was deposited onto the Cu−TEM grid during the plating process in Li||Cu cells. The current density of deposition was 0.25 mA/cm^2 and the deposition time was 1 h, followed by half striping of the lithium for better observation. After cycling, the coin cells were disassembled in glove box, and then the Cu−TEM grid was extracted and washed with DME to eliminate residual salts and electrolytes. Subsequently, the Cu−TEM grid was dried and sealed to avoid the air contact. After being transferred out of the glove box, the grid was placed within an automated cryogenic−TEM autoloader system, operating under a liquid nitrogen environment. The copper grid was then characterized in a cryogenic environment maintained by liquid nitrogen on a Krios G3i Cyro-TEM instrument (Thermo Scientific, USA). All TEM images were captured at a temperature of 77 K using an extremely low electron dose. The probe current employed for electron energy loss spectroscopy (EELS) mapping on the Titan microscope was ≈ 50 pA.

2.3.10 Inductively coupled plasma–mass spectrometry

Inductively coupled plasma–mass spectrometry (ICP-MS) is an analytical technique used for the sensitive and precise determination of trace elements and isotopes in a wide range of samples. In this thesis, the ICP-MS was used to detect the dissolution of transition metals from cathodes.

The sample preparation procedure involved: disassembling the NCM811||Li and LCO||Li cells after 100 cycles. The Lithium foils were extracted and dissolved in a 3% nitric acid solution for 12 hours. Subsequently, the resulting solution was analyzed using ICP-MS after 100-fold water dilution.

2.3.11 X-ray Diffraction

X-ray Diffraction (XRD) is a commonly used material analysis technique based on the principle of X-ray diffraction by the atomic arrangement in crystals. It is used to study the crystal structure and crystallographic properties of materials. In this thesis, XRD was utilized to confirm the crystal structure of electrode materials. In this thesis, XRD was employed to test the cathode plates before cycling, including LCO and NCM811. The 2 Theta value ranges from 0° to 90°, and the scan speed was set at 5°/min.

2.4 In situ gas analysis

2.4.1 Introduction to Differential Electrochemical Mass Spectrometry

Differential electrochemical mass spectrometry (DEMS) is a powerful analytical technique that integrates the principles of electrochemistry and mass spectrometry, enabling comprehensive investigations of the gas-phase products arising from electrochemical reactions. This method offers the unique advantage of facilitating real-time monitoring and precise identification of reaction intermediates and end products, thereby imparting invaluable insights into the underlying mechanisms and dynamics of various electrochemical processes.

By combining the strengths of electrochemistry and mass spectrometry, DEMS empowers researchers to gain a deeper understanding of complex electrochemical reactions. The real-time nature of DEMS facilitates the continuous tracking of reaction progress, enabling researchers to capture the evolution of gas-phase products as the electrochemical reaction unfolds. This capability not only allows for the identification of key species but also provides quantitative information regarding their concentrations and temporal profiles.

2.4.2 Working principle of DEMS

In DEMS, the working principle involves the following steps:

Step 1: Electrochemical Cell Setup: The experimental setup consists of a newly designed electrochemical cell. The working electrode is where the electrochemical reaction takes place.

Step 2: Electrochemical Reaction: An electrochemical reaction is initiated by applying a potential to the working electrode. This potential drives the electron transfer processes at the electrode-electrolyte interface, leading to the formation of reaction intermediates and gas-phase products.

Step 3: Gas-Phase Product Evolution: During the electrochemical reaction, volatile reaction products are generated. These products can diffuse into the gas phase above the electrolyte.

Step 4: Gas Analysis: A mass spectrometer is coupled to the electrochemical cell, allowing the detection and quantification of gas-phase reaction products. The mass spectrometer continuously analyzes the gas composition in real time during the electrochemical reaction.

2.4.3 Device Components of DEMS

Figure 2.10 shows the working scheme of the DEMS setup.
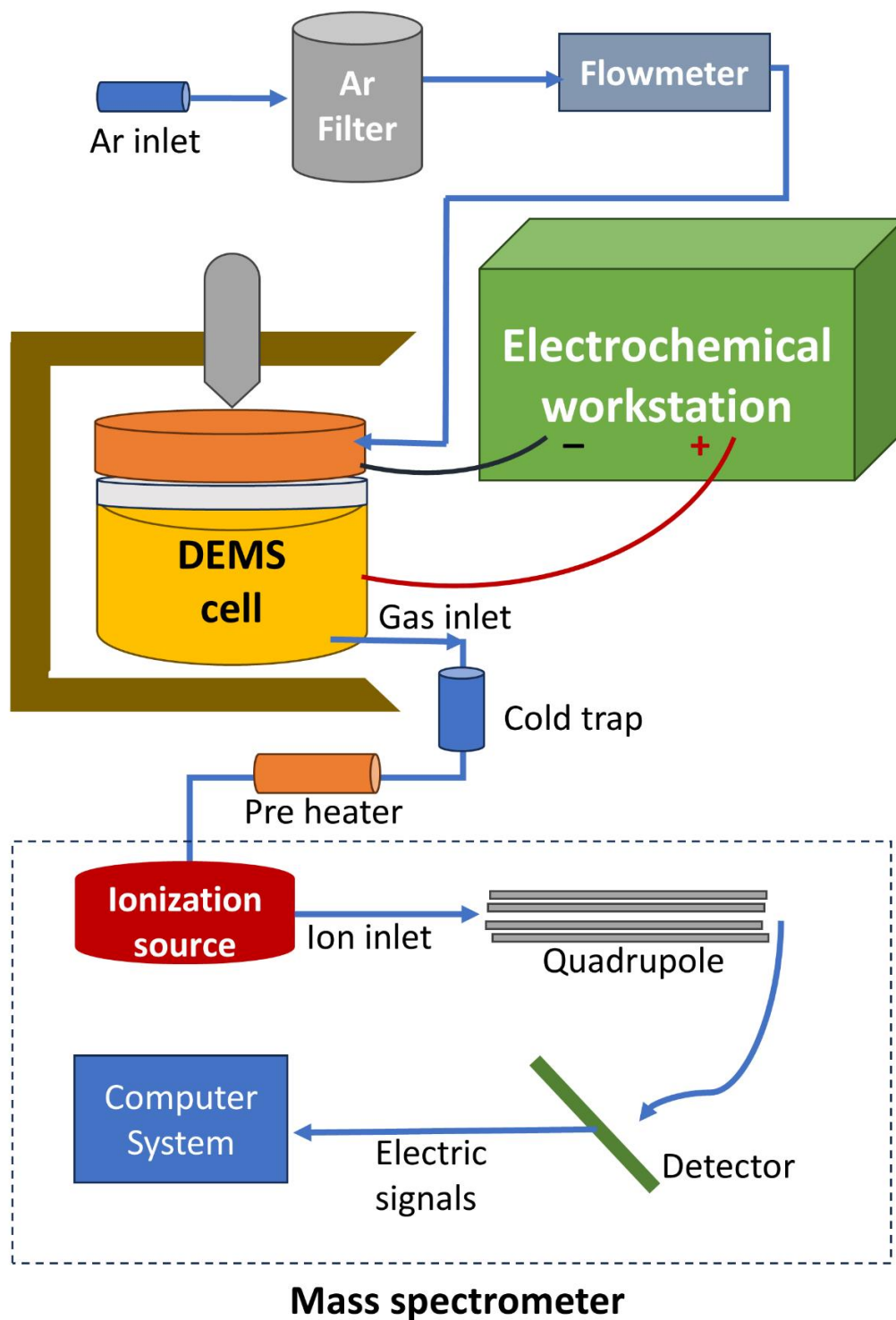
Fig. 2.11. Schematic drawing of the DEMS setup.

The key components of the DEMS setup include:

a. Ar filter: The argon gas filter enables the input carrier gas (argon) to reach a

purity level of 99.99%.

b. Flowmeter: The flowmeter controls the flow rate of argon gas at 2.0 mL/min.

c. DEMS cell: The assembled cell is shown in Fig. 2. 11. The DEMS setup comprises a three-electrode configuration where lithium serves as both the counter electrode and reference electrode. The cell is equipped with inlet and outlet ports for the gas phase.

Fig. 2.12. An assembled DEMS cell.

The electrodes were prepared by mixing active materials (graphite or NCM811), conductive additives (Super P), and binder (poly(vinylidene) fluoride) at a weight ratio of 80:10:10. The pastes were cast onto Celgard 2400 separators to form electrodes. The mass loading of the graphite was controlled at ≈ 30

mg/cm^2, and the mass loading of NCM811 was ≈ 18 mg/cm^2. Three layers of glass fiber (MA-EN-SE-01, Canrd) were used as the separators. 300 μL electrolyte was used for each DEMS test.

d. Electrochemical workstation: The electrochemical workstation provides stable cyclic voltammetry (CV) testing for DEMS cells. In this case, Li||NCM811 cells were cycled from 2.5 V to 5.0 V, and Li||graphite cells were cycled from 2.5 V to 0 V.

e. Cold trap: The cold trap is used to cool and condense the gas emitted from the battery, selectively capturing volatile components of the electrolyte. Through this process, only small gas molecules (H_2, O_2, CO, CO_2, etc.) generated from internal electrochemical reactions within the battery can pass through and be detected.

f. Pre-heater: The pre-heater facilitates the temperature stabilization, ensuring the accurate detection and measurement of gas-phase species in the mass spectrometry analysis.

g. Mass spectrometer: Consists of the following components:

　　1.) Ionization source: In DEMS, the gas-phase products are ionized using an ion source within the mass spectrometer, and sample molecules are ionized by electron impact to generate positive ions.

　　2.) Quadrupole: The ionized gas-phase products enter the mass analysis section of the mass spectrometer. Only ions with specific mass-to-charge ratios

can pass through the quadrupole rods and reach the detector. By adjusting the voltage parameters, the mass spectrometer can select different ion masses for analysis.

3.) Detector: The detector in the mass spectrometer records the arrival time and intensity of ions. When ions reach the detector, they cause the release of electrons or generate an electric current, resulting in an electric signal proportional to the number of ions.

4.) Computer system: A computer system receives and processes these signals, converting them into mass spectra that display the intensities and mass information of ion peaks.

2.4.4 Data analysis

In order to determine the concentration rate (nmol/min) of the evolution gas during the DEMS measurements, the mass signals of the measured gases (H_2 at $m/z = 2$, CO_2 at $m/z = 44$, CO at $m/z = 28$, O_2 at $m/z = 32$) were normalized to the ion current of the carrier gas Ar (I_{40}), denoted as I_z/I_{40}. This normalization process compensates for signal fluctuations arising from changes in pressure and temperature during the measurement. The evolution rate of the target gas is subsequently calculated by multiplying I_z/I_{40} by the flow rate of the carrier gas (2.0 mL/min)[162].

Chapter 3: Synthesis of 1,1,1-trifluoro-2-[(2,2,2-trifluoroethoxy) methoxy] ethane (TTME) and characterization of the electrolyte solvation structure

3.1 Introduction

3.1.1 Fluorinated ethers

The application of fluorinated ethers in electrolytes is mainly targeted towards lithium ion batteries and other similar battery systems. The electrolyte is a crucial component of the battery, providing the medium for ion transport and significantly influencing the battery's performance, stability, and safety. Adding fluorinated ethers to the electrolyte can improve the battery's performance and stability, particularly under high voltage and high-temperature conditions.

The main applications of fluorinated ethers in electrolytes include[163–167]:

(1) Solubility Enhancer: Fluorinated ethers, being polar and non-aqueous solvents, can enhance the solubility of electrolyte salts like LiFSI. This improves the ion conductivity of the electrolyte, leading to increased energy density and power output of the battery.

(2) Stabilizer: Fluorinated ethers possess high chemical stability, reducing the reactivity of the electrolyte. This helps mitigate capacity decay and cycle life

attenuation, thereby enhancing the cyclic stability and lifespan of the battery.

3. Suppression of Lithium Dendrite Growth: In lithium-ion batteries, the growth of lithium dendrites is a major cause of internal short-circuits and safety issues. Fluorinated ethers can form a stable interfacial film on the lithium metal surface, suppressing lithium dendrite growth and improving battery safety.

4. Inhibition of Electrolyte Reduction: Under high-voltage conditions, electrolyte salts are prone to undergo reduction reactions, leading to electrolyte degradation and decreased battery performance. Fluorinated ethers act as reducing "trapping agents" by forming stable complexes with electrolyte reduction products, preventing further reactions.

5. Reduction of Battery Overpotential: The addition of fluorinated ethers can reduce the battery's overpotential [j], reducing internal resistance and improving energy efficiency and power output.

6. Expansion of Battery Operating Temperature Range: The inclusion of fluorinated ethers can enhance the low-temperature performance of the battery, allowing it to maintain good electrochemical performance in low-temperature environments.

Overall, the application of fluorinated ethers in electrolytes significantly

---

[j] Overpotential refers to the phenomenon in the electrochemical reactions of a battery where the required potential difference at the electrode exceeds the theoretical potential difference. Overpotential reduces the efficiency of the battery because it requires additional electrical energy to overcome these potential differences. Therefore, reducing overpotential is a key objective in enhancing the performance of LIB.

improves the performance, stability, and safety of lithium-ion batteries and other battery systems, driving advances in electric vehicles, portable electronic devices, energy storage, and other related fields. With ongoing advances in science and technology, research on fluorinated ethers and other novel electrolyte additives is expected to further optimize battery system performance, helping to meet the growing demand for energy globally.

3.1.2 Localized high concentration electrolyte

Localized high concentration electrolyte (LHCE) is a novel type of electrolyte used in lithium-ion batteries and other similar battery systems. Unlike traditional electrolytes, LHCE introduces a diluent that helps to maintain a high concentration of electrolyte salt (e.g., LiFSI) while reducing the overall electrolyte concentration[147,168].

The design of an LHCE electrolyte aims to optimize battery performance and safety. By modifying the solvent structure around the lithium ions, LHCE adjusts the solubility and ion transport properties of the electrolyte to enhance the battery's energy density, power output, and cycling stability. Additionally, LHCE electrolyte inhibits the growth of lithium dendrites, reducing the risk of internal short circuits and improving battery safety.

Several hydrofluoroethers (HFEs), such as bis(2,2,2-trifluoroethyl) ether (BTFE), 1,1,2,2-tetrafluoroethyl-2,2,3,3-tetrafluoropropyl ether (TTE), and

tris(2,2,2-trifluoroethyl) orthoformate (TFEO), have been utilized as diluents in LHCEs[147,169–171]. However, the inert diluent molecules used in LHCEs do not participate in the dissociation of lithium salts themselves. In contrast, a co-solvent diluent that has limited ability to dissolve lithium salts on its own but can assist the solvent in dissociating lithium salts is believed to simultaneously improve the electrolyte's solvation structure and the interfacial stability of lithium metal anode. Hence, the development of a dual-purpose co-solvent is imperative for the creation of innovative LHCEs.

In this chapter, inspired by the significant advantages of the aforementioned fluorinated ethers and LHCEs, we conducted an in-depth study of their structural characteristics with the aim of designing a fluorinated ether molecule with similar properties and applying it to LHCE. The goal is to maintain the excellent properties of fluorinated ether diluents while further enhancing their performance and application range through molecular structure design. Starting from the molecular structure of BTFE (as shown in Figure 3.8b), the highly fluorinated terminals ($-CF_3$ groups) significantly enhance the molecular oxidation stability, while its symmetrical structure results in low overall polarity, making it suitable as a diluent in LHCE. To maintain this structural characteristic, we considered symmetrically increasing the chain length at both ends based on the BTFE molecule. In addition to the conventional -C- bonds, adding symmetric -O- structures can also achieve similar structural characteristics,

leading to the conception of 1,1,1-trifluoro-2-[(2,2,2-trifluoroethoxy) methoxy] ethane (TTME) molecule. Interestingly, through observing the TTME molecule, we found that due to the strong electronegativity of oxygen and the competitive interaction between the $-CF_3$ group, its electron cloud density is relatively high, giving it an advantage over other diluents. The TTME molecule serves as both a diluent in LHCE and a participant in the inner solvation shell structure. TTME retains a portion of the electron cloud around its polar group, providing energy for the coordination of Li^+ ions. Considering the high synthesis cost of BTFE, we synthesized the required TTME molecule in a highly productive manner using easily available simple materials (2,2,2-trifluoroethanol and dichloromethane) in the laboratory, providing a more practical and economical solution for the exploration and utilization of high-voltage lithium metal batteries.

To investigate this unique solvation structure, molecular dynamics (MD) simulations were employed, along with Raman spectroscopy, Fourier transform infrared absorption spectroscopy (FTIR), and nuclear magnetic resonance (NMR) characterizations.

3.2 Chemicals

The chemicals needed for TTME molecule synthesis and electrolyte preparation in this chapter are listed below.

Table 3. 1 Chemicals used in the experiments.

Chemicals	Supplier	Purity
potassium hydroxide	Aladdin	99%
N-methyl-2-pyrrolidone (NMP)	Aladdin	99.9%
2,2,2-trifluoroethanol	Macklin	98%
dichloromethane	Macklin	99%
ethyl ether	Aladdin	99.9%
sodium chloride	Aladdin	99%
anhydrous magnesium sulfate	Macklin	98%
calcium hydride	Sigma	Analytical Reagent
lithium hydride	Sigma-Aldrich	98%
sodium hydride	Sigma-Aldrich	99%
molecular sieve	Sigma-Aldrich	4 Å
1,2-dimethoxyethane (DME)	Capchem	battery grade
lithium bis(fluorosulfonyl)imide (LiFSI)	Capchem	battery grade

3.3 Synthesis of 1,1,1-trifluoro-2-[(2,2,2-trifluoroethoxy) methoxy] ethane (TTME)

The synthetic route for the TTME molecule is shown schematic in Figure 3.1 and described below.
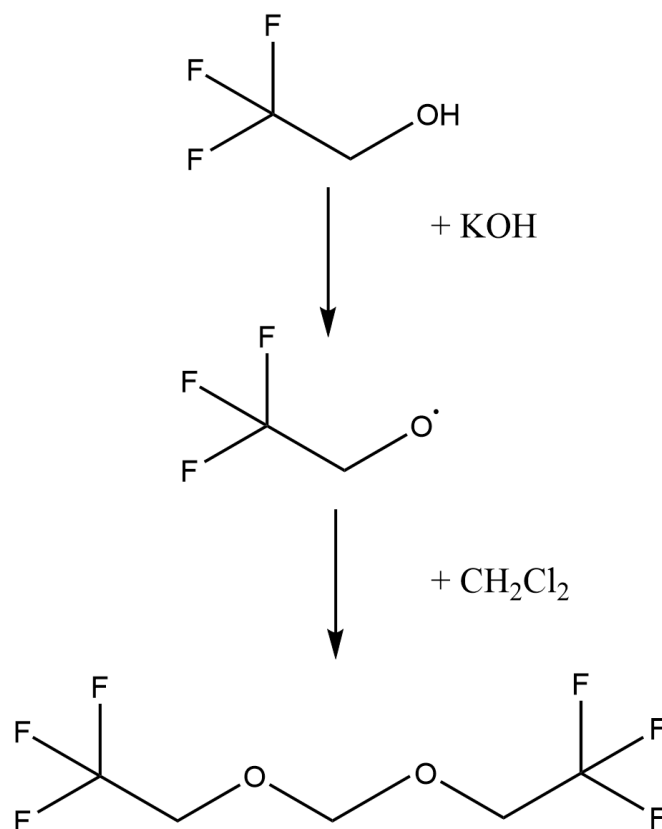
Fig. 3.1. The synthetic route schematic of the TTME. The starting reactant is 2,2,2-trifluoroethanol.

Step 1: A round bottom flask was charged with an appropriate quantity (30g) of potassium hydroxide. Subsequently, a 10 mL of N-methyl-2-pyrrolidone (NMP) was added as the solvent, and the resulting mixture was continuously stirred at a temperature of -5ºC, maintaining a cold environment with the use of ice bath.

Step 2: The next phase involved the slow dropwise addition of 50 g of 2,2,2-trifluoroethanol into the flask, meticulously performed using a pressure-dropping funnel. Following this, 23 g of dichloromethane was introduced into the reaction mixture.

Step 3: To facilitate the reaction, the temperature was gradually increased to 95ºC, and the reaction was allowed to proceed for a duration of 30 hours, ensuring sufficient time for the desired chemical transformations to occur.

Step 4: After the reaction reached completion, the entire system underwent a thorough washing process with ethyl ether, which was repeated three times. Subsequently, the mixture was subjected to a Buchner funnel with 2-micron pore size filter paper, separating any solid residues.

Step 5: In an additional step, the resulting liquid was then treated with saturated saline solution and underwent liquid-liquid extraction to remove NMP. This step was repeated three times to ensure thorough removal of NMP.

Step 6: To further refine the product, the resulting liquid was treated with anhydrous magnesium sulfate and calcium hydride, effectively eliminating any remaining traces of water.

Step 7: Following the removal of solid residues through suction filtration, ethyl ether was carefully evaporated using a rotary evaporator, yielding the crude TTME product.

Step 8: To obtain the pure product, the crude TTME product underwent distillation at a controlled temperature of 120ºC, ensuring the removal of any impurities.

Step 9: 2 g of lithium hydride was introduced into the system, and the system was subjected to condensation at 95ºC for 48 hours. Subsequently, the system

was heated to 120ºC for another round of distillation.

Step 10: In the final step, 1 g of sodium hydride was utilized as a replacement for lithium hydride, and the condensation cycle was repeated for three more iterations.

Upon completing all these meticulous steps, the TTME molecule was obtained, boasting a purity exceeding 99.9%. The average yield of TTME was found to be 83%. Detailed information about its purity can be found in the appendices section, where the purity report is included for reference. Figure 3.2 presents the schematic representation of the TTME molecule, providing a visual insight into its structural features for further analysis and comparison.

Fig. 3.2. The schematic structure of the TTME molecule.

After repeating the synthesis several times to achieve a sufficient quantity of prepared electrolyte, the obtained product was subjected to NMR characterization, including proton (H) and fluorine (F) NMR spectroscopy, as shown in Figure 3.3. The positions of the carbon atoms were labeled as 1 and

2 in both Figure 3.2 and Figure 3.3.

The H NMR spectrum reveals two distinct peaks around 3.6 ppm and 4.3 ppm, corresponding to different H atoms in the TTME molecule. The peak at 3.6 ppm corresponds to the H atom attached to the carbon (C) atom (position 1) closer to the fluorine (F) atom. On the other hand, the peak at 4.3 ppm corresponds to the H atom on the symmetric center C (position 2). It should be noted that although fluorine is more electronegative than oxygen, the H atom bonded to the C atom at position 2 exhibits a larger chemical shift. This is due to the direct connection of this C atom to two O atoms, which affects the local electronic environment and results in a greater chemical shift for the associated H atom.

Furthermore, due to the symmetrical structure of the molecule, the F atoms at both ends have identical chemical shifts, resulting in a single peak of around 77 ppm in the F NMR spectrum. This observation confirms that the F atoms in the TTME molecule are in an equivalent chemical environment, leading to the same chemical shift value in the NMR spectrum.

Following the analysis, the NMR spectra provide valuable information about the chemical environment and bonding patterns of the TTME molecule. These findings contribute to a better understanding of its structural characteristics and interactions, and its suitability for use as an electrolyte co-solvent.
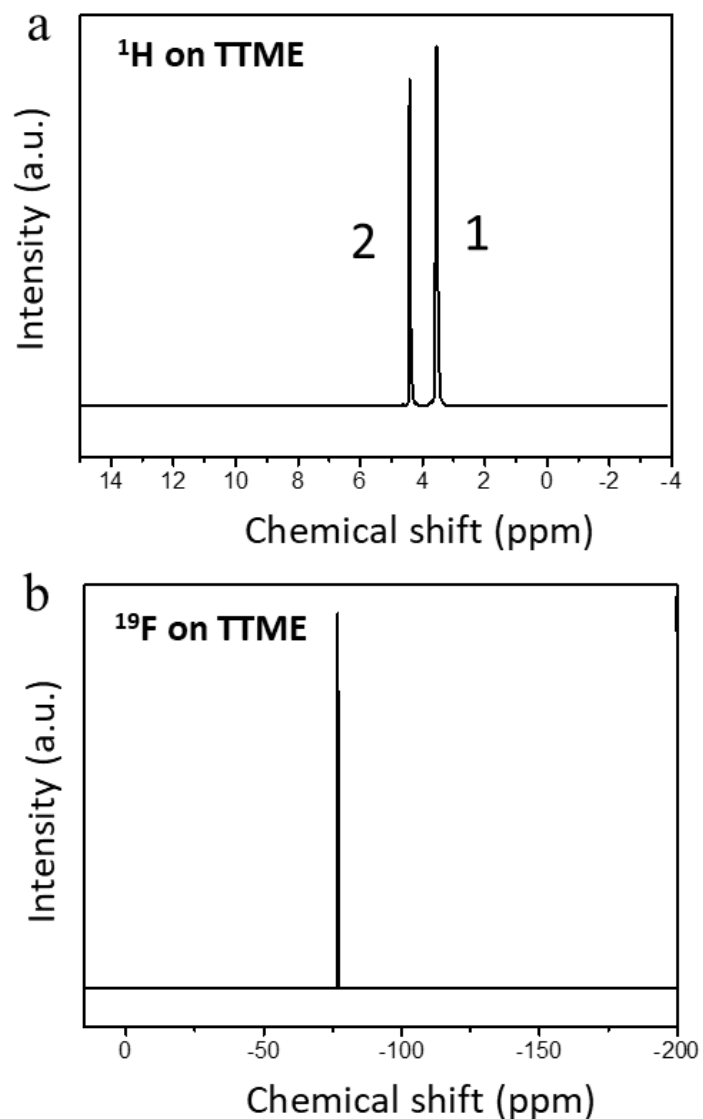
Fig. 3.3. The NMR results: (a) ^{1}H and (b) ^{19}F spectra of TTME.

3.4 Preparation and Selection of Electrolyte

To prepare the electrolytes, a carefully measured amount (374 mg) of LiFSI was

meticulously dissolved in 1 mL of a mixed solvent containing TTME and DME

at various volume ratios, including 1:1, 2:1, 3:1, 4:1, and 5:1. Each resulting

solution was obtained as a distinct electrolyte with its specific composition. As

a reference electrolyte for comparison and consistency, an identical amount

(374 mg) of LiFSI was dissolved in 1 mL of pure DME, forming the reference electrolyte referred to as **DME-d** in this thesis.

Figure 3.4 illustrates the electrolytes that were prepared. It was observed that when the volume ratio of TTME and DME was 5:1, there were residual lithium salts at the bottom of the bottle, indicating incomplete dissolution of the lithium salt under this condition. Therefore, only the first four electrolytes, in which the lithium salt was fully dissolved, along with DME-d as a blank reference, were used for further analysis.
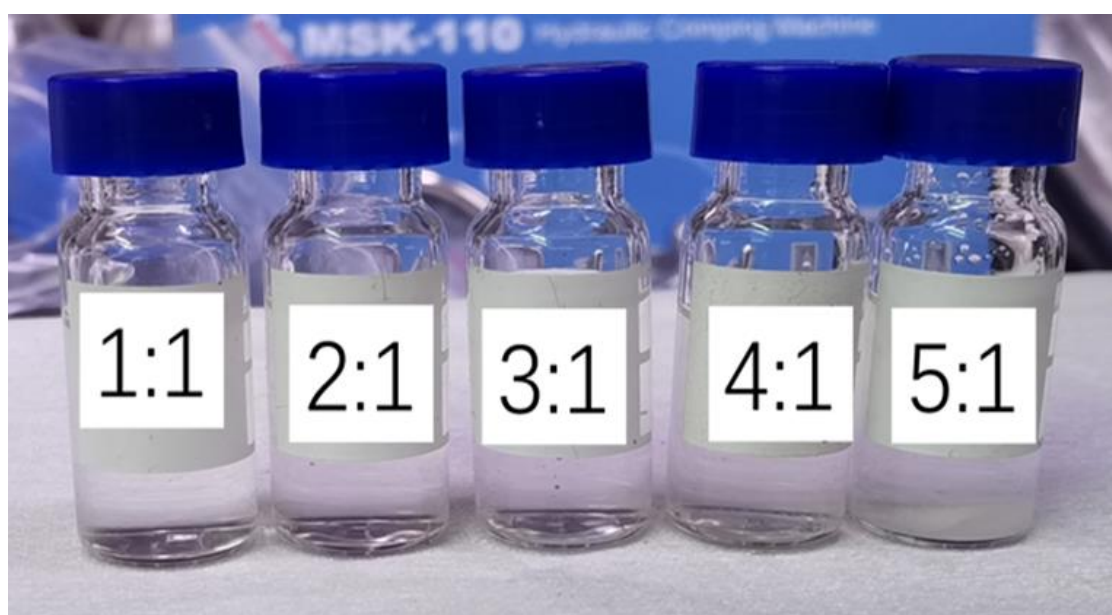
Fig. 3.4. Photo images of the solubility measurements of lithium salts in mixed solvents of TTME and DME at different volume ratios.

The lithium-ion diffusion coefficients of these electrolytes were determined using PFG-NMR, and the results are presented in Table 3.2 and Figure 3.5. The detailed reports with formulas are included in the appendices. From Figure 3.5

it can be observed that the electrolyte with a volume ratio of TTME: DME = 4:1 exhibits the smallest diffusion coefficient for lithium ions. This suggests that the solvent molecules have the strongest interaction with Li ions at this specific TTME : DME ratio. As a result, for the subsequent experiments, an electrolyte composed of TTME : DME in a 4:1 volume ratio, along with 1.4 mol/L LiFSI, was selected and is referred to as **TTME-d**.

Table 3.2 Li$^+$ diffusion coefficient of electrolytes with different TTME: DME ratios.

Electrolyte	Li$^+$ diffusion coefficient (E-10 m^2/s)
Blank (DME-d)	1.550
TTME: DME=1:1	1.378
TTME: DME=2:1	1.435
TTME: DME=3:1	1.274
TTME: DME=4:1	0.912
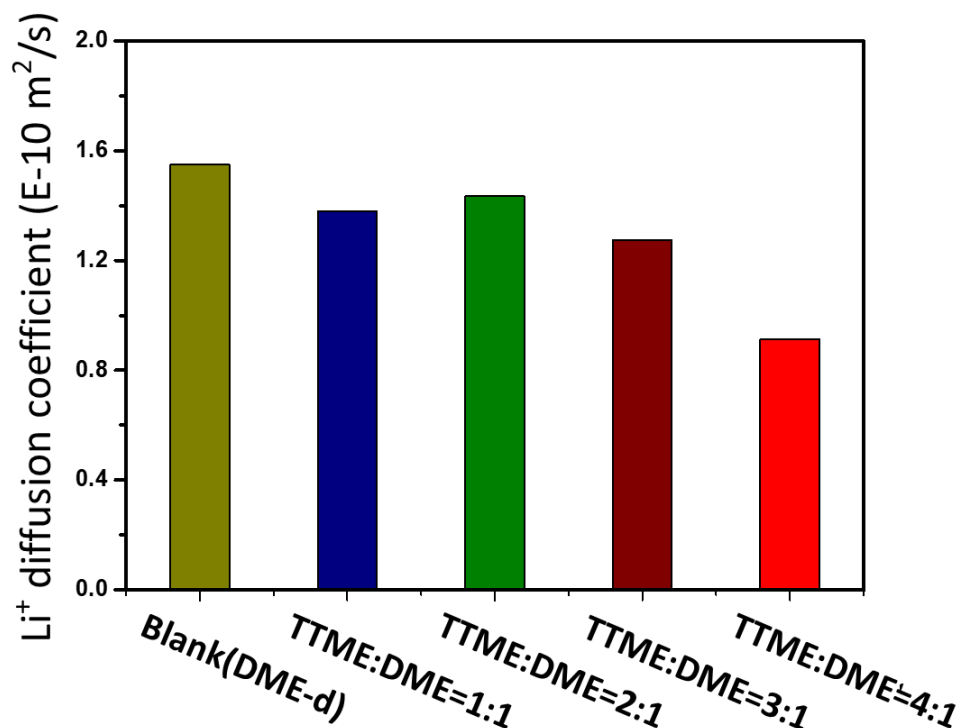
Fig. 3.5. Li$^+$ diffusion coefficient of electrolytes with different ratios of TTME: DME.

3.5 DFT analysis of TTME molecule

According to the DFT calculation results shown in Fig. 3.6, the highest occupied molecular orbital (HOMO) of TTME (−7.76 eV) is obviously lower than that of DME (−6.82 eV), and the substitution of a large amount of F in the molecule greatly improves the electrochemical oxidation stability of the molecule. The lowest unoccupied molecular orbital (LUMO) energy level of TTME is 1.49 eV, marginally lower than that of DME at 2.32 eV. This observation further suggests that TTME could contribute to the establishment of the primary solvation shell, and it becomes susceptible to reduction, which is involved in the SEI formation process.
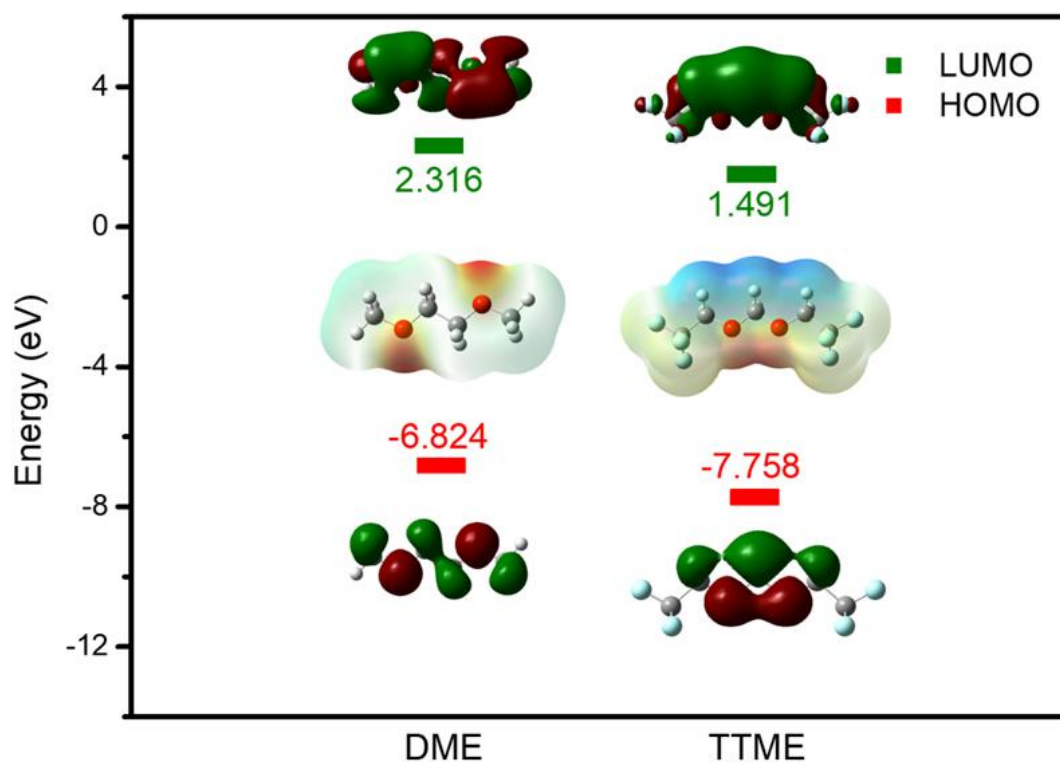
Fig. 3.6. LUMO and HOMO values of DME and TTME.

It can also be seen from the linear sweep voltammetry (LSV) curves of the electrolytes in Figure 3.7 that the addition of TTME improves the electrochemical stability window to a certain extent, and at the same time, the TTME−d electrolyte can still maintain a small current after the failure of the electrolyte in the high−voltage region.
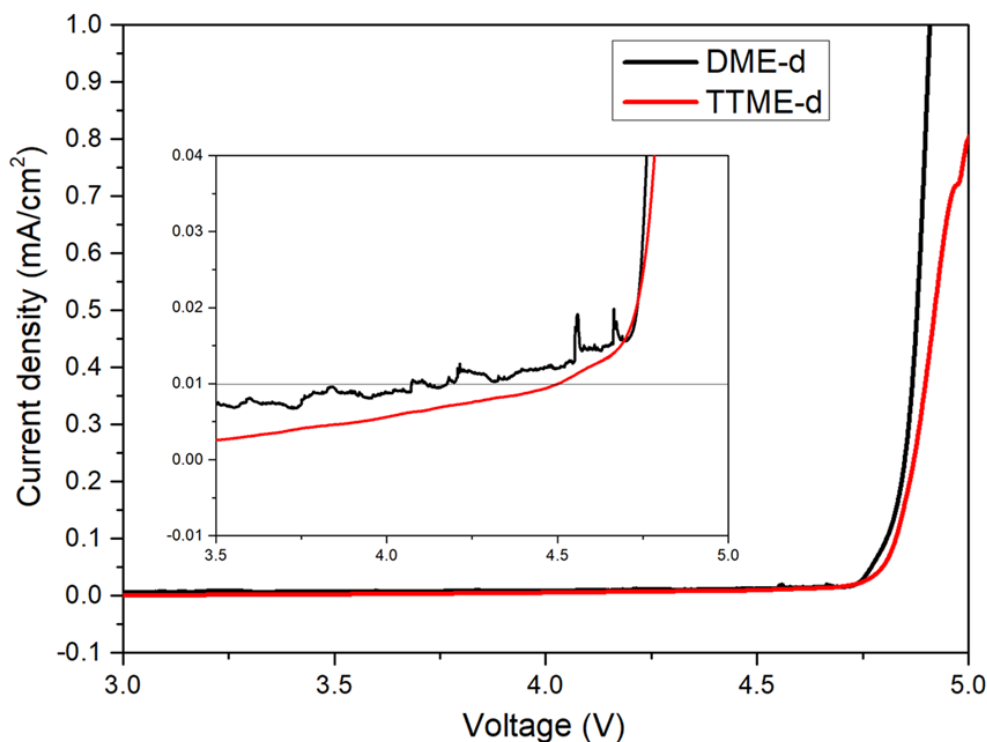
Fig. 3.7. Linear sweep voltammetry (LSV) curves of DME-d and TTME-d electrolytes. Inset: Enlarged curves.

Based on the electrostatic potential diagrams of TTME, TTE and BTFE molecules (Figure 3.8), it can be seen that the electron cloud density between the two oxygen atoms of TTME molecule is highest, which means that compared with conventional diluent molecules (TTE, BTFE), TTME can have stronger interaction with Li$^+$ ions.
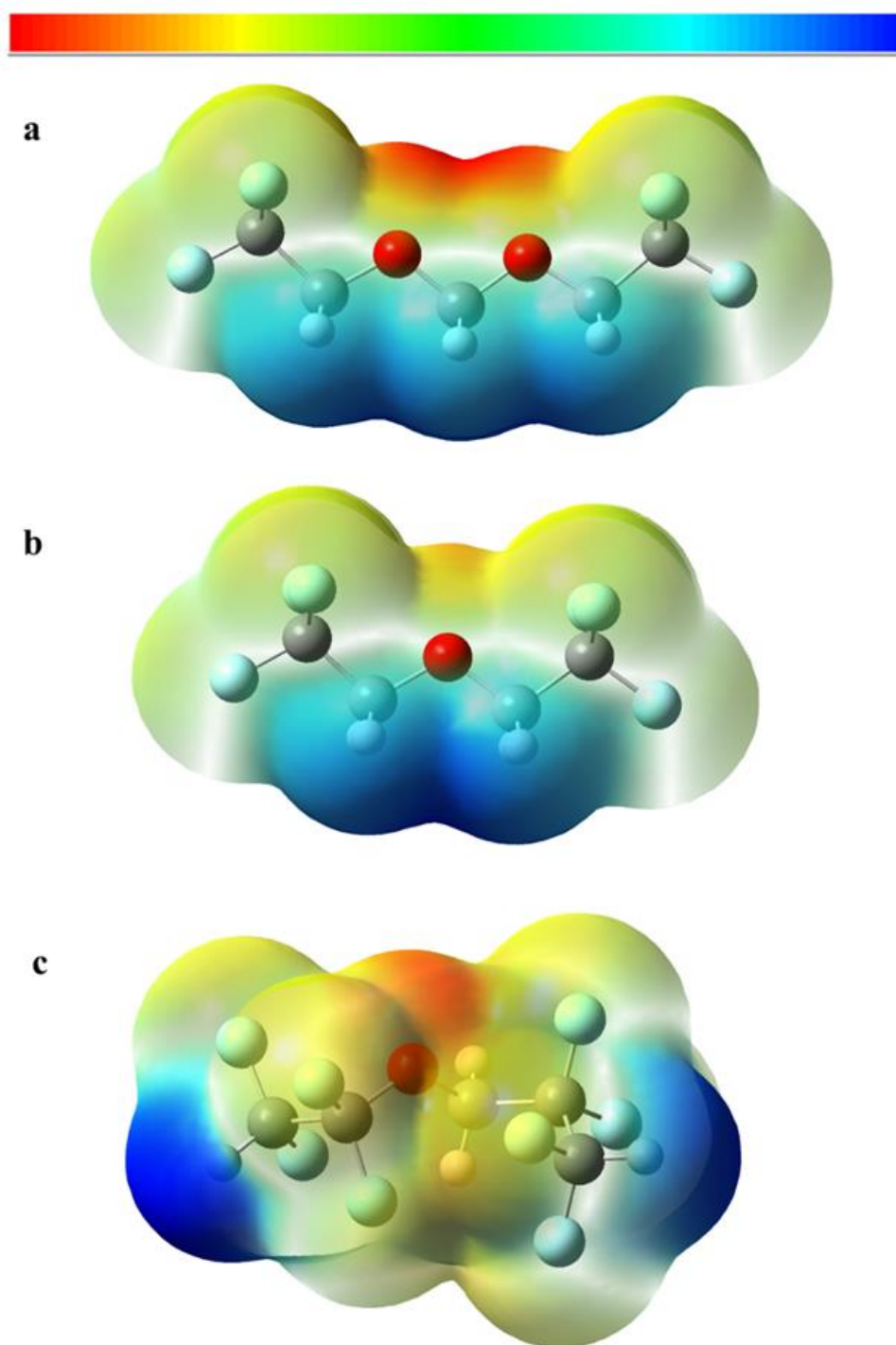
Fig. 3.8. Electrostatic potential diagrams of (a) TTME, (b) bis(2,2,2-trifluoroethyl) ether (BTFE), and (c) 1,1,2,2-tetrafluoroethyl-2,2,3,3-tetrafluoropropyl ether (TTE) molecule.

3.6 Molecular dynamics simulation

3.6.1 The system used for the simulation

All-atom molecular dynamics (MD) simulations were conducted to further investigate the solvation structure of the TTME-d electrolyte using Gromacs software. The molecules present in the system are depicted in Figure 3.9.
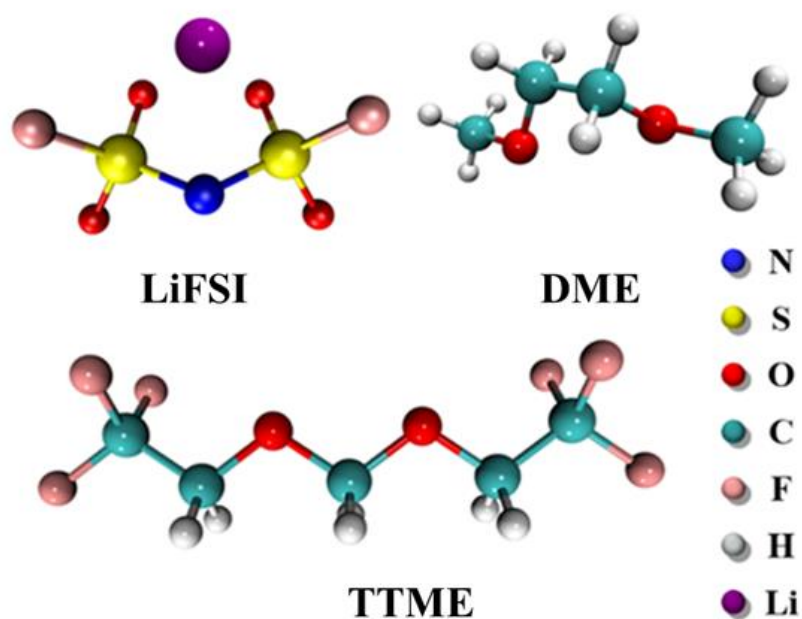
Fig. 3.9. Molecules contained in the TTME-d electrolyte system and evaluated via MD simulations.

600 LiFSI molecules, 600 DME molecules and 1500 TTME molecules were used in the simulation system. The simulation duration was set as 50 ns and the time step was set as 1 fs. The simulations were conducted at a temperature of 303 K (V-rescale temperature control) and a pressure of 1 bar (Berendsen pressure control). The simulation was started from a random conformation, and

a reasonable lowest energy conformation was obtained through energy minimization, pre-equilibrium, and 50 ns equilibrium dynamics simulation.

3.6.2 The equilibrium structure obtained from the simulation

The equilibrium structure obtained from the MD simulation is elegantly portrayed in Figure 3.10. For enhanced visual clarity, the molecular rendering in the simulation is thoughtfully color-coded with Li$^+$ ions in purple, FSI$^-$ ions in orange, TTME molecules in blue, and DME molecules in green.
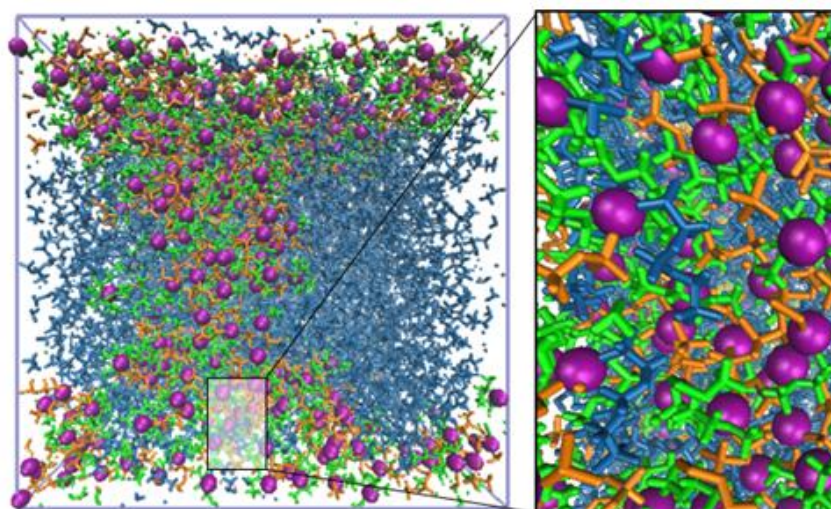
Fig. 3.10. Equilibrium structure obtained from MD simulations.
Inset: Enlarged structure. Li$^+$ ions are shown in purple, FSI$^-$ ions in orange, TTME molecules in blue, and DME molecules in green.

To further investigate the coordination structure, a selection of molecules involved in coordination was highlighted within a 5 Å radius around the Li$^+$ ions, as illustrated in Figure 3.11. Notably, the rendered TTME molecules predominantly reside at the interface with Li$^+$ ions. While the compatibility

between TTME and FSI⁻ / DME is somewhat limited, at the boundary, a discernible coordination structure emerges, showcasing the involvement of FSI⁻ / DME / TTME molecules, as depicted in the right-hand portion of Figure 3.11.
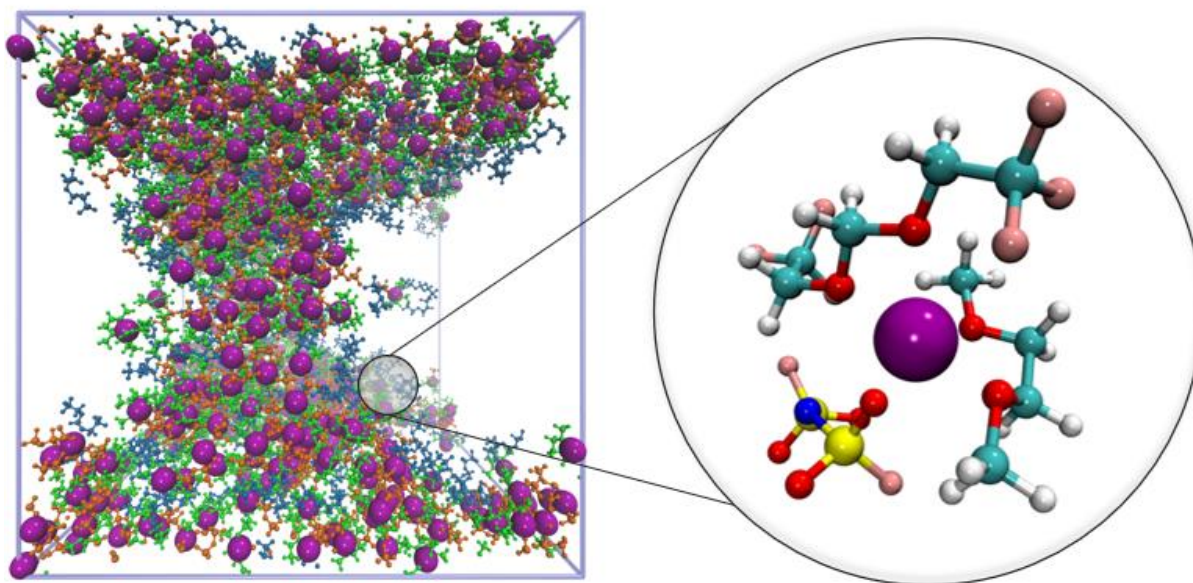
Fig. 3.11. MD simulated electrolyte structure (within 5 Å of Li$^+$ ions). Li$^+$ ions are shown in purple, FSI$^-$ ions in orange, TTME molecules in blue, and DME molecules in green. Inset: The representative Li$^+$ solvation structure extracted from the MD simulations. Here C atoms are blue, O atoms are red, H are white, F are pink, and S are yellow (as per Fig. 3.8).

These simulation results can be simplified into the model shown in Figure 3.12, in which DME and FSI$^-$ ions exhibit strong coordination with Li$^+$ ions, while a fraction of TTME molecules weakly interact with Li$^+$ ions in the inner solvation layer, and the remaining TTME molecules form a randomly dispersed outer shell in the electrolyte.
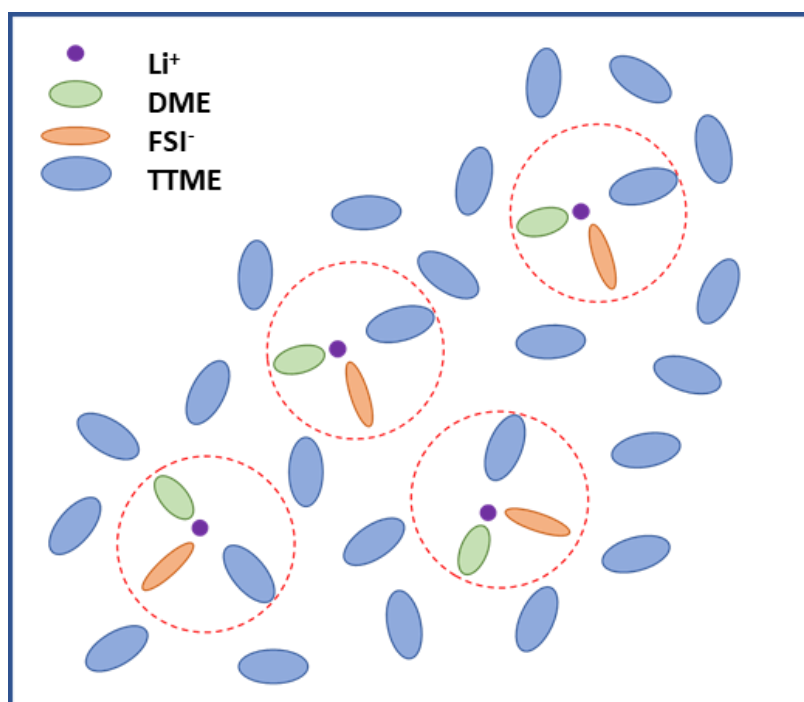
Fig. 3.12. Schematic illustration model of the TTME-d electrolyte solvation structure.

Figure 3.13 shows the positional relationship between Li$^+$ ions and all FSI$^-$ /DME/TTME molecules in the system. The visualization vividly portrays that there is a notable absence of free DME and FSI$^-$ ions, underscoring their substantial involvement in coordination with the Li$^+$ ions. However, the participation of TTME molecules in coordination appears to be more selective, in alignment with the solvation structure depicted in the model (Figure 3.12). This observation highlights the different coordination behaviors of the individual components and their interactions within the system.
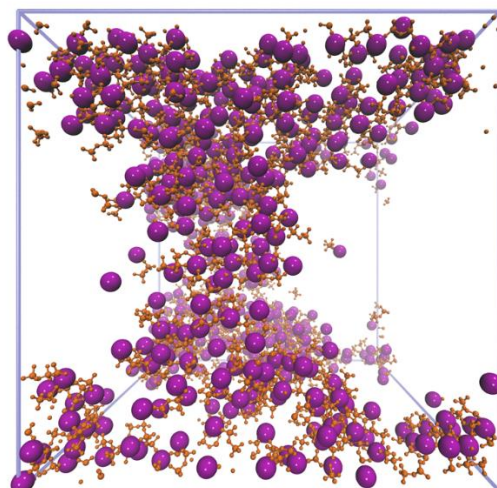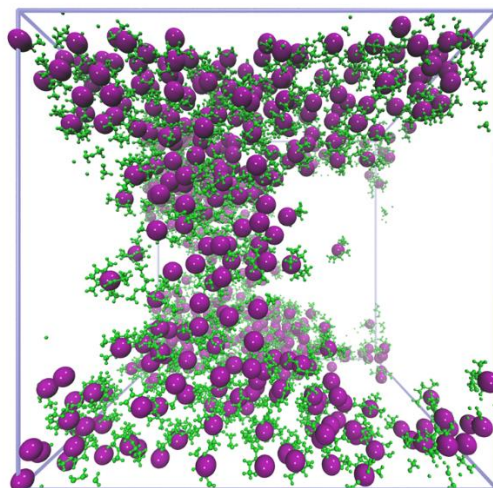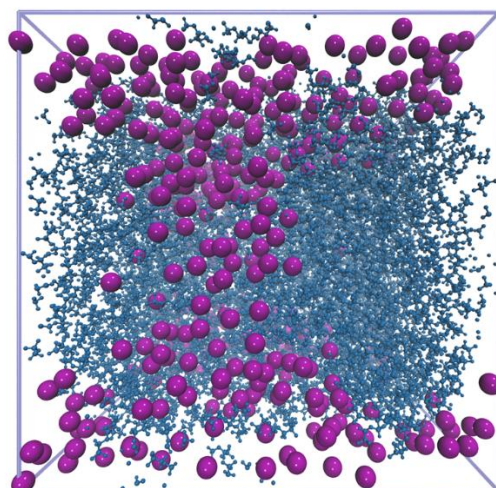
Fig. 3.13. Interactions of FSI⁻/DME/TTME and Li⁺ ions in the system.

3.6.3 Radial distribution function

In order to quantitatively analyze the microstructural properties of the FSI⁻/DME/TTME system, the radial distribution function between Li⁺ ions and O atoms was employed, as shown in Figure 3.14. The radial distribution function is a critical tool for gaining insights into the spatial distribution of atomic interactions, especially in ionic systems like the one under investigation.
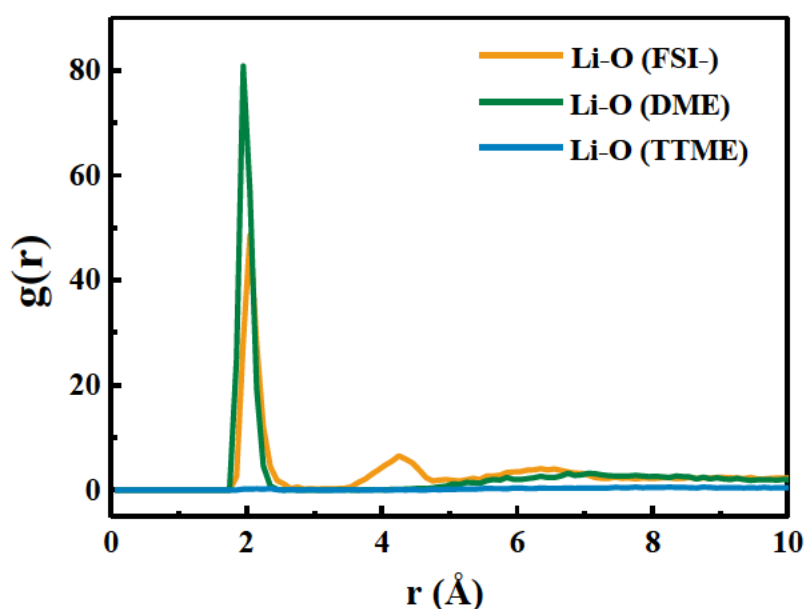
Fig. 3.14. Radial distribution function between Li⁺ ions and the O atoms in FSI⁻ / DME / TTME.

Upon analyzing the radial distribution function, it was evident that both FSI⁻ and DME molecules exhibited significant coordination with Li⁺ ions, indicating the formation of stable ion pairs. DME demonstrated a notably stronger interaction with Li⁺ ions than FSI⁻, possibly due to its unique solvation characteristics and ability to form more stable ion complexes.

Regarding TTME, as depicted in Figure 3.15 (enlarged view), its coordination with Li$^+$ ions exhibited an intriguing trend with distance, likely due to its unique distribution characteristics within the system. As the distance increased, the coordination between TTME and Li$^+$ ions gradually increased, indicating the presence of diverse solvation structures around the Li$^+$ ions.
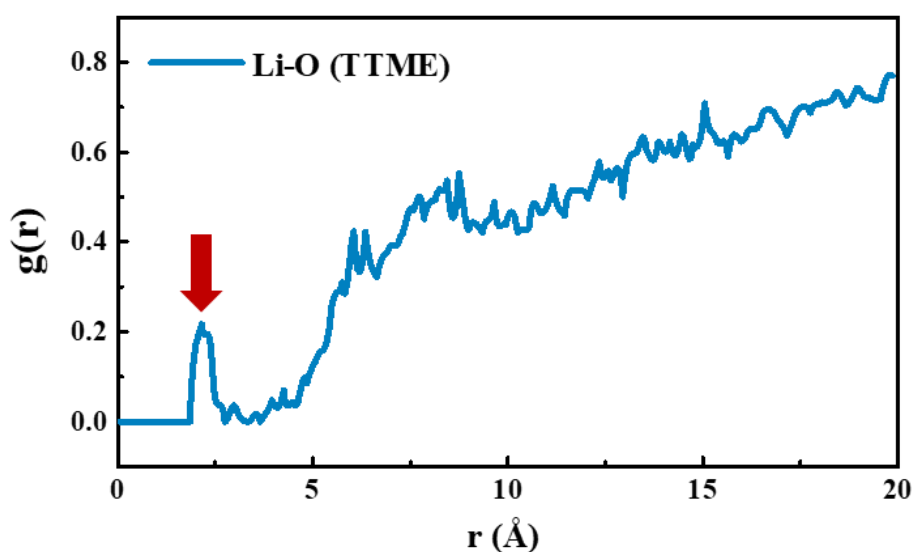
Fig. 3.15. Radial distribution function between Li$^+$ ions and O atoms in TTME.

Of particular interest was the minor yet distinct peak at approximately 2.0 Å, as indicated by the red arrow. This peak suggested that a small fraction of TTME molecules were actively involved in the coordination with Li$^+$ ions at a specific distance range, contributing to the overall solvation structure. This observation might be attributed to the unique spatial arrangement of TTME molecules, allowing them to interact selectively with Li$^+$ ions and influence the local coordination environment.

3.6.4 Coordination number

The coordination number was calculated via the following steps:

(i) The number of O atoms present in the specific components (FSI$^-$ / DME / TTME) in the designated location around the Li$^+$ ions was calculated;

(ii) The number of O atoms in the molecular structure of the component was divided (2/4) to determine how many molecules participated in the coordination of all Li$^+$ ions in the system; and

(iii) The number of Li$^+$ ions in the system (600) was divided to obtain the coordination number of FSI$^-$ / DME / TTME around each Li$^+$ ion on average.

As shown in Figure 3.16, the coordination number of DME changes with distance, indicating that the coordination of DME is more likely to occur in the inner side of the shell, and as the distance increases, the probability of DME and FSI$^-$ appearing becomes similar. However, due to the limited involvement of TTME in solvation, its participation in coordination only slightly increases with distance. These results collectively contribute to the demonstration and validation of the solvation structure model, in which TTME molecules act not only as the diluent in the electrolyte but also participate in the solvation structure of the inner layer.
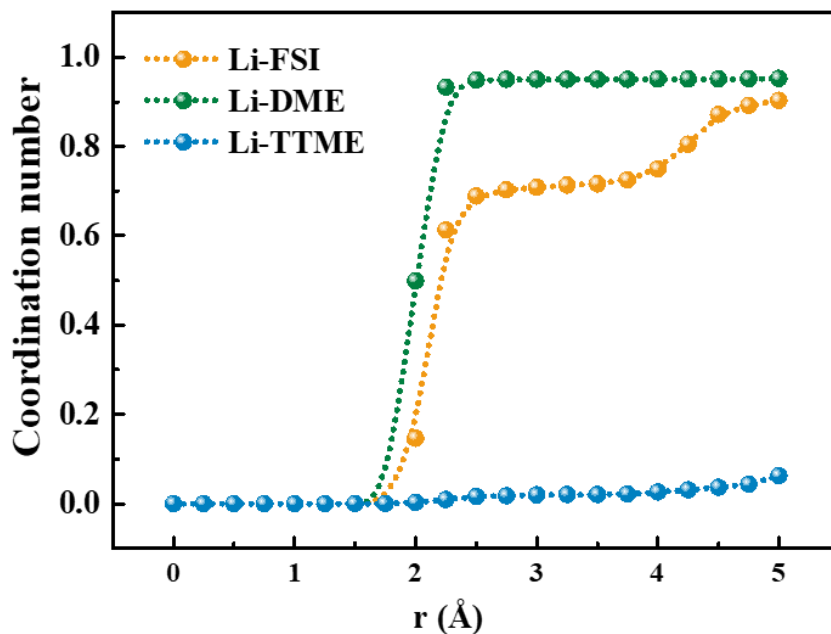
Fig. 3.16. Distance-dependent FSI⁻/DME/TTME coordination number around Li⁺ ions.

3.7 Characterization of the TTME-d electrolyte

To further provide substantial evidence for the distinct solvation structure, the electrolyte was thoroughly analyzed using Raman vibrational spectroscopy and FTIR absorption spectroscopy.

3.7.1 Raman vibrational spectroscopy

The Raman spectra, as shown in Figure 3.17, exhibit significant changes in the DME peaks upon the dissolution of LiFSI. The appearance of a new peak at ≈ 870 cm^{-1} indicates the interaction between Li⁺ ions and DME, corroborating the involvement of DME in the solvation sheath. Additionally, the Raman peak corresponding to the C-O-C stretching vibration in TTME undergoes a slight shift from 847.5 cm^{-1} to 852.1 cm^{-1}, suggesting the participation of TTME in

forming the first solvation sheath.
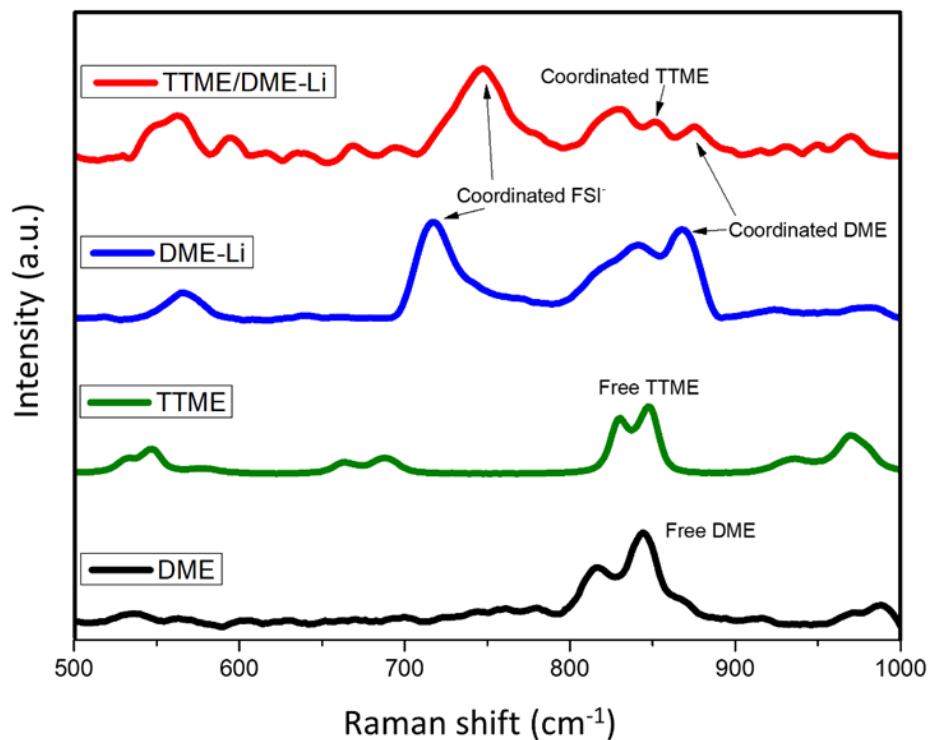
Fig. 3.17. Raman spectra of DME, TTME, DME-d, and TTME-d.

Moreover, the Raman peak of FSI⁻ in the TTME-d electrolyte is located at 748.1 cm^{-1}, contrasting with 717.4 cm^{-1} in the DME-d electrolyte. This observation confirms the presence of aggregates and tight ion pairs in the TTME-d electrolyte, while a considerable amount of free FSI⁻ anions exist in the DME-d electrolyte, further supporting the unique solvation structure in the TTME-d electrolyte system.

3.7.2 Fourier transform infrared spectrometry

The FTIR spectra (Figure 3.18) also provide supporting evidence, as the

characteristic peak of free DME weakens upon dissolving LiFSI but remains present. However, when LiFSI, DME, and TTME are dissolved together, the characteristic peak of free DME disappears entirely, confirming the complete surrounding of DME by TTME in the envisioned solvation structure, without any free DME molecules.
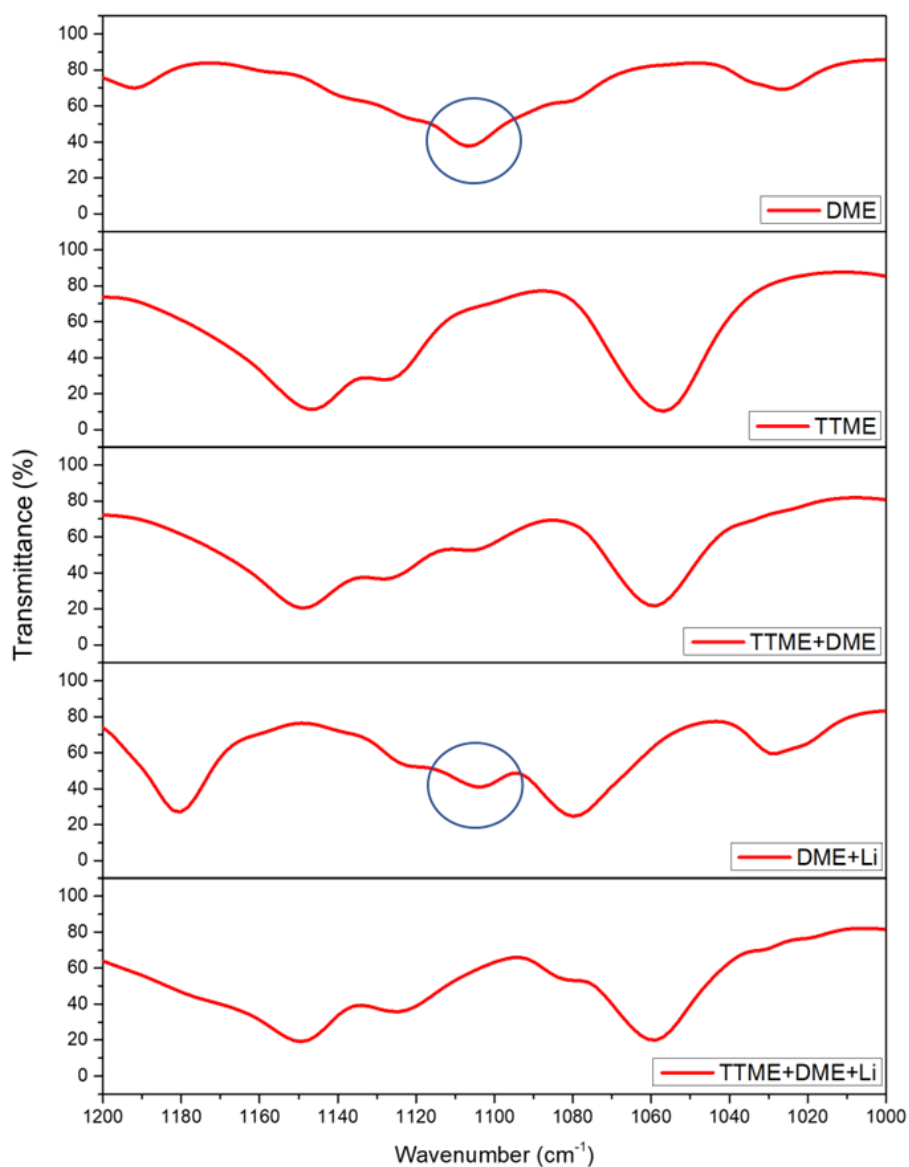
Fig. 3.18. Fourier Transform Infrared Spectrometer (FTIR) spectra of DME, TTME, TTME+DME, DME-d, and TTME-d.

3.7.3 Nuclear magnetic resonance spectroscopy

To substantiate the involvement of TTME in forming the solvation structure, the chemical shifts of lithium and fluorine (from LiFSI) in the TTME-d electrolyte were examined using NMR (Figure 3.19). The downshift of the ^{7}Li signal on LiFSI, from -1.20 ppm to -0.88 ppm after adding TTME, indicates an increase in the electron cloud density around Li$^+$ ions in the electrolyte, leading to a more orderly environment. The F signal of FSI$^-$ moves from 52.0 ppm to 51.8 ppm, confirming the transformation of FSI$^-$ ions from the free state to the dense ion pair in the TTME-d electrolyte. Additionally, the NMR results demonstrate that the addition of TTME can facilitate the dissociation of LiFSI, separating large ion clusters into small ion pairs, and supporting the co-solvent effect of TTME.

Overall, the combined results from Raman spectroscopy, FTIR, and NMR analyses consistently reinforce the involvement of TTME in the formation of the unique solvation structure in the TTNE-d electrolyte.
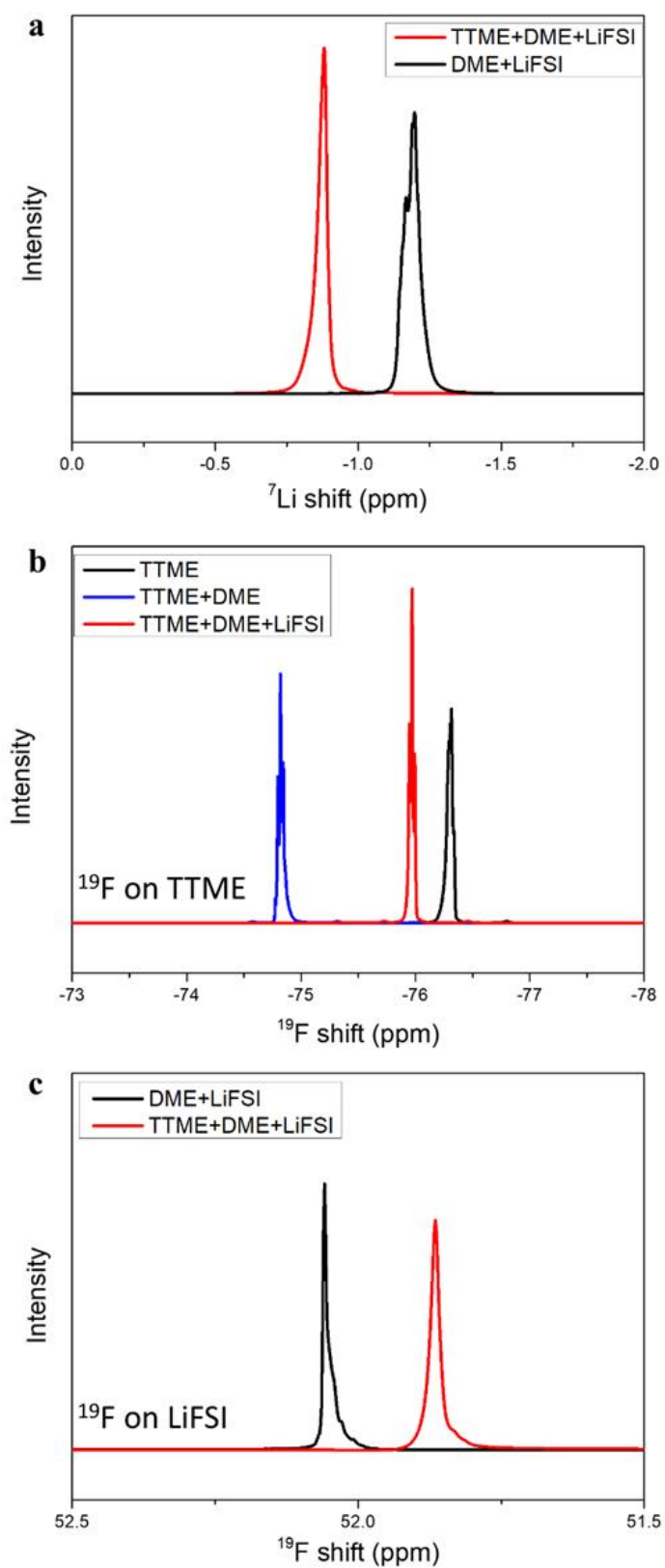
Fig. 3.19. Nuclear magnetic resonance results: (a) ^{7}Li NMR of DME-d and TTME-d. (b) ^{19}F NMR of TTME, TTME+DME and TTME-d. (c) ^{19}F NMR of TTME-d and DME-d.

3.8 Conclusion

In this chapter, a new molecule called TTME was meticulously designed and synthesized. This remarkable molecule serves a dual role in the Localized High-Concentration Electrolyte as both a diluent and an active participant in the inner solvation shell structure. The unique structure of TTME enables it to retain a portion of the electron cloud around its polar group, which plays a crucial role in facilitating the coordination of Li^+ ions.

To gain profound insights into this exceptional solvation structure, molecular dynamics (MD) simulations were employed, including radial distribution function and the calculation of the Coordination number (see Section 3.6.4 and Figure 3.16 for further details). Complementary experimental techniques, including Raman spectroscopy, Fourier transform infrared absorption spectroscopy (FTIR), and nuclear magnetic resonance (NMR) characterizations, were also utilized to validate the findings.

The investigation of TTME and its role in the solvation structure advances our understanding of LHCE electrolytes' intricate properties and lays the foundation for optimizing their performance in various battery systems. The combination of sophisticated simulations and experimental analyses paves the way for further advances in energy storage technologies and contributes to the development of safer, more efficient batteries for the future.

Chapter 4: Unique Double-Layer Solid Electrolyte Interphase Formed with TTME-Based Electrolytes for High-Voltage Lithium Metal Batteries

4.1 Introduction

Li metal is regarded as one of the most promising anodes for high−energy−density batteries due to its high theoretical specific heat capacity (3,860 mAh g^{-1}) and low reduction potential (−3.04 V compared to that of a standard hydrogen electrode (SHE) whose reduction potential is exactly zero). When coupled with a high−voltage layered oxide cathode, an improvement of energy density to 500 Wh kg^{-1} is can be realized. However, numerous fundamental challenges, arising from the highly reactive nature of both Li metal anode and high−voltage cathodes, preclude the practical realization of rechargeable Li metal batteries.

Many studies have shown that localized high concentration electrolytes can form a stable SEI to significantly suppress the continuous consumption of lithium metal and electrolyte, greatly extending the lifespan of lithium metal batteries. At the same time, the CEI generated on the positive electrode side of LHCE can inhibit the phase transition of the cathode and prevent the leaching of transition metals[148,153-155,170–172]. Therefore, in this chapter, we investigate the application of the specially synthesized and formulated localized high concentration electrolyte TTME-d, which we prepared in the previous chapter, in high-voltage Li metal batteries.

Owing to the bifunctional role played by the TTME molecule, as both a diluent and an active participant in the inner solvation shell structure (see Chapter 3 for full details), the selected electrolyte (TTME−d) with 1.4 M lithium bis(fluorosulfonyl)imide (LiFSI)/1,2−dimethoxyethane (DME)−TTME (1:4 by volume) was explored for its electrochemical performance in both Li||Cu and Li||Li cells. The reason for the excellent performance of lithium metal cells was explored and found to stem from the double−layer stable electrolyte interphase (SEI) structure formed by the TTME−d electrolyte on the lithium metal surface. This unique SEI, which was extensively characterized and found to have both optimal rigidity and flexibility, as characterized by cryo−TEM. Furthermore, lithium metal cells using two commercial cathodes displayed outstanding cycling performance. In detail, Li||LiNi$_{0.8}$Co$_{0.1}$Mn$_{0.1}$O$_2$ (NCM811) cell was found to retain 85% capacity after 240 cycles at a cut−off charge voltage at 4.4 V, and

a Li||LiCoO$_2$ (LCO) cell was determined to deliver capacity retention of 90% after 170 cycles at a cut−off charge voltage of 4.5 V. Many characterization methods were used to prove the existence of a robust CEI formed on the cathode surface with the TTME−d electrolyte and to demonstrate that this CEI prevented the pulverization of the cathode at high temperature and inhibited the dissolution of transition metal ions, thus ensuring a long cycle life for the batteries.

4.2 Experimental details

4.2.1 Electrolytes and electrodes preparation

All the reagents, with a purity of above 99.9% (including lithium salts and solvents), were provided by Capchem Technology Co. Ltd (Shenzhen, China). The TTME-based electrolyte. named TTME-d. was formed by dissolving 374 mg lithium LiFSI in 1 mL mixed solvent of TTME and DME at a volume ratio of 4:1. The final concentration of lithium salt was 1.4 mol/L. Electrolyte containing DME with 1.4 mol/L LiFSI (named DME-d) was used as the control electrolyte for comparison.

For the coin cells, all electrochemical measurements were carried out using 2032-type coin cells. All the electrode plates, except lithium metal, were obtained from pouch cell disassembly. The active material loading of NCM811 was 3.13 mAh/cm^2, and the loading of LCO was 2.96 mAh/cm^2. Lithium foils

with thickness values of 20 μm and 400 μm were used as anodes. All cells were fabricated in an argon-filled glovebox, with 50 μL electrolyte and one layer of Celgard 2400 separator used in each cell.

4.2.2 Electrochemical measurements

For Li||Cu half cells, five pre−cycles between 0 and 1 V were initialized, and then cycling was done by depositing 1 mAh/cm^2 of Li onto the Cu electrode, followed by stripping to 1 V. Li||NCM811 coin cells were cycled between 2.8 V and 4.4 V. After the first two activation cycles at 0.1 C charge/discharge (1 C = 200 mA/g), the Li||NCM811 cells were cycled at 0.33 C. Li||LCO coin cells were cycled between 3.0 V and 4.5 V. After the first two activation cycles at 0.1 C charge/discharge (1 C = 180 mA/g), the Li||LCO cells were cycled at 0.2 C charge/ 0.5 C discharge rate. Cyclic voltammetry (CV) was performed in the voltage range from OCV to 0.01 V and then to 2.0 V with a scan rate of 0.1 mV/s.

4.3 Results and discussion

4.3.1 Electrochemical performance of TTME−d electrolyte on lithium metal anode

To verify the advantageous solvated structure of the TTME−d electrolyte for ensuring the stability of the lithium metal anode, Li||Cu cells and Li||Li symmetric cells were assembled using the TTME−d and DME−d electrolytes with an equal

Li$^+$ volume concentration.

The Coulombic efficiency (CE) of the Li||Cu cell reflects the reversibility of lithium deposition and stripping. The initial five cycles were utilized to clean the surface of the Cu electrode, followed by cycling with 1 mAh/cm^2 of Li deposition onto the Cu electrode and subsequent stripping to 1 V. The current density employed was 1 mA/cm^2. Figure 4.1 demonstrates that both the cells with the TTME−d and DME−d electrolytes exhibited consistently high CE values within the first 100 cycles. The CE of the cell with the TTME−d electrolyte was 99.35% after 100 cycles, slightly surpassing that of the cell with the DME−d electrolyte (99.09% after 100 cycles). However, after 130 cycles, the CE of the cell employing the DME−d electrolyte could not be maintained at more than 99% and rapidly declines thereafter. In contrast, the cell with the TTME−d electrolyte kept CE values higher than 99.3%. The CE of the TTME−d cell remained stable at 99.28% until 300 cycles, with a noticeable decrease occurring after approximately 350 cycles.
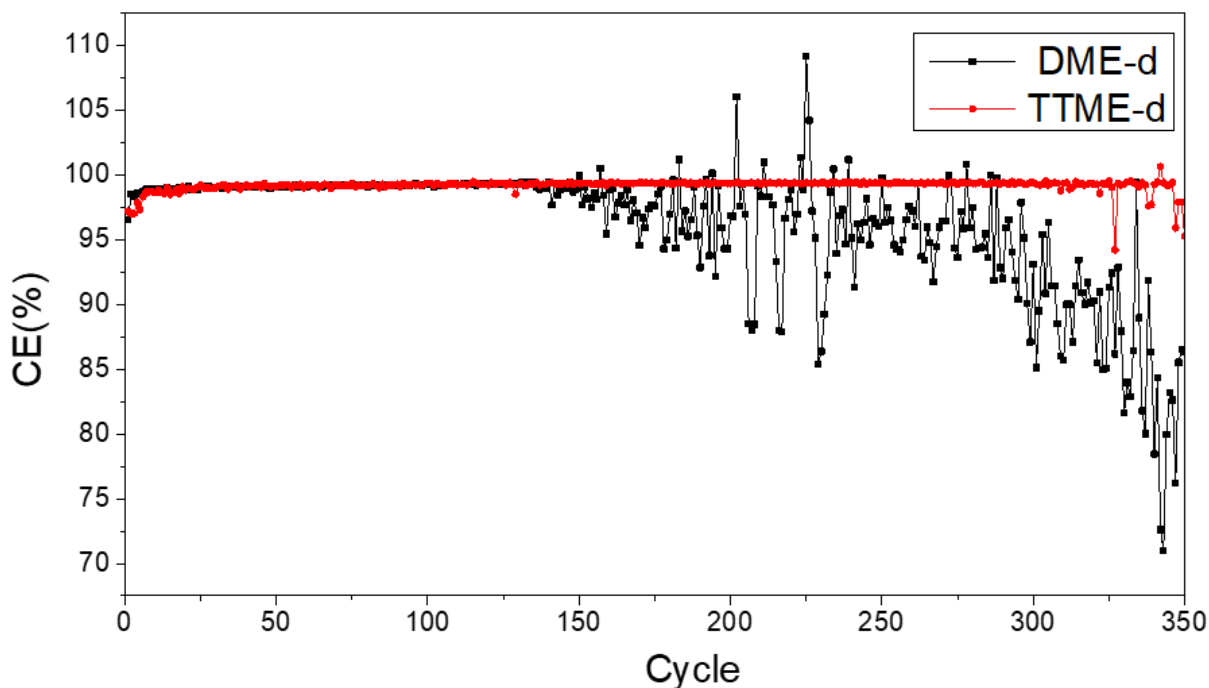
Fig. 4.1. The Coulombic efficiency of the Li||Cu cell with the different electrolytes assessed over 350 cycles.

The activation curves of the Li||Cu cells with the two electrolytes in the first cycle are analyzed. As depicted in Figure 4.2, the TTME−d electrolyte exhibits a smaller minimum potential voltage and nucleation overpotential for lithium metal compared to the DME−d electrolyte. This observation indicates that lithium metal can be more uniformly deposited and stripped in the TTME−d electrolyte environment.
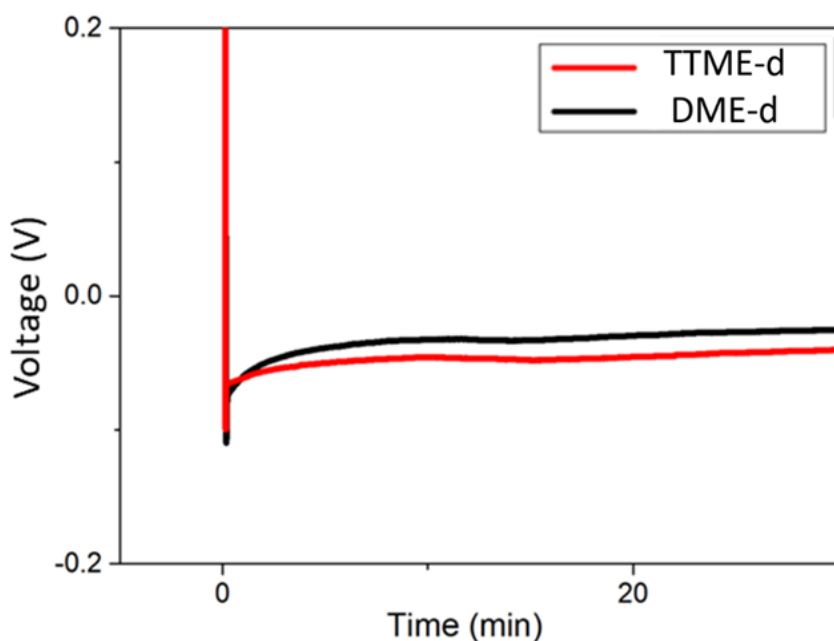
Fig. 4.2. The minimum potential voltage and the nucleation overpotential of Li||Cu cells in first cycle with the different electrolytes determined using battery tester.

Additionally, the Li||Cu cells were subjected to cyclic voltammetry (CV) measurements, as shown in Figure 4.3. The first CV curves demonstrate that the symmetry of the TTME−d curve is significantly higher than that of the DME−d curve, with smaller reduction and oxidation peaks, which indicates that the TTME−d is capable of forming a stable SEI with a lesser consumption of solvent and lithium salt. These results suggest that the TTME−d electrolyte system allows for more reversible lithium deposition and stripping.
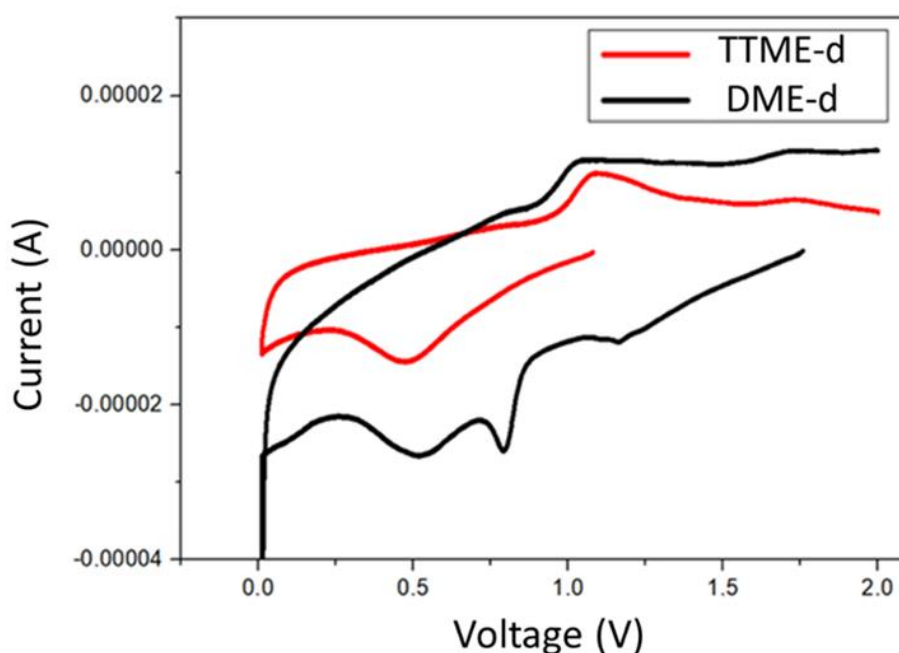
Fig. 4.3. Cyclic voltammetry curves of Li||Cu cells with the different electrolytes.

The compatibility of the electrolytes with the lithium metal anode can be further reflected through the evaluation of Li||Li symmetric cells. It can be seen from Figure 4.4 that the cell using the TTME−d shows much longer cycling time than the cell using the DME−d at a low current density of 0.5 mA/cm^2 and an area capacity of 1 mAh/cm^2. Although the polarization voltage of the cell with the TTME−d system is slightly higher than that of the cell with the DME−d system at the beginning due to the characteristics of TTME as a localized high concentration electrolyte (LHCE), the increase of the polarization voltage for the TTME−d can almost be ignored during 1,500 h of cycling. In comparison, the polarization voltage of the DME−d system increases rapidly after 1,200 h of

cycling, and then the cell fails quickly. The TTME−d's excellent compatibility with lithium metal ensures that the cell can keep cycling for more than 3700 h. The higher polarization observed in the TTME−d group is primarily attributed to the reduction in overall electrolyte ion conductivity upon the addition of the TTME diluent. The relatively lower ion conductivity of the electrolyte somewhat hampers the migration of Li^+ ions within the electrolyte, leading to an increase in the cell's overpotential. At 30°C, the ion conductivity of electrolyte TTME-d is 2.01 mS/cm, while that of electrolyte DME-d is 14.53 mS/cm. It is worth noting that although the conductivity of TTME-d is significantly lower than that of DME-d, it is still comparable to the majority of LHCE electrolytes currently used, which typically range from 1.5 to 3 mS/cm [150]. Despite this drawback in the TTME−d electrolyte, its distinctive solvation structure endows it with excellent cycling longevity.
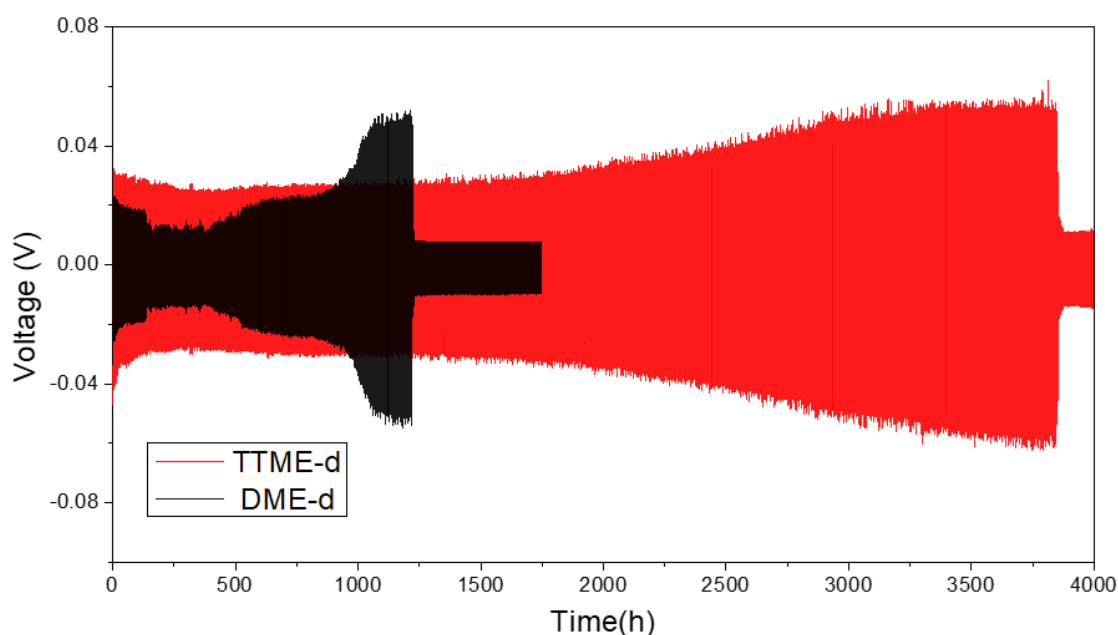
Fig. 4.4. Cycling behaviors of Li||Li cells at 0.5 mA/cm^2, 1 mAh/cm^2 with the different electrolytes.

In parallel, the symmetric cells were evaluated under a severer condition with increasing the current density and deposition time (Figure 4.5). Although the polarization voltage of the cell using the TTME−d electrolyte is still slightly higher than that of the cell with the DME−d electrolyte, TTME−d shows better cycling performance under the severe condition of 1 mA/cm^2 and 4 mAh/cm^2, and it maintains stable cycling for 700 h whereas the DME-d electrolyte destabilized rapidly at around 650 h. Larger deposits of lithium metal not only lead to increased absorption of electrolyte by larger porous lithium but also facilitate recurrent SEI damage and regeneration, resulting in a continuous consumption of electrolyte. These factors collectively contribute to the narrowing of the performance gap between the TTME-d and DME-d.
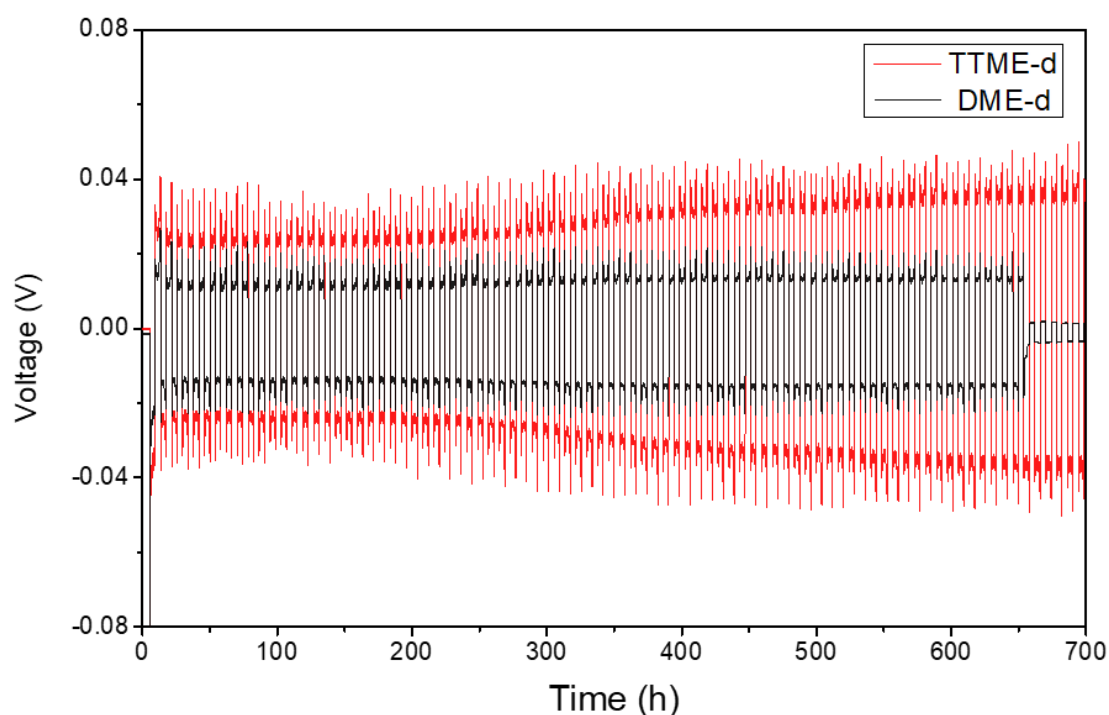
Fig. 4.5. Cycling behaviors of Li||Li cells at 1 mA/cm^2, 4 mAh/cm^2 with the different electrolytes.

4.3.2 Characterization of lithium metal anode using TTME−d electrolyte

In order to further explain the excellent stabilizing effect of the TTME−d electrolyte on lithium metal, lithium metal deposited onto the surface of copper foil with TTME-d versus DME-d was characterized by SEM. The current density of the deposition was 0.5 mA/cm^2 for 10 h or 1 mA/cm^2 for 5 h, and a total of 5 mAh/cm^2 lithium metal was deposited. It can be seen from comparison of the SEM images in Figures 4.6a and 4.6b that the lithium deposition surface formed by the TTME−d electrolyte is more uniform and denser, while the lithium deposition surface formed by the DME−d electrolyte is inhomogeneous with some obvious loose voids. It can also be seen from Figures 4.6c and 4.6d that the lithium metal particles deposited at the higher current density of 1 mA/cm^2 for 5 h with the TTME−d are larger than those formed with the DME−d, and the particle size is more uniform with a flatter surface. From the cross−section of lithium deposition in Figures 4.6e and 6f, it is observed that the size of the deposited lithium metal is different in the longitudinal distribution also. This is because that there are lithium metal nucleation points near the copper foil surface at the bottom layer, on which lithium metal is continuously deposited and grows upward. Regarding the overall horizontal trend and the cross−section of lithium metal deposition, the lithium metal in the TTME−d grows more evenly (than the DME-d) under the same deposition conditions.

At the same time, when depositing the same amount of lithium (5 mAh/cm²), distinct thicknesses of lithium metal are obtained for the two cases. In the TTME−d group, the resulting lithium metal thickness measures around 30 μm, slightly surpassing the theoretical value of 25 μm (In scenarios with larger deposition quantities, the inevitable volume expansion due to the formation of porous lithium metal contributes to this deviation). Conversely, in the DME−d group, the thickness of obtained lithium metal significantly exceeds the above value, reaching 46 μm, nearly twice the theoretical value. Such substantial thickness disparity clearly underscores the performance contrast between the two electrolytes. The SEM results show that compared with the DME−d system, the TTME−d system is conducive to uniform and dense deposition of lithium metal.
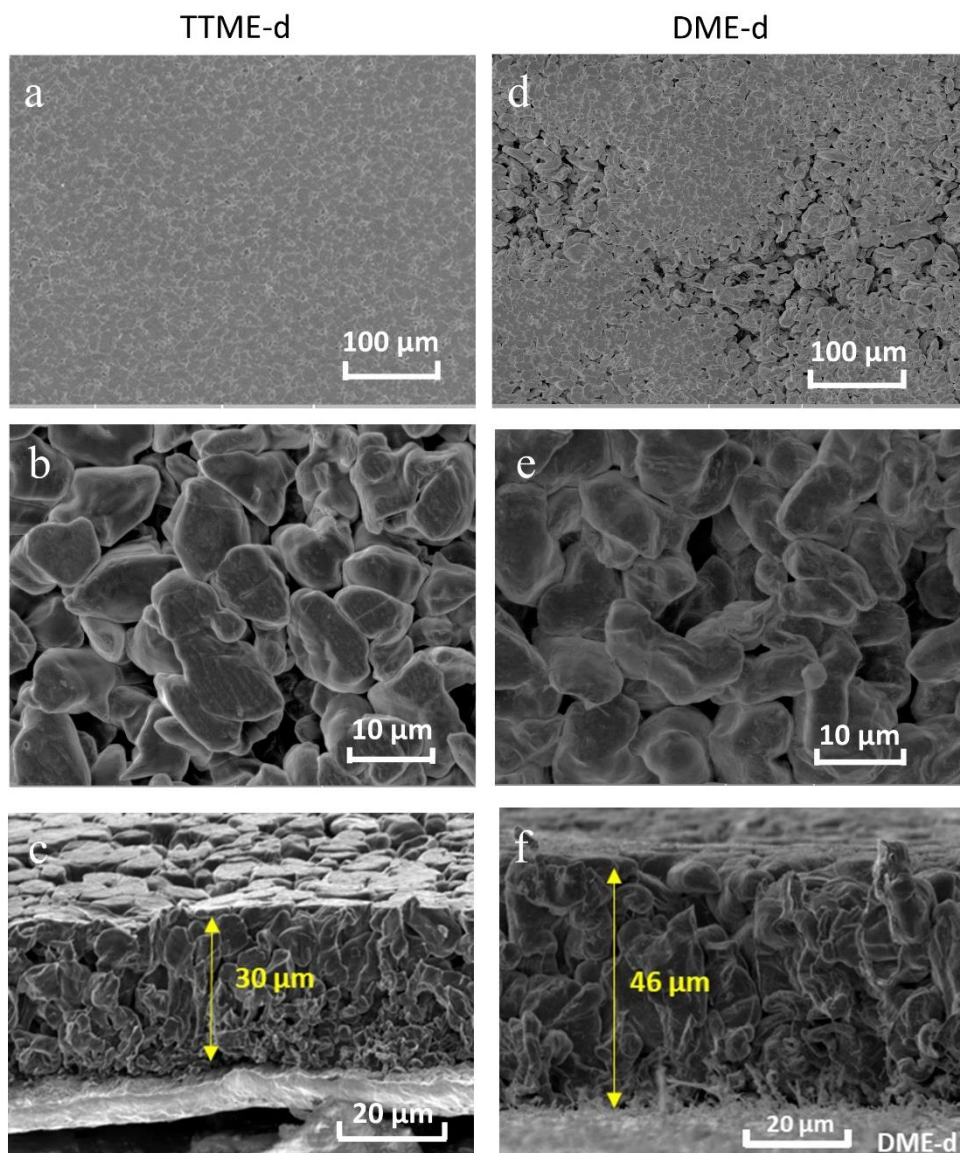
Fig. 4.6. The morphologies of deposited lithium metal with the different electrolytes. (a) Top view SEM image with TTME−d at 0.5 mA/cm^2 for 10 h. (b) Top view SEM image with DME−d at 0.5 mA/cm^2 for 10 h. (c) SEM image with TTME−d at 1 mA/cm^2 for 5 h. (d) SEM image with DME−d at 1 mA/cm^2 for 5 h. (e) Cross−section SEM image with TTME−d at 0.5 mA/cm^2 for 10 h. (f) Cross−section SEM image with DME−d at 0.5 mA/cm^2 for 10 h.

In order to observe the SEI on the surface of lithium metal more intuitively, the deposited lithium metal on the copper mesh was further characterized by cryo−TEM. A copper-TEM grid was deliberately positioned onto the copper

surface of the working electrode. A certain amount of lithium metal was deposited onto the Cu-TEM grid during the plating process. The current density of deposition was 0.25 mA/cm^2 and the deposition time was 1 h, followed by half striping of the lithium for better observation. After cycling, the coin cells were disassembled in glove box, and then the Cu-TEM grid was extracted and washed with DME to eliminate residual salts and electrolytes. Subsequently, the Cu-TEM grid was dried and sealed to avoid the air contact. After being transferred out of the glove box, the grid was placed within an automated cryogenic-TEM autoloader system, operating under a liquid nitrogen environment[170].

Figure 4.7 shows the coarse-scale low−temperature TEM image of the plated lithium metal using the TTME−d electrolyte. It can be observed that although a few lithium dendrites exist inside, the surface of lithium metal in the whole area is very smooth and flat, demonstrating that an effective SEI on the surface of lithium metal is generated.
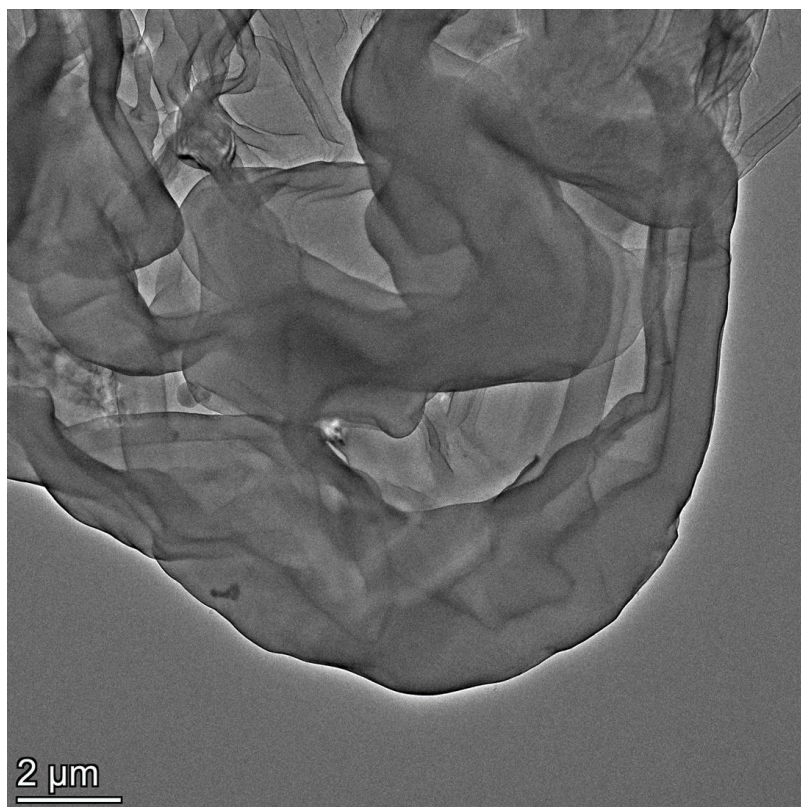
Fig. 4.7. Low−magnification cryo−TEM images showing plated Li metal formed with the TTME-d electrolyte.

The high−magnification image, shown in Figure 4.8a, indicates that there is a uniform SEI film on the lithium metal surface with TTME-d, and the SEI film is obviously divided into outer and inner layers. Further analysis of the double−layer SEI shows that a layer of crystalline phase and a layer of amorphous phase exist outside the dense lithium metal, as shown by the crystalline phase in Figure 4.8b, and in the fast Fourier transform (FFT) diagram in Figure 4.8c. The outer SEI shows more amorphous materials, while the inner SEI shows more lattice stripes. Through FFT analysis, it can be seen that the inner crystal is mainly composed of crystalline substances such as Li_2O and LiF

(Figures 4.8d and 4.8e) in the presence of TTME-d. In general, ethers like DME tend to form SEI with inorganic components such as Li_2O during discharge. This suggests the involvement of the solvated DME structure in SEI formation. There are more amorphous substances in the outer SEI, in which some crystalline islands are also distributed.

According to the electron energy loss spectroscopy (EELS) elemental maps in Figure 4.9, it can be inferred that the outer SEI formed with TTME-d is composed of mostly organic components containing C, N, and F elements. These organic components confirm that not only DME, but also TTME is involved in the solvation structure of the electrolyte and participates in the formation of effective SEI components.
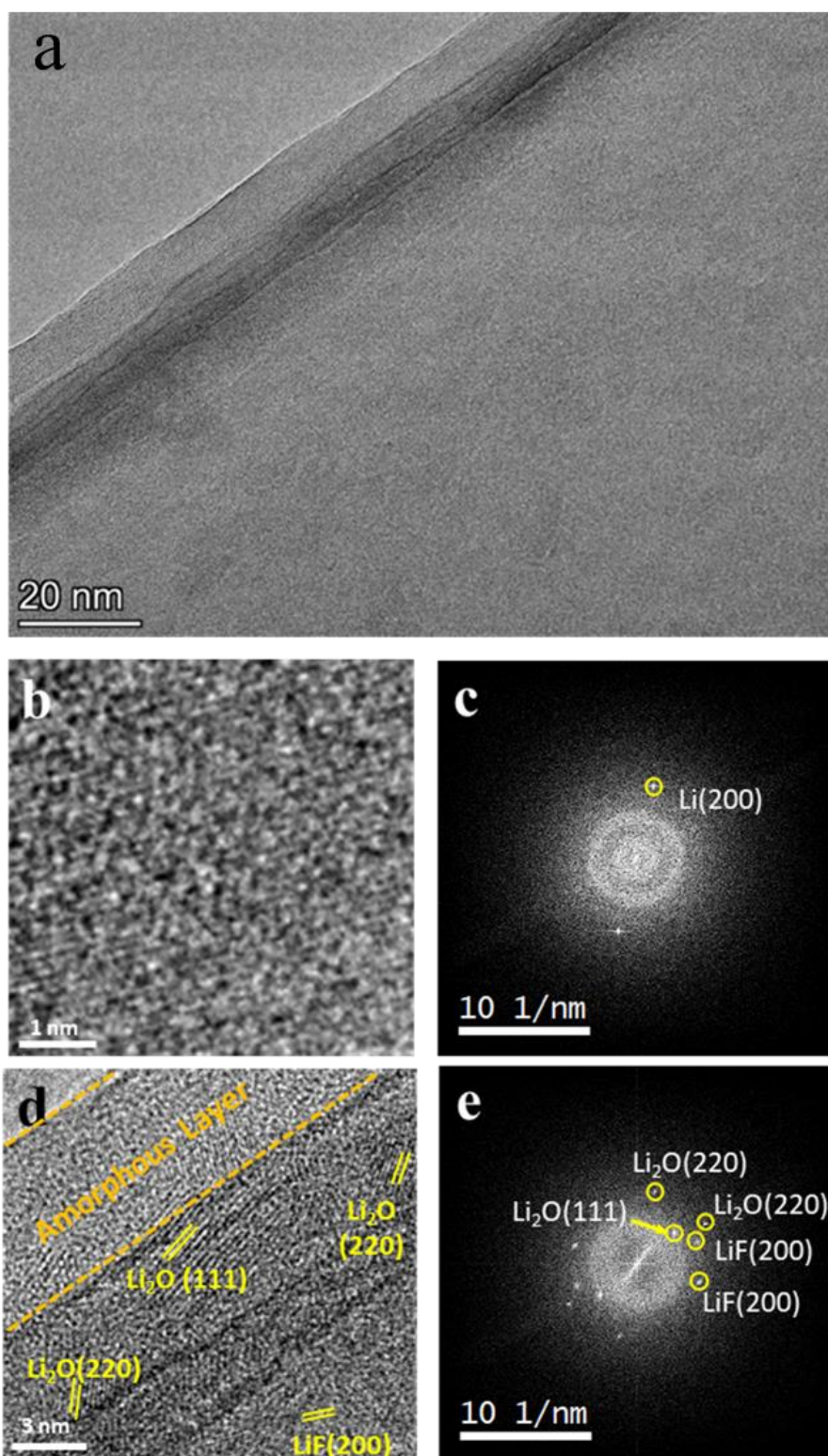
Fig. 4.8. Cryo−TEM analysis of the SEI formed using TTME−d electrolyte. (a) Low−magnification cryo−TEM image showing plated Li metal and its SEI. (b) HR-TEM image showing Li nanocrystal and (c) the corresponding FFT diagram. (d) Distribution map of different phases in the SEI skin layer and (e) the corresponding FFT diagram, showing Li_2O and LiF nanocrystals (indicated by yellow lines) inside the SEI.
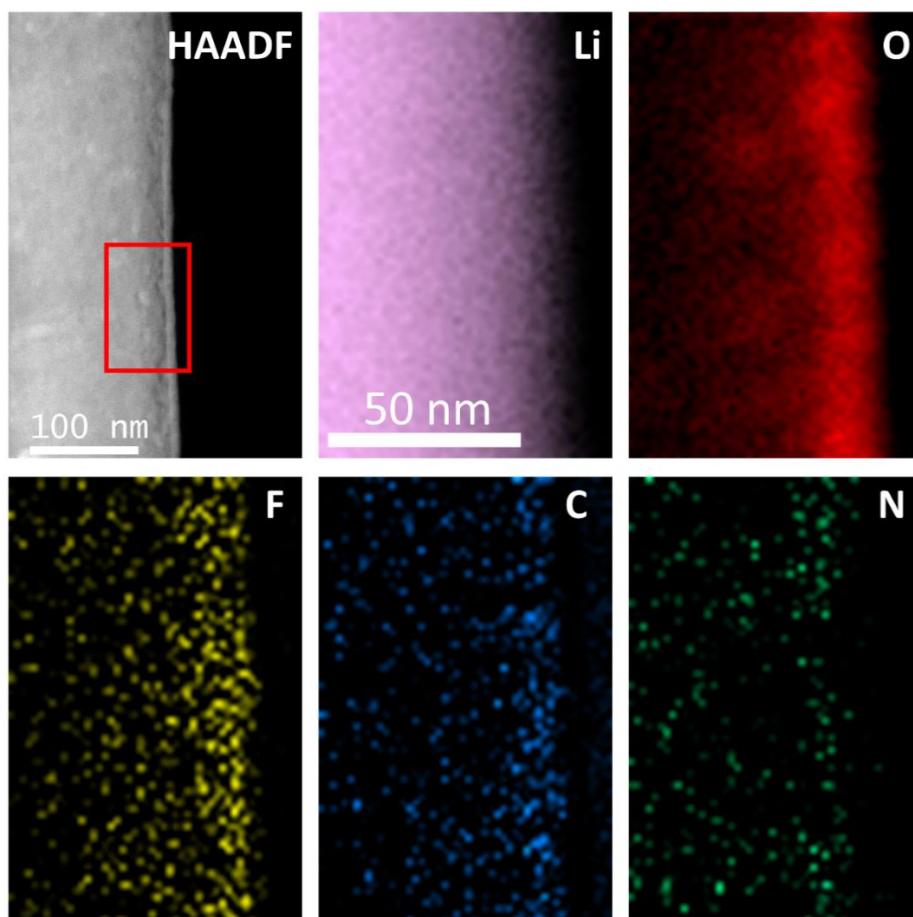
Fig. 4.9. HAADF images and EELS elemental maps of Li, O, N, F, and C in the SEI formed on plated Li metal in the presence of TTME-d.

In the following analysis, I speculate on potential outcomes based on existing evidence. Additionally, once I have access to an atomic force microscope (AFM) located in the glovebox, I plan to measure the stress−strain curves of SEI on lithium metal surface to validate my hypotheses. Due to TTME's relatively low LUMO energy level, a small fraction of TTME molecules participating in the primary solvation structure undergo reduction. Initially, TTME molecules are reduced to form $-CF_3$, followed by further reduction at the lithium surface to

generate LiF and primarily −CF$_x$ based organic components. The remaining portion tends to be reduced into organic components containing .This unique double−layer structure gives SEI both mechanical strength (crystalline part) and flexibility (organic part). The mechanical strength of the inner SEI prevents lithium dendrites from growing longitudinally and does not damage the external film structure. At the same time, the internal mechanical strength ensures that the SEI shrinks but does not collapse in the process of complete lithium stripping, which consolidates the integrity of the structure. The flexibility of the outer layer enables the SEI to maintain the integrity of the membrane structure in the state of complete lithium deposition or complete lithium stripping. This complete and flexible SEI is beneficial for the repeated migration of lithium ions, stabilizes the nucleation and growth of lithium during the cycle, and greatly improves the reversibility of the reaction, thus improving the Coulombic efficiency (CE) of the cells.

In contrast, the cryo−TEM images for the DME−d, Fig. 4.10 reveal the presence of only one SEI layer on the lithium metal surface. The edges of this SEI exhibit a jagged appearance, far less smooth and uniform compared to the SEI observed in the TTME−d. Furthermore, the distribution of SEI components appears highly uneven, lacking the well−defined layer structure observed in the TTME−d.
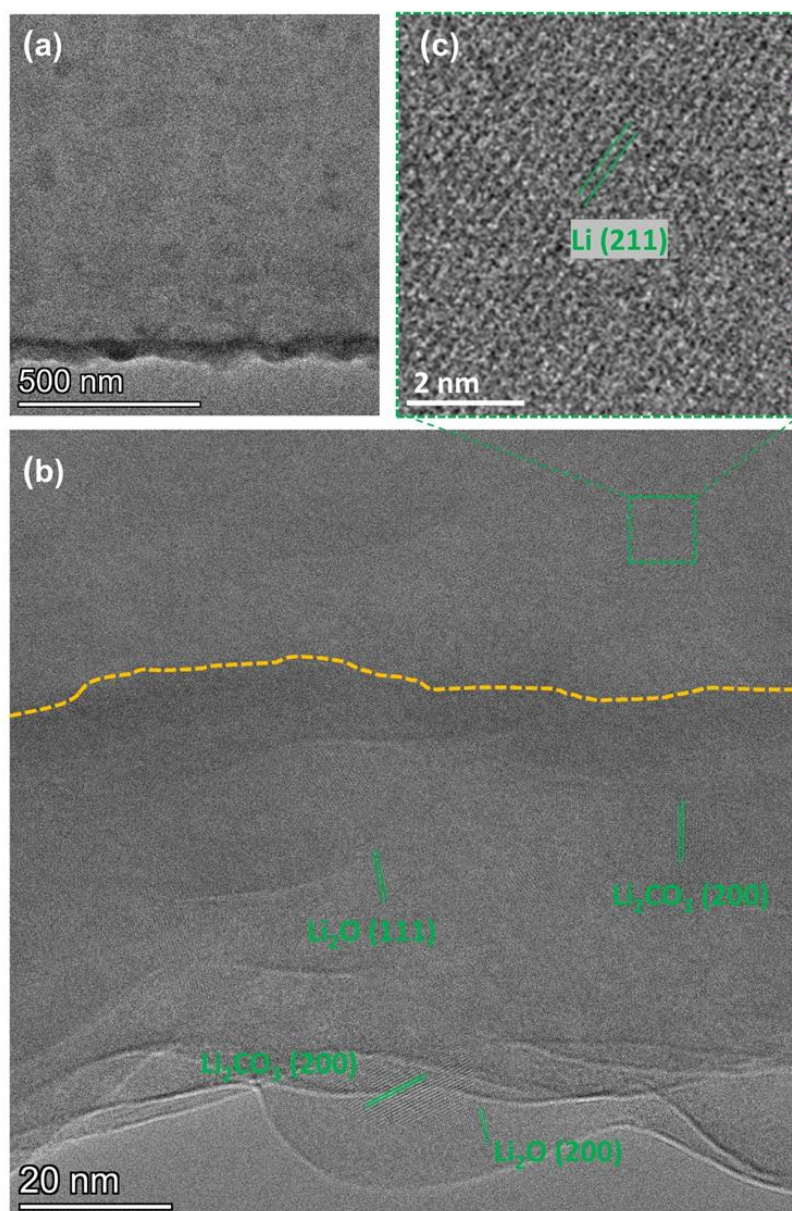
Fig. 4.10. Cryo−TEM analysis of SEI formed using DME−d electrolyte. (a) Low−magnification cryo−TEM images showing plated Li metal and its SEI. (b) Distribution map of different phases in the Li part and SEI skin layer. (c) Enlarged HRTEM showing Li nanocrystal.

XPS analysis of the lithium metal after 50 cycles in Li||Cu cell was performed to further investigate the elemental composition of the SEI. In order to obtain data of different depths, the samples were etched with argon ions for 6 s. Figure 4.11 shows the C, F and O spectra of the lithium metal on the copper foil after 50 cycles of Li||Cu cells. Combined with C 1s and F 1s spectra, it can be observed

that, corresponding to the results of cryo−TEM, there are more CF_x bonds on the surface of the TTME−d system, which indicates that TTME participates in the formation of the SEI as a part of the solvated structure in the TTME-d system. Moreover, it can be seen from O 1s spectra that the content of Li_2O on the surface of the TTME−d system is also higher than in the DME-d system, and the content of Li_2O is slightly enhanced after 6 s etching, which also proved that it exists in the SEI, contributing to the mechanical strength of the SEI.
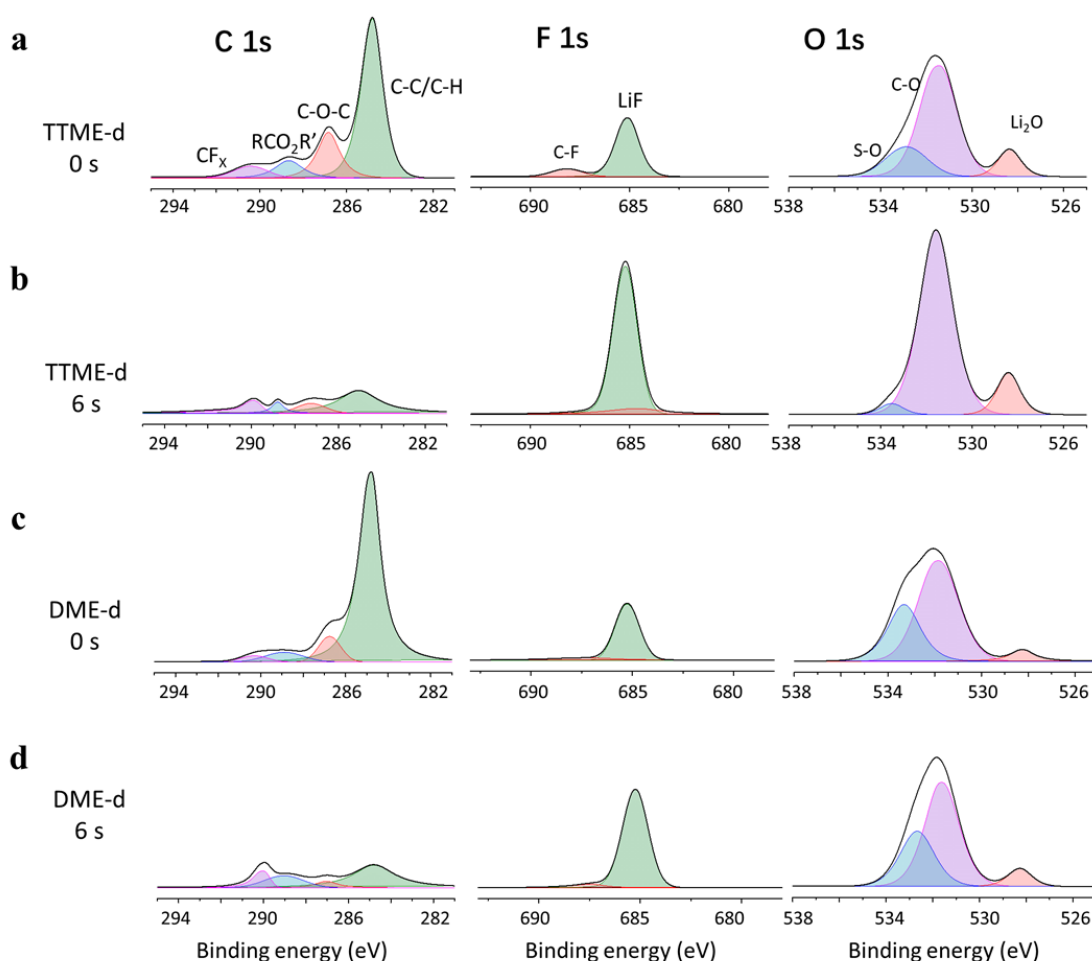
Fig. 4.11. The C 1 s, F 1 s and O 1 s XPS spectra of Li anodes after 50 cycles plating/stripping with different electrolytes: (a) TTME−d after 0 s etching, (b) TTME−d after 6 s etching, (c) DME−d after 0 s etching, and (d) DME−d after 6 s etching.

Based on the results from cryo-TEM, EELS, and subsequent XPS analysis, a model for the possible lithium metal surface SEI in the TTME-d electrolyte system was developed, as shown in Figure 4.12. In this double-layer SEI structure, the inner layer resembles a traditional SEI mosaic model, composed of stacked crystalline structures mainly consisting of Li_2O and LiF (approximately 8 nm thick), while the outer layer is predominantly amorphous. Combining the etching results from XPS and the distribution of C, F, and O elements from EELS (where O is distributed in both the inner and outer layers due to the presence of Li_2O in the inner layer), it is speculated that the amorphous structure of the outer layer contains a significant amount of $-CH_2O-$ organic compounds and amorphous substances containing F. This model differs from the traditional mosaic model structures reported in many LHCEs[153,172] and is also distinct from single-layer pure amorphous SEI or single-layer "crystalline island" models[170].
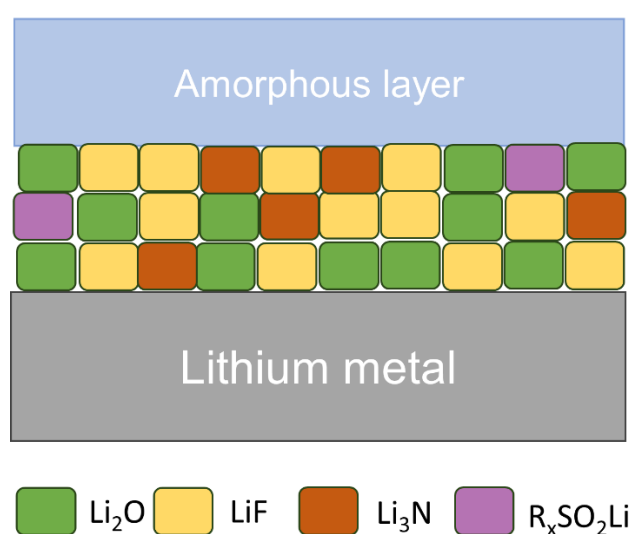
Fig. 4. 12 Schematic illustration of the double-layer model of the SEI formed on the lithium metal surface in the TTME-d electrolyte.

4.3.3. Electrochemical performance of TTME−d electrolyte for high−voltage cells

The TTME−d electrolyte was used to evaluate the performance of high−voltage lithium metal cells. The high−voltage cathodes are from commercial cells (see Section 1.2.1), of which the loading of NCM811 is 3.13 mAh/cm^2, and the loading of LCO is 2.96 mAh/cm^2. As shown in Figure 4.13, under the same ether electrolyte (lithium metal friendly) environment and with the same lithium salt concentration, the capacity of the Li||LCO cell with the DME−d electrolyte decays rapidly, and after 45 cycles the capacity quickly fades to less than 80% capacity retention. After 80 cycles, the capacity decreases to less than 70%, and the cell fails in the subsequent cycles. In contrast, the cell with the TTME−d electrolyte can maintain a capacity retention of more than 90% and a CE of more than 99.5% in the first 170 cycles, and the capacity decreases to less than 85% in 180 cycles and starts to fail gradually thereafter.
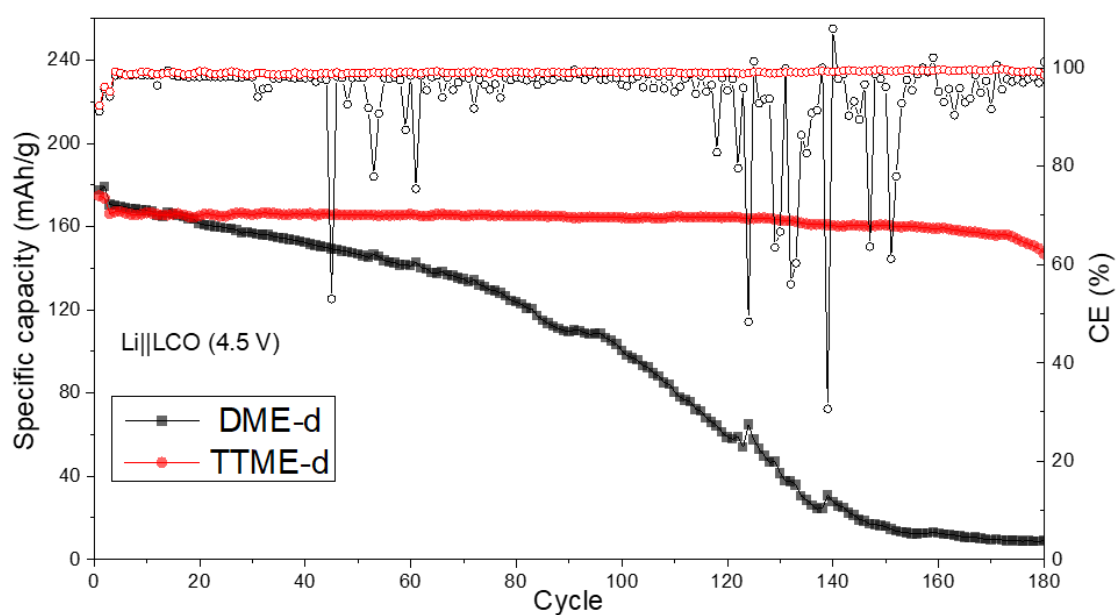
Fig. 4.13. Cycling performance of Li||LCO (4.5 V) cells using different the electrolytes.

It can also be seen from the charge/discharge curves of the TTME-d and DME-d systems (Figure 4.14) that the charge and discharge platforms of the cell using the TTME−d are always stable in the first 150 cycles, and that the charge and discharge curves maintain a high degree of coincidence for a long period of time after the initial activation, indicating the high reversibility of the cell in high−voltage cycles. In comparison, the charge and discharge curves of the cell using the DME−d change obviously during cycling, corresponding to its poor reversibility.
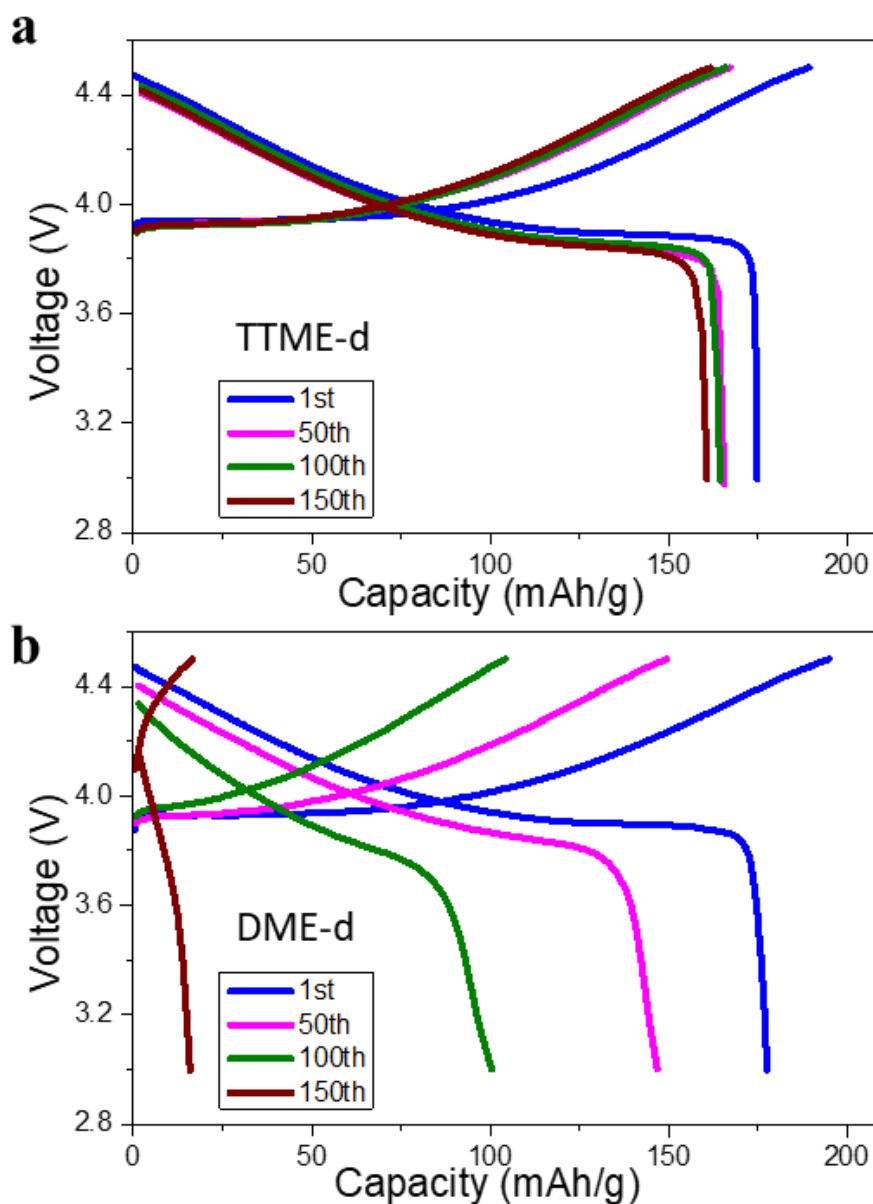
Fig. 4.14. Charge/discharge curves of Li||LCO cells using TTME-d and DME-d electrolytes.

As shown in Figure 4.15, there are similar cycle results for high−nickel NCM811. The capacity of the cell with the DME−d electrolyte decreases to less than 80% after 60 cycles, and then the cell goes to complete failure rapidly. Noticeably, with the TTME−d electrolyte, the capacity retention of the cell remains above

85% after 240 cycles, and the average CE is above 99.8%.
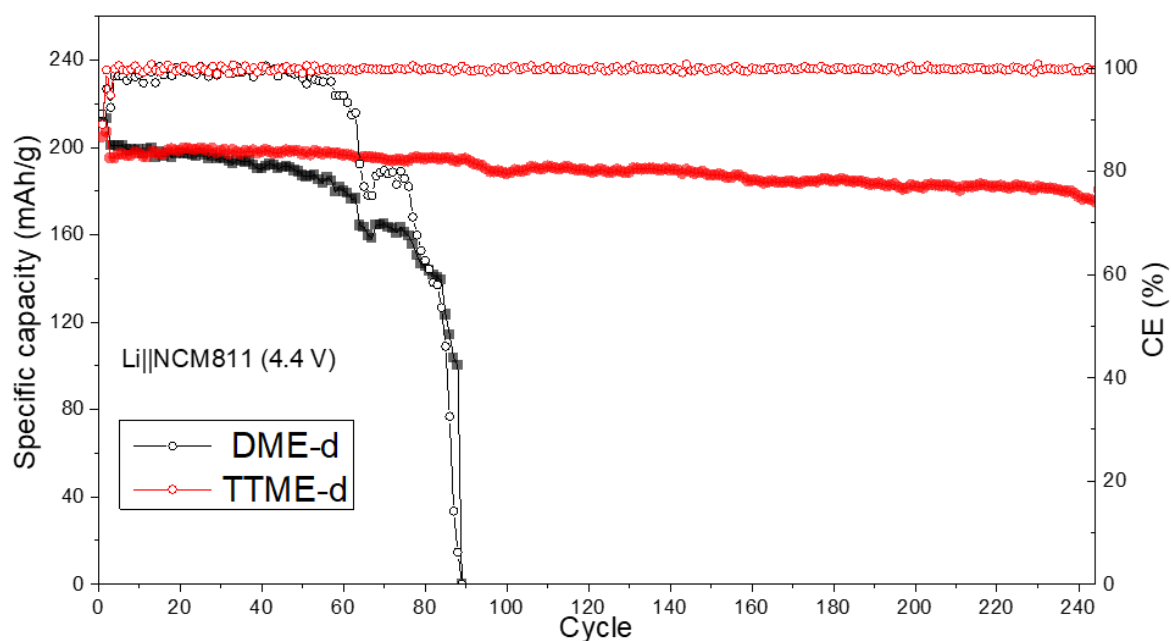
Fig. 4.15. Cycling performance of Li||NCM811 (4.4 V) cells using different electrolytes.

The charge/discharge curves (Figure 4.16) similarly demonstrate the enhanced stability of the TTME−d cell within the initial 150 cycles. Furthermore, the charge and discharge curves of the TTME−d cell maintain substantial alignment over a relatively long period after initial activation, with curves for the 100th and 150th cycles nearly entirely overlapping. This aspect indirectly suggests a high CE for the cell in high−voltage cycles. In contrast, for the DME−d cell, the charge and discharge curves exhibit conspicuous variations during cycling, with rapid degradation occurring after approximately 80 cycles.
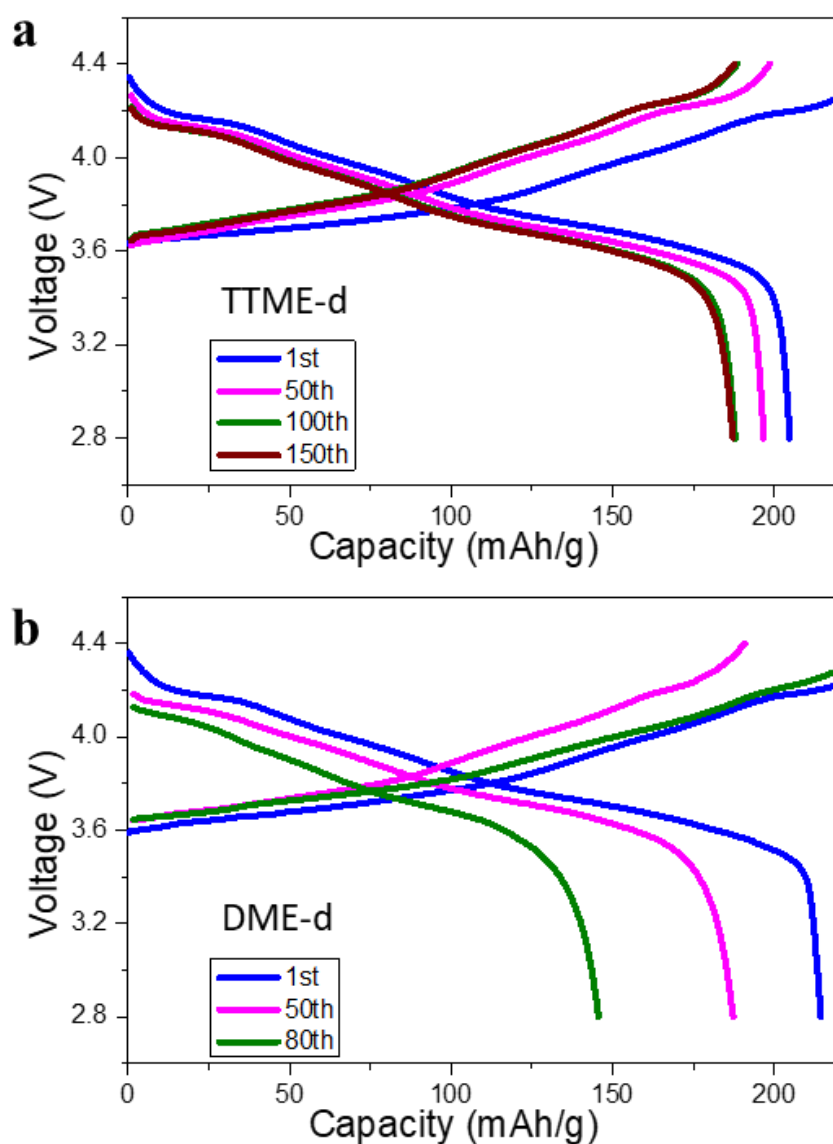
Fig. 4.16. Charge/discharge curves of Li||NCM811 cells using TTME-d and DME-d electrolytes.

The high performance of the TTME−d system for high−voltage cathodes was also validated using an ultra−thin lithium foil (20 μm). From Figure 4.17, it can be seen that although the capacities of the cells with these two electrolytes decrease under the severe condition of ultra−thin lithium, the cell with the

TTME−d still displays twice the capacity retention of the cell with the DME−d.
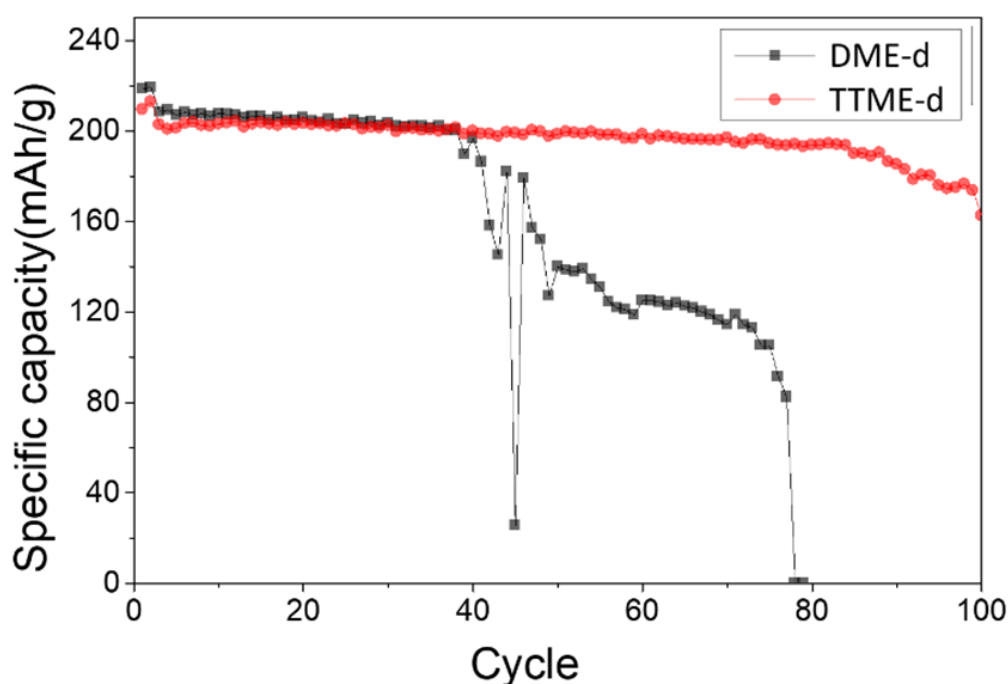
Fig. 4.17. Cycling performance of Li||NCM811 (4.4 V) full cells with ultra-thin Li foil (20 μm) using different electrolytes.

The cycle performance at high temperature was also studied for the Li||LCO and Li||NCM811 cells. It can be seen from Figure 4.18 that under the operating condition of 45 ºC and without additives, both cells employing the DME−d electrolyte display significant capacity decay, with the Li||NCM811 cell even experiencing failure in fewer than 40 cycles. On a promising note, the Li||LCO and Li||NCM811 cells utilizing the TTME−d electrolyte demonstrate consistent cycling behavior for over 100 cycles, showcasing the favorable compatibility of the TTME−d electrolyte under high voltage and elevated temperature conditions.
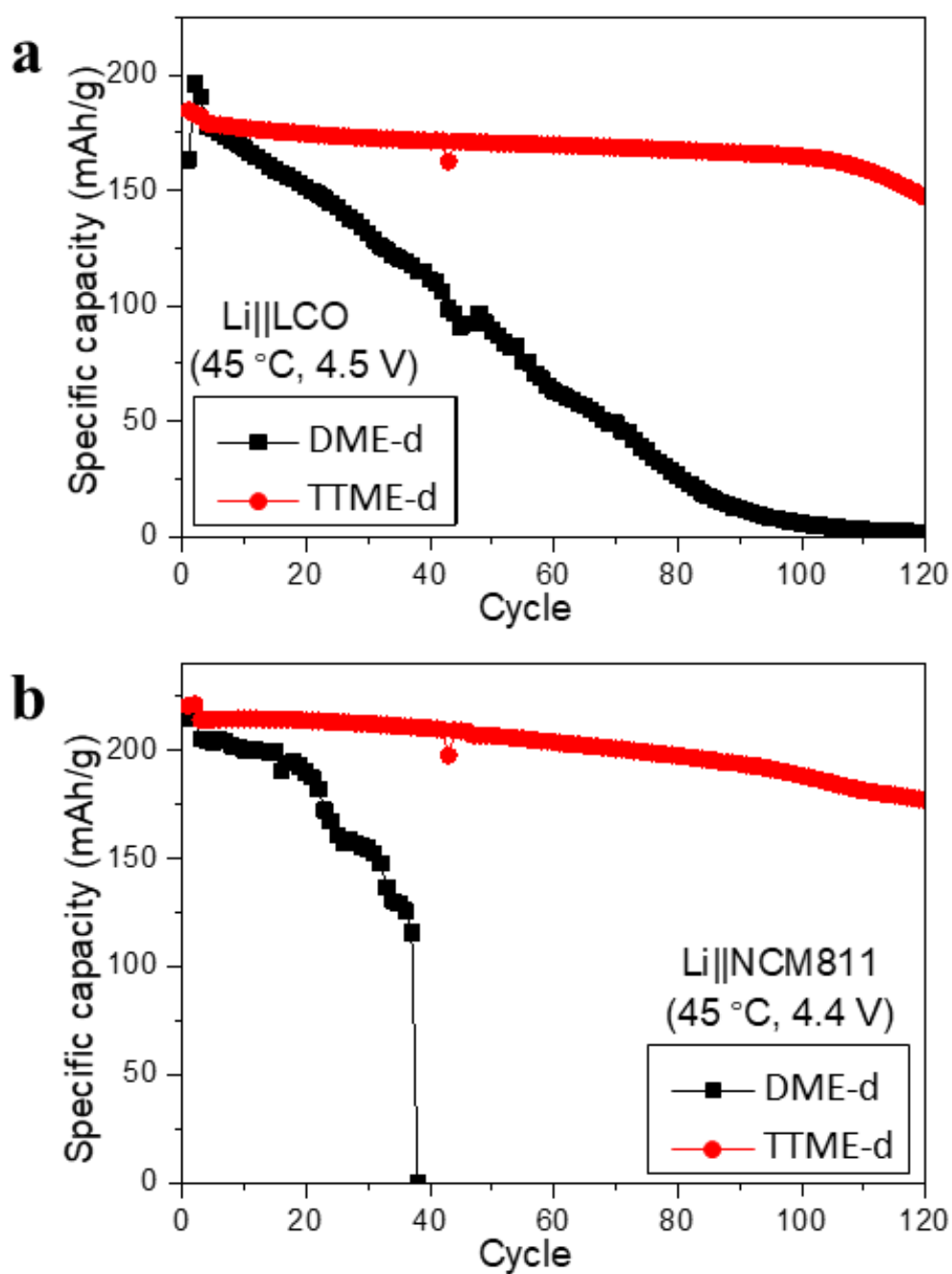
Fig. 4.18. (a) Cycling performance of Li||LCO cells at 45 °C with two difference electrolytes. (b) Cycling performance of Li||NCM811 cells at 45 °C with two difference electrolytes.

4.3.4 Characterization of high-voltage cathode using TTME−d electrolyte

In order to explore the difference of the CEI formed on the cathode between the TTME−d electrolyte and the ordinary ether electrolyte without the influence of additives (i.e., DME-d), the LCO and NCM811 cathodes after 100 cycles were characterized by SEM and XPS, and the corresponding lithium metal anodes were dissolved in 3% nitric acid solution to detect the content of dissolved transition metals, as described in section 2.3.10 in the methods section.

By comparing SEM images in Figure 4.19 a−f, it can be seen that with both LCO and NCM811 electrodes, the surface of the cathode plate with the TTME−d is flatter after cycling, and the shape of the cathode particles is still clearly visible, whereas after the corresponding cycle, the surface of the cathode plate with the DME−d is uneven. The LCO particles are severely pulverized in the DME-d case, and this problem is even worse for the NCM811 in DME-d.
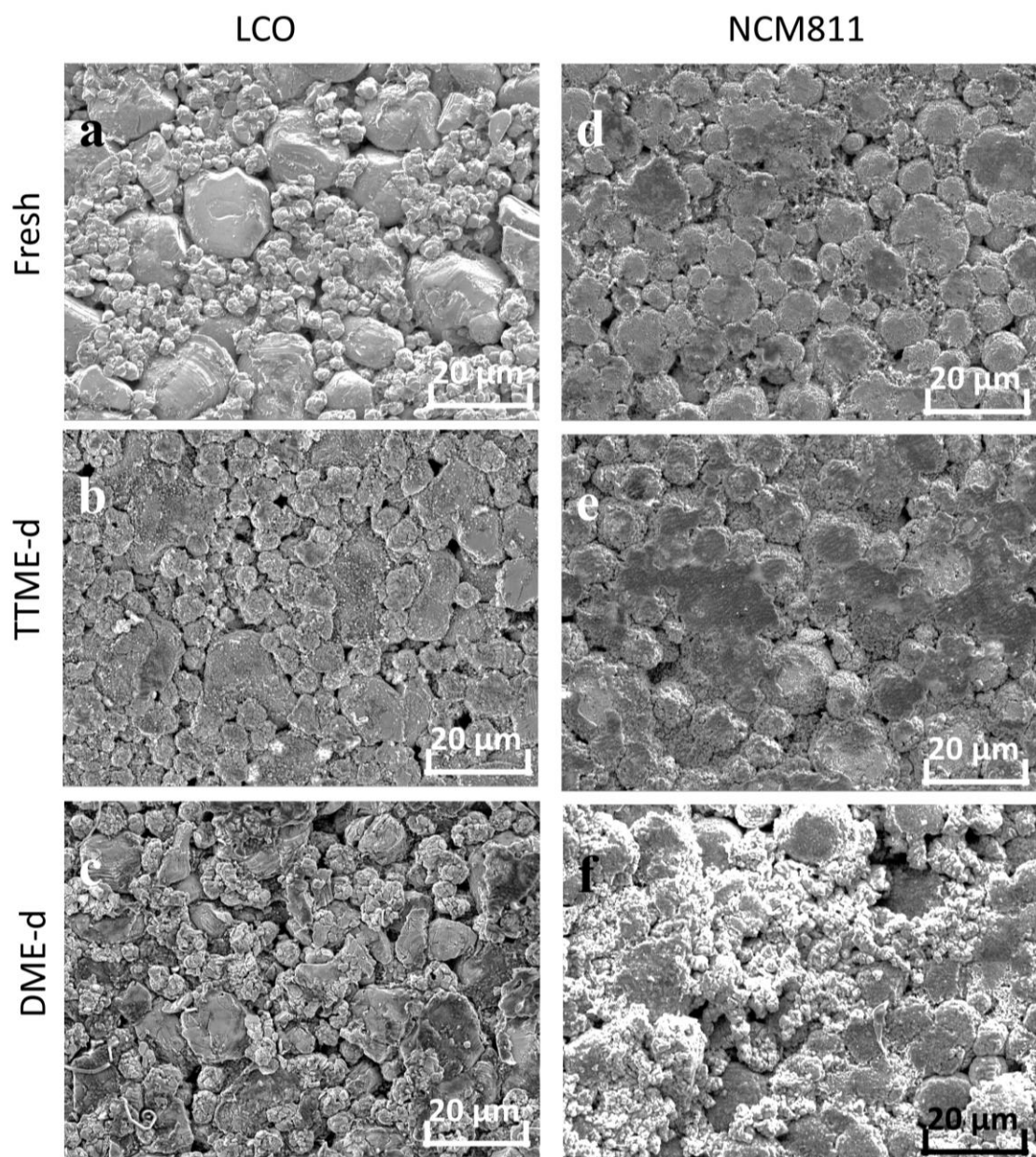
Fig. 4. 19. SEM images of (a) fresh and (b, c) cycled LCO electrodes (after 100 cycles) with (b) TTME−d and (c) DME−d electrolytes. SEM images of (d) fresh and (e. f) cycled NCM811 electrodes (after 100 cycles) with (e) TTME−d and (f) DME−d electrolytes.

In addition, the dissolution of transition metals was investigated using inductively coupled plasma mass spectrometry (ICP−MS).The results are shown in Tables 4.1 and 4.2, and Figure 4.20. For the NCM811 cathode, there

are nearly no Co and Mn ions detected by ICP−MS in the case of the TTME−d system, and the content of Ni is also less than one-sixth of that detected with the DME−d system. The dissolved Co from the LCO plate with the TTME−d system is also far less than that from the LCO plate with the DME−d system, again confirming the much-improved cycling stability and more effective CEI in the presence of TTME-d.

Table 4.1. Dissolved transition metals detected by ICP-MS from in the LCO||Li cell after 100 cycles.

	TTME-d	DME-d
Co	0.02 ppm	0.33 ppm
Ni	0.48 ppm	3.05 ppm
Mn	0.04 ppm	0.39 ppm

Table 4. 2 Dissolved transition metals detected by ICP-MS from the in NCM811||Li cell after 100 cycles.

	TTME-d	DME-d
Co	0.24 ppm	2.17 ppm
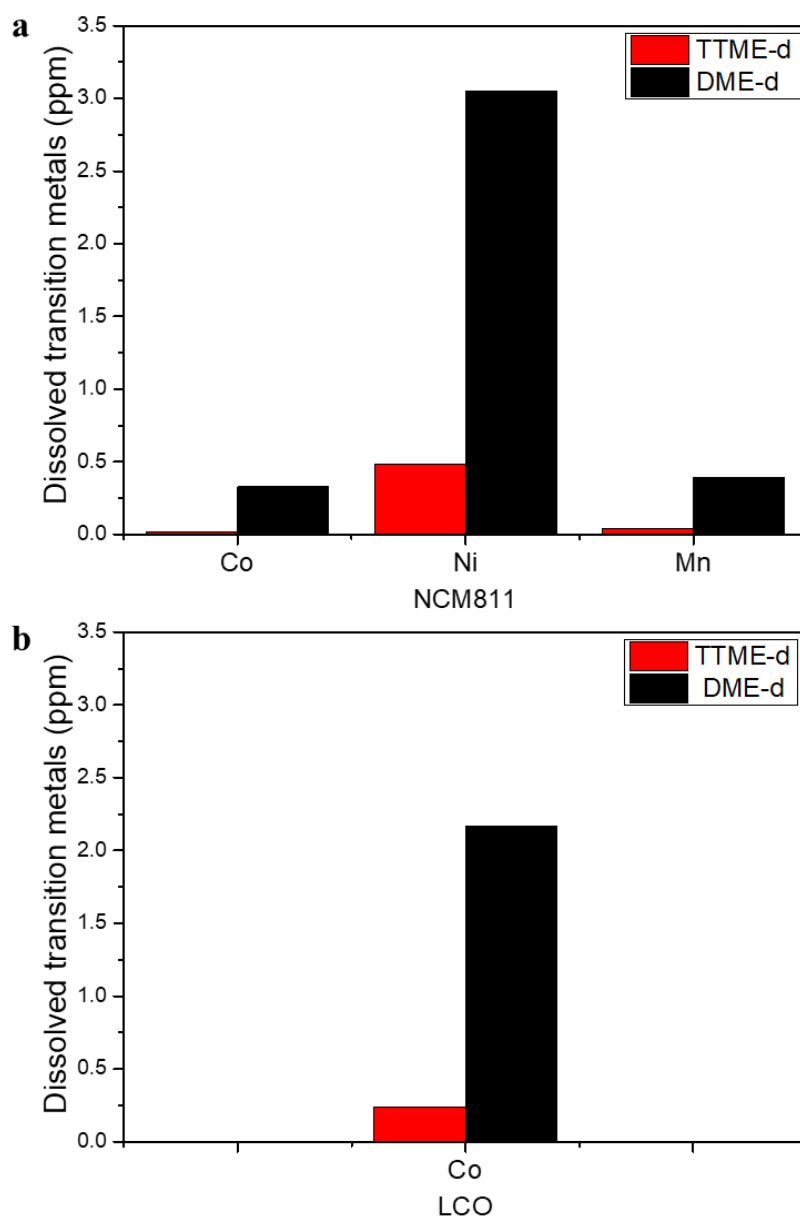
Fig. 4.20. Dissolved transition metals in (a) Li||NCM811 and (b) Li||LCO cells measured with ICP−MS after 100 cycles with the different electrolytes.

The XPS results presented in Figure 4.21 provide further insights. The fluorine

signal at 685 eV indicates significantly higher levels of LiF in the LCO and

NCM811 cathode plates employing the TTME-d electrolyte, as compared to

those using the DME-d electrolyte. This suggests that the CEI formed on the cathode surface with the TTME-d electrolyte is enriched with LiF, which due to the stability of the Li-F bond effectively impedes pulverization and inhibits the dissolution of transition metal ions.

Collectively, these results highlight that the TTME-d electrolyte promotes the formation of an LiF-rich CEI on the cathode surface, which helps prevent pulverization and suppress the dissolution of transition metal ions, resulting in excellent stability over extended periods even under extreme conditions.
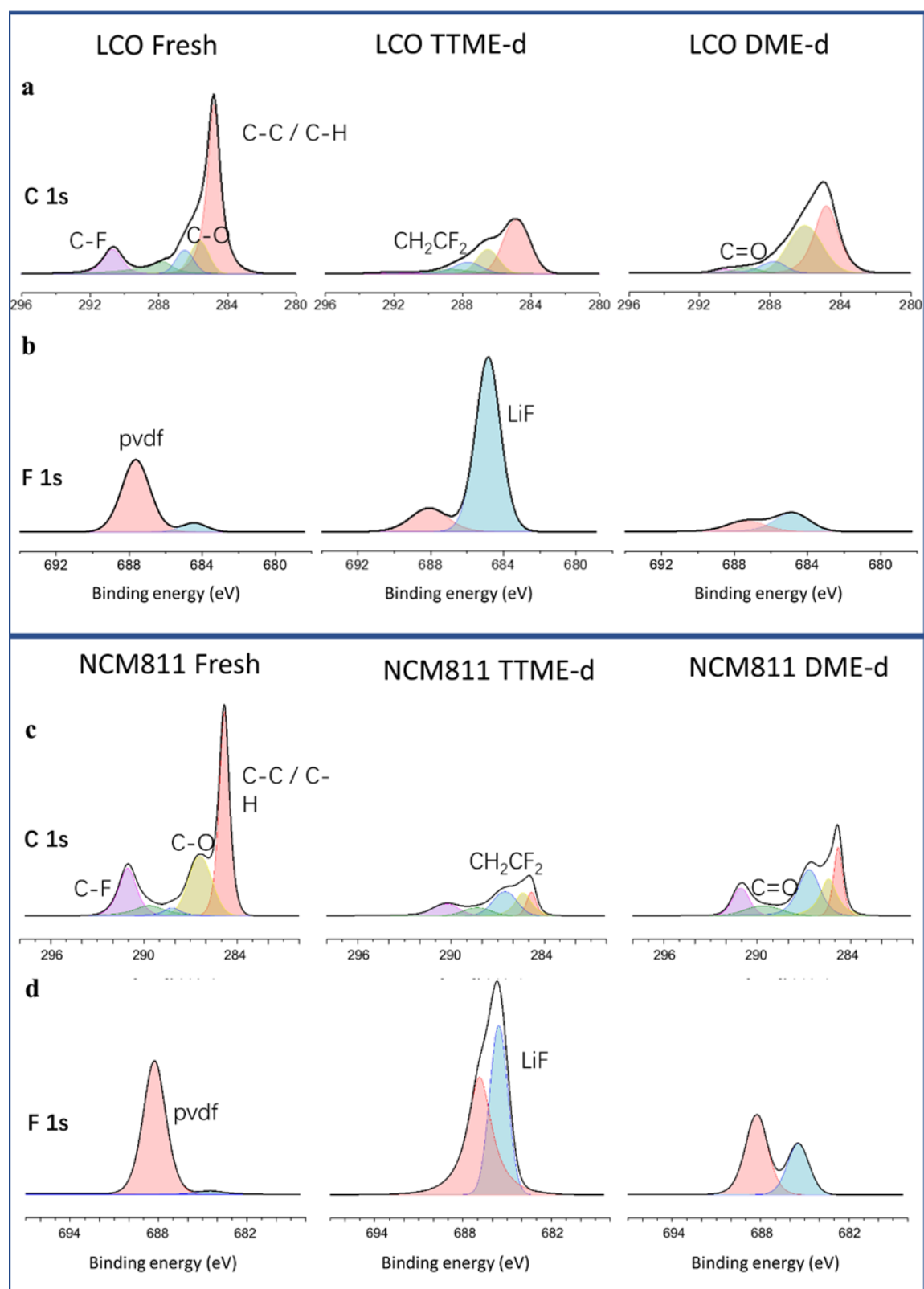
Fig. 4.21. X-ray photoelectron spectroscopy (XPS) results of cycled cathodes after 100 cycles. (a) C 1s and (b) F 1s spectra of LCO plates with the different electrolytes. (c) C 1s and (d) F 1s spectra of NCM811 plates with the different electrolytes.

At the end of this chapter, a comparison was made between Li||Cu cells and Li||Li cells in LHCE using TTME-d electrolyte and some other diluents mentioned in the literature, demonstrating the superior electrochemical performance of the TTME-d electrolyte developed in this thesis..

Table 4. 3 Comparative performance of Li||Cu cells in various literature sources

Electrolyte	Current density (mA/cm^2)	Capacity (mAh/cm^2)	Cycling performance	Ref.
1.4 M LiFSI TTME/DME	0.5	1.0	350 cycles	This work
1.4 M LiFSI BDE/DME	0.5	1.0	250 cycles	[147]
LiFSI-1.2DME-3TTE (in molar)	0.5	1.0	300 cycles	[153]
2M DMC/BTFE	0.5	0.5	350 cycles	[154]
1.3 M LiFSI + 0.7 M LiTFSI + 0.02 M LiPF6 in DMC/1,2-dfBen	0.5	0.5	200 cycles	[154]
1.0 M LiFSI FDMB	0.5	1.0	300 cycles	[163]
1.0 m LiFSI/DMTMSA	0.5	1.5	1,100 cycles	[173]

Table 4. 4 Comparative performance of Li||Li cells in various literature sources

Electrolyte	Current density (mA/cm^2)	Capacity (mAh/cm^2)	Cycling performance	Ref.
1.4 M LiFSI TTME/DME	0.5	1.0	3,200 h (1,600 cycles)	This work

1.4 M LiFSI BDE/DME	0.5	1.0	2,000 h	[147]
1.0 M LiFSI TFEO/DME	0.5	1.0	750 h	[154]
1.0 M LiFSI FDMB	0.5	1.0	420 h	[163]
1.0 m LiFSI/DMTMSA	0.5	1.5	1,100 cycles	[173]

4.4 Conclusion

In conclusion, the utilization of the bifunctional TTME molecule in the selected electrolyte (TTME-d) consisting of 1.4 M LiFSI and DME-TTME (1:4 by volume) has demonstrated remarkable electrochemical performance. The Li||Cu cells exhibited a high Coulombic efficiency of 99.28% after 300 cycles, while the Li||Li cells demonstrated exceptional stability with over 3,200 hours of continuous cycling. These exceptional results can be attributed to the unique double-layer solid electrolyte interphase (SEI) structure formed on the lithium metal surface by the TTME-d electrolyte.

The cryo-TEM characterization clearly revealed the distinct characteristics of the SEI formed by the TTME-d electrolyte, which combines both rigidity (from the crystalline components) and flexibility (from the organic constituents). Moreover, lithium metal cells utilizing two commercially available cathodes showcased outstanding cycling performance. Specifically, the NCM811 cell exhibited 85% capacity retention after 240 cycles at a cut-off charge voltage of 4.4 V, while the LCO cell maintained 90% capacity after 170 cycles at a cut-off charge voltage of 4.5 V.

The robust cathode-electrolyte interphase (CEI) formed on the cathode surface with the TTME-d electrolyte was confirmed through various characterization methods, demonstrating its capability to prevent cathode pulverization and inhibit the dissolution of transition metal ions.

In summary, the utilization of the TTME-d electrolyte, enabled by the bifunctional TTME molecule, has proven to be highly advantageous for achieving exceptional electrochemical performance in lithium metal cells. The formation of a robust SEI, with a combination of rigidity and flexibility, plays a crucial role in ensuring long-term stability and preventing performance degradation. These findings offer significant insights for the development of advanced electrolyte systems for next-generation lithium-based energy storage devices.

Chapter 5: Highly fluorinated TTME co-solvent enabling ether electrolyte for high-voltage lithium ion batteries with graphite anode

5.1 Introduction

Graphite anodes combined with high-voltage cathode materials such as layered oxides including $LiCoO_2$ (LCO) and $LiNi_{0.8}Co_{0.1}Mn_{0.1}O_2$ (NCM811) are currently widely used in high-energy-density commercial lithium ion batteries[174].

Ether compounds are promising electrolyte solvents and have been widely used in different battery systems, such as those based on lithium metal anodes and silicon anodes, due to their low melting point, low viscosity and good reduction stability. However, reports in the literature suggested that ether electrolytes are not compatible with graphite anodes [175]. It has been reported that ether electrolytes lead to solvent co-intercalation, graphite exfoliation, and

electrolyte decomposition, with which the cells show decreased Coulombic efficiency (CE) and poor cycle stability. In recent years, due to the rapid development of hydrofluoroethers (HFEs) used as co-solvents in other anode systems, researchers have turned their attention to the possibility of designing ether electrolytes that are suitable for graphite electrodes [176,177]. Some electrolytes based on fluorinated ether co-solvents have been reported to deliver stable cycling of graphite anodes. In addition to the regulation of the solvation structure, the formation of a stable anion-based solid electrolyte interphase (SEI) film on the graphite surface is the key to suppressing the co-intercalation of solvent molecules with graphite and thus to maintaining their functionality and performance over extended charge/discharge cycles[178,179].

Building upon these studies, we explore whether the LHCE electrolyte TTME-d, when applied to the lithium metal anode, can also be suitable for graphite anodes. Given the widespread commercialization of high-voltage graphite batteries, successful application of this electrolyte could potentially lead to its commercialization in a short period.

In this chapter, the TTME-d electrolyte was applied to high-voltage||graphite batteries and tests were conducted using both coin cells and pouch cells simultaneously. On one hand, we anticipate that TTME's solvation structure can prevent solvent co-intercalation on the graphite. On the other hand, due to the high degree of fluorination of TTME, the overall oxidation stability of the fluorinated ether electrolyte is improved, making it less susceptible to oxidative

degradation, as demonstrated in Chapter 3.

The EC/DEC carbonate electrolyte containing 1 wt.% vinylene carbonate (VC) and 1 wt.% 1,3-propanesultone (PS) reported previously as having good performance for high-voltage full-cell cycling was used as a control electrolyte for comparison [161,174,180].

The results show that the fluorinated ether electrolyte system presented here (TTME-d) stabilizes both high-voltage layered oxide cathodes and the graphite anode more effectively than the carbonate electrolyte system. The NCM811||graphite cells with the fluorinated ether electrolyte (TTME-d) exhibit stable cycling at a cut-off voltage of 4.4 V, maintaining a capacity retention greater than 90% after 200 cycles. When the fluorinated ether electrolyte is applied to the LCO||graphite cells with a cut-off voltage of 4.5 V, the cells deliver capacity retention of 97% after 100 cycles. Moreover, the large-capacity NCM811||graphite pouch cells (1780 mAh) using the fluorinated ether electrolyte (TTME-d) perform better in terms of their cycling performance than the carbonate electrolyte at both room temperature and elevated temperature.

5.2 Experimental details

5.2.1 Electrolytes and electrode preparation

All the reagents, with a purity of above 99.9% (including lithium salts and solvents), were provided by Capchem Technology Co. Ltd (Shenzhen, China).

The TTME-based electrolyte, named TTME-d, was formed by dissolving 374 mg lithium LiFSI in 1 mL mixed solvent with TTME (synthesized as described in Chapter 3) and DME at a volume ratio of 4:1. The final concentration of lithium salt was 1.4 mol/L. Electrolyte containing DME with 1.4 mol/L LiFSI (named DME-d) and an electrolyte containing 1 mol/L $LiPF_6$ in a mixture of ethylene carbonate (EC)/ diethyl carbonate (DEC) (30:70, wt./wt.) with 1 wt.% vinylene carbonate (VC) and 1 wt.% 1,3-propanesultone (PS) were used as the two control electrolytes.

For the coin cells, all electrochemical measurements were carried out using 2032-type coin cells. All the electrode plates, except lithium metal, were obtained from pouch cell disassembly. The active material loading of NCM811 was 3.13 mAh/cm^2, and the loading of LCO was 2.96 mAh/cm^2. Lithium foils with thickness values of 400 μm were used as the anode in half cells. All cells were fabricated in an argon-filled glovebox, with 50 μL electrolyte and one layer of Celgard 2400 separator used in each cell.

Dry NCM811|| Artificial graphite (AG) pouch cells (with 1780 mAh capacity) were provided by Capchem Technology Co. Ltd. The dry pouch cells were cut and then dried at 85 ⁰C under vacuum for 24 hours. The pouch cells were then injected with 5.8 g of the designed electrolyte (or a control electrolyte) and then sealed under a vacuum in an Ar-filled glove box. The commercial-standard formation and aging process were applied to pouch cells before further electrochemical measurements (as described in Chapter 2, Section 2.1.2

Pouch cell preparation).

In order to perform the differential electrochemical mass spectrometry (DEMS) experiments, the electrodes were prepared by mixing active materials (graphite or NCM811), Super P, and poly(vinylidene) fluoride at a weight ratio of 80:10:10. The pastes were cast onto Celgard 2400 separators to form electrodes. The mass loading of the graphite was controlled at $\approx$ 30 mg/cm^2, and the mass loading of NCM811 was $\approx$ 18 mg/cm^2.

5.2.2 Electrochemical measurements

NCM811 coin cells were cycled between 2.8 V and 4.4 V (1 C = 200 mA), and LCO coin cells were cycled between 3.0 V and 4.5 V (1 C = 180 mA). After the first two activation cycles at 0.1 C charge/discharge, the cells were cycled at a rate of 0.33 C. Cyclic voltammetry (CV) was performed in the voltage range from OCV to 0.01 V and then to 2.0 V with a scan rate of 0.1 mV/s. Electrochemical impedance spectrometry (EIS) was conducted in the frequency range of 0.01 Hz to 106 Hz at an amplitude voltage of 5 mV.

After completing the aforementioned formation process (see also Chapter 2, Section 2.1.2 Pouch cell preparation), the cells underwent a charging procedure to reach 3.8 V at a rate of 0.1 C (where 1 C corresponds to 1780 mA). Subsequently, the cells were subjected to a 24-hour aging period at a temperature of 45 °C. Following this, a second charging step was performed,

raising the voltage to 4.25 V at a rate of 0.1 C using a constant current-constant voltage (CC-CV) mode, with a limiting current of 0.05 C. The cells were then discharged to 3.0 V at 0.2 C. Next, the cells underwent CC-CV charging/CC discharging cycles at different rates: 0.5 C/1.0 C, 1.0 C/1.0 C, and 2.0 C/1.0 C, all within the voltage range of 3.0 to 4.25 V. Finally, based on their capacity, the cells were selected for further investigation. For cycling measurements, the voltage range was set as 3.0-4.25 V, the temperature was set at 25 °C and 45 °C.

In the DEMS experiments, Li||NCM811 cells were cycled from 2.5 V to 5.0 V, and Li||graphite cells were cycled from 2.5 V to 0 V.

Density functional theory (DFT) calculations were performed as described in Chapter 2, Section 2.3.1.

5.3 Results and discussion

5.3.1. Selection of the electrolyte solvent and co-solvent

Through the DFT calculation, the highest occupied molecular orbital (HOMO) energy value and the lowest unoccupied molecular orbital (LUMO) energy value of the different solvents and additives were investigated. As shown in Figure 5.1, the LUMO energy level of TTME (1.491 eV) is slightly lower than that of DME (2.316 eV), but still higher than that of general carbonate solvents and additives, indicating its strong reduction stability on the anode side. In addition,

due to the high fluorine substitution of the TTME molecule, its HOMO energy level (-7.758 eV) is obviously lower than those of traditional ether molecules, and even lower than that of some carbonate solvents and additive molecules (e.g., DEC: -7.2779 eV, VC: -6.999 eV). This shows that the substitution of hydrogens by fluorine can improve the oxidation stability of ether molecules.
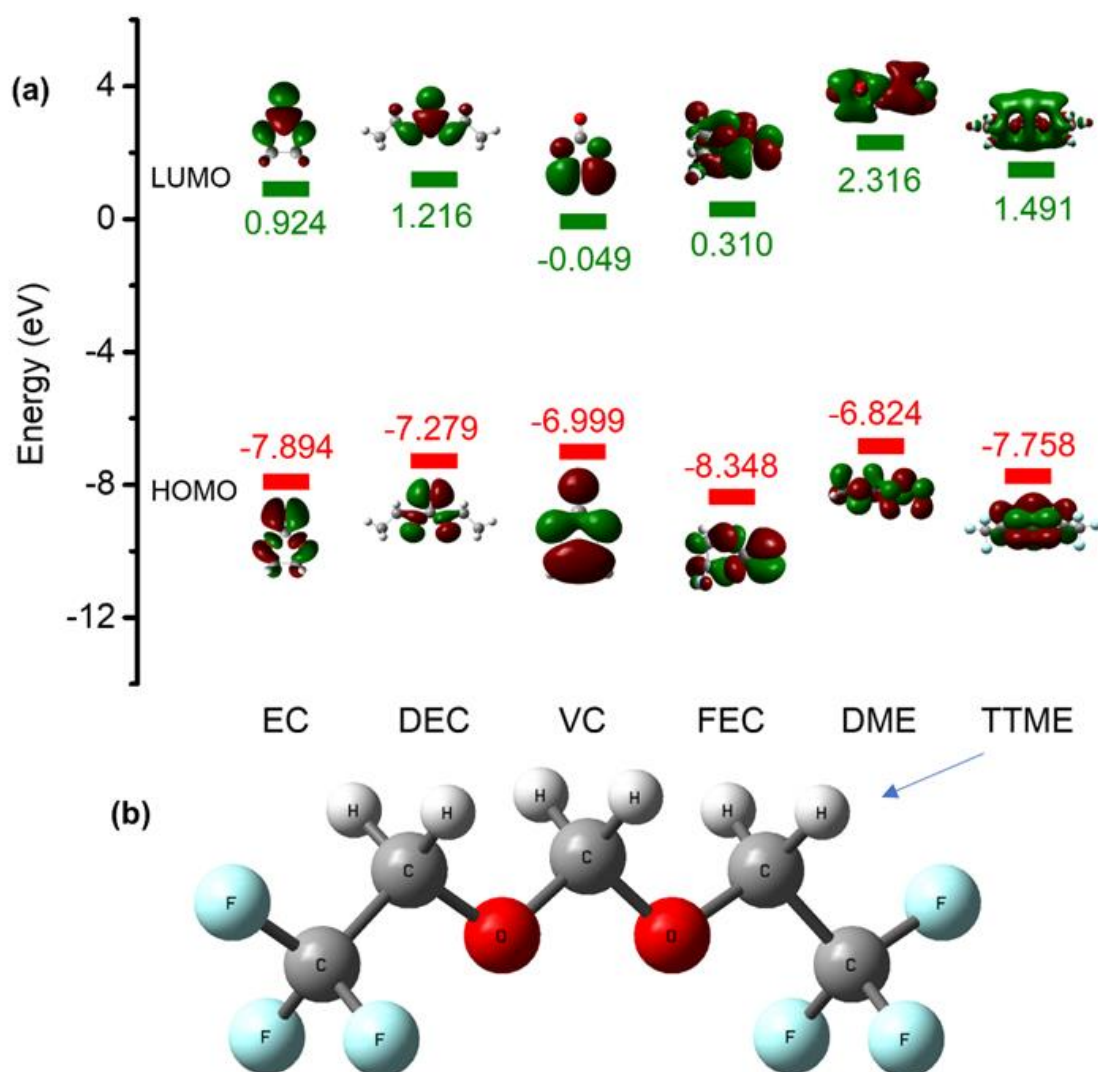
Fig. 5.1. (a) LUMO and HOMO values of DME, TTME, and some carbonates. (b) Schematic molecular structure of TTME.

5.3.2. Performance of the electrolytes in half cells

DME was found to have the best reduction stability among the tested solvents and additives, it easily co-intercalated with graphite during charge/discharge, resulting in the stripping of graphite and the decomposition of the electrolyte. This problem can be clearly seen from the cyclic voltammetry (CV) curves presented in Figure 5.2. As the discharge progresses, the CV curve of the Li||graphite half cell using the DME-d ether electrolyte begins to show peaks when the voltage drops to ≈ 1.2 V, and as the discharge process continues, the peaks become larger and the shape of the curves is increasingly irregular. During the delithiation process, the internal reactions of the cell with the ether electrolyte are also extremely unstable. As the voltage increases, small peaks not for the charge-discharge platform continue to appear in the CV curve. In the subsequent four cycles, such irregular small peaks are always observed, and none of them overlap, indicating that various side reactions constantly occur. This shows that DME cannot form a stable SEI film on graphite when it is used alone, and that the co-intercalation process with graphite leads to the collapse of the graphite structure and the decomposition of the electrolyte.
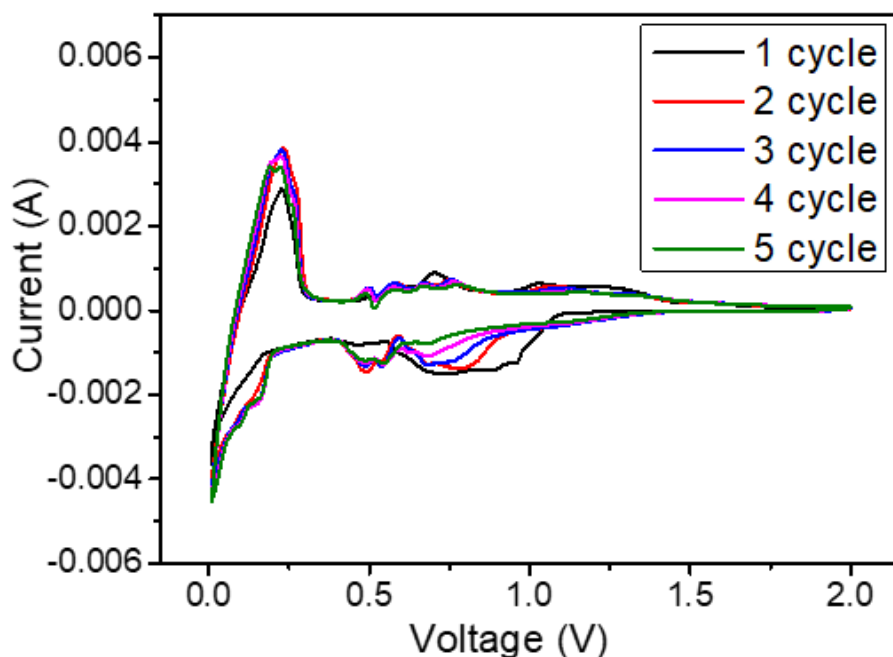
Fig. 5.2. CV curves of Li||graphite half cells using DME-d electrolyte showing the occurrence of peaks when the voltage drops to ≈ 1.2 V, which become larger and increasingly irregular shaped. The numerous small peaks indicated that several side reactions are occurring simultaneously.

The electrolyte developed in this work contains two ethers, DME and TTME, and the addition of TTME as the co-solvent prevents the occurrence of the above problems. Considering the entire electrolyte system, the addition of TTME weakens the interaction between the DME solvent and the Li^+ ions of the anode, enhancing the desolvation process of Li^+ ions, which would be beneficial for inhibiting the co-intercalation with graphite. As can be seen from the CV curves of the Li||graphite half cell using the fluorinated ether TTME-d electrolyte in Figure 5.3, except for the process of generating the SEI during the first cycle of discharge, the CV curves of the five charge/discharge cycles have a high

degree of coincidence overall. This indicates that the SEI generated in the first

cycle has a good protective effect on the electrode structure, and can prevent

the delamination of the graphite structure and thus inhibit the decomposition of

the electrolyte and the occurrence of side reactions. These results indicate that

the cell formed using the fluorinated ether electrolyte as a co-solvent has a high

degree of cycle reversibility on the graphite anode.
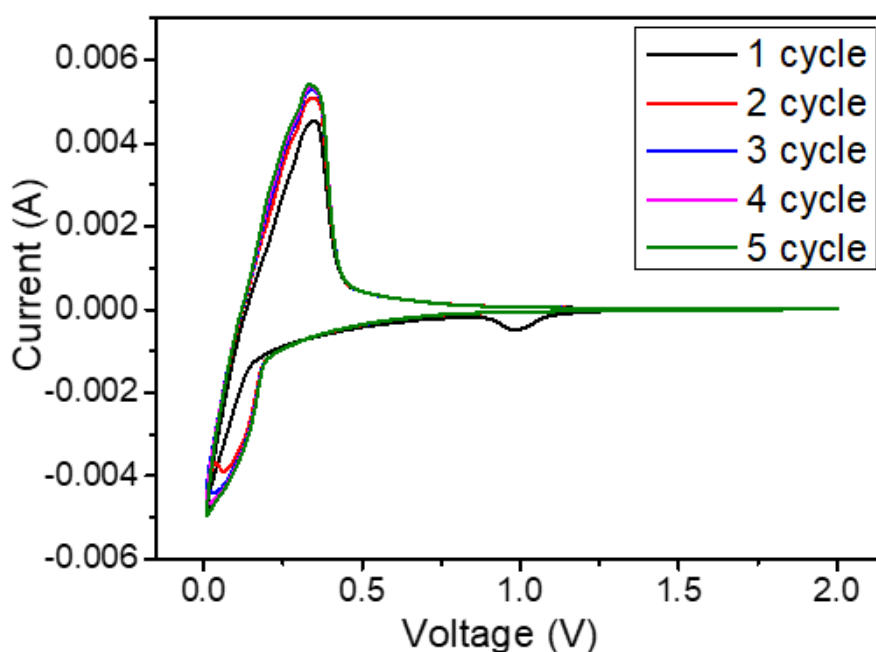
Fig. 5.3. CV curves of Li||graphite half cells using TTME-d electrolyte in which
TTME is added as a cosolvent with DME, resulting in excellent overlap of the
curves over the 5 cycles and demonstrating the stability of the SEI formed on
the anode during cycle 1.

The electrochemical performance of the Li||graphite half cells using the ether

and fluorinated ether electrolytes was further investigated. As shown in Figure

5.4, the Li||graphite half cell using the fluorinated ether electrolyte (TTME-d)

delivers 91.7% capacity retention after 300 cycles and 88.7% capacity retention

after 350 cycles. In contrast, the Li||graphite half cell using the ether electrolyte (DME-d) could not release the full capacity even at the beginning of the cycle and experienced a rapid capacity decay. After 100 cycles, the capacity of the cell with the ether electrolyte (DME-d) is less than 50% of its original capacity.
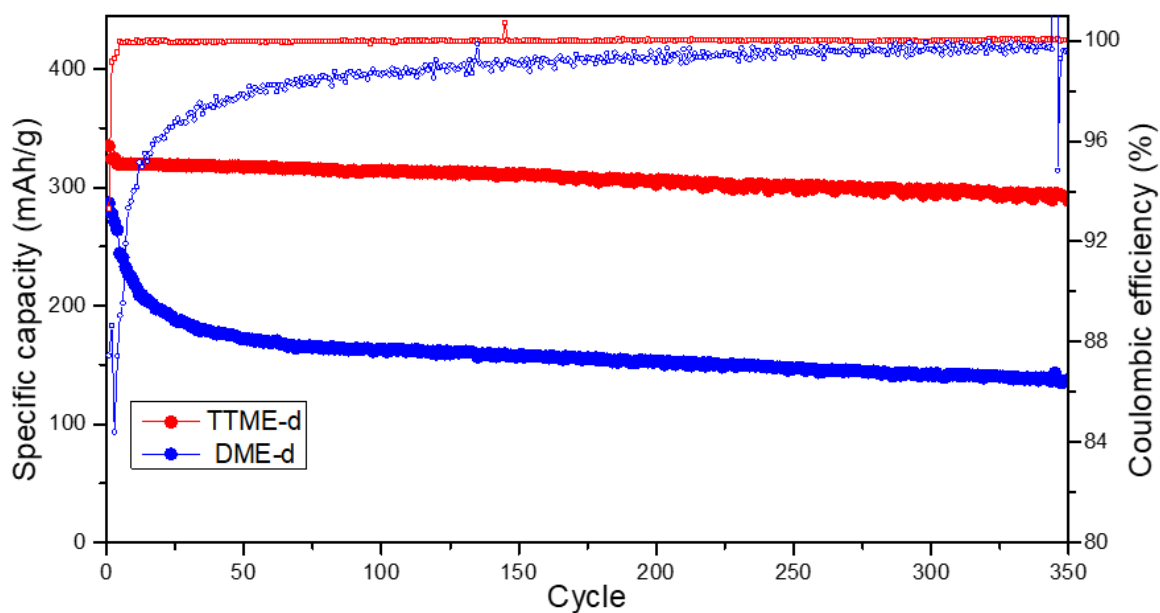
Fig. 5.4. Cycling performance of Li||graphite half cells using DME-d and TTME-d electrolytes.

The Nyquist plots presented in Figure 5.5 show that the impedance increase in the cell with the fluorinated ether electrolyte (TTME-d) is much smaller than that in the cell with the ether electrolyte (DME-d). These results further prove that in Li||graphite cells, the addition of TTME as a co-solvent significantly improves the compatibility between ethers and the graphite anode. At the same time, the results indicate that a stable SEI can be generated on the graphite anode with the fluorinated ether electrolyte (TTME-d) so that the cell has stable cycling performance for more than 300 cycles.
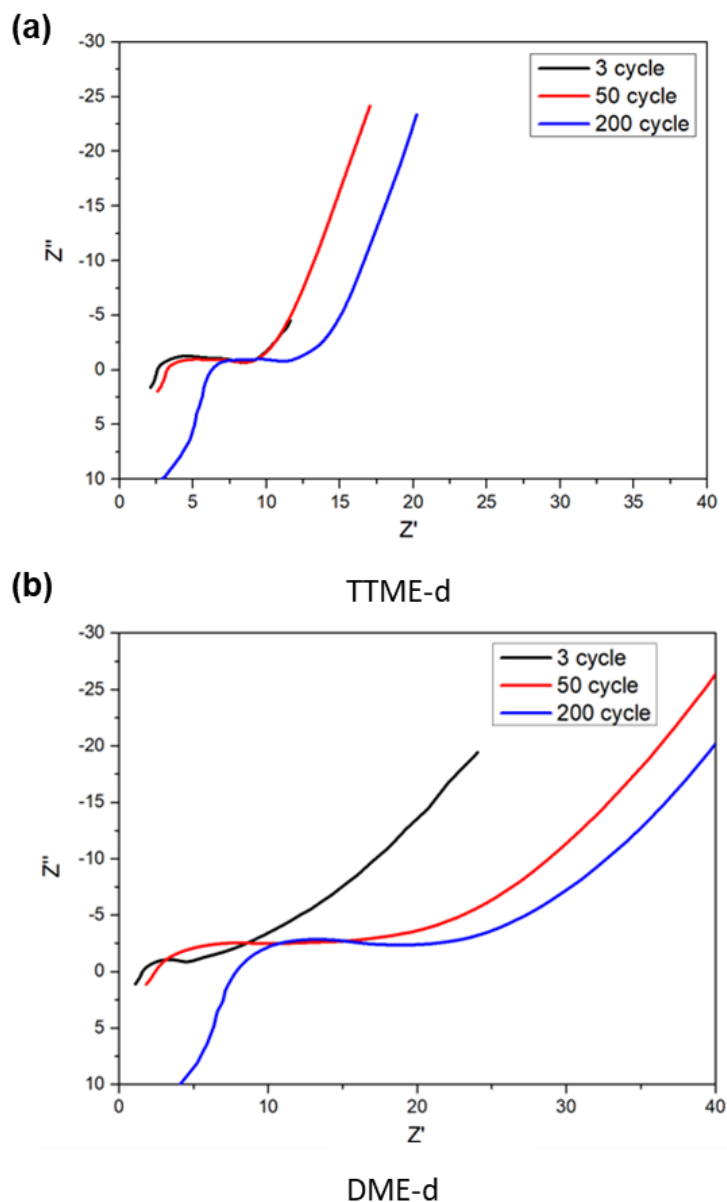
Fig. 5.5. Nyquist plots of Li||graphite cells after different cycle numbers with (a) TTME-d and (b) DME-d electrolytes.

5.3.3. Performance of the electrolytes in full cells

On the basis of its good cycling performance in Li||graphite half cells, the TTME-d electrolyte was applied to high-voltage full cells with two different commercial cathode plates (LCO and NCM811). For better comparison to current

commercially utilized systems, the carbonate electrolyte (1 mol/L LiPF$_6$ in a

mixture of EC/DEC (30:70, wt./wt.) with 1 wt.% VC and 1 wt.% PS) which have

demonstrated good cycle performance at high voltage was introduced as a

control sample. It can be seen from the results presented below that the cycle

performance of the cells with the fluorinated ether TTME-d electrolyte, for both

the high-voltage cathodes, is much better than those of the cells with the two

controls electrolytes.

As shown in Figure 5.6, for the NCM811||graphite full cells (between 2.8 V and

4.4 V), the capacity retention rate of the cell with the fluorinated ether TTME-d

electrolyte remains at 94.7% after 100 cycles, is >90% after 200 cycles,

decreases slightly to 84% after 300 cycles, and drops to ≈ 70% after 600 cycles.
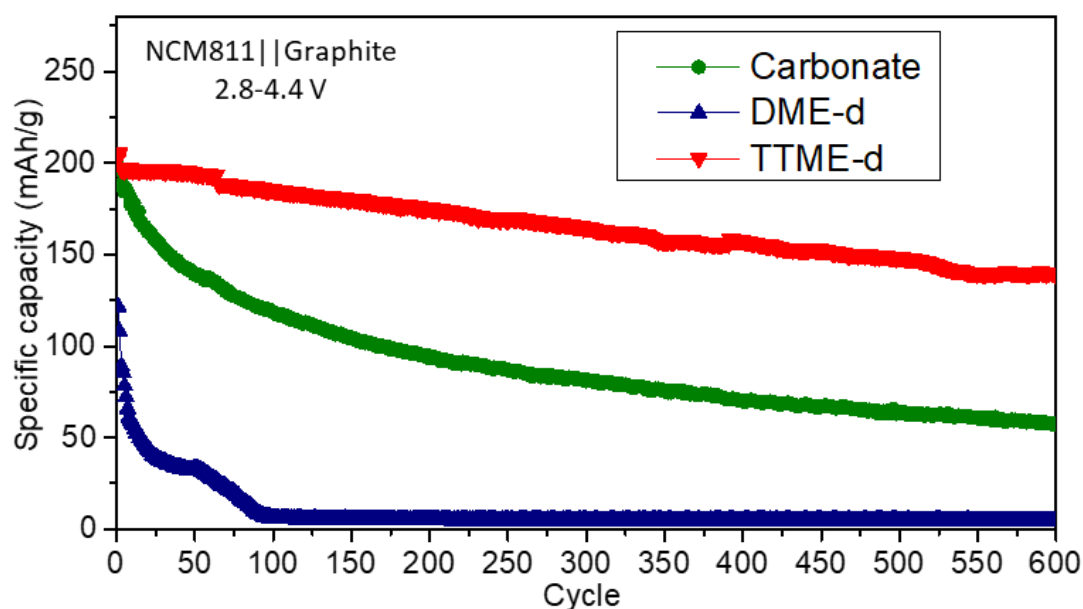
Fig. 5.6. Cycling performance of NCM811||graphite cells with different electrolyte systems, showing the enhanced performance of the TTME-d system over extended cycles (up to 600 cycles).

Ineed, the NCM811||graphite cells with TTME-d works well over 1000 cycles without failure, and the terminal capacity after 1000 cycles is about 50% of the initial capacity (Figure 5.7).
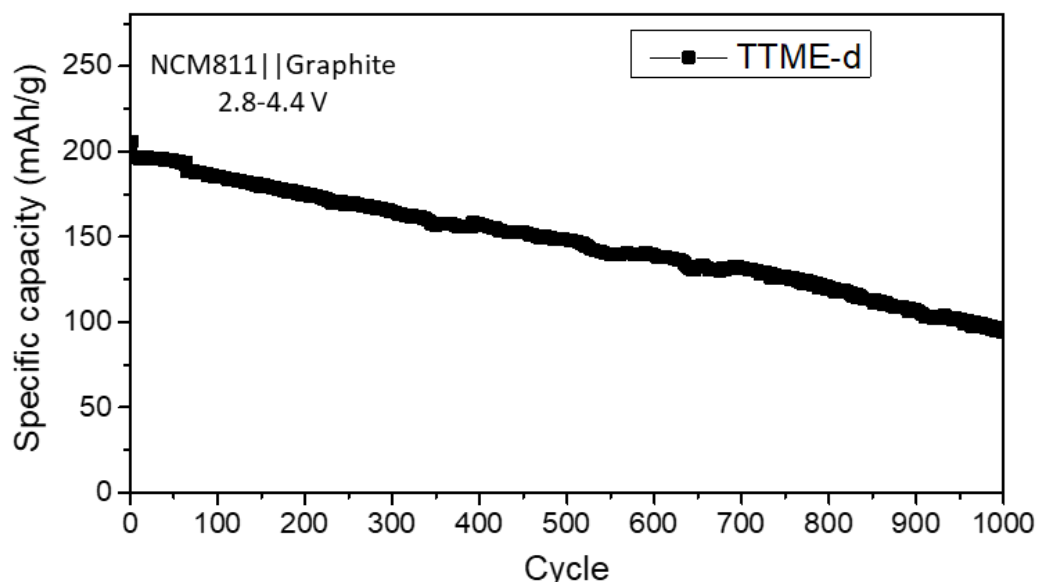
Fig. 5.7. Cycling performance of NCM811||graphite full cell with TTME-d electrolyte over 1,000 cycles, indicating sustained performance.

As a comparison, the capacity of the cell with the ether electrolyte (DME-d) cannot be fully utilized. The charge specific capacity of the first cycle is 172 mAh/g, the discharge specific capacity is 122 mAh/g, and the Coulombic efficiency of the cell in the first cycle is only 70.8%. As noted above, this is due to the co-intercalation of the DME solvent and the graphite anode, and the poor oxidation stability of DME. DME would be oxidized and decomposed rapidly on the high-voltage cathode side of the NCM811 plate. The combined effect of these two factors leads to the rapid failure of the cell with the DME-d. In addition, the cell using the carbonate electrolyte has a relatively high Coulombic

efficiency (82.2%) in the first cycle, but the capacity rapidly declines. After 100

cycles, the capacity retention is only 62.9%, which is far lower than that of the

cell with the fluorinated ether (TTME-d) electrolyte (which is 94.7%), and it is

less than 30% of the original capacity, after which it tends to slowly decay and

stabilize (Figure 5.8).
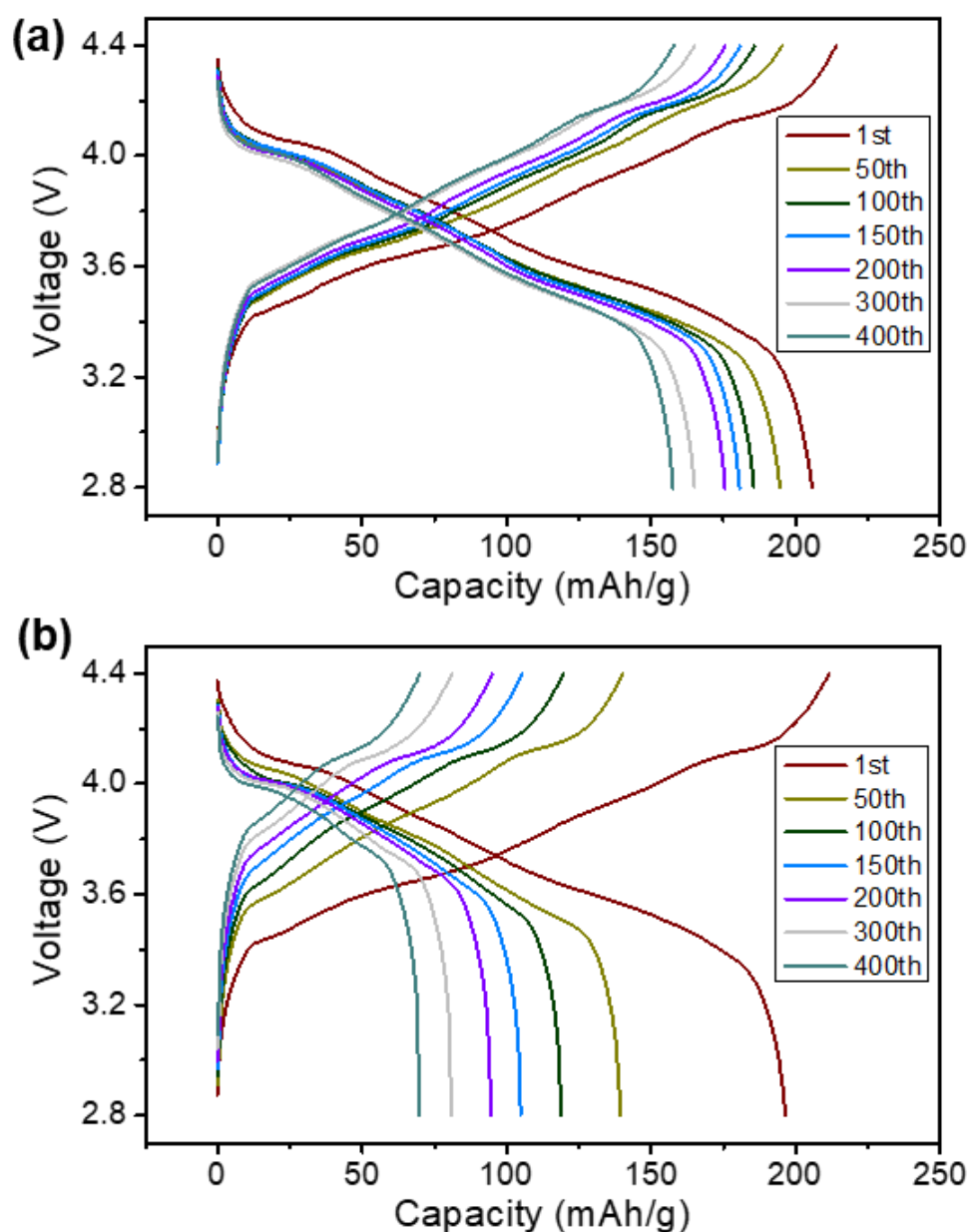
Fig. 5.8. Charge-discharge curves of NCM811||graphite cells with (a) TTME-d
electrolyte and (b) the current commercial standard Carbonate electrolyte.

Furthermore, the performance of the cells using the LCO cathodes with different electrolytes was investigated at a higher cut-off voltage (4.5 V) to further study the electrolyte compatibility with high-voltage cathodes. As shown in Figure 5.9, for the LCO||graphite full cells, the capacity retention of the cell with the fluorinated ether (TTME-d) is higher than 97% after 100 cycles, and the cell can still cycle stably with a capacity retention of 71.9% after 300 cycles. The capacity of the cell with the ether DME-d electrolyte cannot be fully exerted under these conditions either. The charge specific capacity and discharge specific capacity of the first cycle are 164 mAh/g and 109 mAh/g, respectively, and the Coulombic efficiency of the cell in the first cycle is low (66.9%). The side reactions that occur on both the cathode and anode surfaces make the cell with the DME-d electrolyte rapidly invalid. The cell with the carbonate electrolyte has a capacity retention rate of 69.3% after 100 cycles, which is also much lower than that of the cell with the TTME-d electrolyte. After about 200 cycles, the carbonate electrolyte cell experiences unstable fluctuations and the capacity decreases at a faster rate.
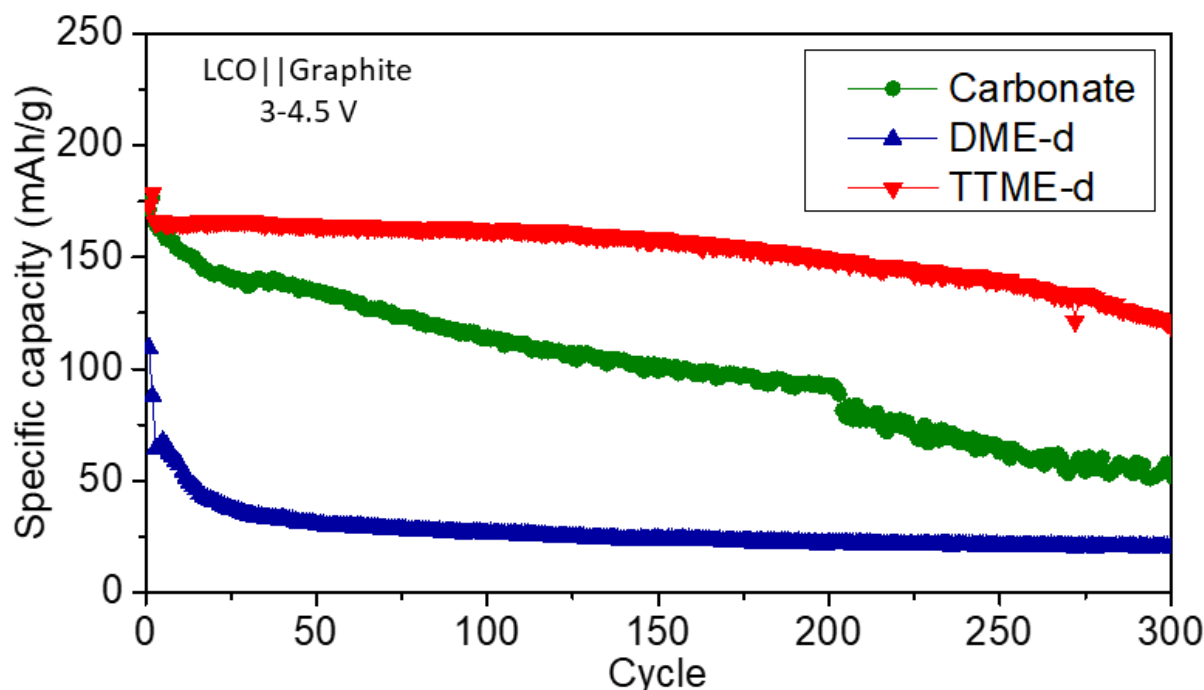
Fig. 5.9. Cycling performance of LCO||graphite cells at a cut-off voltage of 4.5 V with different electrolyte systems.

It can also be seen from the charge-discharge curves in Figure 5.10 that the charge-discharge platform of the cell with the carbonate electrolyte basically disappears after 150 cycles. The possible reasons for this are that the additives VC and PS and even some solvents in the carbonate electrolyte are excessively decomposed under the high-voltage environment of 4.5 V, which results in the capacity fade of the cell. At the same time, due to the absence of a stable cathode electrolyte interphase (CEI) layer formation during the first charge/discharge cycle, the continuous destruction of the layered LCO structure is one of the main reasons for the capacity decay. These results show that even the EC/DEC electrolyte with the addition of additives (1%VC and

1%PS) cannot maintain a stable cycle under the severe 4.5 V high-voltage condition, which highlights the excellent performance of the fluorinated ether electrolyte (TTME-d) for high-voltage applications.
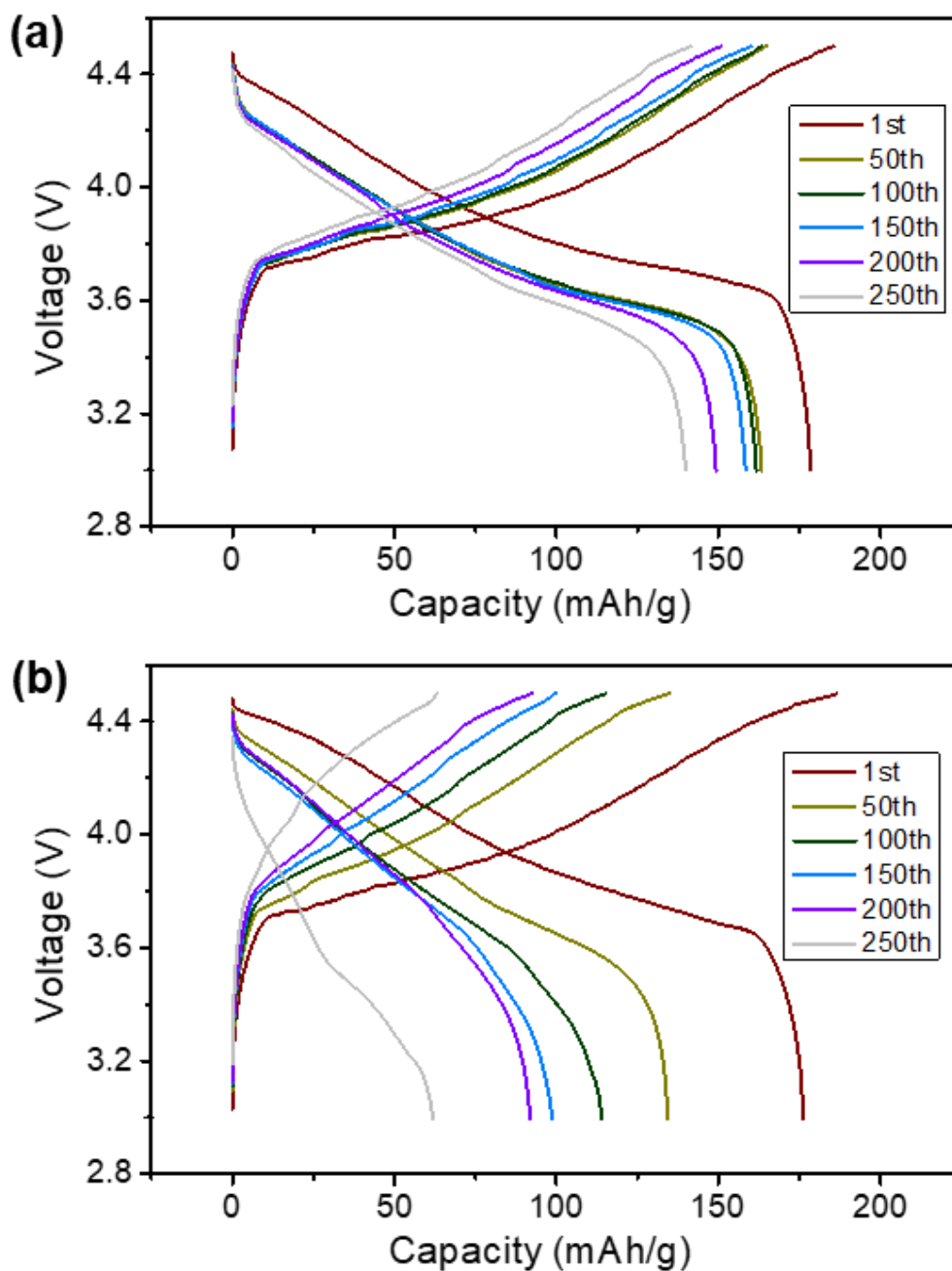
Fig. 5.10. Charge-discharge curves of LCO||graphite cells at high voltage (4.5 V) with (a) TTME-d electrolyte and (b) Carbonate electrolyte.

5.3.4. Performance of the electrolytes in pouch cells

Moreover, large-capacity commercial NCM811||graphite pouch cells (1780 mAh) were assembled to further evaluate the performance of the fluorinated ether electrolyte (TTME-d). The pouch cells were subjected to cycling measurements at room temperature (25 ℃) and high temperature (45 ℃), and the Direct Current Internal Resistance (DCIR) was measured during cycling. As shown in Figure 5.11, as the voltage range decreases, the cycle performance of the pouch cell with the control carbonate electrolyte is significantly improved (Figure 5.11). Interestingly, the cycle performance of the pouch cell with the fluorinated ether electrolyte (TTME-d) is still better than that of the pouch cell with the carbonate electrolyte. Through the statistical analysis of all the measured pouch cells, it is determined that the average first-cycle Coulombic efficiency of the cells using the TTME-d is 88.9%, which is slightly higher than that of the cells using the carbonate electrolyte (88.3%). Although the cells using both electrolytes maintain a capacity retention rate of more than 90% in the first 300 cycles, the capacity retention of the TTME-d cell is slightly higher than that of the cell using the carbonate electrolyte.
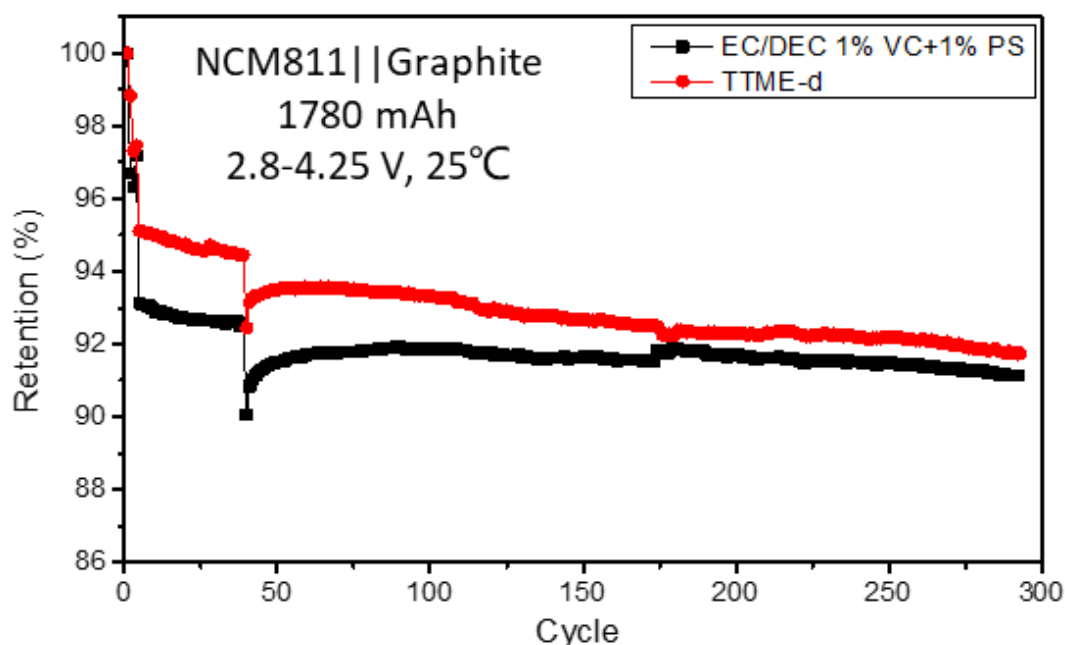
Fig. 5.11. Cycling performance of NCM811||graphite pouch cells with different electrolyte systems at 25 ºC.

Figure 5.12 shows that the DCIR of the cell with the TTME-d electrolyte is larger than that of the cell with the carbonate electrolyte during the formation stage, and that the growth rate of DCIR of TTME-d is much smaller than that of the carbonate ether during the subsequent cycles. This indicates that in the TTME-d cell , both the CEI on the cathode and the SEI on the anode have been formed in the formation stage, and both the interphases remain stable in the subsequent cycles, which are the key to the cycling stability of the pouch cells with the fluorinated ether electrolyte. In contrast, the DCIR of the cell with the carbonate electrolyte shows a large increase from the electrolyte assembly (formation) to the first cycle, and continues to increase in the subsequent cycles. This indicates that the complete formation of CEI and SEI with this carbonate electrolyte occurs

only after the completion of the first charge/discharge cycle. Moreover, the stabilities of these two interphase layers are insufficient, as the carbonate electrolyte is continuously decomposed, accompanied by the formation of new interphase layers.
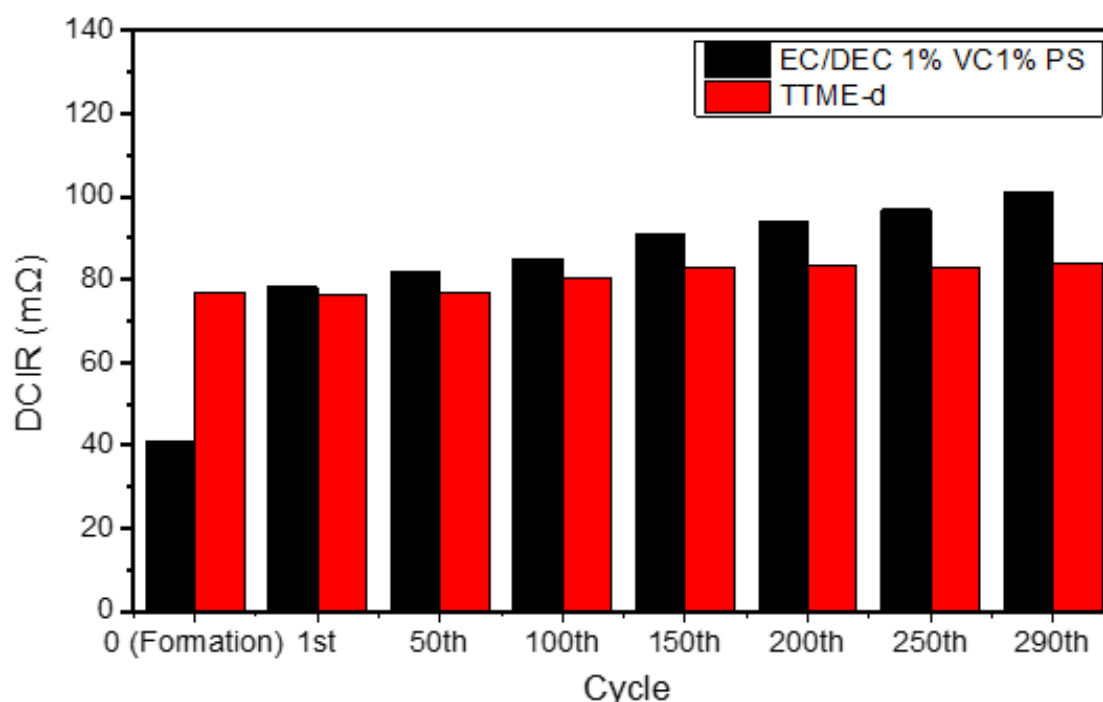
Fig. 5.12. Discharge direct current internal resistance (DCIR) changes of NCM811||graphite pouch cells at 25 ºC over the charge/discharge cycles in the different electrolyte systems.

Figure 5.13 shows that the cycle results at high temperature (45 ºC) are similar to those at room temperature, and that the cell with the fluorinated ether electrolyte ((TTME-d) still has higher first-cycle Coulombic efficiency and capacity retention than the carbonate electrolyte.
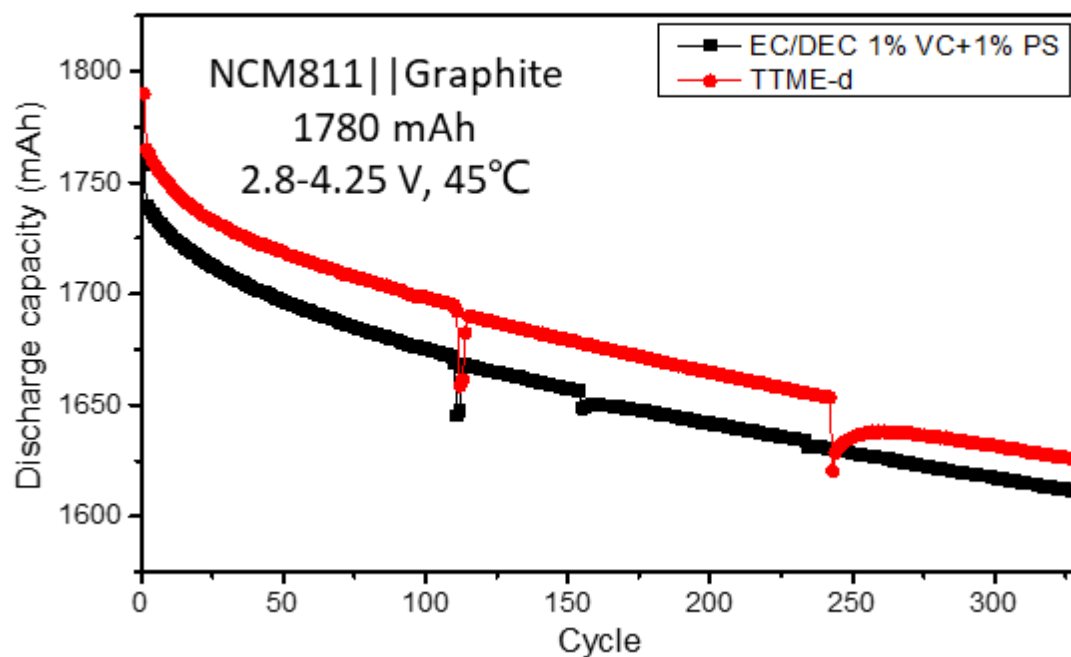
Fig. 5.13. Cycling performance of NCM811||graphite pouch cells with different electrolyte systems at 45 ℃.

In addition, it can be seen from Figure 5.14 that although the initial DCIR of the TTME-d cell is slightly higher than that of the carbonate electrolyte cell at 45 ℃, the DCIR growth rate of the former (12.5% after 300 cycles) is smaller than that of the latter (31.1% after 300 cycles).
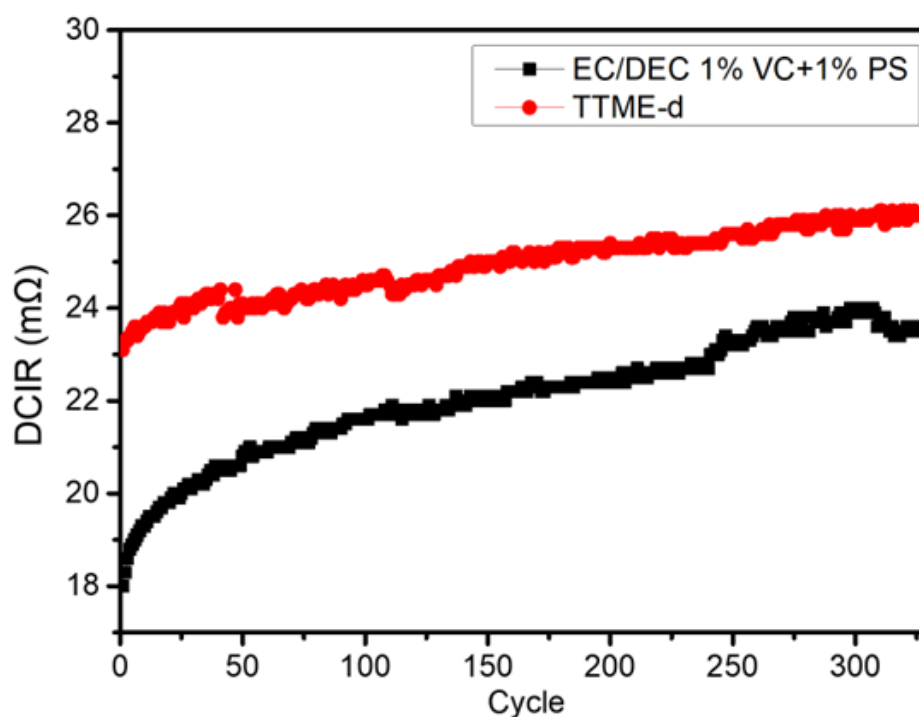
Fig. 5.14. DCIR of NCM811||graphite pouch cells with different electrolytes at 45 ºC.

Figure 5.15 presents a comparison of DCIR cycled at different temperatures, wherein it can be seen that the DCIR of the cells with the two control electrolytes increases significantly at 0 ºC, which is related to the limited internal charge transfer and lithium-ion migration at low temperatures. However, by comparison, the impedance value of the cell with the TTME-d electrolyte is still smaller than that of the cell with the carbonate electrolyte, indicating that the fluorinated ether electrolyte has application potential at low temperature also.
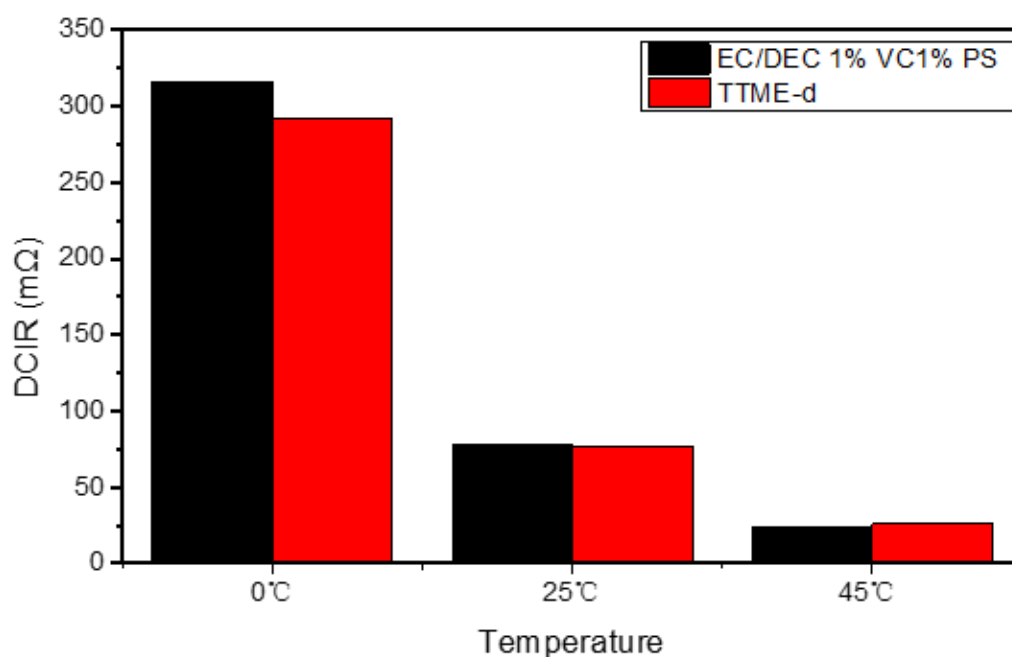
Fig. 5.15. DCIR of NCM811||graphite pouch cells at different temperatures with the different electrolytes.

5.3.5. Gas production

In order to further explore the gas production from the different components in the electrolyte during the formation of the cathode and anode interphases, DEMS measurements were conducted on the different electrolyte systems with Li||graphite and Li||NCM811 cells[181]. As shown in Figure 5.16, the Li||graphite cells using both the fluorinated ether (TTME_d) and carbonate (EC/DEC) electrolytes periodically generate hydrogen (H_2) as the discharge process progresses, while the cell with the ether (DME-d) electrolyte does not. Combined with the analysis of cell cycle performance, it can be inferred that the generation of H_2 is related to the formation of the SEI on the graphite side in the fluorinated ether electrolyte. The addition of the TTME molecule enables

the fluorinated ether electrolyte to effectively generate a robust and homogeneous SEI, which facilitates the migration of lithium ions towards the graphite side. The addition of film-forming additives makes the peak of H_2 more noticeable in the carbonate electrolyte group, and the highest peak in the first cycle can reach 9 nmol/min. However, the ether electrolyte system does not produce H_2 periodically because of the occurrence of irregular side reactions on the graphite side.
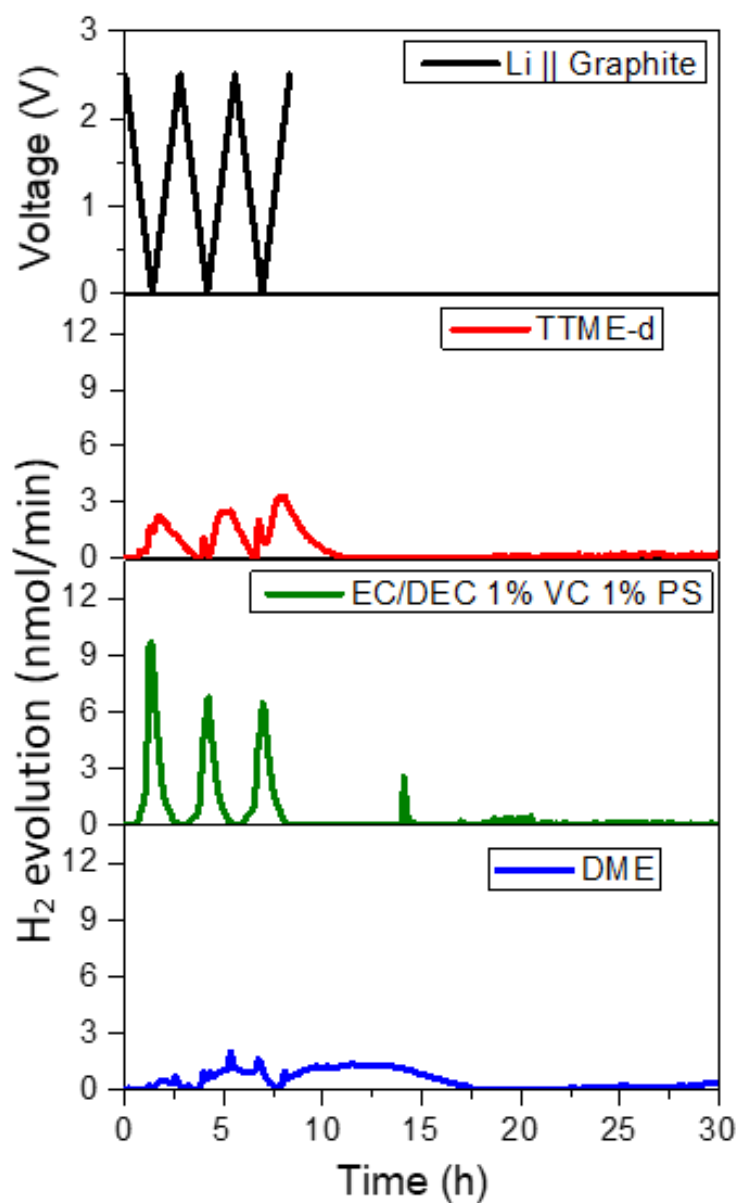
Fig. 5.16. Gaseous evolution rates of H_2 measured in Li||graphite DEMS cells containing different electrolytes.

The source of H_2 is the reduction of proton hydrogen in the electrolyte. Some of the proton hydrogen comes from trace amounts of water and alcohol impurities in the electrolyte, while the other part comes from the decomposition of solvents. The proposed formation mechanism of H_2 is displayed in Figure

5.17. As for the ether electrolyte system, the possible reason for less hydrogen generation is that the fragmentation of the graphite structure creates many binding sites for C atoms, which bind to proton hydrogen in the electrolyte.
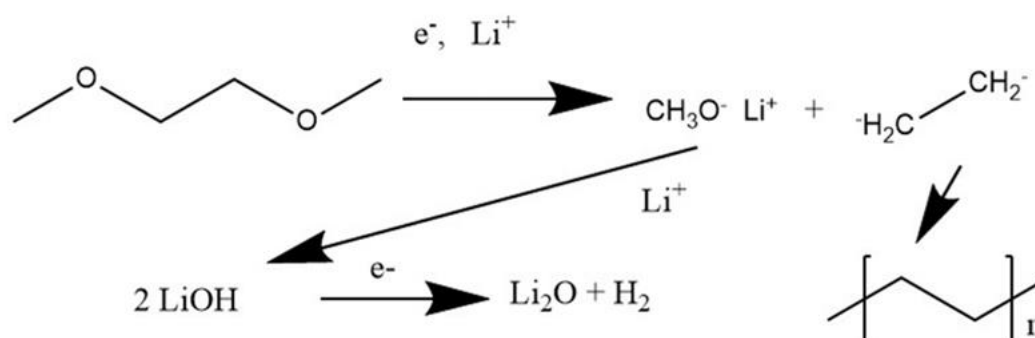
Fig. 5.17. Proposed mechanism of H_2 formation with the H atoms coming from decomposition of DME.

It can be inferred from Figure 5.18 that the co-intercalation of DME with graphite and the accompanying structural exfoliation and electrolyte decomposition process are the main sources of CO gas generation. Previous reports suggest that the decomposition of EC is accompanied by the generation of a small amount of CO. It can be inferred that the source of trace CO production in the other two cells with the ether and fluorinated ether electrolytes is a consequence of the slight decomposition of ether solvents.
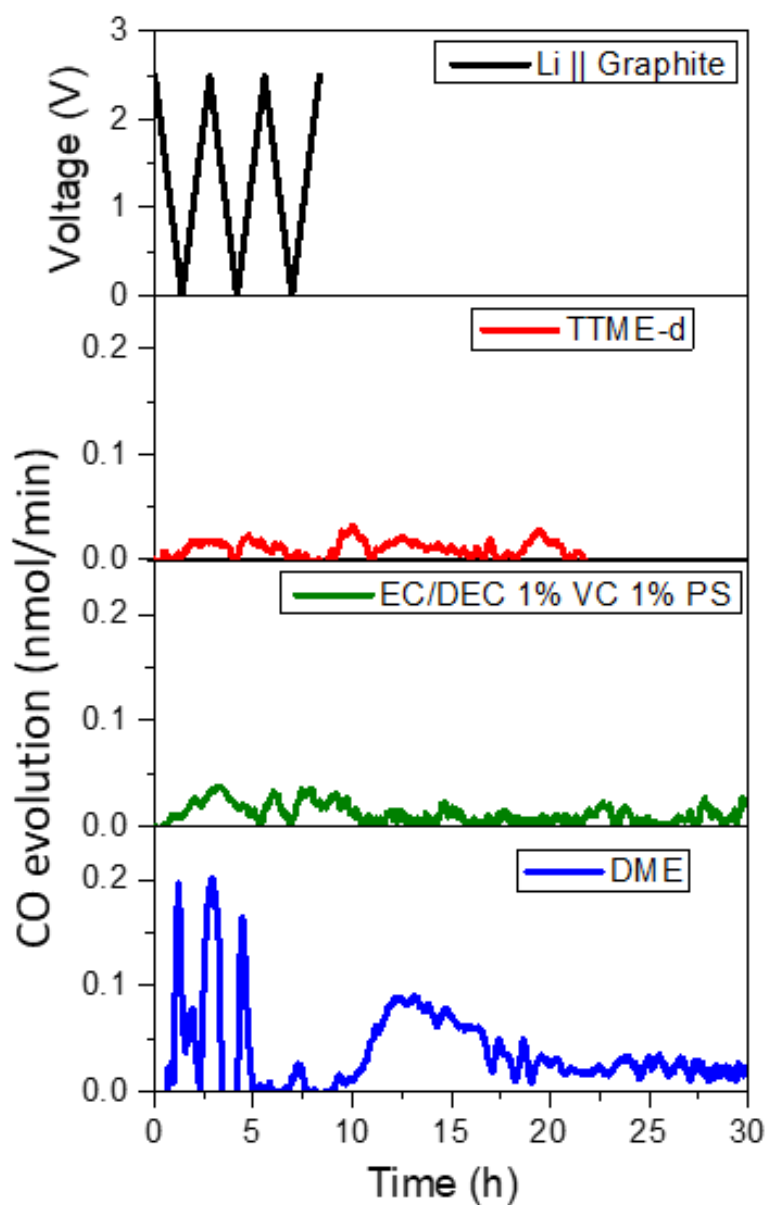
Fig. 5.18. Gaseous evolution rates of CO measured in Li||graphite DEMS cells with different electrolytes.

Figure 5.19 shows that the cell with the ether (DME-d) and fluorinated ether (TTME-d) electrolytes do not produce CO_2. For the carbonate electrolyte system, the generation of CO_2 is attributed to the consumption of the additive VC [162].
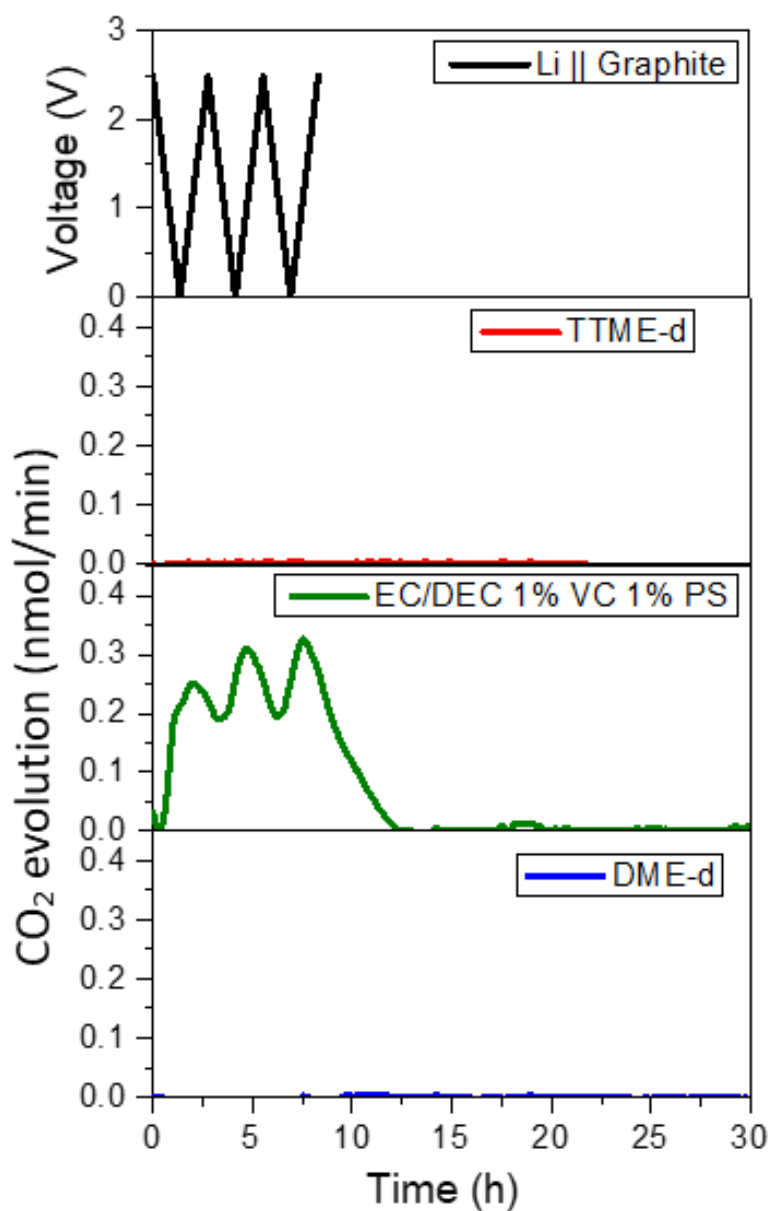
Fig. 5.19. Gaseous evolution rates of CO_2 measured in Li||graphite DEMS cells.

The gas generation on the cathode of the NCM811 is slightly different. Figure 5.20 reveals that the cells using the three electrolyte systems produce a certain amount of O_2 during the high voltage cycle. Since the amount of O_2 produced is small, it is difficult to clearly observe the periodicity, but it can be seen from

the overall volume that the gas production of the TTME-d is much less than that

of the two control groups, which confirms the excellent CEI generated on the

cathode with the fluorinated ether electrolyte.
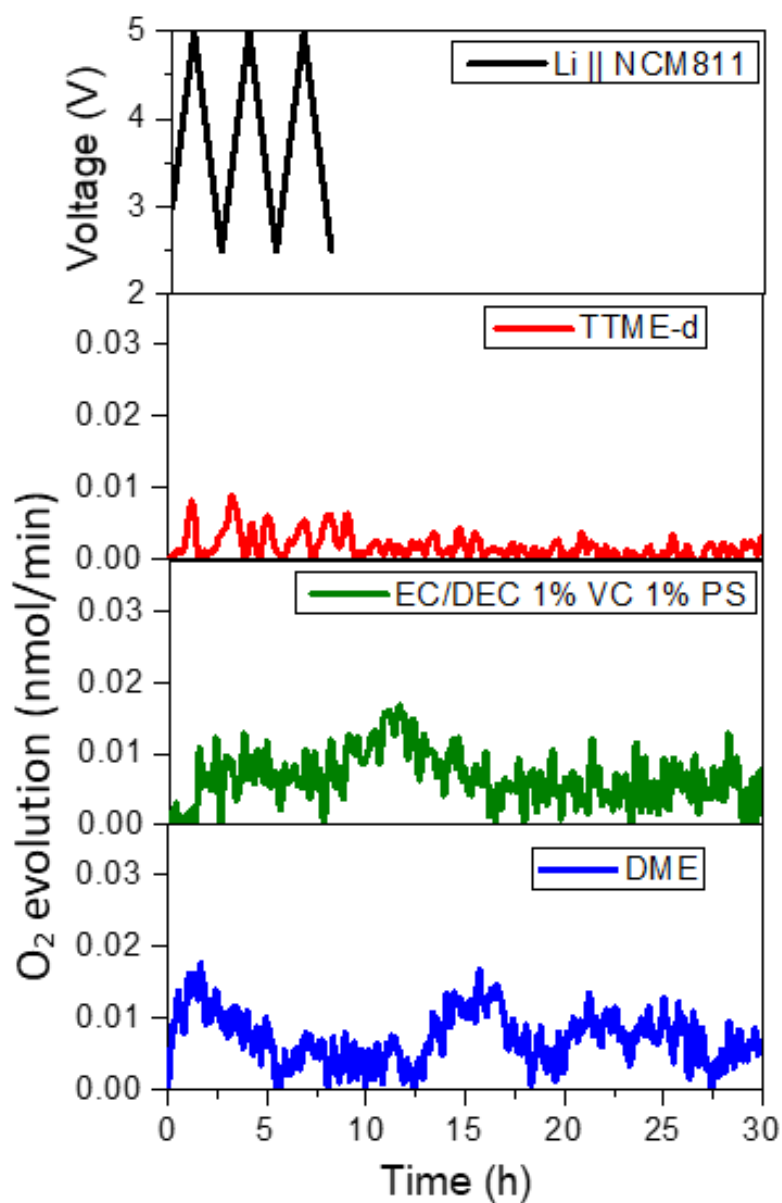
Fig. 5.20. Gaseous evolution rates of O_2 measured in Li||NCM811 DEMS cells with different electrolytes.

It can be seen from Figure 5.21 that all three electrolyte systems produce CO

gas at high voltage (4.5 V). For the ether and fluorinated ether electrolytes, the generation of CO gas mainly comes from the decomposition of ethers at high voltage, but some differences can be seen by comparing the curves. The CO production of the TTME-d is mainly concentrated in the cycle and has periodic peaks. However, more CO gas is generated in the cell with the conventional ether electrolyte (DME-d), and CO continues to be generated throughout the measurement period, indicating that DME is oxidized and decomposed in large quantities at high voltage.

Analyzing the spectral in Figures 5.21 and 5.22, it is clear that the production of CO and CO_2 in the carbonate electrolyte cells are significantly higher than those in the ether and fluorinated ether cases, and there are periodic changes. The main sources of CO and CO_2 in the carbonate electrolyte are due to the oxidative decomposition of cyclic carbonates (VC and EC).
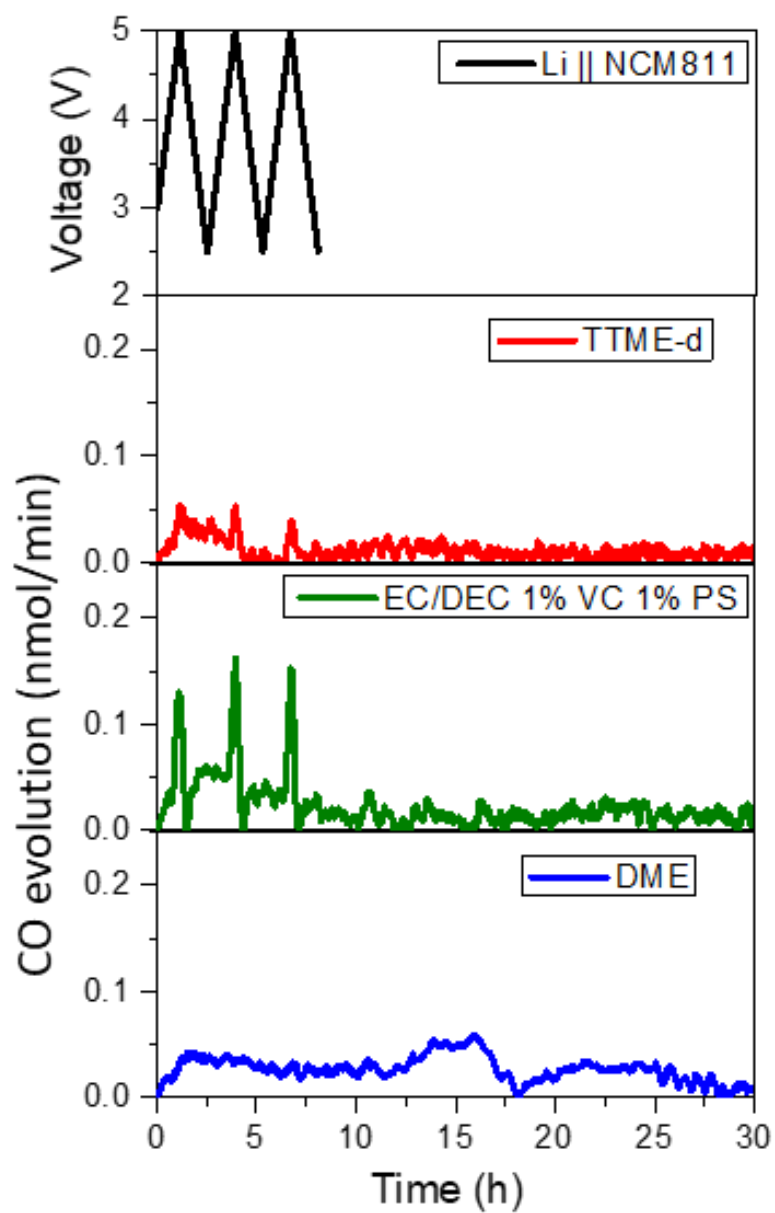
Fig. 5.21. Gaseous evolution rates of CO measured in Li||NCM811 DEMS cells at high voltage (4.5 V) with different electrolytes.
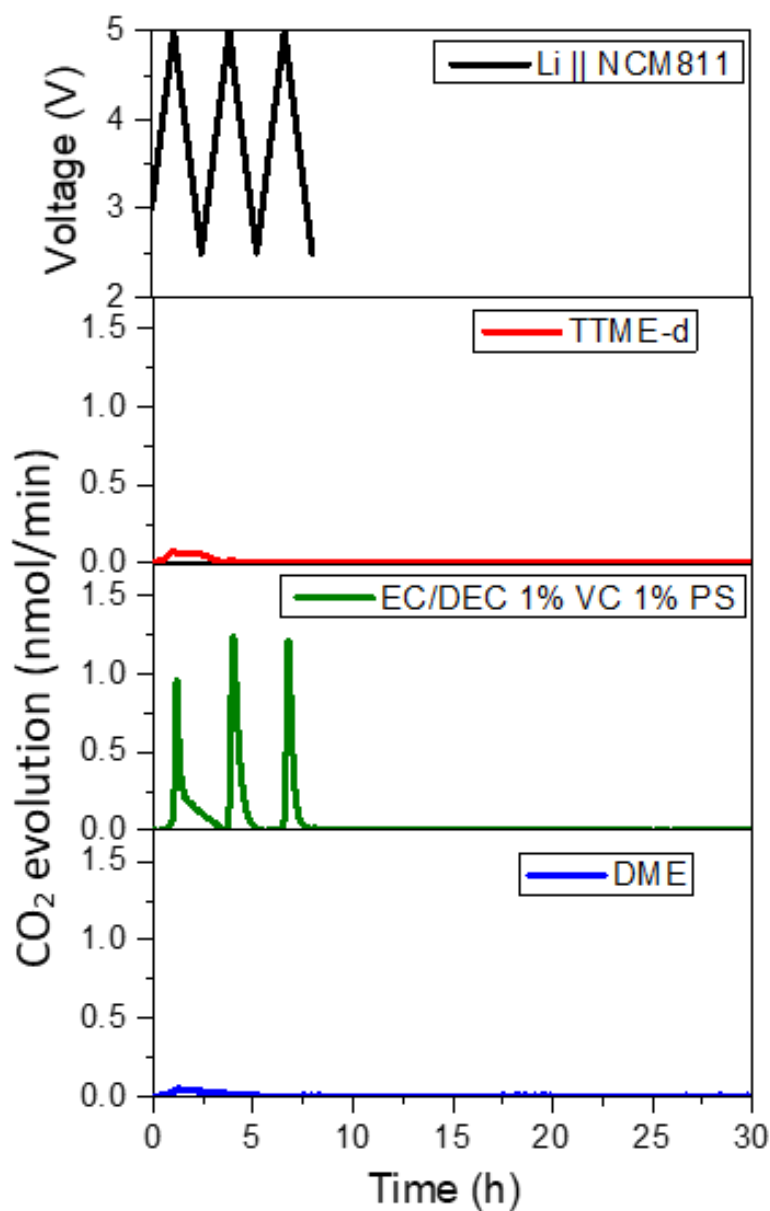
Fig. 5.22. Gaseous evolution rates of CO_2 measured in Li||NCM811 DEMS cells at high voltage (4.5 V) using different electrolytes.

5.3.6. Interphase composition analysis

In order to explore the effect of the stable interphase formed by different electrolytes on the cathode and anode sides of the cell, after 100 cycles in different electrolyte systems the cells were disassembled and the electrodes

were taken for SEM and XPS characterization (see details in Chapter 2). Since

the conventional ether electrolyte system is unstable at high voltage, only the

electrodes with TTME-d and carbonate electrolytes are selected for

characterization. Figure 5.23 shows the SEM images of the cycled LCO, NCM

811, and graphite electrodes with the TMME-d and carbonate electrolytes.
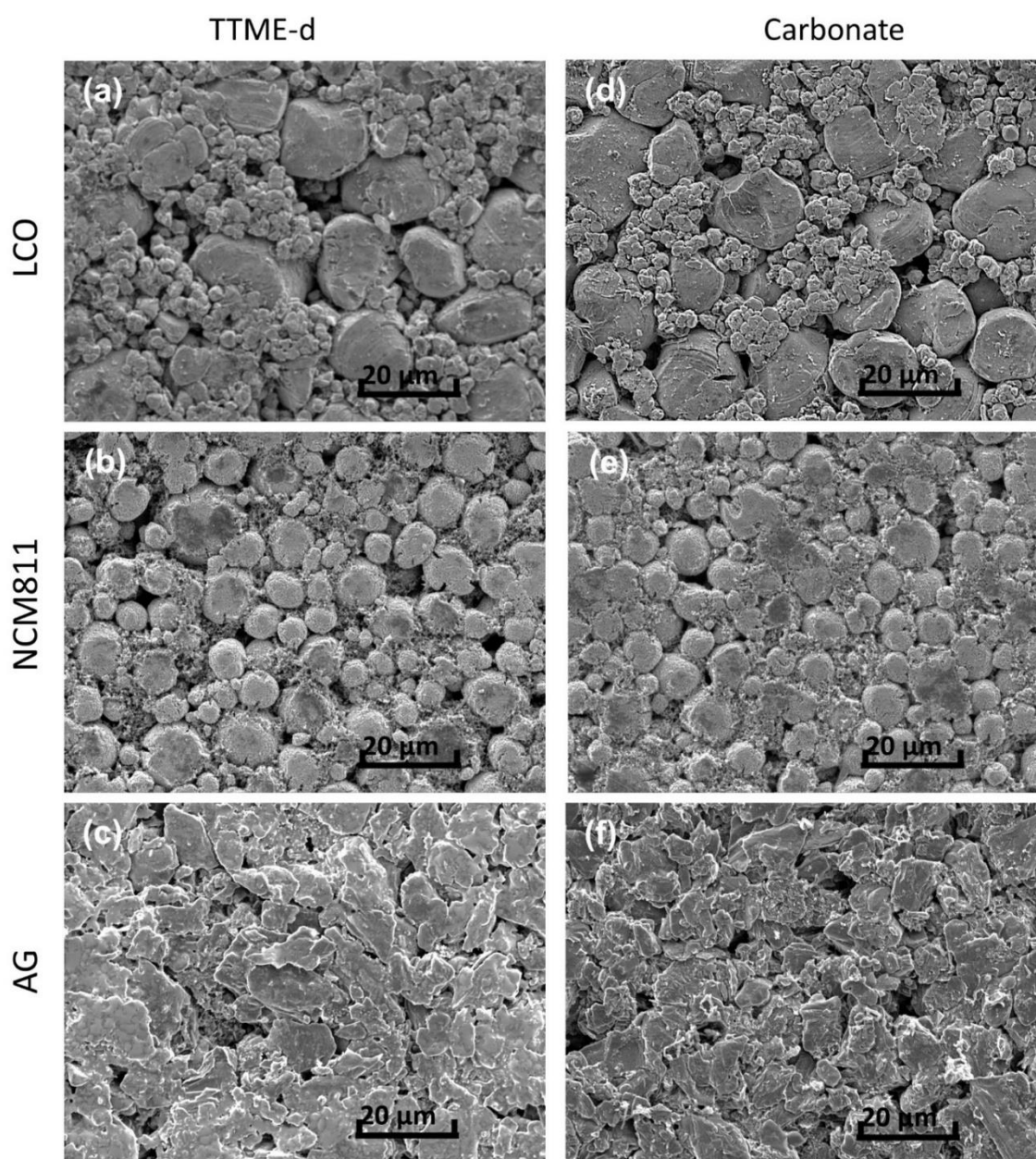
Fig. 5.23. SEM images of cycled electrodes after 100 cycles: (a) LCO, (b) NCM811, and (c) graphite using fluorinated ether electrolyte (TTME-d); (d) LCO, (e) NCM811 and (f) graphite using a carbonate electrolyte.

As can be seen, the surface of the LCO electrode with the fluorinated ether electrolyte (TTME-d) is smoother and flatter compared to that with the carbonate electrolyte (EC/DEC), in which more LCO particles are broken. In addition, the surface of the cycled NCM811 cathode with the TTME-d electrolyte is clean and not covered by a thick passivation layer, while that with the EC/DEC electrolyte has a thick passivation layer covering patches of it. A similar phenomenon can be observed for the cycled graphite electrodes, and the surface of the graphite with the TTME-d electrolyte is smoother and flatter in comparison with that with the EC/DEC electrolyte.

In terms of the composition of the interphase, the TTME-d system produces less carbonate and more organic components on the SEI surface compared to the EC/DEC system, as characterized by XPS in Figure 5.24 a and b.
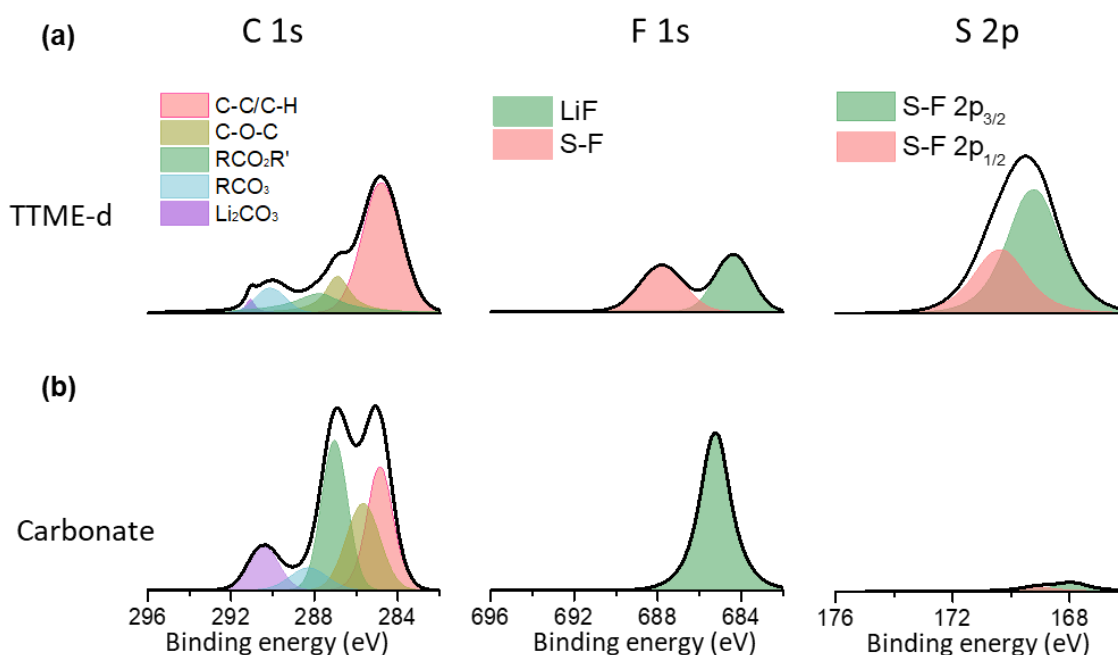
Fig. 5.24. C 1s, F 1s, and S 2p XPS spectra of graphite electrodes after 100 cycles with (a) TTME-d electrolyte and (b) EC/DEC 1% VC 1% PS electrolyte.

From the F 1s XPS spectra, it can be clearly seen that in addition to LiF, a considerable S-F peak is present in the TTME-d system. A unique N element peak can also be seen in Figure 5.25 for this system. Combined with the S 2p and N 1s spectra, it can be determined that the organic components, rich in F, S and N, are responsible for the robust SEI formation in the TTME-d system. The decomposition of the film-forming additives in the EC/DEC system results in the formation of a conventional SEI. Although there is a certain amount of S signal due to the reduction of the additive PS in the EC/DEC system, it is relatively weak compared to that obtained in the TTME-d system.
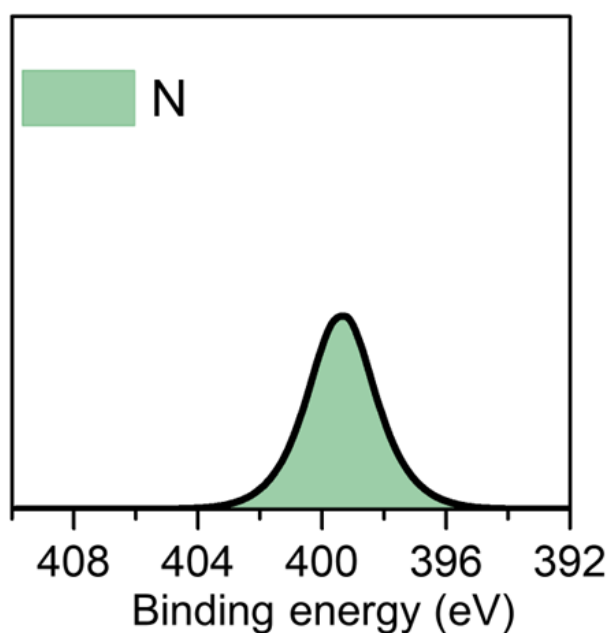
Fig. 5. 24 N 1s XPS spectrum of the graphite electrode after 100 cycles with TTME-d electrolyte.

Figure 5.26 a and b present the XPS spectra of the cycled NCM811 cell. It is worth noting that there is a unique CF_x peak in the C 1s spectrum of the TTME-d system. At the same time, there is a strong peak from $C-SO_x$ in the TTME-d

system, but the peak of the S element is too weak to be detected in the EC/DEC system. It can be concluded that the stable SEI and CEI formed by the TTME-d system are related to the high contents of F and S containing organic components in the interphases.
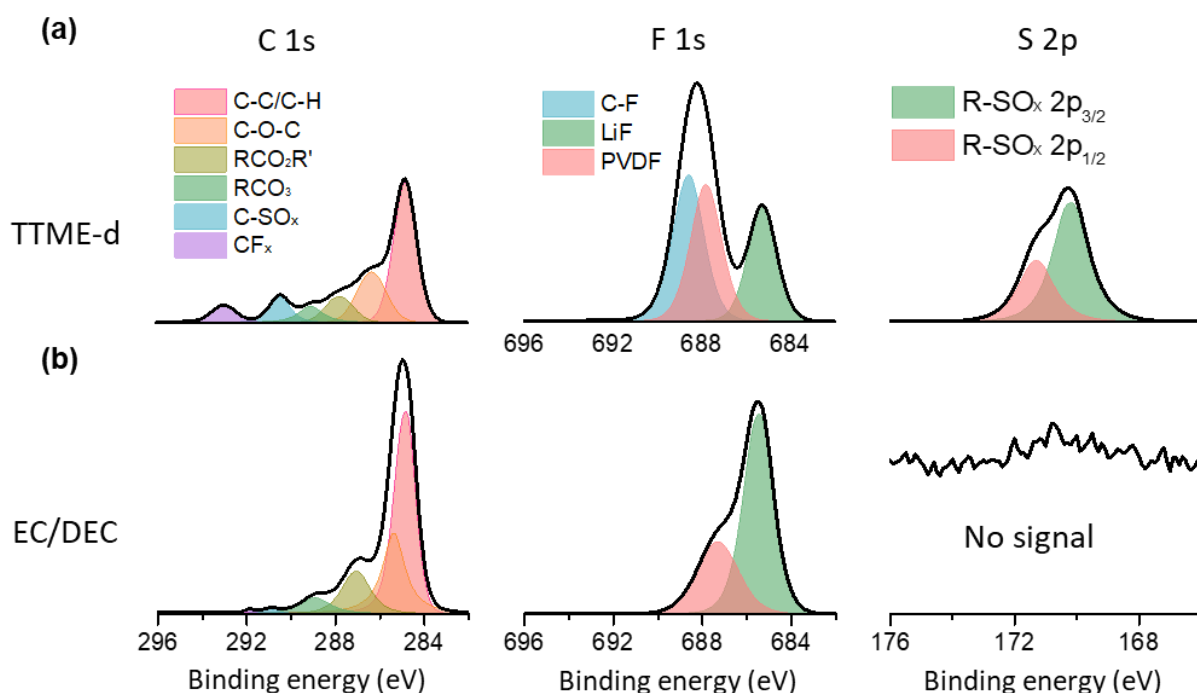
Fig. 5.26. C 1s, F 1s and S 2p XPS spectra of NCM811 electrodes after 100 cycles with (a) TTME-d electrolyte and (b) EC/DEC 1% VC 1% PS carbonate electrolyte.

Furthermore, STEM characterization of the cathode plates after cycling with the TTME-d and EC/DEC electrolyte systems was carried out to observe the thicknesses of the CEI formed on the cathode surfaces, and the results are displayed in Figure 5.27.
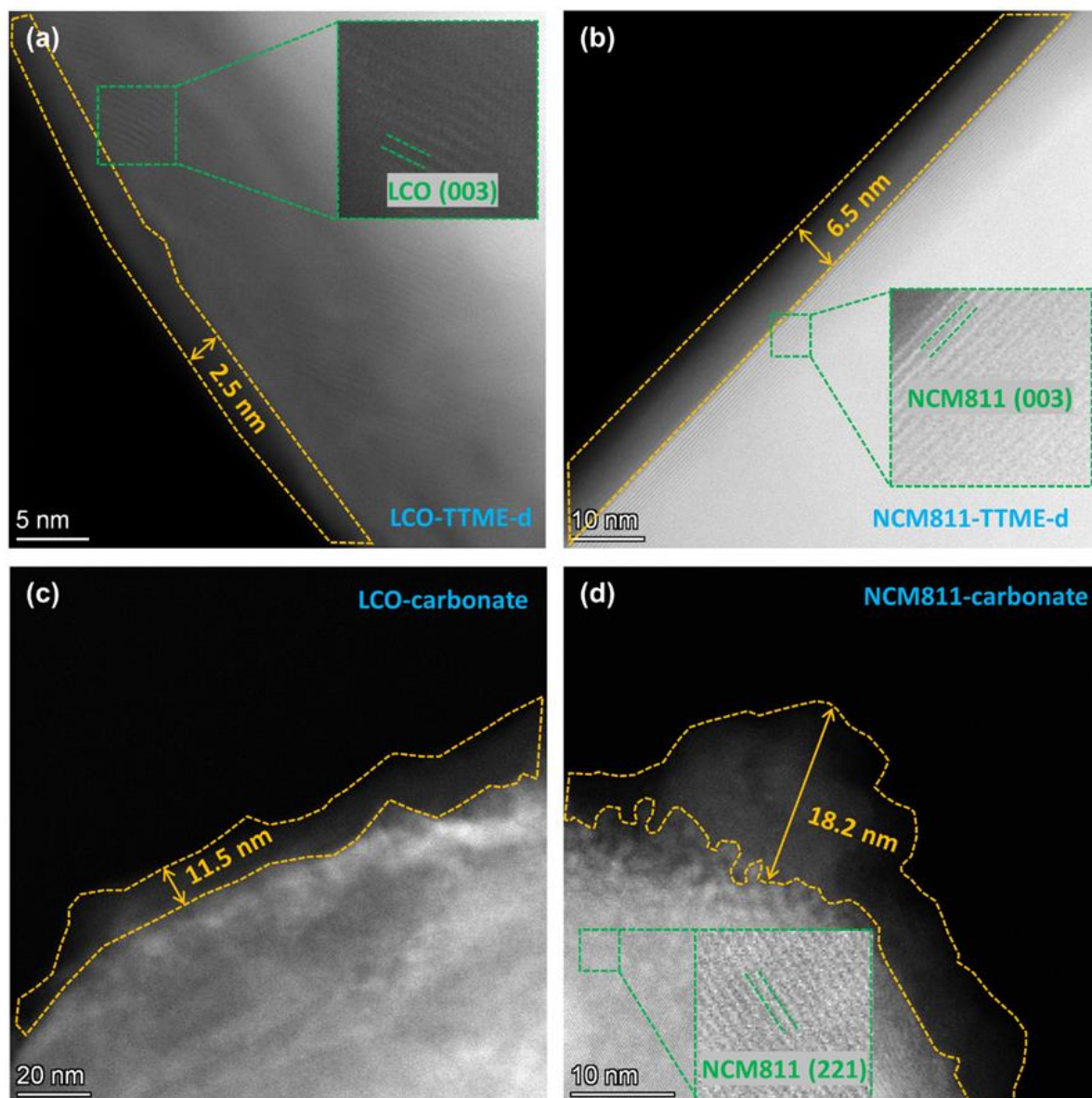
Fig. 5.27. STEM images of cycled electrodes after 100 cycles: (a) LCO and (b) NCM811 electrodes using TTME-d electrolyte; STEM images of cycled (c) LCO and (d) NCM811 electrodes using EC/DEC 1%VC 1%PS electrolyte.

It is evident that the CEI films formed on both the surfaces of the cycled LCO and NCM811 cathodes with the TTME-d electrolyte are smooth and flat, except for the occasional small gaps observed on the surface of the cycled LCO. The internal lattice structures are also clearly visible, which are consistent with their

raw layered structures. The thickness of the CEI formed on the surface of the cycled LCO is 2.5 nm, and the thickness of the CEI formed on the surface of the NCM811 is 6.5 nm. This demonstrates that the CEI formed with the TTME-d electrolyte system is complete, dense, and capable of maintaining structural stability throughout extended cycling. The dense yet appropriately thin CEI also imparts a good protection effect on the structure of the cathode active material in the inner layer. In comparison, the CEI films on the surfaces of the cycled LCO and NCM811 cathodes with the carbonate electrolyte (EC/DEC) system have an average thickness of 11.5 nm on the surface of the cycled LCO and reaches 18.2 nm at the thickest part on the surface of the cycled NCM811. Besides, the overall distribution of the CEI films formed with the EC/DEC electrolyte system is not uniform, and there are thick areas and bare areas observed on the surface. What's worse, irregular zigzag areas are observed on the surface of the cycled cathodes, indicating the structural deterioration of the cathode materials at high voltage.

5.4 Conclusion

In this chapter, the selected electrolyte (TTME-d) formulation was demonstrated to effectively address the issue of co-intercalation between DME and graphite, thereby stabilizing the performance of Li||graphite cells, which exhibited an impressive 91.7% capacity retention after 300 charge / discharge

cycles.

Furthermore, the fluorinated ether (TTME-d) electrolyte system demonstrated superior stability compared to the carbonate (EC/DEC) electrolyte system, both in relation to high-voltage layered oxide cathodes and graphite anodes. NCM811||graphite cells utilizing the TTME-d electrolyte exhibited stable cycling at a cut-off voltage of 4.4 V, maintaining a capacity retention of over 90% after 200 cycles at a rate of 0.33 C. Similarly, LCO||graphite cells using the TTME-d electrolyte, with a cut-off voltage of 4.5 V, displayed an impressive capacity retention of 97% after 100 cycles at the same rate. Moreover, large-capacity NCM811||graphite pouch cells (1780 mAh) employing the TTME-d electrolyte outperformed cells utilizing the EC/DEC electrolyte at both room temperature and elevated temperature conditions.

Through comprehensive characterization including SEM, TEM, XPS, and DEMS, it has been determined that the dense and robust solid electrolyte interphase (SEI) formed on the anode side, as well as the cathode-electrolyte interphase (CEI) formed on the cathode side, are critical factors ensuring stable cycling performance. These findings provide valuable design principles for the utilization of ether electrolytes in high-voltage LIBs.

In summary, the incorporation of the highly fluorinated ether, TTME, into the DME/LiFSI electrolyte system has proven to be an effective strategy for achieving enhanced stability and performance in LIBs. The fluorinated ether

electrolyte offers advantages in terms of avoiding undesirable side reactions and enabling the formation of robust interphases on both the anode and cathode sides for a range of battery materials. These results contribute to the advancement of ether electrolyte designs for high-voltage LIB applications, paving the way for the development of more efficient and reliable energy storage systems.

Chapter 6: Conclusions and future work

In this doctoral thesis, three key chapters have been dedicated to advancing the field of lithium secondary batteries (including LIB and LMB) through the development and characterization of novel electrolytes.

At the beginning of this thesis, the meticulously designed and synthesized molecule, TTME, took a central role in Chapter 3 as it served as the fundamental building block for the development of the Localized High-Concentration Electrolyte (LHCE). Serving both as a diluent and an active participant in the inner solvation shell structure, the unique structure of TTME enabled it to retain a portion of the electron cloud around its polar group, facilitating the coordination of Li+ ions. Molecular dynamics (MD) simulations and complementary experimental techniques, including Raman spectroscopy, FTIR, and NMR characterization, provided profound insights into this exceptional solvation structure.

In Chapter 4, the remarkable bifunctional TTME molecule led to the selection of the TTME-d electrolyte, consisting of 1.4 M LiFSI and DME-TTME (1:4 by volume), enabling an exploration of its distinguished electrochemical performance. Lithium metal cells using this electrolyte demonstrated excellent stability, with a Coulombic efficiency of 99.28% after 300 cycles for Li||Cu cells and over 3,200 hours of stable cycling for Li||Li cells. The formation of a double-

layer solid electrolyte interphase (SEI) structure on the lithium metal surface, with a unique combination of rigidity and flexibility, was clearly characterized by cryo-TEM. Furthermore, lithium metal cells employing two commercial cathodes, NCM811 and LCO, exhibited outstanding cycling performance, retaining 85% and 90% of their capacity after 240 and 170 cycles, respectively. A robust cathode-electrolyte interphase (CEI) formed on the cathode surface with the TTME-d electrolyte which effectively prevented cathode pulverization and inhibited the dissolution of transition metal ions.

In Chapter 5, the utilization of the TTME-d electrolyte successfully addressed the co-intercalation issue of DME with graphite, stabilizing the performance of Li||graphite cells, which retained 91.7% of their capacity after 300 cycles. Moreover, the fluorinated ether electrolyte (TTME-d) system demonstrated superior stability compared to the carbonate electrolyte system, exhibiting excellent cycling performance for both NCM811||graphite cells and LCO||graphite cells, with capacity retention exceeding 90% and 97% after 200 and 100 cycles, respectively. Large-capacity NCM811||graphite pouch cells utilizing the fluorinated ether electrolyte (TTME-d) outperformed cells with the carbonate electrolyte at both room temperature and elevated temperature conditions. Through comprehensive characterization techniques, including SEM, TEM, XPS, and DEMS, it was established that the dense and robust SEI and CEI formed by the TTME-d electrolyte on the anode and cathode sides, respectively, were critical factors ensuring stable cycling performance. These

findings offer valuable design principles for the utilization of ether electrolytes in high-voltage LIBs, contributing to the development of more efficient and reliable energy storage systems.

In conclusion, the synthesis and utilization of the TTME molecule in electrolytes have shown great promise in enhancing the electrochemical performance and stability of both LIB and LMB. The exceptional solvation structure of TTME, combined with the unique double-layer SEI formation and the robust CEI on the cathode surface, has played a vital role in achieving outstanding cycling performance and stability for lithium metal and graphite-based cells. The insights gained from this research provide valuable contributions to the field of LIBs, opening new avenues for the design and optimization of advanced electrolyte systems to meet the growing demand for high-performance energy storage technologies.

Future work

Building on the achievements and insights obtained in this doctoral thesis, there are several avenues for future research and development in the field of lithium secondary batteries:

(1) Further Investigation of Solvation Structures: It would be interesting to delve deeper into the solvation structures of novel electrolytes, similar to the TTME-based system explored in this thesis. For example, the synthesis and

characterization of other innovative fluorinated ether molecules that could enhance solvation structures and improve battery performance could be explored.

(2) Scale-Up and Commercialization: A critical next step will be to assess the feasibility of the transition from laboratory-scale experiments to pilot-scale and eventually commercial-scale production of the advanced electrolytes. This involves optimizing the synthesis processes to maximise the yield and reduce chemical and solvent waste, and evaluating the feasibility of large-scale manufacturing.

(3) Exploration of Additional Cathode Materials: Another avenue is to extend the study to include a wider range of cathode materials beyond NCM811 and LCO. To support commercialization it would be useful to investigate the compatibility and performance of the developed electrolytes with emerging cathode materials, such as high-nickel and lithium-rich oxide cathodes.

(4) Exploration of Additional Anode Materials: Extending the research scope to include a broader range of anode materials beyond lithium metal is also needed. Investigation of the compatibility and performance of the developed electrolytes with alternative anode materials, such as silicon, tin, or lithium alloy anodes would further demonstrate its utility and functionality. Assessment of the impact of these materials on the overall performance, cycle life, and safety of lithium secondary batteries, is needed in order to

expand the applicability of advanced electrolytes to diverse anode chemistries.

(5) Safety and Environmental Impact Assessment: A key next steps is to conduct comprehensive safety assessments of the novel electrolytes, considering factors like thermal stability, flammability, and long-term stability under extreme conditions. It will also be necessary to evaluate the environmental impact of these advanced electrolyte systems, taking into account their materials and manufacturing processes, any reliance on critical raw materials, the potential for recovery and recycling of critical elements, the potential for closed loop systems where toxicity of components is identified and the overall potential for circular economy approaches for battery systems overall.

Reference

1.   B.K. Bose. Global warming: Energy, environmental pollution, and the impact of power electronics. *IEEE Industrial Electronics Magazine*. **2010**, 4 (1), 6–17.

2.   B. Yu, Y.M. Wei, G. Kei, Y. Matsuoka. Future scenarios for energy consumption and carbon emissions due to demographic transitions in Chinese households. *Nature Energy.* **2018**, 3 (2), 109–118.

3.   A. Alvarez-Herranz, D. Balsalobre-Lorente, M. Shahbaz, J.M. Cantos. Energy innovation and renewable energy consumption in the correction of air pollution levels. *Energy Policy.* **2017**, 105, 386–397.

4.   F. Díaz-González, A. Sumper, O. Gomis-Bellmunt, R. Villafáfila-Robles. A review of energy storage technologies for wind power applications. *Renewable and Sustainable Energy Reviews*. **2012**, 16 (4), 2154–2171.

5.   N. Narayan, T. Papakosta, V. Vega-Garita, et al. Estimating battery lifetimes in Solar Home System design using a practical modelling methodology. *Applied Energy*. **2018**, 228, 1629–1639.

6.   B. Drew, A.R. Plummer, M.N. Sahinkaya. A review of wave energy converter technology. *Proceedings of the Institution of Mechanical Engineers, Part A: Journal of Power and Energy*. **2009**, 223 (8), 887–902.

7.   A. Benato, A. Stoppato. Pumped Thermal Electricity Storage: A technology overview. *Thermal Science and Engineering Progress*. **2018**, 6, 301–315.

8.   J. Guo, R. Ma, H. Zou. Compressed Air Energy Storage and Future Development. *Journal of Physics: Conference Series*. **2021**, 2108, 012037.

9.   A. Arabkoohsar, M. Sadi. Flywheel energy storage. *Mechanical and Chemical Technologies and Principles*. **2023**, 507–541.

10. K. Yanamandra, D. Pinisetty, A. Daoud, N. Gupta. Recycling of Li-Ion and Lead Acid Batteries: A Review. *Journal of the Indian Institute of Science*. **2022**, 102, 281–295.

11. W. Liu, J. Sang, L. Chen, et al. Life cycle assessment of lead-acid batteries used in electric bicycles in China. *Journal of Cleaner Production.* **2015**, 108, 1149–1156.

12. S. Zhang, Y. Yao, Y. Yu. Frontiers for Room-Temperature Sodium-Sulfur Batteries. *ACS Energy Letters*. **2021**, 6 (2), 529–536.

13. K. Lourenssen, J. Williams, F. Ahmadpour, R. Clemmer, S. Tasnim. Vanadium redox flow batteries: A comprehensive review. *Journal of Energy Storage*. **2019**, 25, 100844.

14. P. Sirisinudomkit, P. Iamprasertkun, A. Krittayavathananon, et al. Hybrid Energy Storage of Ni(OH)$_2$-coated N-doped Graphene Aerogel//N-doped Graphene Aerogel for the Replacement of NiCd and NiMH Batteries. *Science Report.* **2017**, 7 (1), 1124.

15. A. Shukla, S. Venugopalan, B. Hariprakash. Nickel-based rechargeable

batteries. *Journal of Power Sources*. **2001**, 100 (4), 125-148.

16. J. Xie, Y.C. Lu. A retrospective on lithium-ion batteries. *Nature Communications*. **2020**, 11, 2499.

17. X. Wang, Y. Yang. Effective energy storage from a hybridized electromagnetic-triboelectric nanogenerator. *Nano Energy.* **2017**, 32, 36–41.

18. A. Sharma, V. V. Tyagi, C.R. Chen, D. Buddhi. Review on thermal energy storage with phase change materials and applications. *Renewable and Sustainable Energy Reviews*. **2009**, 13 (2), 318–345.

19. M.M. Farid, A.M. Khudhair, S.A.K. Razack, S. Al-Hallaj. A review on phase change energy storage: Materials and applications. *Energy Conversion and Management*. **2004**, 45, 1597–1615.

20. B. Dunn, H. Kamath, J.-M. Tarascon. Electrical Energy Storage for the Grid: A Battery of Choices System power ratings, module size. *Materials for Grid Energy.* **2011**, 334, 928–935.

21. K. Brandt. Historical development of secondary lithium batteries. *Solid State Ion.* **1994**, 69, 173–183.

22. J.T. Frith, M.J. Lacey, U. Ulissi. A non-academic perspective on the future of lithium-based batteries. *Nature Communications*. **2023**, 14, 420.

23. U.K. Das, P. Shrivastava, K.S. Tey, et al. Advancement of lithium-ion battery cells voltage equalization techniques: A review. *Renewable and Sustainable Energy Reviews*. **2020**, 134,110227.

24. L. Lu, X. Han, J. Li, J. Hua, M. Ouyang. A review on the key issues for lithium-ion battery management in electric vehicles. *Journal of Power Sources*. **2013**, 226, 272–288.

25. V. Etacheri, R. Marom, R. Elazari, G. Salitra, D. Aurbach. Challenges in the development of advanced Li-ion batteries: A review. *Energy and Environmental Science*. **2011**, 4, 3243–3262.

26. N. Nitta, F. Wu, J.T. Lee, G. Yushin. Li-ion battery materials: Present and future. *Materials Today*. **2015**, 18 (5), 252–264.

27. S. Nowak, M. Winter. Elemental analysis of lithium ion batteries. *Journal of Analytical Atomic Spectrometry*. **2017**, 32 (10), 1833–1847.

28. D. Aurbach, Y. Talyosef, B. Markovsky, et al. Design of electrolyte solutions for Li and Li-ion batteries: A review. *Electrochimica Acta*. **2004**, 50, 247–254.

29. S. Goriparti, E. Miele, F. De Angelis, et al. Review on recent progress of nanostructured anode materials for Li-ion batteries. *Journal of Power Sources*. **2014**, 257, 421–443.

30. S.S. Zhang. A review on the separators of liquid electrolyte Li-ion batteries. *Journal of Power Sources*. **2007**, 164 (2), 351–364.

31. J.B. Goodenough, K.S. Park. The Li-ion rechargeable battery: A perspective. *Journal of the American Chemical Society*. **2013**, 135 (4), 1167–1176.

32. R. Marom, S.F. Amalraj, N. Leifer, D. Jacob, D. Aurbach. A review of

advanced and practical lithium battery materials. *Journal of Materials Chemistry.* **2011**, 21 (27), 9938–9954.

33. J.B. Goodenough, Y. Kim. Challenges for rechargeable batteries. *Journal of Power Sources.* **2011**, 196 (16), 6688–6694.

34. S. Zhao, Z. Guo, K. Yan, et al. Towards high-energy-density lithium-ion batteries: Strategies for developing high-capacity lithium-rich cathode materials. *Energy Storage Materials*. **2021**, 34, 716–734.

35. W. He, W. Guo, H. Wu, et al. Achieving Remarkable Charge Density via Self-Polarization of Polar High-k Material in a Charge-Excitation Triboelectric Nanogenerator. *Advanced Materials.* **2022**, 34 (13), 2109918.

36. J. Xu, S. Dou, H. Liu, L. Dai. Cathode materials for next generation lithium ion batteries. *Nano Energy.* **2013**, 2 (4), 439–442.

37. J.W. Fergus. Recent developments in cathode materials for lithium ion batteries. *Journal of Power Sources*. **2010**, 195 (4), 939–954.

38. A. Yamada, S.C. Chung, K. Hinokuma. Optimized $LiFePO_4$ for Lithium Battery Cathodes. *Journal of The Electrochemical Society.* **2001**, 148 (3), A224.

39. G. Liang, V.K. Peterson, K.W. See, Z. Guo, W.K. Pang. Developing high-voltage spinel $LiNi_{0.5}Mn_{1.5}O_4$ cathodes for high-energy-density lithium-ion batteries: Current achievements and future prospects. *Journal of Materials Chemistry A*. **2020**, 8 (31), 15373–15398.

40. H.W. Lee, P. Muralidharan, R. Ruffo, et al. Ultrathin spinel $LiMn_2O_4$ nanowires as high power cathode materials for Li-ion batteries. *Nano Letters.* **2010**, 10 (10), 3852–3856.

41. W. Lee, S. Muhammad, C. Sergey, et al. Advances in the Cathode Materials for Lithium Rechargeable Batteries. *Angewandte Chemie.* **2020**, 132 (7), 2598–2626.

42. J. Liu, J. Wang, Y. Ni, et al. Recent breakthroughs and perspectives of high-energy layered oxide cathode materials for lithium ion batteries. *Materials Today*. **2021**, 43, 132–165.

43. K. Wang, J. Wan, Y. Xiang, et al. Recent advances and historical developments of high voltage lithium cobalt oxide materials for rechargeable Li-ion batteries. *Journal of Power Sources*. **2020**, 460, 228062.

44. S. Zhang, J. Ma, Z. Hu, G. Cui, L. Chen. Identifying and Addressing Critical Challenges of High-Voltage Layered Ternary Oxide Cathode Materials. *Chemistry of Materials*. **2019**, 31 (16), 6033–6065.

45. X. Wang, X. Wang, Y. Lu. Realizing high voltage lithium cobalt oxide in lithium-ion batteries. *Industrial and Engineering Chemistry Research.* **2019**, 58 (24), 10119–10139.

46. J. Xiang, Y. Wei, Y. Zhong, et al. Building Practical High-Voltage Cathode Materials for Lithium-Ion Batteries. *Advanced Materials*. **2022**, 34 (52), 2200912.

47. S. Zhao, K. Yan, J. Zhang, B. Sun, G. Wang. Reaction Mechanisms of Layered Lithium-Rich Cathode Materials for High-Energy Lithium-Ion Batteries. *Angewandte Chemie - International Edition*. **2021**, 60 (5), 2208–2220.

48. Y. Lei, J. Ni, Z. Hu, et al. Surface Modification of Li-Rich Mn-Based Layered Oxide Cathodes: Challenges, Materials, Methods, and Characterization. *Advanced Energy Materials*. **2020**, 10 (41), 2002506.

49. Y. Huang, Y. Zhu, H. Fu, et al. Mg-Pillared $LiCoO_2$: Towards Stable Cycling at 4.6 V. *Angewandte Chemie - International Edition.* **2021**, 60 (9), 4682–4688.

50. Y. Wang, Q. Zhang, Z.C. Xue, et al. An In Situ Formed Surface Coating Layer Enabling $LiCoO_2$ with Stable 4.6 V High-Voltage Cycle Performances. *Advanced Energy Materials.* **2020**, 10 (28), 2001413.

51. Y. Bi, W. Yang, R. Du, et al. Correlation of oxygen non-stoichiometry to the instabilities and electrochemical performance of $LiNi_{0.8}Co_{0.1}Mn_{0.1}O_2$ utilized in lithium ion battery. *Journal of Power Sources.* **2015**, 283, 211–218.

52. J.U. Choi, N. Voronina, Y.K. Sun, S.T. Myung. Recent Progress and Perspective of Advanced High-Energy Co-Less Ni-Rich Cathodes for Li-Ion Batteries: Yesterday, Today, and Tomorrow. *Advanced Energy Materials*. **2020**, 10 (42), 2002027.

53. H.J. Noh, S. Youn, C.S. Yoon, Y.K. Sun. Comparison of the structural and electrochemical properties of layered $Li[Ni_xCo_yMn_z]O_2$ (x = 1/3, 0.5, 0.6, 0.7, 0.8 and 0.85) cathode material for lithium-ion batteries. *Journal of Power Sources.* **2013**, 233, 121–130.

54. H. Maleki Kheimeh Sari, X. Li. Controllable Cathode–Electrolyte Interface of $LiNi_{0.8}Co_{0.1}Mn_{0.1}O_2$ for Lithium Ion Batteries: A Review. *Advanced Energy Materials*. **2019**, 9 (39), 1901597.

55. S.K. Hu, G.H. Cheng, M.Y. Cheng, B.J. Hwang, R. Santhanam. Cycle life improvement of ZrO2-coated spherical $LiNi_{1/3}Co_{1/3}Mn_{1/3}O_2$ cathode material for lithium ion batteries. *Journal of Power Sources.* **2009**, 188 (2), 564–569.

56. S.S. Jan, S. Nurgul, X. Shi, H. Xia, H. Pang. Improvement of electrochemical performance of $LiNi_{0.8}Co_{0.1}Mn_{0.1}O_2$ cathode material by graphene nanosheets modification. *Electrochimica Acta.* **2014**, 149, 86–93.

57. Y. Zhang, X.G. Zhang, H.L. Zhang, et al. Composite anode material of silicon/graphite/carbon nanotubes for Li-ion batteries. *Electrochimica Acta.* **2006**, 51 (23), 4994–5000.

58. L. Ji, Z. Lin, M. Alcoutlabi, X. Zhang. Recent developments in nanostructured anode materials for rechargeable lithium-ion batteries. *Energy and Environmental Science*. **2011**, 4 (8), 2682–2689.

59. T. Ohzuku, Y. Iwakoshi, K. Sawai. Formation of Lithium-Graphite Intercalation Compounds in Nonaqueous Electrolytes and Their

Application as a Negative Electrode for a Lithium Ion (Shuttlecock) Cell. Journal of The Electrochemical Society. **1993**, 140, 2490.

60. X. Xin, X. Zhou, F. Wang, et al. A 3D porous architecture of Si/graphene nanocomposite as high-performance anode materials for Li-ion batteries. *Journal of Materials Chemistry.* **2012**, 22 (16), 7724–7730.

61. H. Kim, G. Yoon, K. Lim, K. Kang. A comparative study of graphite electrodes using the co-intercalation phenomenon for rechargeable Li, Na and K batteries. *Chemical Communications.* **2016**, 52 (85), 12618–12621.

62. X. Shen, Z. Tian, R. Fan, L. Shao, D. Zhang, G. Cao, L. Kuo, Y. Bai. Research progress on Si/C composites as anode for lithium ion batteries. *Journal of Energy Chemistry.* **2018**, 27(4), 1067-1090.

63. W. Tang, X. Yin, S. Kang, et al. Lithium silicide surface enrichment: A solution to lithium metal battery. *Advanced Materials.* **2018**, 30 (34).

64. X. Su, Q. Wu, J. Li, et al. Silicon-Based nanomaterials for lithium-ion batteries: A review. *Advanced Energy Materials.* **2014**, 4 (1), 1300882.

65. P. Li, G. Zhao, X. Zheng, et al. Recent progress on silicon-based anode materials for practical lithium-ion battery applications. *Energy Storage Materials.* **2018**, 15, 422–446.

66. J. Ji, H. Ji, L.L. Zhang, et al. Graphene-encapsulated Si on ultrathin-graphite foam as anode for high capacity lithium-ion batteries. *Advanced Materials.* **2013**, 25 (33), 4673–4677.

67. X. Zuo, J. Zhu, P. Müller-Buschbaum, Y.J. Cheng. Silicon based lithium-ion battery anodes: A chronicle perspective review. *Nano Energy.* **2017**, 31, 113–143.

68. W. Xu, J. Wang, F. Ding, et al. Lithium metal anodes for rechargeable batteries. *Energy and Environmental Science.* **2014**, 7 (2), 513–537.

69. J. Qian, W.A. Henderson, W. Xu, et al. High rate and stable cycling of lithium metal anode. *Nature Communications.* **2015**, 6, 6362.

70. H. Zhang, X. Liao, Y. Guan, et al. Lithiophilic-lithiophobic gradient interfacial layer for a highly stable lithium metal anode. *Nature Communications.* **2018**, 9 (1), 3729.

71. D. Lin, Y. Liu, Y. Cui. Reviving the lithium metal anode for high-energy batteries. *Nature Nanotechnology.* **2017**, 12, 194–206.

72. A. Jana, S.I. Woo, K.S.N. Vikrant, R.E. García. Electrochemomechanics of lithium dendrite growth. *Energy and Environment Science.* **2019**, 12 (12), 3595–3607.

73. D. Aurbach. Review of selected electrode-solution interactions which determine the performance of Li and Li ion batteries. *Journal of Power Sources.* **2000**, 89 (2), 206-218.

74. K. Xu. Nonaqueous liquid electrolytes for lithium-based rechargeable batteries. *Chemical Reviews.* **2004**, 104 (10), 4303–4417.

75. J. Zhang, X. Yao, R.K. Misra, Q. Cai, Y. Zhao. Progress in electrolytes for beyond-lithium-ion batteries. *Journal of Materials Science and*

Technology. **2020**, 44, 237–257.

76. D. Aurbach, E. Zinigrad, Y. Cohen, H. Teller. A short review of failure mechanisms of lithium metal and lithiated graphite anodes in liquid electrolyte solutions. Solid State Ionics. **2002**, 148 (3-4), 405-416.

77. L. Li, S. Zhou, H. Han, et al. Transport and Electrochemical Properties and Spectral Features of Non-Aqueous Electrolytes Containing LiFSI in Linear Carbonate Solvents. *Journal of The Electrochemical Society* **2011**, 158 (2), A74.

78. W. Märkle, N. Tran, D. Goers, M.E. Spahr, P. Novák. The influence of electrolyte and graphite type on the PF_6^- intercalation behaviour at high potentials. *Carbon.* **2009**, 47 (11), 2727–2732.

79. H.B. Han, S.S. Zhou, D.J. Zhang, et al. Lithium bis(fluorosulfonyl)imide (LiFSI) as conducting salt for nonaqueous liquid electrolytes for lithium-ion batteries: Physicochemical and electrochemical properties. *Journal of Power Sources.* **2011**, 196 (7), 3623–3632.

80. S.J. Kang, K. Park, S.H. Park, H. Lee. Unraveling the role of LiFSI electrolyte in the superior performance of graphite anodes for Li-ion batteries. *Electrochimica Acta.* **2018**, 259, 949–954.

81. A.M. Haregewoin, A.S. Wotango, B.J. Hwang. Electrolyte additives for lithium ion battery electrodes: Progress and perspectives. *Energy and Environmental Science.* **2016**, 9 (6), 1955–1988.

82. Y. Zhu, Y. Li, M. Bettge, D.P. Abraham. Positive Electrode Passivation by LiDFOB Electrolyte Additive in High-Capacity Lithium-Ion Cells. *Journal of The Electrochemical Society.* **2012**, 159 (12), A2109–A2117.

83. S.S. Zhang, K. Xu, T.R. Jow. Study of LiBF[sub 4] as an Electrolyte Salt for a Li-Ion Battery. *Journal of The Electrochemical Society.* **2002**, 149 (5), A586.

84. T. Kawamura, S. Okada, J. ichi Yamaki. Decomposition reaction of LiPF6-based electrolytes for lithium ion cells. *Journal of Power Sources.* **2006**, 156 (2), 547–554.

85. K. Xu, S. Zhang, T.R. Jow, W. Xu, C.A. Angell. LiBOB as salt for lithium-ion batteries. A possible solution for high temperature operation. *Electrochemical and Solid-State Letters* **2002**, 5 (1), A26.

86. M. Xu, L. Zhou, L. Hao, et al. Investigation and application of lithium difluoro(oxalate)borate (LiDFOB) as additive to improve the thermal stability of electrolyte for lithium-ion batteries. *Journal of Power Sources* **2011**, 196 (16), 6794–6801.

87. C.L. Campion, W. Li, B.L. Lucht. Thermal Decomposition of $LiPF_6^-$ Based Electrolytes for Lithium-Ion Batteries. *Journal of The Electrochemical Society.* **2005**, 152 (12), A2327.

88. B.S. Parimalam, B.L. Lucht. Reduction Reactions of Electrolyte Salts for Lithium Ion Batteries: $LiPF_6$, $LiBF_4$, LiDFOB, LiBOB, and LiTFSI. *Journal of The Electrochemical Society.* **2018**, 165 (2), A251–A255.

89. K. Xu. Electrolytes and interphases in Li-ion batteries and beyond.

Chemical Reviews. **2014**, 114 (23), 11503–11618.

90. S.J. An, J. Li, C. Daniel, et al. The state of understanding of the lithium-ion-battery graphite solid electrolyte interphase (SEI) and its relationship to formation cycling. *Carbon*. **2016**, 105, 52–76.

91. D. Lu, J. Tao, P. Yan, et al. Formation of Reversible Solid Electrolyte Interface on Graphite Surface from Concentrated Electrolytes. *Nano Letters*. **2017**, 17 (3), 1602–1609.

92. S. Hong, B. Hong, W. Song, et al. Communication—Lithium Difluorophosphate as an Electrolyte Additive to Improve the High Voltage Performance of $LiNi_{0.5}Co_{0.2}Mn_{0.3}O_2$/Graphite Cell. *Journal of The Electrochemical Society*. **2018**, 165 (2), A368–A370.

93. C. Wang, L. Yu, W. Fan, et al. Enhanced high-voltage cyclability of $LiNi_{0.5}Co_{0.2}Mn_{0.3}O_2$-based pouch cells via lithium difluorophosphate introducing as electrolyte additive. *Journal of Alloys and Compounds*. **2018**, 755, 1–9.

94. Y. Li, B. Cheng, F. Jiao, K. Wu. The Roles and Working Mechanism of Salt-Type Additives on the Performance of High-Voltage Lithium-Ion Batteries. *ACS Applied Materials and Interfaces*. **2020**, 12 (14), 16298–16307.

95. G. Xu, S. Huang, Z. Cui, et al. Functional additives assisted ester-carbonate electrolyte enables wide temperature operation of a high-voltage (5 V-Class) Li-ion battery. *Journal of Power Sources* **2019**, 416, 29–36.

96. W. Wang, C. Liao, L. Liu, et al. Comparable investigation of tervalent and pentavalent phosphorus based flame retardants on improving the safety and capacity of lithium-ion batteries. *Journal of Power Sources*. **2019**, 420, 143–151.

97. R. Mogi, M. Inaba, S.-K. Jeong, et al. Effects of Some Organic Additives on Lithium Deposition in Propylene Carbonate. *Journal of The Electrochemical Society*. **2002**, 149 (12), A1578.

98. Z. Zou, H. Xu, H. Zhang, Y. Tang, G. Cui. Electrolyte Therapy for Improving the Performance of $LiNi_{0.5}Mn_{1.5}O_4$ Cathodes Assembled Lithium-Ion Batteries. *ACS Applied Materials and Interfaces*. **2020**, 12 (19), 21368–21385.

99. G.G. Eshetu, M. Martinez-Ibañez, E. Sánchez-Diez, et al. Electrolyte Additives for Room-Temperature, Sodium-Based, Rechargeable Batteries. *Chemistry - An Asian Journal*. **2018**, 13 (19), 2770–2780.

100. X. Shangguan, G. Xu, Z. Cui, et al. Additive-Assisted Novel Dual-Salt Electrolyte Addresses Wide Temperature Operation of Lithium–Metal Batteries. *Small*. **2019**, 15 (16), 1900269.

101. Z.A. Ghazi, Z. Sun, C. Sun, et al. Key Aspects of Lithium Metal Anodes for Lithium Metal Batteries. *Small*. **2019**, 15 (32), 1900687.

102. M.K. Ohno, M. Sato, Y. Arita. A Comparative Study of Synthetic Graphite and Li Electrodes in Electrolyte Solutions Based on Ethylene Carbonate-

Dimethyl Carbonate Mixtures. *Journal of The Electrochemical Society*. **1996**, 143, 3809.

103. A. Zaban, D. Aurbach. Impedance spectroscopy of lithium and nickel electrodes propylene carbonate solutions of different lithium salts A comparative study. *Journal of Power Sources.* **1995**, 54 (2), 289-295.

104. P.Y. Hou, J. Stringer, J.S. Lee, H.B. Im, A.L. Fahrenbruch. Identification of Surface Films Formed on Lithium in Propylene Carbonate Solutions. *Journal of The Electrochemical Society*. **1987**, 134, 1611.

105. D. Aurbach, A. Zaban, Y. Gofer, et al. Recent studies of the lithium-liquid electrolyte interface Electrochemical, morphological and spectral studies of a few important systems. *Journal of Power Sources.* **1995**, 54 (1), 76-84.

106. D. Aurbach. The electrochemical behavior of selected polar aprotic systems. *Electrochimica Acta*. **1989**, 34 (2), 141-156.

107. A. Schechter, D. Aurbach, H. Cohen. X-ray photoelectron spectroscopy study of surface films formed on Li electrodes freshly prepared in alkyl carbonate solutions. *Langmuir.* **1999**, 15 (9), 3334–3342.

108. P. Shi, F. Liu, Y. Feng, et al. Lithium Metal Batteries: The Synergetic Effect of Lithium Bisoxalatodifluorophosphate and Fluoroethylene Carbonate on Dendrite Suppression for Fast Charging Lithium Metal Batteries. *Small.* **2020**, 16 (30), 2070164.

109. Y. Xu, H. Wu, H. Jia, et al. Sweeping potential regulated structural and chemical evolution of solid-electrolyte interphase on Cu and Li as revealed by cryo-TEM. *Nano Energy.* **2020**, 76, 105040.

110. Y. Zhang, Y. Zhong, Z. Wu, et al. Solvent Molecule Cooperation Enhancing Lithium Metal Battery Performance at Both Electrodes. *Angewandte Chemie - International Edition.* **2020**, 59 (20), 7797–7802.

111. J. Fu, X. Ji, J. Chen, et al. Lithium Nitrate Regulated Sulfone Electrolytes for Lithium Metal Batteries. *Angewandte Chemie - International Edition.* **2020**, 59 (49), 22194–22201.

112. F. Ding, W. Xu, G.L. Graff, et al. Dendrite-free lithium deposition via self-healing electrostatic shield mechanism. *Journal of The American Chemical Society.* **2013**, 135 (11), 4450–4456.

113. W. Jia, C. Fan, L. Wang, et al. Extremely Accessible Potassium Nitrate (KNO3) as the Highly Efficient Electrolyte Additive in Lithium Battery. *ACS Applied Materials and Interfaces.* **2016**, 8 (24), 15399–15405.

114. Z. Peng, J. Song, L. Huai, et al. Enhanced Stability of Li Metal Anodes by Synergetic Control of Nucleation and the Solid Electrolyte Interphase. *Advanced Energy Materials.* **2019**, 9 (42), 1901764.

115. X. Liang, Q. Pang, I.R. Kochetkov, et al. A facile surface chemistry route to a stabilized lithium metal anode. *Nature Energy.* **2017**, 2, 17119.

116. J. Dong, H. Dai, Q. Fan, C. Lai, S. Zhang. Grain refining mechanisms: Initial levelling stage during nucleation for high-stability lithium anodes. *Nano Energy.* **2019**, 66, 104128.

117. L. Liu, S. Gu, S. Wang, X. Zhang, S. Chen. A $LiPO_2F_2$/$LiPF_6$ dual-salt electrolyte enabled stable cycling performance of nickel-rich lithium ion batteries. *RSC Advances.* **2020**, 10 (3), 1704–1710.

118. P. Shi, F. Liu, Y.Z. Feng, et al. The Synergetic Effect of Lithium Bisoxalatodifluorophosphate and Fluoroethylene Carbonate on Dendrite Suppression for Fast Charging Lithium Metal Batteries. *Small.* **2020**, 16 (30), 2070164.

119. S. Lin, J. Zhao. Bifunctional Lithium Carboxylate for Stabilizing Both Lithium-Metal Anode and High-Voltage Cathode in Ether Electrolyte. *ACS ACS Applied Materials and Interfaces.* **2019**, 11 (43), 39715–39721.

120. X.R. Chen, Y.X. Yao, C. Yan, et al. A Diffusion--Reaction Competition Mechanism to Tailor Lithium Deposition for Lithium-Metal Batteries. *Angewandte Chemie - International Edition.* **2020**, 59 (20), 7743–7747.

121. Y.M. Song, J.G. Han, S. Park, K.T. Lee, N.S. Choi. A multifunctional phosphite-containing electrolyte for 5 V-class $LiNi_{0.5}Mn_{1.5}O_4$ cathodes with superior electrochemical performance. *Journal of The American Chemical Society.* **2014**, 2 (25), 9506–9513.

122. X. Liao, Q. Huang, S. Mai, et al. Self-discharge suppression of 4.9 V $LiNi_{0.5}Mn_{1.5}O_4$ cathode by using tris(trimethylsilyl)borate as an electrolyte additive. *Journal of Power Sources.* **2014**, 272, 501–507.

123. X. Wang, W. Xue, K. Hu, et al. Adiponitrile as Lithium-Ion Battery Electrolyte Additive: A Positive and Peculiar Effect on High-Voltage Systems. *ACS Applied Energy Materials* **2018**, 1 (10), 5347–5354.

124. N. Xu, H. Zhou, Y. Liao, et al. A facile strategy to improve the cycle stability of 4.45 V $LiCoO_2$ cathode in gel electrolyte system via succinonitrile additive under elevated temperature. *Solid State Ion.* **2019**, 341, 115049.

125. X.T. Wang, Z.Y. Gu, W.H. Li, et al. Regulation of Cathode-Electrolyte Interphase via Electrolyte Additives in Lithium Ion Batteries. *Chemistry - An Asian Journal*. **2020**, 15 (18), 2803–2814.

126. L. Yang, T. Markmaitree, B.L. Lucht. Inorganic additives for passivation of high voltage cathode materials. *Journal of Power Sources.* **2011**, 196 (4), 2251–2254.

127. Q. Zhang, J.J. Chen, X.Y. Wang, et al. Enhanced electrochemical performance and thermal stability of $LiNi_{0.5}Mn_{1.5}O_4$ using an electrolyte with sulfolane. *Physical Chemistry Chemical Physics.* **2015**, 17 (16), 10353–10357.

128. L. Xue, K. Ueno, S.Y. Lee, C.A. Angell. Enhanced performance of sulfone-based electrolytes at lithium ion battery electrodes, including the $LiNi_{0.5}Mn_{1.5}O_4$ high voltage cathode. *Journal of Power Sources.* **2014**, 262, 123–128.

129. C.C. Su, M. He, P. Redfern, et al. Alkyl Substitution Effect on Oxidation Stability of Sulfone-Based Electrolytes. *ChemElectroChem.* **2016**, 3 (5), 790–797.

130. S. Tan, Y.J. Ji, Z.R. Zhang, Y. Yang. Recent progress in research on high-

voltage electrolytes for lithium-ion batteries. *ChemPhysChem*. **2014**, 15 (10), 1956–1969.

131. A.J. Gmitter, I. Plitz, G.G. Amatucci. High Concentration Dinitrile, 3-Alkoxypropionitrile, and Linear Carbonate Electrolytes Enabled by Vinylene and Monofluoroethylene Carbonate Additives. *Journal of The Electrochemical Society*. **2012**, 159 (4), A370–A379.

132. K. Matsumoto, M. Martinez, T. Gutel, et al. Stability of trimethyl phosphate non-flammable based electrolyte on the high voltage cathode ($LiNi_{0.5}Mn_{1.5}O_4$). *Journal of Power Sources.* **2015**, 273, 1084–1088.

133. K. Matsumoto, J. Hwang, S. Kaushik, C.Y. Chen, R. Hagiwara. Advances in sodium secondary batteries utilizing ionic liquid electrolytes. *Energy and Environmental Science*. **2019**, 12 (11), 3247–3287.

134. Y. Xu, L. Wan, J. Liu, L. Zeng, Z. Yang. γ-butyrolactone and glutaronitrile as 5 V electrolyte additive and its electrochemical performance for $LiNi_{0.5}Mn_{1.5}O_4$. *Journal of Alloys and Compounds.* **2017**, 698, 207–214.

135. M. Hu, X. Pang, Z. Zhou. Review Recent progress in high-voltage lithium ion batteries. *Journal of Power Sources*. **2013**, 237, 229–242.

136. D. Zhao, S. Li. Regulating the Performance of Lithium-Ion Battery Focus on the Electrode-Electrolyte Interface. *Frontiers in Chemistry*. **2020**, 8, 821.

137. Y. Lee, T.K. Lee, S. Kim, et al. Fluorine-incorporated interface enhances cycling stability of lithium metal batteries with Ni-rich NCM cathodes. *Nano Energy.* **2020**, 67, 104309.

138. Y. Yamada, K. Furukawa, K. Sodeyama, et al. Unusual stability of acetonitrile-based superconcentrated electrolytes for fast-charging lithium-ion batteries. *Journal of The American Chemical Society.* **2014**, 136 (13), 5039–5046.

139. Y. Jie, X. Ren, R. Cao, W. Cai, S. Jiao. Advanced Liquid Electrolytes for Rechargeable Li Metal Batteries. *Advanced Functional Materials*. **2020**, 30 (25), 1910777.

140. B.D. Adams, E. V. Carino, J.G. Connell, et al. Long term stability of Li-S batteries using high concentration lithium nitrate electrolytes. *Nano Energy.* **2017**, 40, 607–617.

141. Y. Li, Y. An, Y. Tian, et al. High-Safety and High-Voltage Lithium Metal Batteries Enabled by a Nonflammable Ether-Based Electrolyte with Phosphazene as a Cosolvent. *ACS Applied Materials and Interfaces.* **2021**, 13 (8), 10141–10148.

142. S. Jiao, X. Ren, R. Cao, et al. Stable cycling of high-voltage lithium metal batteries in ether electrolytes. *Nature Energy.* **2018**, 3 (9), 739–746.

143. G. Zhang, J. Chang, L. Wang, et al. A monofluoride ether-based electrolyte solution for fast-charging and low-temperature non-aqueous lithium metal batteries. *Nature Communications.* **2023**, 14 (1), 1–13.

144. X. Ren, L. Zou, S. Jiao, et al. High-concentration ether electrolytes for stable high-voltage lithium metal batteries. *ACS Energy Letters.* **2019**, 4

(4), 896–902.

145. W. Dai, N. Dong, Y. Xia, et al. Localized concentrated high-concentration electrolyte enhanced stability and safety for high voltage Li-ion batteries. *Electrochimica Acta.* **2019**, 320, 134633.

146. C. V. Amanchukwu, Z. Yu, X. Kong, et al. A New Class of Ionically Conducting Fluorinated Ether Electrolytes with High Electrochemical Stability. *Journal of The American Chemical Society.* **2020**, 142 (16), 7393–7403.

147. G. Zhang, X. Deng, J. Li, et al. A bifunctional fluorinated ether co-solvent for dendrite-free and long-term lithium metal batteries. *Nano Energy.* **2022**, 95, 107014.

148. J. Qian, W.A. Henderson, W. Xu, et al. High rate and stable cycling of lithium metal anode. *Nature Communications.* **2015**, 6, 6362.

149. F. Huang, G. Ma, Z. Wen, et al. Enhancing metallic lithium battery performance by tuning the electrolyte solution structure. *Journal of Materials Chemistry A.* **2018**, 6 (4), 1612–1620.

150. Y. Yamada, J. Wang, S. Ko, E. Watanabe, A. Yamada. Advances and issues in developing salt-concentrated battery electrolytes. *Nature Energy.* **2019**, 4 (4), 269–280.

151. S. Ko, Y. Yamada, A. Yamada. A 4.8 V Reversible Li_2CoPO_4F/Graphite Battery Enabled by Concentrated Electrolytes and Optimized Cell Design. *Batteries and Supercaps.* **2020**, 3 (9), 910–916.

152. J. Qian, W.A. Henderson, W. Xu, et al. High rate and stable cycling of lithium metal anode. *Nature Communications.* **2015**, 6, 6362.

153. X. Ren, L. Zou, X. Cao, et al. Enabling High-Voltage Lithium-Metal Batteries under Practical Conditions. *Joule.* **2019**, 3 (7), 1662–1676.

154. D.J. Yoo, S. Yang, K.J. Kim, J.W. Choi. Fluorinated Aromatic Diluent for High-Performance Lithium Metal Batteries. *Angewandte Chemie - International Edition.* **2020**, 59 (35), 14869–14876.

155. S. Chen, J. Zheng, L. Yu, et al. High-Efficiency Lithium Metal Batteries with Fire-Retardant Electrolytes. *Joule.* **2018**, 2 (8), 1548–1558.

156. X. Chen, Q. Zhang. Atomic insights into the fundamental interactions in lithium battery electrolytes. *Accounts of Chemical Research.* **2020**, 53 (9), 1992–2002.

157. O. Borodin. Challenges with prediction of battery electrolyte electrochemical stability window and guiding the electrode – electrolyte stabilization. *Current Opinion in Electrochemistry.* **2019**, 13, 86–93.

158. J. Newman, K.E. Thomas, H. Hafezi, D.R. Wheeler. Modeling of lithium-ion batteries. *Journal of Power Sources.* **2003**, 119–121, 838–843.

159. Y. Sun, T. Yang, H. Ji, et al. Boosting the Optimization of Lithium Metal Batteries by Molecular Dynamics Simulations: A Perspective. *Advanced Energy Materials.* **2020**, 10 (41), 2002373.

160. Z. Shi, J. Zhou, R. Li. Application of Reaction Force Field Molecular Dynamics in Lithium Batteries. *Frontiers in Chemistry.* **2021**, 8, 634379.

161. H. Zhao, Y. Qian, G. Luo, et al. Cathode-anode reaction products interplay enabling high performance of LiNi0.8Co0.1Mn0.1O2/artificial graphite pouch batteries at elevated temperature. *Journal of Power Sources.* **2021**, 514, 230583.

162. H. Zhao, J. Wang, H. Shao, K. Xu, Y. Deng. Gas Generation Mechanism in Li-Metal Batteries. *Energy and Environmental Materials* **2022**, 5 (1), 327–336.

163. Z. Yu, H. Wang, X. Kong, et al. Molecular design for electrolyte solvents enabling energy-dense and long-cycling lithium metal batteries. *Nature Energy.* **2020**, 5 (7), 526–533.

164. B. Nan, L. Chen, N.D. Rodrigo, et al. Enhancing Li$^+$ Transport in NMC811||Graphite Lithium-Ion Batteries at Low Temperatures by Using Low-Polarity-Solvent Electrolytes. *Angewandte Chemie - International Edition.* **2022**, 61 (35), e202205967.

165. D.T. Boyle, Y. Li, A. Pei, et al. Resolving Current-Dependent Regimes of Electroplating Mechanisms for Fast Charging Lithium Metal Anodes. *Nano Letters.* **2022**, 22 (20), 8224–8232.

166. J. Zheng, G. Ji, X. Fan, et al. High-Fluorinated Electrolytes for Li–S Batteries. *Advanced Energy Materials.* **2019**, 9 (16), 1–9.

167. X. Ren, L. Zou, X. Cao, et al. Enabling High-Voltage Lithium-Metal Batteries under Practical Conditions. *Joule.* **2019**, 3 (7), 1662–1676.

168. J. Zhang, X. Yao, R.K. Misra, Q. Cai, Y. Zhao. Progress in electrolytes for beyond-lithium-ion batteries. *Journal of Materials Science and Technology.* **2020**, 44, 237–257.

169. X.B. Cheng, R. Zhang, C.Z. Zhao, Q. Zhang. Toward Safe Lithium Metal Anode in Rechargeable Batteries: A Review. *Chemical Reviews.* **2017**, 117 (15), 10403–10473.

170. B. Han, X. Li, S. Bai, et al. Conformal three-dimensional interphase of Li metal anode revealed by low-dose cryoelectron microscopy. *Matter.* **2021**, 4 (11), 3741–3752.

171. N. von Aspern, M. Leissing, C. Wölke, et al. Non-Flammable Fluorinated Phosphorus(III)-Based Electrolytes for Advanced Lithium-Ion Battery Performance. *ChemElectroChem.* **2020**, 7 (6), 1499–1508.

172. B. Jagger, M. Pasta. Solid electrolyte interphases in lithium metal batteries. *Joule.* **2023**, 2228–2244.

173. W. Xue, M. Huang, Y. Li, et al. Ultra-high-voltage Ni-rich layered cathodes in practical Li metal batteries enabled by a sulfonamide-based electrolyte. *Nature Energy* **2021**, 6 (5), 495–505.

174. D. Xu, Y. Kang, J. Wang, et al. Exploring synergetic effects of vinylene carbonate and 1,3-propane sultone on LiNi0.6Mn0.2Co0.2O2/graphite cells with excellent high-temperature performance. *Journal of Power Sources.* **2019**, 437, 226929.

175. Y. Yamada, K. Usui, C.H. Chiang, et al. General observation of lithium intercalation into graphite in ethylene-carbonate-free superconcentrated

electrolytes. *ACS Applied Materials and Interfaces.* **2014**, 6 (14), 10892–10899.

176. S. Chen, Z. Yu, M.L. Gordin, et al. A Fluorinated Ether Electrolyte Enabled High Performance Prelithiated Graphite/Sulfur Batteries. *ACS Applied Materials and Interfaces.* **2017**, 9 (8), 6959–6966.

177. H. Kim, K. Lim, G. Yoon, et al. Exploiting Lithium–Ether Co-Intercalation in Graphite for High-Power Lithium-Ion Batteries. *Advanced Energy Materials.* **2017**, 7 (19), 1–10.

178. X. Fan, C. Wang. High-voltage liquid electrolytes for Li batteries: Progress and perspectives. *Chemical Society Reviews.* **2021**, 50 (18), 10486–10566.

179. D. Xia, E.P. Kamphaus, A. Hu, et al. Design Criteria of Dilute Ether Electrolytes toward Reversible and Fast Intercalation Chemistry of Graphite Anode in Li-Ion Batteries. *ACS Energy Letters.* **2023**, 8 (3), 1379–1389.

180. H. Kim, K. Lim, G. Yoon, et al. Exploiting Lithium–Ether Co-Intercalation in Graphite for High-Power Lithium-Ion Batteries. *Adv Energy Mater* **2017**, 7 (19), 1–10.

181. X. Teng, C. Zhan, Y. Bai, et al. In Situ Analysis of Gas Generation in Lithium-Ion Batteries with Different Carbonate-Based Electrolytes. *ACS Appl Mater Interfaces.* **2015**, 7 (41), 22751–22755.

Appendix

GC-MS
TTME
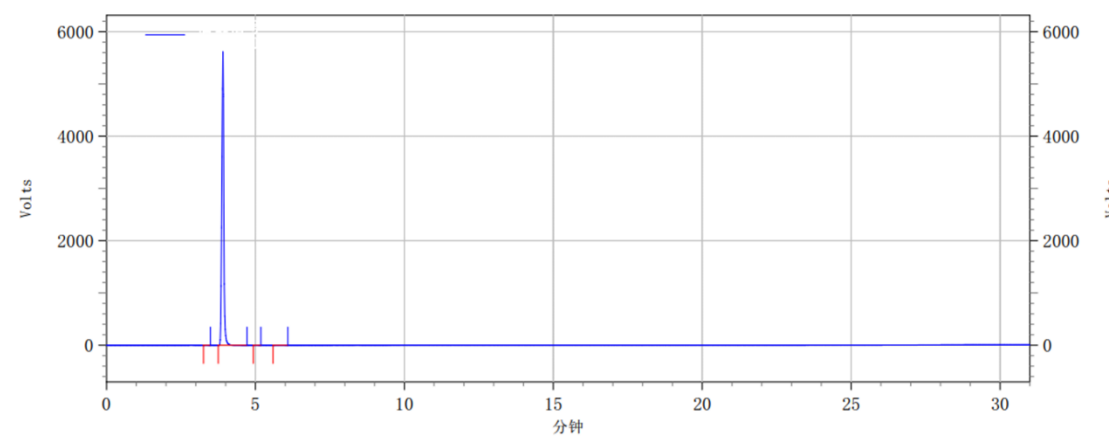
No.		Retention Time	Area	Percentage
1		3.337	41129	0.0207
2	TTME	3.911	198681224	99.9376
3		5.021	11657	0.0059
4		5.749	71216	0.0358
TAL			198805226	100.0000

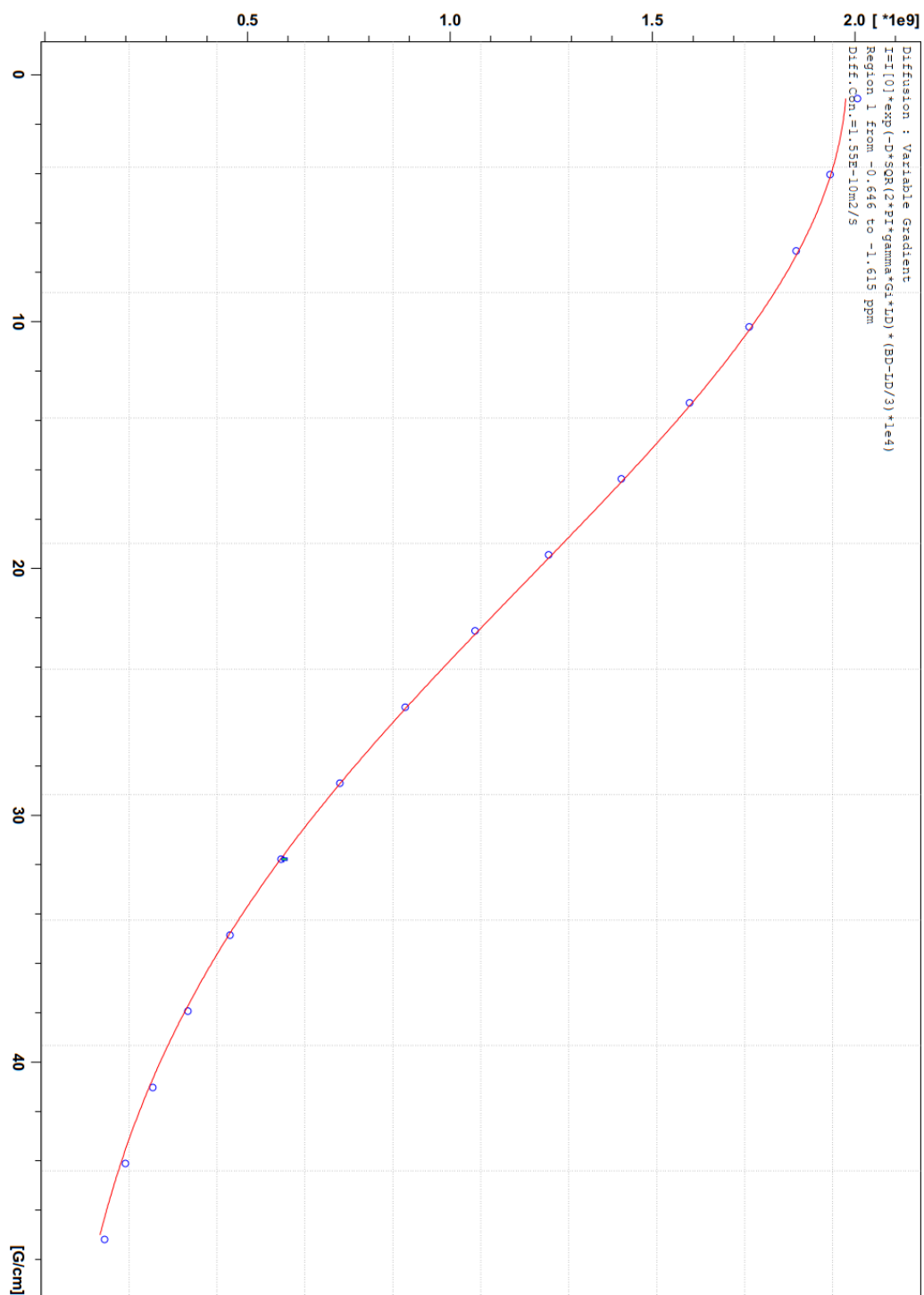Fig. A1. Gas chromatography - mass spectrometry (GC-MS) result for the TTME molecule.
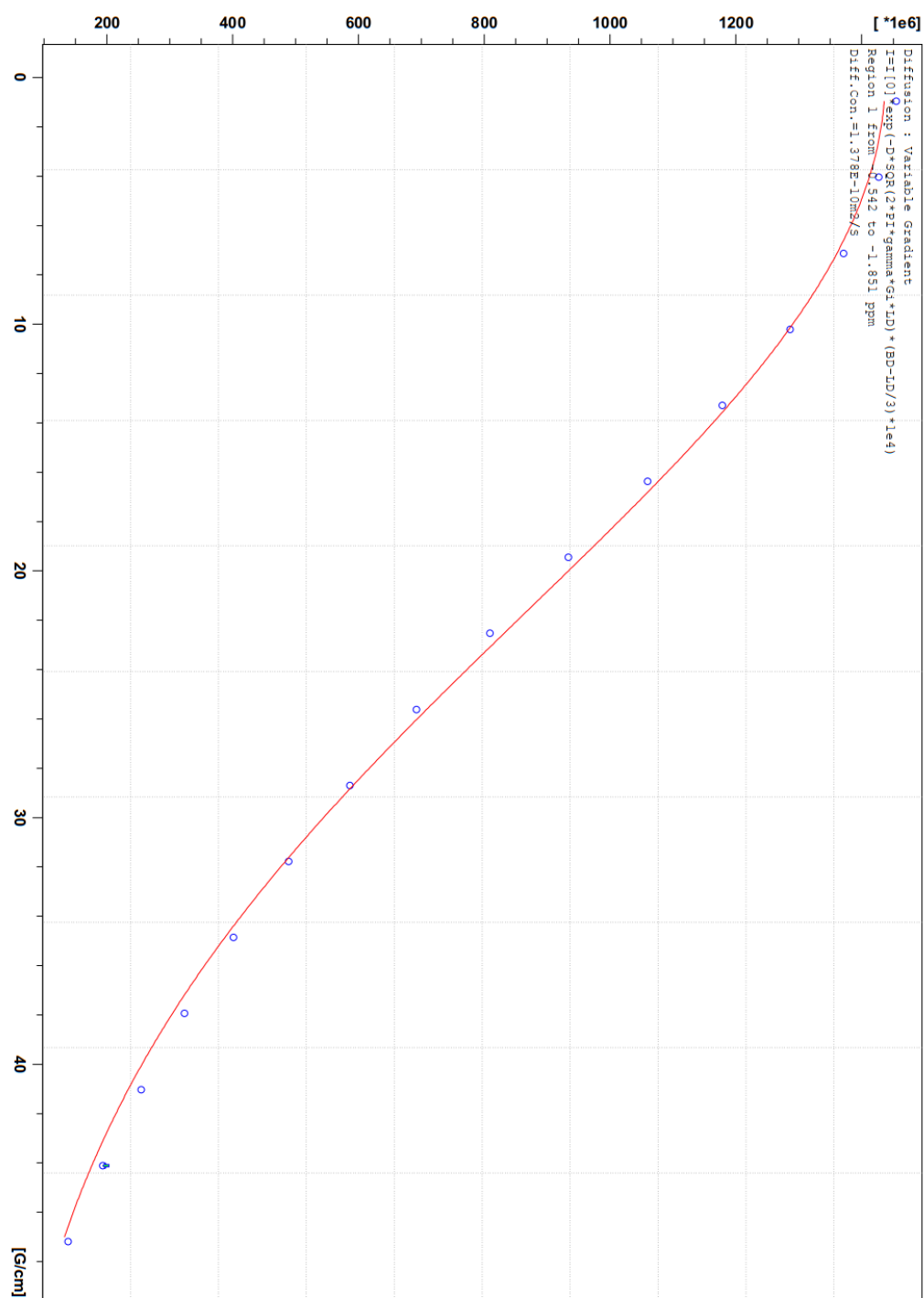
210

Fig. A2. PFG-NMR result of electrolyte DME-d.

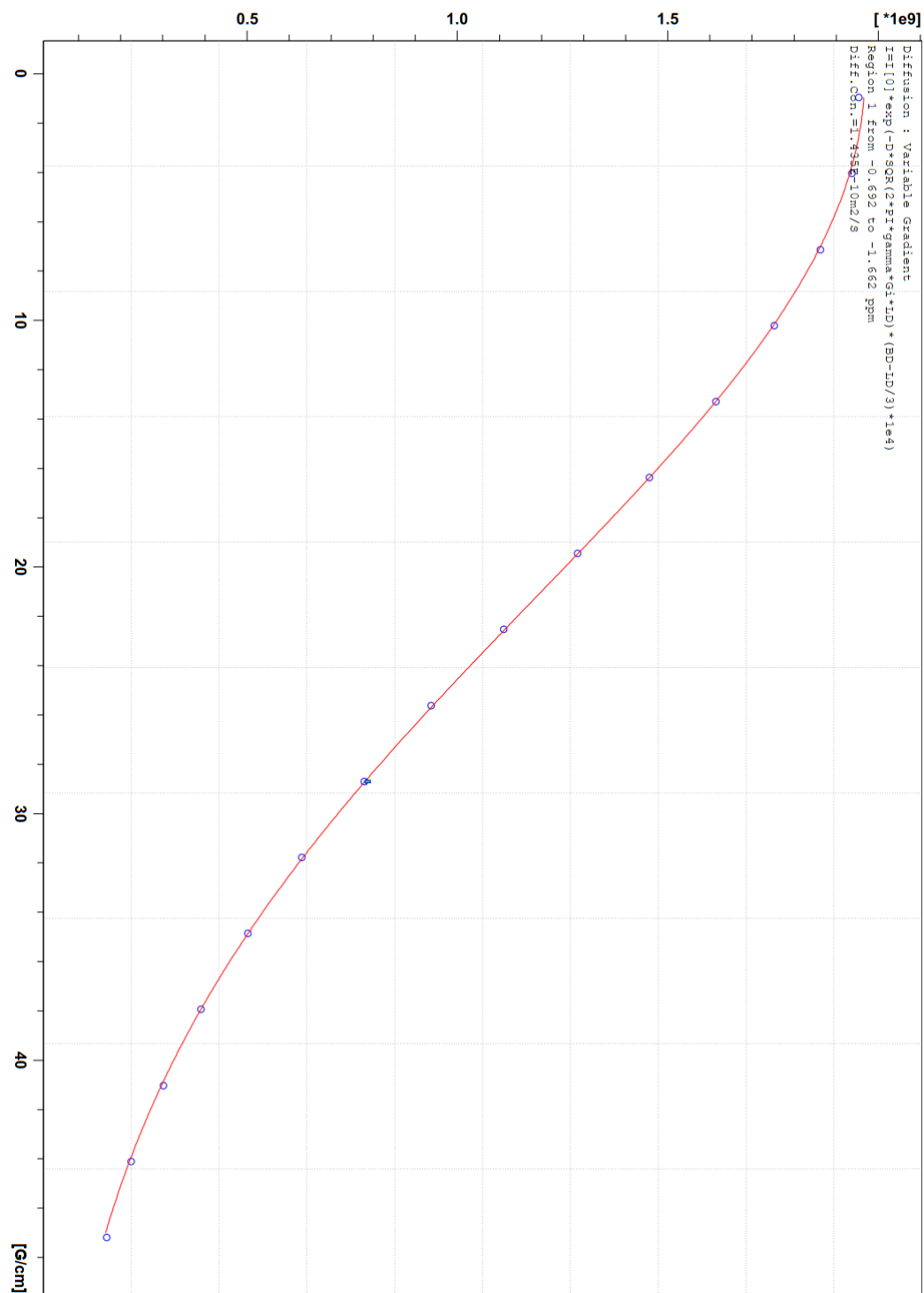Fig. A3. PFG-NMR result of electrolyte composed of TTME : DME in a 1:1 volume ratio, along with 1.4 mol/L LiFSI.

Fig. A4. PFG-NMR result of electrolyte composed of TTME : DME in a 2:1 volume ratio, along with 1.4 mol/L LiFSI.
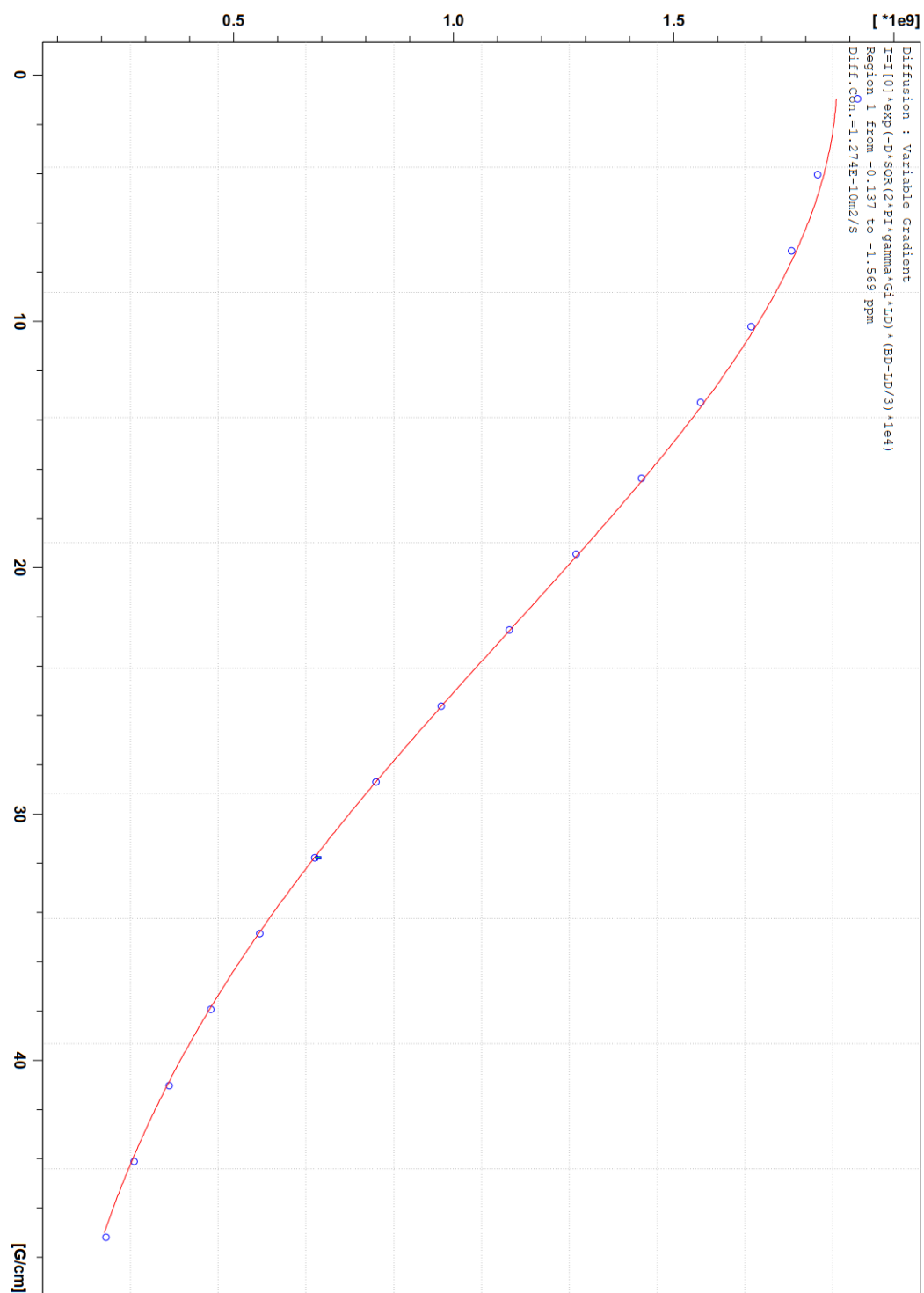
Fig. A5. PFG-NMR result of electrolyte composed of TTME : DME in a 3:1 volume ratio, along with 1.4 mol/L LiFSI.
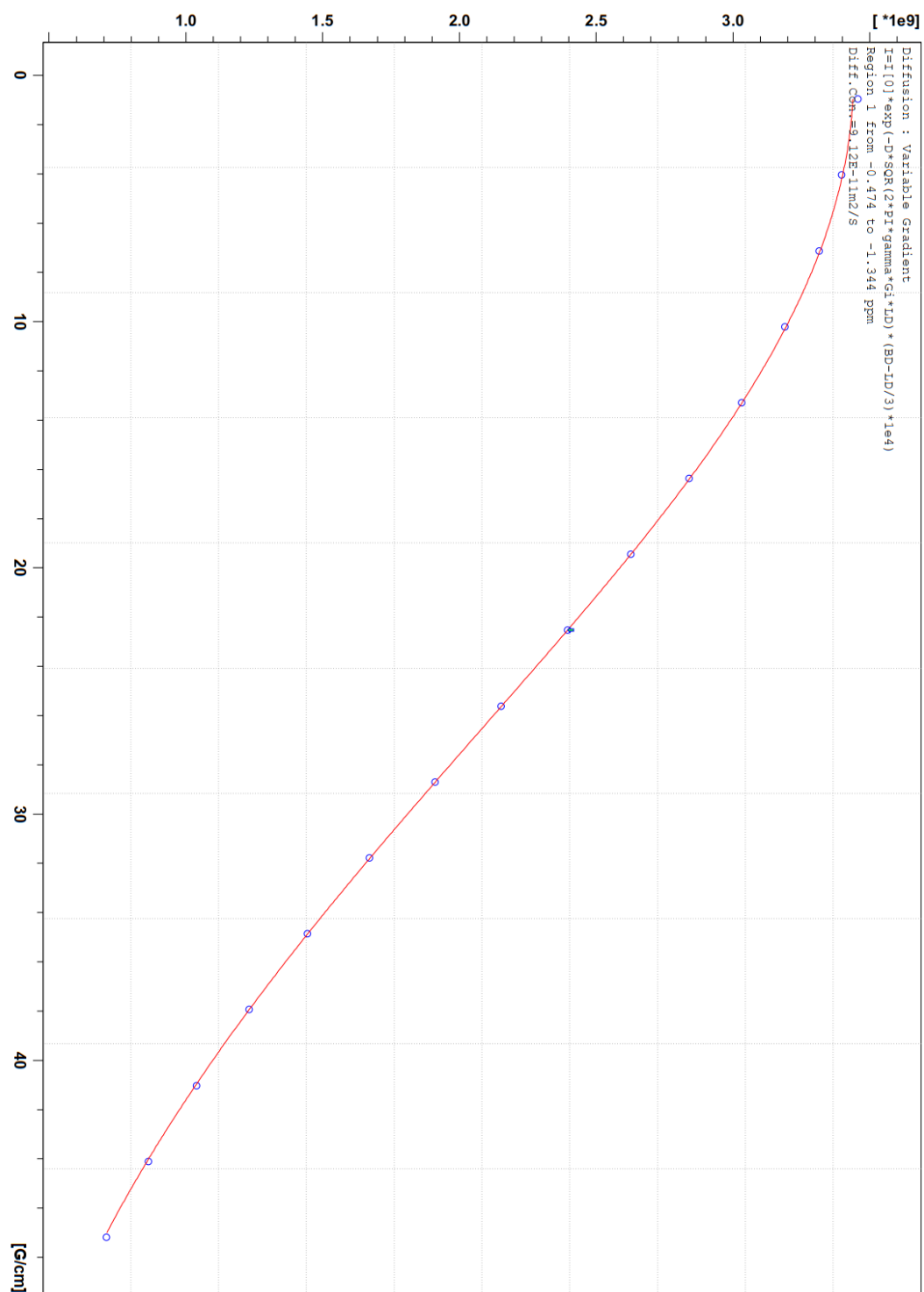
Fig. A6. PFG-NMR result of electrolyte composed of TTME : DME in a 4:1 volume ratio, along with 1.4 mol/L LiFSI (TTME-d).
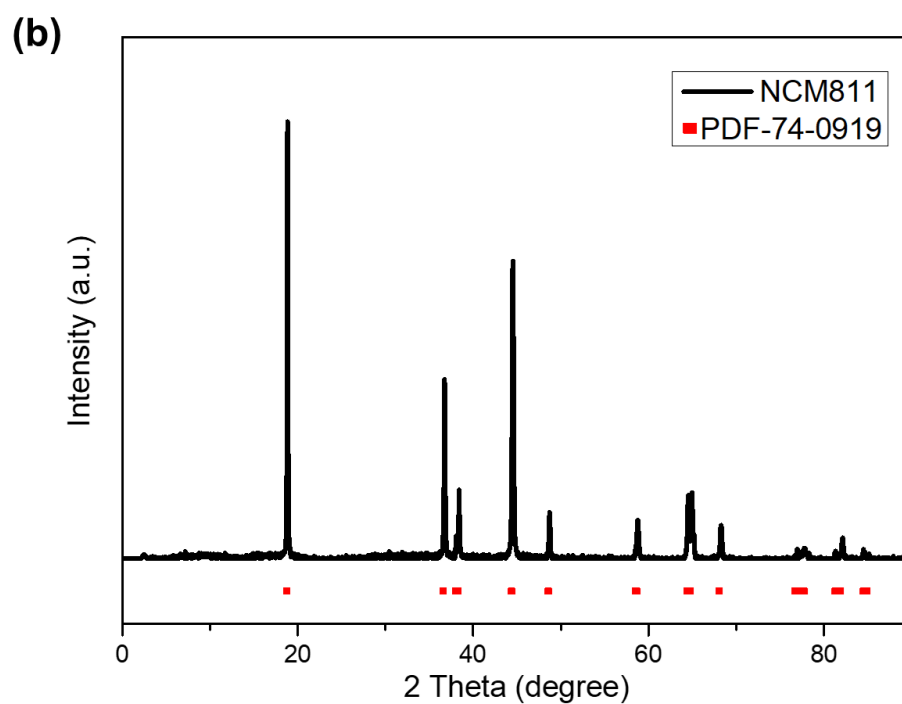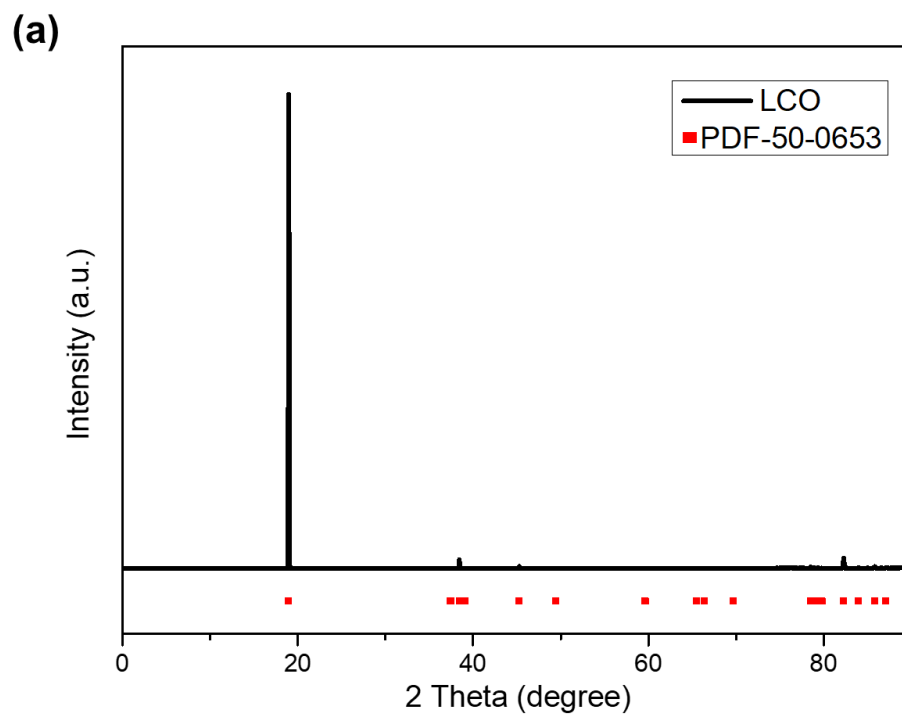
Fig. A7. XRD results of LCO and NCM811 with standard PDF cards.